THE STARK EFFECT ON HELIUM

IN THE BEAM-FOIL SOURCE

Carl John Sofield

A thesis submitted as a requirement

for the degree of

Doctor of Philosophy

at the Australian National University

Canberra,

February, 1974

To

Irja and Brigitta

PREFACE

The work reported in this thesis was carried out in the Department of Nuclear Physics at the Australian National University.

I wish to express my gratitude to Dr. H.J. Hay for his supervision. His ability to impart his experience has enriched many discussions and contributed to the solution of many problems encountered during the course of this work.

The low intensity of the beam-foil source necessitated long hours of data collection which were shared with Dr. Hay and my fellow students M.H. Doobov and C.S. Newton. The beam-foil chamber used for the latter part of this work was constructed by C.S. Newton. Part of the computer programme used for the He II data analysis (§6.1) was supplied by M.H. Doobov.

I would like to thank all members of the technical staff in the Department of Nuclear Physics for their efforts in maintaining the necessary equipment. The skill of Allen Freeman in producing large numbers of very thin carbon foils and maintaining the 2 MeV accelerator is appreciated. I also thank all nuclear physicist members of this department, not only for tolerating "those beam-foilers" on the time-shared computer, but also for their willingness to assist when able.

It is a pleasure to acknowledge the helpful discussions with Dr. L.J. Tassie of the Department of Theoretical Physics.

I am grateful to Prof. Sir E.W. Titterton and Prof. J.O. Newton for allowing me the use of the excellent facilities of this laboratory and to the Australian National University for the scholarship which provided the opportunity to undertake this course.

The help and encouragement given by my wife, Irja, is a source of strength for any task undertaken. I cannot express my appreciation for her contribution in words. My daughter Brigitta has displayed a tolerance of missed outings for which I am grateful.

Some of the work reported here has appeared in the following publications:

G.W. Carriveau, M.H. Doobov, H.J. Hay, and C.J. Sofield,
"Reduction of Doppler Broadened Line-widths in Beam-foil Spectroscopy",
Nucl. Instr. Meth. 99, 439 (1972).

C.S. Newton, R.J. MacDonald, C.J. Sofield and H.J. Hay,
"Further Evidence Against a Channelling Effect in the Optical Excitation of Ion Beams Transmitted through Single Crystals of Gold".
Phys. Lett. 42A, 47 (1972).

The work reported in this thesis, unless otherwise acknowledged, is my own and has not been submitted for a degree at any other University.

C. J. Sofield.

C. J. SOFIELD

CONTENTS

LIST OF FIGURES

LIST OF TABLES

ABSTRACT

Relative intensities of the Stark components of the He II spectral line F_α (4686 Å) have been measured following excitation in a beam-foil source, with several beam energies and electric field strengths. Similar measurements have been made for the He I transitions $4^3F \rightarrow 2^3P$, $4^1F \rightarrow 2^1P$ and $4^1D \rightarrow 2^1P$.

A model of the time evolution of the $n = 4$ excited states of He II was constructed to include the effects of weak and strong field Stark perturbations. The model selects, from a wide range of postulated initial population distributions, a distribution which is consistent with the observed F_α ($n = 4 \rightarrow n = 3$ transitions) Stark patterns. It is inferred that the cross-sections for excitation to the $n = 4$ states decrease as the orbital angular momentum (L) of the excited state increases. For the higher L states, significant alignment, referred to the beam direction, is indicated by a decrease in populations as the z component of the orbital angular momentum ($|M|$) increases. The alignment was most pronounced for the 4^2F term. The energy dependence of the population of $n = 4$ states was found to be weak for the He beam energy range 400 to 800 keV.

A similar model of the time evolution of the He I $n = 4$ excited states has been constructed including quadratic Stark perturbations. This establishes a direct relationship between the relative initial populations of excited states and the observed Stark component relative intensities, to within the M degeneracy. The cross-sections were found to be less for each 4^1F state than for the 4^1D state with the same M, and also less for the 4^3F term than for the 4^3D term. Alignment was observed in the 4^1D term at 250 keV but not at 410 keV He beam energies. The alignment in the 4^1F term was greater than the 4^1D term at both energies and decreased at the higher energy.

CHAPTER 1

INTRODUCTION

§1.1 THE BEAM-FOIL SOURCE

The dependence of spectral line intensity on source conditions is a basic reason why new spectral sources may make accessible information concerning atoms and ions in various states of excitation which is not readily obtained with other sources. It is important to know about the physical conditions and modes of excitation occurring in a particular source in order to utilize the source to greatest advantage. The general features of the source used in this work, a beam-foil source, are outlined below. More comprehensive reports concerning the properties and applications of the beam-foil source may be found in the *Proceedings of the First, Second* and *Third International Beam-Foil Conferences* [BFS 68, BFS 70, BFS 72].

The beam-foil source [Ka 63, Ba 64] consists of a beam of excited atoms or ions all travelling with nearly the same velocity at a speed which is usually of the order of one per cent of the speed of light. The excitation of the high velocity beam of ions occurs during a very brief interaction with a thin solid foil. The interaction of the ion beam with the foil not only produces ions of different charge states but each charge state has a distribution of excited state populations. The accelerated beam of ions can be produced in a high voltage accelerator of the Van de Graaff type, so the range of elements that can be studied is set by the available ion source. The interaction of the ion beam with the foil may produce ions of high charge states that are not readily obtainable in other sources [Ma 70]. Magnetic mass selection of low current ($\approx$ 10 μA) beams from an accelerator and high vacuum techniques results in a source of high mass purity and extremely low density. The low density of the beam ($\approx 10^6$ particles$\cdot$cm^{-3}) gives rise to low emission intensities with consequent experimental difficulties of observing weak spectral lines. The low density of the beam-foil source has the advantage that space-charge effects are negligible ($\approx 10^{-4}$ V$\cdot$cm^{-1}

electric field from one beam particle at its mean interparticle distance) and the collisional excitation or de-excitation of particles is highly improbable (mean free path $\approx 10^3$ cm). Therefore each particle of the beam is independent of all other particles in the system and can decay only by emission of photons or electrons. The use of molecular beams is thought to lead to space-charge effects if only single exciter foils are used [Se 69].

The high speed of the emitting particles gives large Doppler shifts which may give large broadening of spectral lines because the light is collected over a range of angles governed by the aperture of a spectrometer. Fortunately the beam velocity is nearly uniform which results in a correspondence between Doppler shifted wavelength and the angle of emission such that much of the broadening can be cancelled by a suitable arrangement of experimental equipment.

The nearly uniform velocity of the beam of excited atoms or ions gives a correspondence between the position of observation of radiative decay and the time after excitation that the decay occurs. This feature of the beam-foil source led to its early exploitation for excited state lifetime measurements [Be 65, Wi 70] although difficulties with cascade problems have been common [Oo 70]. Two important properties of the beam-foil source have been discovered more recently; the beam-foil interaction produces coherently excited states and excited state alignment [Ba 66, Ma 69, Se 69, An 70]. Methods of spectroscopic study that rely on alignment of excited states can thus be carried out on the beam-foil source. Zero field quantum beats [Be 72], level crossing [Ch 71] and magnetic rf resonance [Li 71] techniques have all been applied to the beam-foil source in recent years.

§1.2 BEAM-FOIL EXCITATION MODELS

The beam-foil interaction that leads to the properties outlined above is still not fully understood. A general discussion of the many possible processes involved is given in the *Third International Beam-Foil Conference* [BFS 72]. Quantitative theoretical studies [Ya 66, Tr 67, Mc 68, Ga 70] are confined to models of the excitation process involving electron capture for hydrogen.

These theoretical studies are limited to calculating cross-sections and their energy dependence for levels of a particular principal

quantum number; individual state cross-sections are not calculated, hence no specific predictions are made with regard to alignment of excited states, although the theory predicts preferential population of states which have a small z component of orbital angular momentum [Mc 68, Ha 73]. Experimental evidence has indicated that most of the beam-foil excitation takes place in the last few atomic layers of a foil [Be 70] and is not very sensitive to the mean distance of approach of beam particles and foil atoms [Ne 72], at least for low Z ions. A model put forward by McLelland [Mc 68] is applicable to the case of semi-metallic and non-conducting exciter foils where the conduction electron density is low. This model involves the formation of an electron shower by the incident protons and subsequent capture of electrons of a velocity near that of the proton velocity. The energy dependence for the total neutral fraction predicted from this model is in qualitative agreement with experimental results [Be 72a]. It is of interest in this context to note that Harrison and Lucas [Ha 70], in experiments on proton passage through thin carbon foils, have observed a peak in the ejected secondary electron spectra which corresponds to electrons travelling with velocities near that of the protons. The situation for medium to high Z ions is more complex. The role of inner shell excitation in establishing charge state equilibrium in solid foils has been discussed [Be 70a] in a semi-quantitative manner, and the contribution to final excited state distributions has been discussed only qualitatively [Bi 70].

§1.3 EXCITED STATE POPULATION DISTRIBUTIONS IN THE BEAM-FOIL SOURCE

The importance of alignment in the methods of spectroscopic measurement previously mentioned makes it desirable to maximize alignment of the ions under investigation. An understanding of the beam-foil excitation mechanism could provide useful information for choosing optimum experimental conditions for alignment studies in a beam-foil source. Furthermore, an understanding of the beam-foil excitation processes may provide means of obtaining information about solid state properties of the exciting foils [Br 71]. Central to this problem is the measurement of excited state population distributions and the subsequent inference of excitation cross-sections. Without an adequate knowledge of state excitation cross-sections, their beam energy dependence and quantum number dependence, comparisons with and guidelines for theoretical models of excitation mechanisms are impossible.

Several methods of obtaining excited state population distributions have been applied to the beam-foil source. In the case of one-electron systems the fine-structure cannot be resolved (at least for low Z), so the population distribution among states of different L cannot be obtained directly by intensity measurements as is possible in some other sources [He 56]. However, as the lifetimes of states in one-electron atoms are L dependent the analysis of decay data for a line composed of several transitions from states of differing L value may provide the L state population distribution at the time of excitation [Do 70]. Difficulties arise with this method due to cascades and coherence [Be 72b]. This technique is not possible in multi-electron systems where the transitions of a given multiplet have the same lifetimes [Co 51, p.98].

Observation of polarization of spectral line radiation, in the absence of external perturbations, indicates the existence of alignment in the excited upper level of the transition [Pe 58]. Polarization measurements for spectral lines may provide population distributions for states of the upper level in the transition for the simple transitions $n_1{}^1S \rightarrow n_2{}^1P$, but it does not provide sufficient information to obtain population distributions in more complex cases [Kl 69]. Even where population distributions cannot be obtained from polarization measurements the data is still useful as a qualitative indicator of state population changes for varying excitation conditions [Re 71].

Quantum beat observations have been used to obtain some relative state occupation numbers in hydrogen and helium [An 70, Do 72]. This method relies on the relation between the amplitude of the quantum beat oscillations and the occupation numbers of the coherently excited states which give rise to the quantum beats [Ma 70a]. Since the extraction of population distributions from quantum beat measurements is most readily carried out when only a few well separated frequencies contribute, it becomes very difficult to apply this method to all but the first few excited levels of one-electron atoms [An 70]. Quantum beat measurements in the presence of small magnetic or electric perturbations have been utilized mainly for studies of fine-structure [Ti 73] and the energy shifts caused by the perturbations [An 70a], but these measurements can also be used to obtain information on populations [Se 70]. The perturbed quantum beat observations also become more difficult to

interpret as the number of contributing frequencies increases. A range of quantum beat patterns may be obtained by applying magnetic and/or electric perturbations to the excited ions. The population distributions can be inferred by comparison of these patterns with patterns calculated from postulated population distributions.

In all of the above methods for obtaining populations, difficulties of interpretation increase as the number of degenerate or near degenerate states increases for the initial level of interest. It is well known that strong magnetic and electric fields remove all or part of the degeneracy occurring in an excited level of an ion thus giving rise to a pattern of separated spectral lines, the Zeeman or Stark patterns respectively [So 72, pp.263-285]. The application of static magnetic fields to a high velocity charged particle beam results in a motional electric field [Wi 16] and hence a combination of magnetic and electric perturbations on the ions; for this reason static electric fields are simpler in their effects.

§1.4 THE STARK EFFECT

The effect of an external electric field, the Stark effect, on ions has been known for 60 years. The application of the early quantum theory to explain the phenomena [Ep 16, Sc 16] was one of the earliest successes of this theory. The solution of the Stark effect perturbation problem has been revised and updated as atomic physics progressed, providing an interesting historical development of atomic physics. A review of the Stark effect and its measurement has been made by Bonch-Bruevich and Kodovoĭ [Bo 67].

The perturbation to the Hamiltonian of an ion in a uniform electric field, F, directed along the z-axis is -eFz (where e is the absolute value of the electronic charge 1.6×10^{-19} C). The matrix elements of the perturbation are proportional to the dipole matrix elements for radiative transitions so that only states of the same term system ($\Delta S = 0$), opposite parity ($\Delta L = \pm 1$), and the same z component of total angular momentum ($\Delta M_J = 0$) are coupled. The perturbation possesses cylindrical symmetry about the z-axis and hence removes any degeneracy of the system except that associated with the sign of M_J.

The perturbation gives rise to a linear Stark effect when the resultant energy shifts are greater than the separation of terms of

different L value and the same principal quantum number, and a quadratic Stark effect when the shifts are smaller than the separations.

For Stark effect problems involving terms with fine-structure it is useful to distinguish between field strengths that give rise to energy shifts less than the fine-structure separation (weak fields) and greater than the fine-structure separation (strong fields). The actual magnitudes of strong or weak fields therefore depend on the ion and spectral term being considered, and there is, of course, an intermediate region. The usefulness of this distinction arises because the total angular momentum is approximately conserved (i.e. J is a good quantum number) for weak fields, whereas in strong fields the uncoupling of the orbital and spin angular momenta result in the z component of the orbital angular momentum M and the spin angular momentum M_S being separately conserved so that J is no longer a good quantum number but $M_J = M + M_S$ is. Hence, for weak fields the electron spin may be treated by calculating the Stark effect of the fine-structure and for strong fields by treating the fine-structure of the Stark effect.

In very weak fields the dipole selection rules for J and M_J are the same as for zero field, namely $\Delta J = 0, \pm 1$ ($J = 0 \nleftrightarrow J = 0$), $\Delta M_J = 0, \pm 1$ ($M_J = 0 \nleftrightarrow M_J = 0$ for $\Delta J = 0$). The strong field Stark components (defined as transitions from levels of given $|M|$) may have fine-structure, and they obey the dipole selection rules $\Delta M_S = 0$, with $\Delta M = 0$ (π polarized components), or $\Delta M = \pm 1$ (σ polarized components). However, L is a good quantum number only for vanishing electric fields. Hence dipole radiative decay channels occur that are forbidden at zero field. In the case of the Stark effect of He I the appearance of the resultant forbidden spectra lines is striking and so also is the removal of metastability of the $2^2S_{\frac{1}{2}}$ states of hydrogenic ions.

§1.4.1 The First-Order Stark Effect

Neglecting spin, the first-order Stark effect for hydrogenic ions may be solved using non-degenerate perturbation theory. This is done using parabolic co-ordinates because in that system the perturbed Hamiltonian matrix is diagonal [Fo 62]. The energy levels of a hydrogenic ion in an electric field are given by,

$$E_{n,n_1,n_2,M} = -\frac{mZ^2e^4}{2\hbar^2n^2} - \frac{3F\hbar^2}{2Zme}\, n(n_2 - n_1) \ , \qquad (1.1)$$

where m is the mass of an electron, Z the atomic number, n the principal quantum number, n_1 and n_2 are the parabolic or electric quantum numbers, and

$$n = n_1 + n_2 + |M| + 1 \ . \tag{1.2}$$

The wavelength of a Stark component arising from a transition between the two states (n,n_1,n_2,M) and (n',n_1',n_2',M'), where the primes indicate the lower level, is shifted from the zero field wavelength by

$$\Delta\lambda_{nn'} = C_{nn'} F \ , \tag{1.3}$$

where

$$C_{nn'} = 5.3169 \times 10^{-4} \frac{n^4 \, n'^4}{(n^2 - n'^2)^2} \frac{X_{nn'}}{Z^5} \ , \tag{1.4}$$

and

$$X_{nn'} = n(n_1 - n_2) - n'(n_1' - n_2') \ , \tag{1.5}$$

for $\Delta\lambda_{nn'}$ in Å and F in $kV \cdot cm^{-1}$. Notice that the wavelength shifts are integer multiples of the displacement for $X_{nn'} = 1$. There may be more than one transition with the same displacement aX $(a = 0, \pm1, \pm2, \pm3, \ldots)$, these being distinguishable if they have different polarizations. This treatment neglects spin so it is only valid for strong fields where the relative displacement of components is given accurately by eqn (1.3). If the Stark components are resolved eqn (1.3) may be used to determine the electric field strength F.

There is a quasi-selection rule which says that transitions in which the sign of $(n_1 - n_2)$ differs from the sign of $(n_1' - n_2')$ will be very weak [Be 57, pp.231, 276]. Consequently most of the highly displaced components are "unobservably" weak.

§1.4.2 The Second-Order Stark Effect

In multi-electron ions the electron-electron interaction removes the L degeneracy characteristic of one-electron ions and therefore there is no first-order Stark effect. The correction to the energy of a Stark perturbed state is, to second order,

$$\Delta E_{\alpha J M_J} = F^2 \sum_{\alpha' J'} \frac{\left| \langle \alpha J M_J \left| e \sum_i z_i \right| \alpha' J' M_J' \rangle \right|^2}{E_{\alpha J} - E_{\alpha' J'}} \ , \tag{1.6}$$

where α includes all the quantum numbers other than J and M_J. The usefulness of eqn (1.6) is limited for general discussion because it contains a sum over all coupled states, which can only be evaluated for

particular cases. The denominator, $E_{\alpha J} - E_{\alpha' J'}$, in eqn (1.6) dominates the magnitude of the level shift and gives rise to the familiar repulsion of coupled states. For the lowest terms of multi-electron ions where $E_{\alpha J} - E_{\alpha' J'}$ is large the Stark effect is negligible up to high field strengths (e.g. ≈ 1 cm^{-1} at 535 kV·cm^{-1} for the $2^1P_1^0$ state of He I). This results in the perturbation of the upper term dominating the wavelength shift of the Stark perturbed transitions. The Stark components arising from transitions ($\Delta M = 0, \pm 1$) between highly excited terms and the first few slightly perturbed terms are both π and σ polarized if the lower term has a state of the same M value as the upper term, otherwise only a σ polarized component occurs.

§1.5 POPULATION OF EXCITED STATES AND THE RELATIVE INTENSITIES OF STARK COMPONENTS

The detected intensity K_{ik} of a Stark component resulting from a dipole transition from state i to state k may be expressed as

$$I_{ik} = K_{ik} |\langle i|P|k\rangle|^2 N_i , \qquad (1.7)$$

where K_{ik} is a constant dependent on the volume of emitting ions, the frequency of the radiation, the direction and solid angle of observation and the wavelength and polarization efficiencies of the detector, and P is the electric dipole operator. If the intensity of a transition from i to k relative to that for j to k, the relative values of K_{ik} and K_{jk}, and the dipole matrix elements for the transitions are known, then the ratio of the populations N_i and N_j can be found from eqn (1.7). Thus it is necessary to know the Stark perturbed dipole matrix elements to determine the relative populations of Stark perturbed states from relative intensity measurements. The populations are indeterminate to the extent of the M_J degeneracy. If the Stark components have unresolved fine-structure, a further indeterminacy in populations results.

For hydrogenic ions, the dipole matrix elements of the strong field Stark components are equal and field independent [Ho 65] for components symmetrically displaced about the wavelength of the unperturbed line [Go 29]. The upper levels contributing to the Stark components at +aX and -aX have equal statistical weights, therefore Stark patterns for hydrogenic ions will display an intensity symmetry unless the upper levels are unequally populated.

Since the interatomic electric fields are much larger than the fields applied to the beam outside the foil, the excitation processes which occur in the foil populate states which are not the Stark states at the point of observation. In order to deduce features of the excitation process, a relationship between the relative populations of the Stark states and the relative populations of the initial states excited in the foil must be obtained. Specifying this relation is in essence a problem of calculating the time dependence of the excited state populations and the coherence terms between these states. The particular time dependence of the problem is determined by the very short time in which excitation occurs in the foil (giving a time origin) and the approximate correspondence between position and the time after excitation due to the nearly uniform velocity of the beam of excited ions. The static electric fields applied to the beam are seen by the high velocity excited ions as time varying electric fields, and therefore time dependent Stark perturbation effects must be accounted for. These time dependent perturbation calculations reduce to simple forms in the case of the sudden, adiabatic, and the resonant time dependent approximations.

A model of the time evolution process embodying the relation of the initial excited state populations to the relative intensities of Stark perturbed transitions has been constructed. The model includes calculations of the change in populations with time due to radiative decay, coherence effects and perturbations. The model is formulated in the density matrix representation to facilitate the calculation of coherence effects and because the relative populations of excited states are averages over the ensemble of excited ions. For input, the model requires the measured relative intensities of Stark components and values of the Stark perturbed transition probabilities and lifetimes. The use of the model is thus restricted to ions for which the Stark effect perturbation problem has been solved.

The early observations by Bashkin and Carriveau on the Stark effect in a beam-foil source [Ba 70] were of interest in that, although individual Stark components were not resolved, the lines in hydorgen, H_β (4861 Å), and $^3He^+$,F_α (4686 Å), were observed to be asymmetric in strong fields of approximately 70 $kV \cdot cm^{-1}$. They ascribed the asymmetry of their Stark patterns to low populations of high J value levels relative to low J value levels in the unperturbed system. Asymmetries in Stark patterns of hydrogen lines have been observed in other sources and shown to result

from the high field ionization of long wavelength components [La 31] or the preferential collision quenching of low wavelength components [Ge 68], but neither of these effects could contribute significantly under the experimental conditions of Bashkin and Carriveau. The possible contribution of excitation or perturbation induced coherence to the observed asymmetry was not considered. The time dependence of the applied electric field was implied to be infinitely slow.

§1.6 SCOPE OF THE PRESENT WORK

This thesis is concerned with strong field Stark effect observations using beam-foil excited $^4He^+$ ions obtained from a 2 MeV Van de Graaff accelerator. The passage of the ions through the foil produces neutral, singly ionized and doubly ionized ^4He particles providing the He I and He II spectra for study. The choice of ^4He allowed the study of the quadratic (He I) and the linear (He II) Stark effects for spectra where theoretical and experimental information on perturbed transition probabilities and Stark perturbed energy level values are available [Lü 51, Ku 73, Fo 28, Pf 66], without extra complications due to the necessity of including hyperfine-structure. The theoretical information was necessary in order to relate the measured Stark relative intensities to the initial populations of excited states. The eigenvalue problem for the linear Stark effect including spin is treated in Appendix B, where the perturbed transition probabilities and lifetimes for strong fields are also given. In Appendix C, the eigenvalue problem for the Stark effect in He I is presented and perturbed transition probabilities and lifetimes for field strengths up to 100 $kV \cdot cm^{-1}$ are tabulated.

To obtain reliable relative intensity measurements of Stark components at strong fields, considerable development of experimental methods was required. The intensity of transitions from He I and He II were found to decrease the higher the excitation of the upper level. The Stark effect measurements were carried out on some terms of principal quantum number $n = 4$ for this reason. The largest separation of Stark components at 100 $kV \cdot cm^{-1}$ was about 2 Å. The linewidth achieved for spectral lines was approximately 1 Å (F.W.H.M.) so that some Stark components were resolved. This resolution was attained by re-focusing a monochromator so as to cancel the Doppler broadening of spectral lines due to the large aperture of the light collection optics. Relative

intensities of lines as close together as 0.6 Å were extracted by non-linear data fitting techniques. Methods of monitoring source conditions had to be developed to obtain reliable relative intensity measurements free of source fluctuations and foil changes during bombardment.

CHAPTER 2

EXPERIMENTAL EQUIPMENT AND METHODS

The equipment used for the Stark component intensity measurements from the beam-foil source falls into three classes. These are apparatus constituting the beam-foil source, that used to measure relative intensities free of the influence of source fluctuations, and that required to obtain resolved Stark components. The latter class involves the attainment of strong uniform electric fields and the improvement of spectral resolution by cancelling the major component of Doppler broadening. The design and use of these combine to determine the success with which the relative intensities can be obtained. Some of the general features of the way in which experimental considerations interact are given before the details of the equipment are discussed.

The strength of the electric field applied to the excited ion beam determines the separation of the Stark components. The electric field strength depends on the electrode design, the beam-foil chamber design and vacuum pressure and the high voltage supplies. The presence of the high energy ion beam and the secondary electrons resulting from its impact on the foil and collimator edges make the achievement of constant electric fields difficult.

The Doppler broadened linewidths of ≈ 10 Å for He spectral lines at about 800 keV beam energy precludes the resolutions of Stark components separated by ≈ 1 Å. The attainment of such Stark splitting often requires uniform electric fields in excess of 100 $kV \cdot cm^{-1}$. Methods of cancelling the major component of Doppler broadening were investigated and the method of re-focusing the monochromator was found to be the best one for strong field Stark effect measurements. The factors limiting the achievable linewidth obtained with a re-focused monochromator were considered. The sensitivity of the re-focusing to beam velocity and wavelength changes had to be investigated in order to establish satisfactory procedures for Stark effect observations. This was necessary because the electric field produces changes in the wavelength of the perturbed transitions and changes in the velocity of charged beams.

The measurement of relative intensities also depends, apart from resolution considerations, on the source intensity, the methods of light collection, and signal processing. The variation of the source efficiency with time was investigated and necessitated monitoring both the beam current and the light intensity from a chosen transition. The effective use of the monitor information was greatly facilitated by the use of digital data acquisition techniques because on-line arithmetic procedures allowed corrective action to be taken before changes in conditions became large enough to lead to the collection of unreliable data.

§2.1 BEAM-FOIL SOURCE EQUIPMENT

The equipment necessary to establish a beam-foil source is found in most low energy nuclear physics laboratories where charged particle accelerators are used. The energy range and ion source of the accelerator determine the range of isotopes, charge states, and the spectral range that may be studied. Source efficiency variations may arise in the accelerator ion beam output or from changes in the exciter foil due to bombardment. Separate monitoring of beam current and a spectral line allowed these two sources of variation to be distinguished.

§2.1.1 Accelerator and Beam-Line

A schematic diagram of the accelerator and beam-line is given in fig. 2.1. The diagram indicates typical positions for a Heath monochromator used to monitor the source light output, a McPherson scanning monochromator used to obtain the spectra of interest, and the Faraday cup used to monitor beam current.

The accelerator was an H.V.E.C. Model AK, 2 MeV Van de Graaff equipped with an r.f. ion source. The 22.5° analyzing magnet (mass energy product 36) bends the accelerated beam into the beam-line where it then passes through a quadrupole lens, stabilizing slits and collimator before passing through a thin foil in a chamber where electric fields could be established and observations could be made. The pressure maintained in the accelerator and beam-line was less than 10^{-5} torr.

§2.1.2 Beam-Foil Chambers

The experimental work was conducted using two different beam-foil chambers. The major portion of the work was performed using a

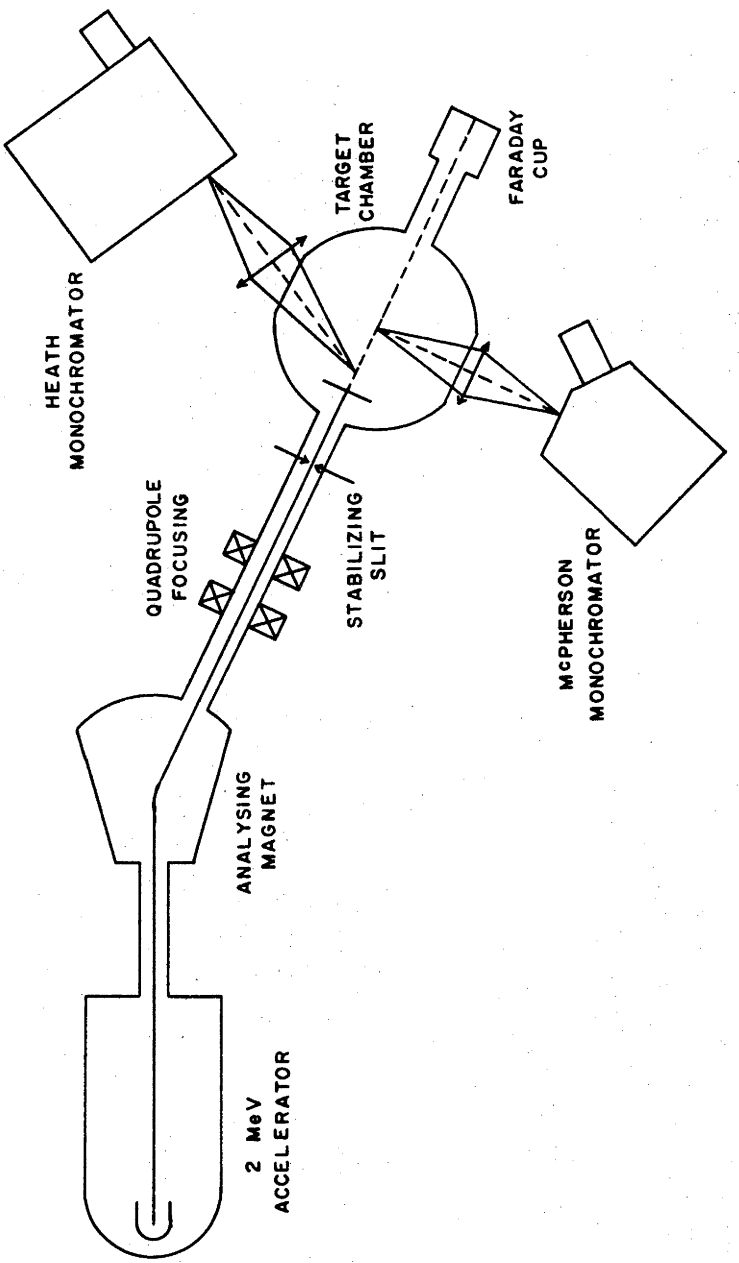

Fig. 2.1: Arrangement of experimental equipment. (Not to scale.)

cylindrical chamber of 15 cm internal diameter and 20 cm high, constructed from mild steel and cadmium plated. A section in the plane of the beam is given in fig. 2.2. The beam path was 75 mm below the top of the chamber. Three 4.1 cm diameter fused quartz observation windows were provided, two cutting the plane of the beam centred on a horizontal diameter perpendicular to the beam axis, and one in the centre of the chamber lid.

The chamber was equipped with a foil wheel which had 22 holes, each 4 mm in diameter. This was mounted so that the hole at the top of the wheel intersected the beam axis. Rotation of the foil wheel from outside the chamber was accomplished by a manually operated worm drive through a rotating vacuum seal. The foils were mounted on tantalum frames (0.4 mm thick with 4 mm diameter holes) which were glued to the foil wheel.

Two insulated electrodes made from automotive spark plugs were mounted on the chamber on a circle 5.2 cm in diameter, spaced 7.3 cm apart and equally spaced from the beam to provide high voltage leadthroughs.

Earthed aluminium plates 2.5 mm thick, 4 mm apart at the beam axis, with 2.5 mm diameter apertures to allow beam passage, were suspended from the chamber lid. These baffles served to shield the foil and the light monitor.

The stabilizing slits (1 to 2 mm gap) and the 1.5 mm aperture at the chamber entrance 4.5 cm from the foil restricted the beam divergence to approximately 0.008 rad. The beam diameter at the chamber centre, measured by charring a cardboard target, was approximately 1.5 mm. The beam divergence was kept small to reduce its contribution to line broadening.

The chamber was pumped by a liquid nitrogen trapped oil diffusion pump mounted below the chamber and separated from it by a flap valve. The chamber pressure was monitored by an ionization gauge situated at the end of the Faraday cup. The pressure indicated at that position was always less than 10^{-5} torr when experiments were in progress.

The second beam-foil chamber was considerably larger, consisting of a stainless steel box with internal dimensions 80 cm long, 26 cm wide and 46 cm deep. It was pumped by a turbo-molecular pump and pressures of better than 10^{-6} torr were obtained. The foil wheel, which

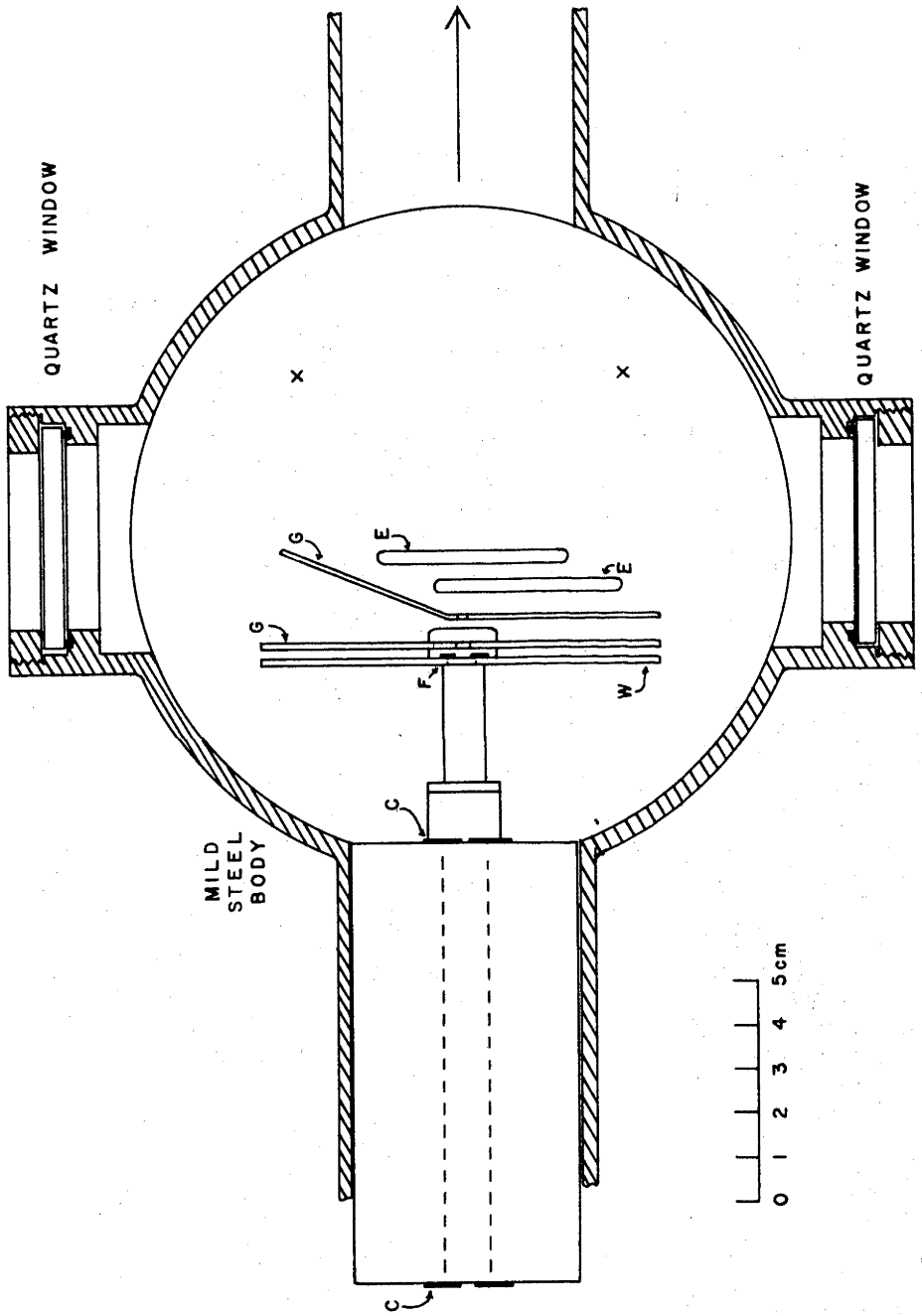

Fig. 2.2: Horizontal section through cylindrical chamber. E. Field electrodes. G. Earthed electrodes and light baffle. W. Foil wheel. F. Foil. C. Beam defining apertures. X. High voltage insulated leadthroughs.

held 60 foils, was rotated by a stepping motor. The insulated high voltage electrodes were brought through the chamber lid 13.5 cm apart and equally spaced about the beam. An earthed stainless steel plate 3 mm thick was suspended from the lid of the chamber 10 mm from the foil wheel and had a 2.5 mm diameter aperture at the beam axis. The beam divergence was about the same as that for the other chamber. Observation ports extended over about 43 cm on both sides of the chamber parallel to the beam axis.

The stray magnetic field in the chambers was measured with a Hall probe and found to be $\leqslant 0.1$ G. This field had no observable effects on the beam-foil source lines since the resultant Zeeman splitting of a Lorentz triplet is approximately 10^{-5} cm^{-1}. The motional electric field (≈ 1 $V \cdot cm^{-1}$) for a singly charged ion of $\beta \approx 0.02$ is also negligible.

§2.1.3 Changes in Foils Under Beam Bombardment

The foils used were thin self-supporting carbon foils produced locally by evaporation onto glass slides coated with RBS 25 detergent. The foils were subsequently floated off with distilled water and picked up on the tantalum foil holders. Thin foils were required in order to reduce the Doppler broadening of spectral lines resulting from scattering. Foil thicknesses were between 2 and 7 $\mu g \cdot cm^{-2}$. The thickness, within this range, was not critical provided the variation between foils of a set was small. The similarity of thickness was estimated visually by the optical transmission of the carbon film on the glass slides. Measurement of α particle energy loss through two thicknesses of foil showed that the thinnest self-supporting foils which could be handled easily were 2.5 ± 0.5 $\mu g \cdot cm^{-2}$ thick.

The excitation efficiency of the foils was found to be time and beam current dependent. A steady decrease in light output was sometimes observed before the more drastic reduction when a foil broke. The time taken for a foil to break was less for heavier ions and for higher beam currents, but no clear relationship was established.

The variations with time of the relative intensity measured by the Heath monitoring monochromator, for the H_β line of hydrogen and the $3^3P \rightarrow 2^3S$ line of He I are shown in fig. 2.3(a) and fig. 2.3(b) respectively. The beam current was ≈ 3 μA in both cases and the effects of current fluctuations have been removed by normalizing to constant

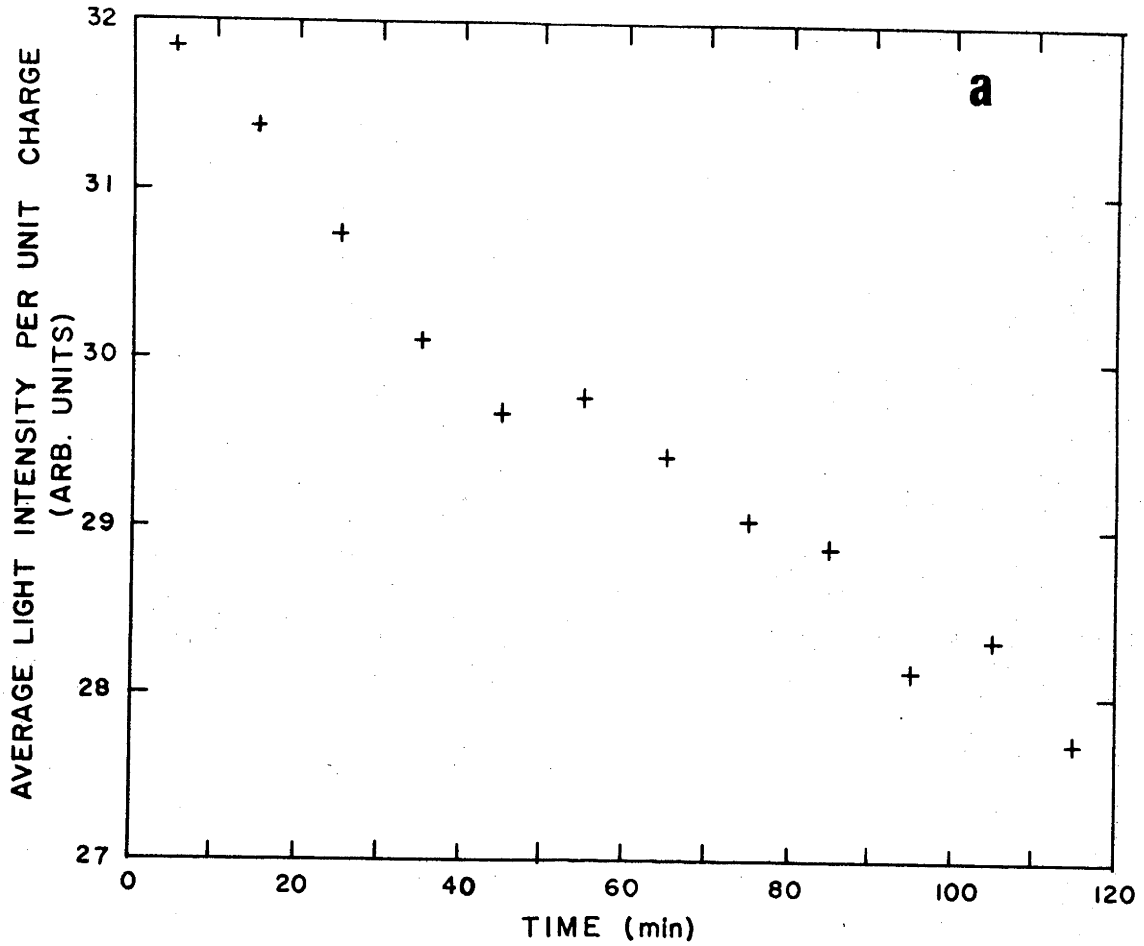

Fig. 2.3(a): Intensity of a hydrogen line during life of foil. H_β intensity as a function of bombardment time, 400 keV H_2^+, $\approx$ 3 μA.

charge per unit time. The large change in light output shown in fig. 2.3(b) is due to a partial breakage of the foil. The gradual change in efficiency, evident in fig. 2.3(a), from damage with a hydrogen beam, was also evident with He^+ beams at lower beam currents ($\approx$ 1 μA). The slow change in efficiency with time of bombardment by a hydrogen beam was a general feature due to damage of the foil and was not due to breaks large enough to detect visually. While the Heath monitored the $3^3P \rightarrow 2^3S$ He I line for the data of fig. 2.3(b), the McPherson monochromator simultaneously observed the $4^3D \rightarrow 2^3P$ He I line. The ratio of these two signals remained constant within counting statistics until the foil broke.

Several foils showing decreases in excitation efficiency of 20% to 50% were examined with an electron microscope and found to have no holes larger than the limit of detectability ($\approx$ 100 Å). A few foils

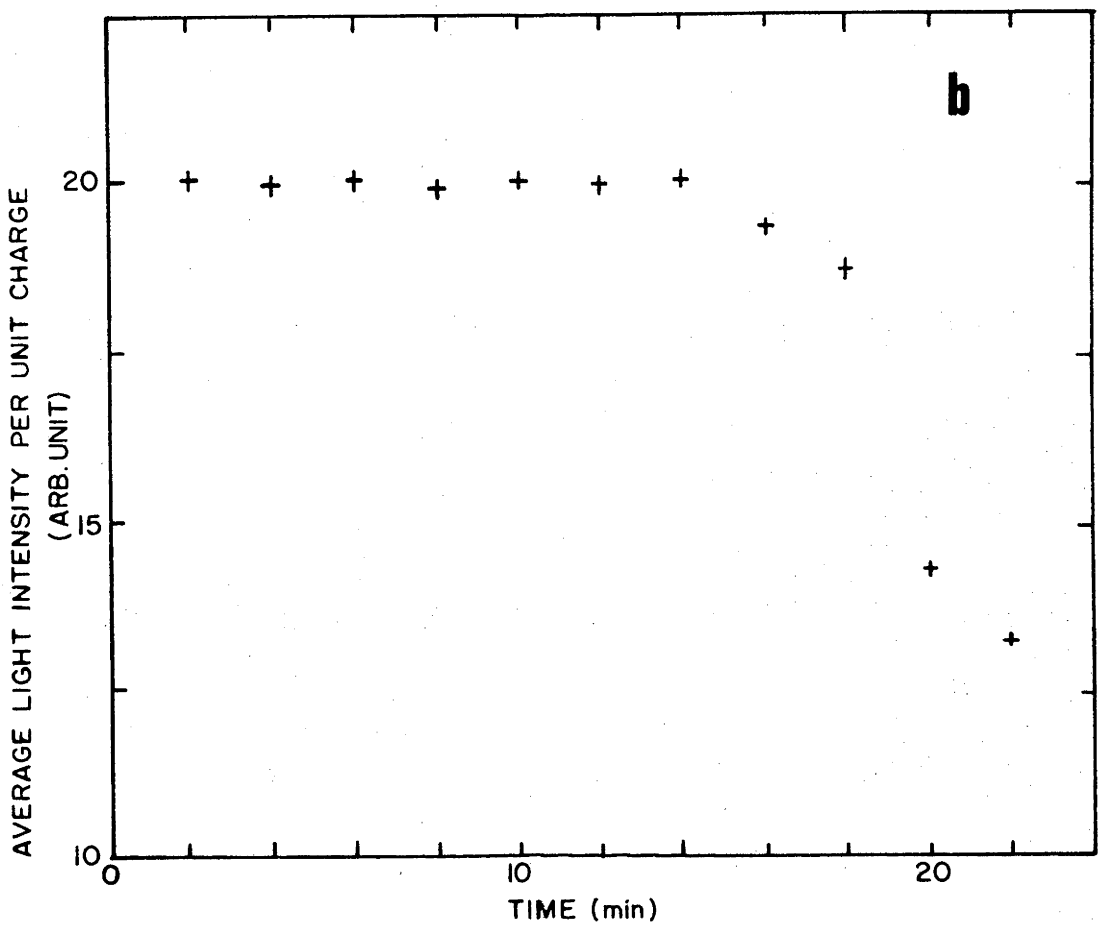

Fig. 2.3(b): Intensity of a helium line during life of foil. $3^3P \rightarrow 2^3S$ He I line as a function of bombardment time, 400 keV He^+, $\approx$ 3 μA.

damaged to breaking point were found to show evidence of thickness changes in the regions subjected to beam damage. The changes appeared as thick areas, $\approx$ 500 Å in diameter randomly distributed through $\approx$ 50% of the foil.

The measurement of spectral linewidth as a function of ion bombardment time also suggested that the foils become thicker. Fig. 2.4 shows changes in light monitor normalized to beam current and the spectral linewidth. For this single observation, the increase in linewidth is not significant but, for many foils, the slope of such plots consistently showed an increase with the amount of bombardment. Similar changes were observed to occur in both the oil diffusion pumped chamber ($< 10^{-5}$ torr) and in the chamber coupled to a turbo-molecular pump ($< 10^{-6}$ torr), hence

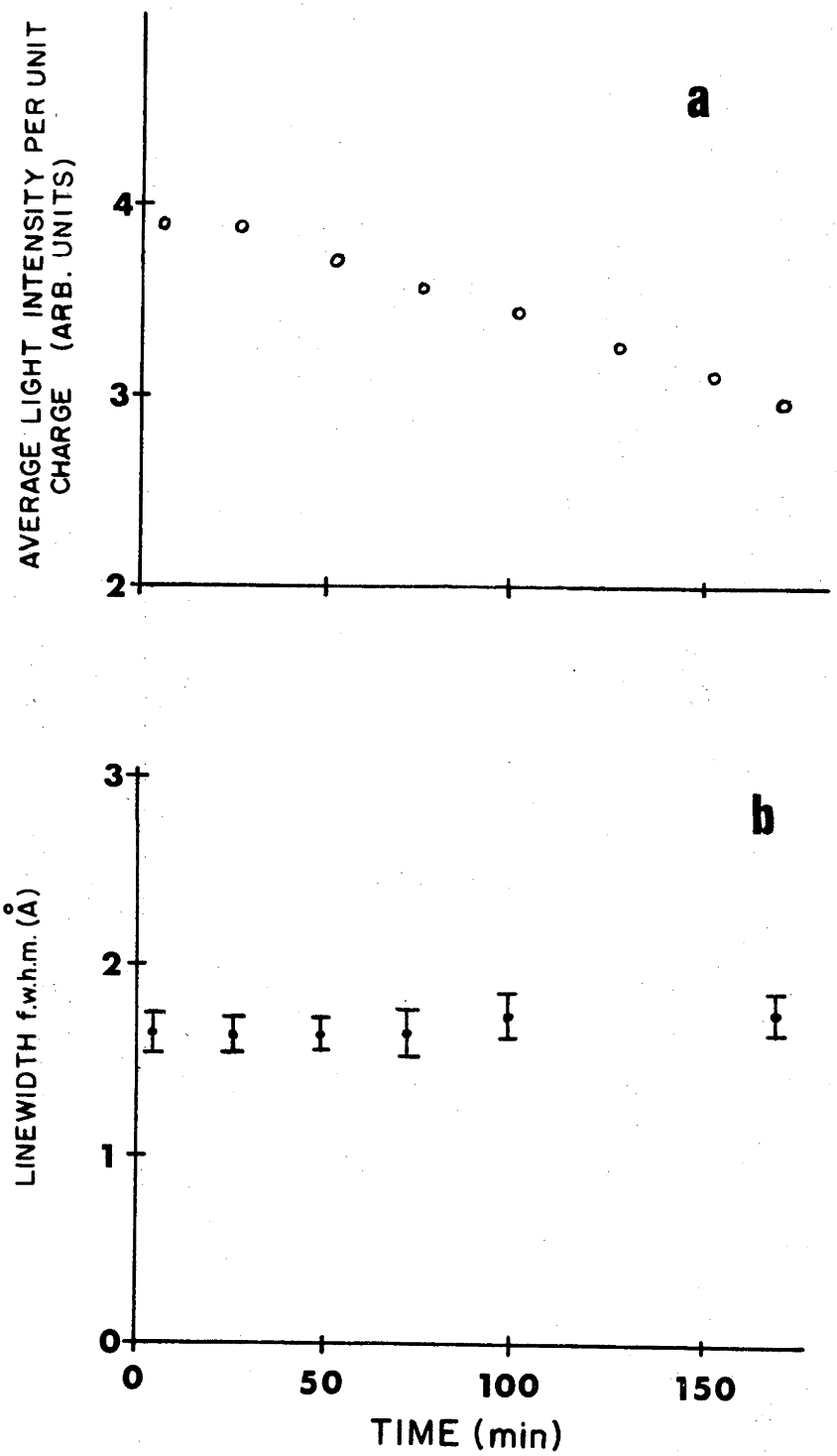

Fig. 2.4: Foil damage. (a) H_β relative intensity per unit charge for 400 keV H_2^+, $\approx$ 3 μA, as a function of time. (b) H_β linewidth as a function of time, monochromator slits set at 125 μm, which gives an instrumental linewidth of $\approx$ 1 Å.

carbon build-up from cracked oil vapours does not appear to account for the increase in thickness.

The combination of light and current monitors served to indicate whether foil damage was extensive enough to affect significantly the width of spectral lines during the time taken to scan over the wavelength range of the Stark spectra. The monitoring procedure became important from this point of view because the scattering in the foils, which is thickness dependent, was a major component of the linewidth after the Doppler broadening from the finite aperture collection optics was cancelled. This was especially so for incompletely resolved Stark components, because data fitting procedures which relied on linewidth estimates from zero field observations prior to obtaining the Stark spectra, were used to obtain the relative intensities of such components.

§2.2 EQUIPMENT FOR RELATIVE INTENSITY MEASUREMENT

The instrument used for relative intensity measurement was a scanning monochromator with a photomultiplier detector operating in the photon counting mode. To compare source emission intensities, the overall dependence of the system's detection efficiency on wavelength was measured, as was also its dependence on polarization. The efficiency of the photocathode and grating, as well as the transmission of the various lenses and chamber window contributed to the system's efficiency.

§2.2.1 Scanning Monochromator

A McPherson 218 scanning monochromator was used to obtain spectra from the region of the beam where electric fields were applied. This instrument has a focal length of 0.3 m, aperture ratio f/5.3 and is based on a crossed Czerny-Turner design to reduce off-axis aberrations at the collimating mirrors and to allow efficient baffling against stray light. The plane-grating used with it had 2400 $\ell \cdot mm^{-1}$ and was blazed for 3000 Å. The reciprocal linear dispersion in first order was about 12 to 8 $Å \cdot mm^{-1}$ over the grating's wavelength range of 1800 Å to 5300 Å giving about 0.2 Å linewidth when the slits were set at 20 μm. The grating was driven by a constant speed motor through a gearbox.

The monochromator had a movable quartz (Suprasil) lens $\approx$ 4 cm in diameter, of focal length $\approx$ 10 cm, mounted before the entrance slit. This coupling lens was positioned to focus the source for a particular

wavelength onto the entrance slit. Unit magnification was used to obtain maximum transfer of light from the beam [Ca 70].

A thin linear polarizer (Polaroid HN22) could be inserted in a rotatable holder just before the entrance slit of the monochromator. The grating reflected light polarized parallel to its rulings less than light polarized perpendicular to them. The beam, electric field, and monochromator orientations (§2.3.4) were such that the relative efficiencies for light polarized in those directions was required.

The instrument was modified by the addition of a lens just inside the exit slit to allow it to be re-focused (§2.3.3) for the beam-foil source. Absorption in the glass lens reduced the wavelength range to 3000 Å to 5300 Å.

The monochromator was also modified by the addition of a cam to the wavelength drive train to operate a microswitch at 10 Å intervals. The microswitch permitted the synchronization of the monochromators, scalers and computer which were used for data collection. The microswitch operation was reproducible to within ±0.03 Å. The differential linearity of the wavelength scale is important; for example a 2% change in electric field strength may give rise to a shift sufficient to change the deduced Stark component intensity by 10%, but for these Stark effect measurements the absolute zero of the wavelength scale does not matter.

For use with the cylindrical chamber the monochromator was mounted on wooden slides to provide motion approximately perpendicular and parallel to the beam. With the stainless steel chamber it was mounted on rigid metal plates driven by accurate lead screws. The slides were used to position the monochromator at each wavelength so that the source was focused at the entrance slit and to position it up and down stream to view between the field electrodes for the Stark effect measurements. The splitting of the H_β line was measured to find the region of maximum field strength.

An intensity versus wavelength calibration was made by means of a source of known spectral energy distribution [Gr 68]. A calibrated Philips tungsten ribbon lamp (W2KGV221) was used to illuminate an Eastman White Reflectance Standard mounted in the experimental chamber in the region where the electric fields were normally applied. Fig. 2.5 shows the measured relative efficiency of the detector system versus wavelength.

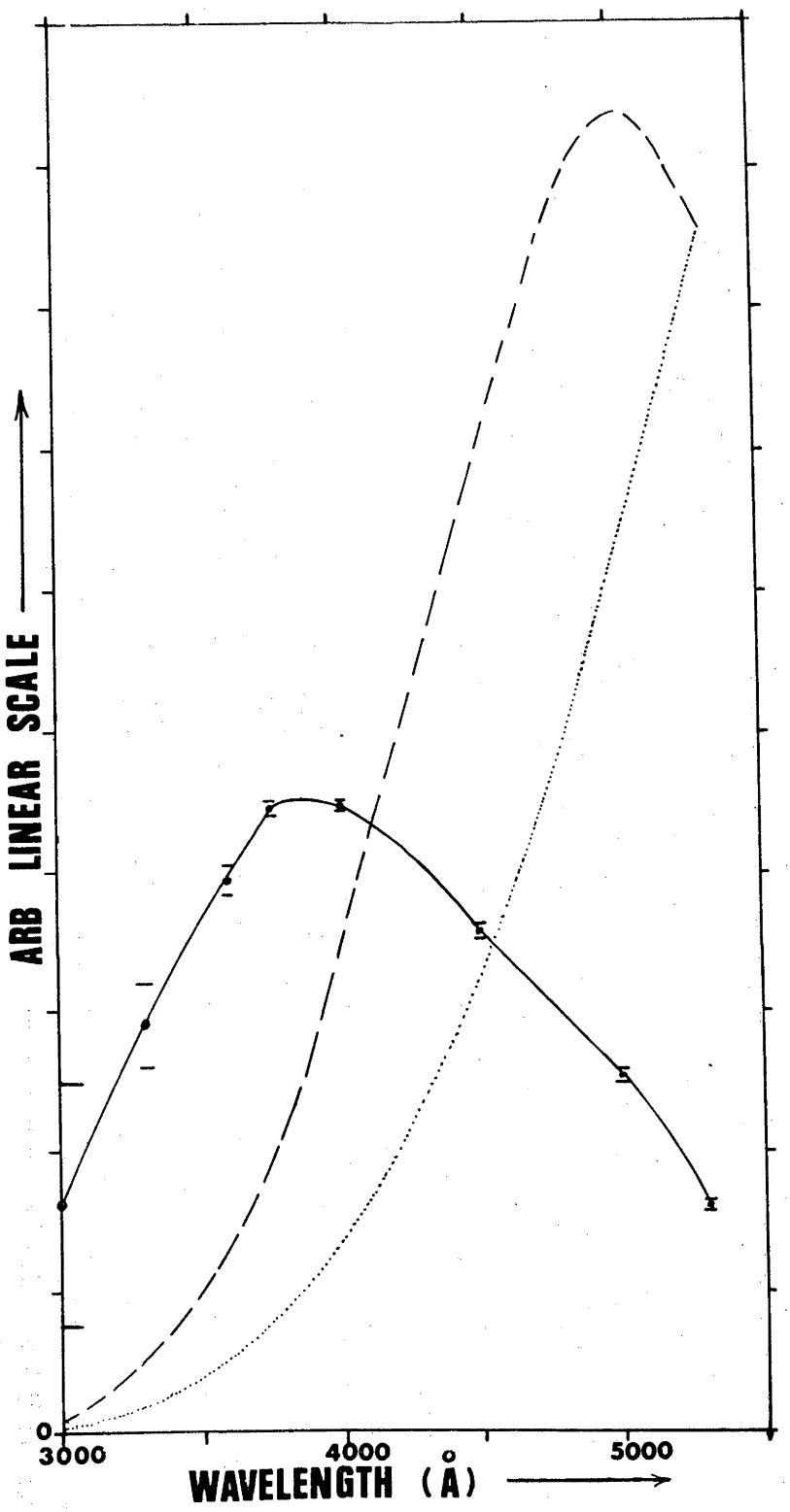

Fig. 2.5: Relative efficiency of detector system versus wavelength.

—— Relative efficiency of detector system.

– – – Measured relative intensity of white reflector.

···· Calibrated relative spectral energy distribution of white reflector.

Note: The error bars shown for a few representative points arise from counting statistics.

The relative intensity of the reflectance standard was also measured with the linear polarizer inserted with its polarization axis first parallel and then perpendicular to the slits. Fig. 2.6 shows the reflector relative intensity as a function of wavelength for the detector system with the polarizer inserted. The F_α Stark perturbed transitions were observed in the wavelength range 4680 ± 20 Å for which interval the ratio of efficiency for light polarized perpendicular to the slits to that polarized parallel to the slits was 3.6 ± 0.2. The transmission through the polarizer was $39 \pm 2\%$ for that wavelength range. These measurements allowed the relative intensities of π components and σ components, obtained with electric field monochromator orientation (a) (§2.4.2), to be corrected for grating efficiency.

Over a 40 Å range, which exceeds the Stark splitting of the F_α (4686 Å) line, the change in overall efficiency is about 4%, which gives a very small correction to the Stark component intensities. The wavelength dependence of the detector efficiency must be allowed for when comparing the intensities of widely separated spectral lines.

§2.2.2 Monitoring Monochromator

A Heath EUE-700 scanning monochromator was used as a light monitor. It has a single-pass Czerny-Turner configuration with aperture ratio f/6.8 and a focal length of 0.35 m. This instrument is equipped with a 1180 $\ell \cdot mm^{-1}$ grating giving a nominal reciprocal linear dispersion of 20 $Å \cdot mm^{-1}$ in first order. The resolution is better than 0.5 Å over its usable range of 1900 Å to 1 μm. The monitor was normally operated with entrance and exit slits at 2000 μm, giving a 40 Å pass band in order to obtain maximum intensity from the Doppler broadened beam-foil lines.

As previously mentioned in §2.1.2 the monitor viewed the beam between two earthed aluminium plates immediately after the foil (fig. 2.2). The plate nearest the foil was required to prevent the light from the beam spot on the foil entering the monitor which viewed the beam at an angle of about 45°. The earthed plate nearest to the applied electric field was used so that the monitor was "seeing" a region of negligible electric field. The plates were spread on the side near the monitor to keep the counting rate as high as possible.

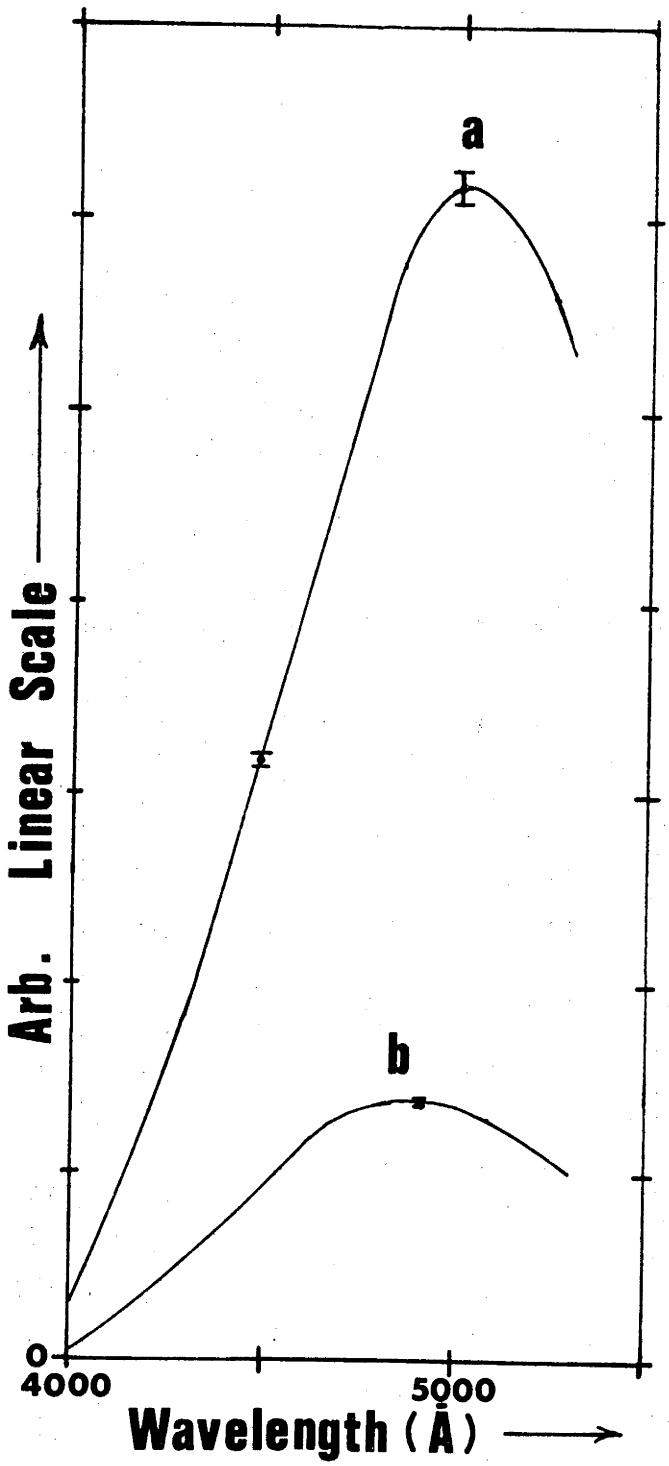

Fig. 2.6: Relative efficiency for polarized light.

(a) Measured relative intensity for light polarized perpendicular to the slits.

(b) Measured relative intensity for light polarized parallel to the slits.

Note: The source intensity is the same for both measurements. The error bars shown for the few representative points arise from counting statistics.

§2.2.3 Single-Photon Counting

E.M.I. 6256S photomultipliers were used as detectors with both monochromators. These phototubes had fused quartz windows and "S" type photocathodes of 10 mm diameter.

The phototubes were mounted in housings that enabled the tubes to be operated at low temperatures ($\approx$ -40 °C) and thus reduce dark current noise. The housing was a modified version of the one developed by Carriveau [Ca 70]. It consisted of an outer brass cylinder separated from a copper cylinder by a ½" thick insulating poly-urethane foam. The end of the copper cylinder adjacent to the exit slit was closed by an annular copper coil with a 10 mm diameter open hole at its centre. The phototube projected into this cylinder with the cathode close to but not touching the coil. Dry nitrogen, boiled from liquid, was re-cooled in a heat exchanger immersed in liquid nitrogen close to the housing, and blown onto the photocathode. An insulating nylon tube pierced the earthed brass enclosure to deliver the cooled gas to the copper coil. Dark count rates of 0.5 to 1 count$\cdot s^{-1}$ were obtained in this way.

A further separate compartment at the end of the brass cylinder contained the voltage divider network for the photomultiplier dynode chain. The voltage divider was constructed to give good performance under single-photon counting conditions [Za xx]. The voltage divider was operated with the anode at ground potential and was coupled to a Fluke 3 kV power supply. A further separate compartment housed a direct-coupled, non-overloading, fast pulse preamplifier (rise time < 10 ns, duration < 30 ns). These were built locally following a design of Jackson's [Ja 65].

The low level pulses from the preamplifier were passed through an ORTEC 410 linear amplifier, with no pulse shaping, to an ORTEC 420 single-channel analyzer operated as an integral discriminator. The threshold of the single-channel analyzer was raised sufficiently to eliminate the low level noise.

The pulse height distributions from the photomultiplier were measured with a multichannel analyzer after the 410 linear amplifier. The typical distributions were found to be exponentially decreasing functions of pulse height, with the dark count pulse heights decreasing more rapidly than the pulses from light through the monochromator. Pulse height distributions were measured for phototube voltages between 1000 V

and 2000 V at 200 V intervals. At low voltages the phototube gain barely overcame the preamplifier noise but the tube signal-to-noise ratio was high. At high voltages the counting rate was much higher, but the signal-to-noise ratio was lower. For low level counting, characteristic of beam-foil sources, the effective accuracy in the light signal measurements depends not only on the signal-to-noise ratio but also on the absolute counting rate. Hence, depending on the lower level of signals one wants to detect, the working tube voltage and discriminator level need to be chosen to give maximum significance to the signal count obtained in a given time.

Defining the signal-to-noise ratio as $R = S/B$ gives

$$T = (R+1)B \ , \tag{2.2.1}$$

where T and B are the total rates estimated from B_1 counts in time t_1 and T_2 counts in t_2. Then the signal in t_2 is

$$S_2 = T_2 - B_1\left(\frac{t_2}{t_1}\right) \tag{2.2.2}$$

and the error in S_2 is

$$E = \sqrt{(R+1)\ B_1(t_2/t_1)} + (t_2/t_1)\ \sqrt{B_1} \ . \tag{2.2.3}$$

To simplify the discussion, suppose $t_2 = t_1 = t$, then

$$E = \sqrt{B}\ (\sqrt{1+R} + 1) \tag{2.2.4a}$$

or

$$E = \sqrt{S}\ (\sqrt{1 + 1/R} + 1/\sqrt{R}) \ . \tag{2.2.4b}$$

If $R << 1$, then $E \approx 2\sqrt{B}$, that is the relative error is

$$E_R \approx 2/\sqrt{R^2 B} \ . \tag{2.2.5}$$

If $R >> 1$, the error in S is simply $\sqrt{S}$. Between these limits the relative error in S, where S now is the signal counting rate, is

$$E_R = 1/\sqrt{St}\ (\sqrt{1 + 1/R} + 1/\sqrt{R}) \ .$$

The relationship between the relative error, the signal-to-noise ratio, and the sampling time can be seen by two examples. The first example is, if the signal and background count rates both double then the signal-to-noise ratio remains the same so E_R is reduced by $\sqrt{2}$ or alternatively the same accuracy can be obtained in half the time. For the second example, consider what happens if the background rate increases more rapidly than the signal rate; say B quadrupoles while S

doubles, so R halves. Then

$$E_R = 1/\sqrt{St}\ (\sqrt{1/2+1/R} + 1/\sqrt{R}) .$$

Notice that although the signal-to-noise ratio has worsened the relative error has decreased, that is the accuracy with which the signal can be measured has improved by an amount depending on R.

Looking now at eqn (2.2.5), for small R, as long as B increases no faster than the square of the increase in S, the accuracy achievable for S in a given time increases even though the signal-to-noise ratio decreases.

By making use of the above principles the optimum tube voltage was found to be 1300 V, some 200 to 300 V lower than would normally have been chosen for operation in the analogue current measuring mode with high signal-to-noise ratio. An increase in the tube voltage of 100 V was found to increase the signal count rate by 10%, but the dark count rate by 25% to 30% for signal-to-noise ratio in the region of 1 to 10. The signal-to-noise ratio did increase as the discriminator level was raised, but the sacrifice in signal count rate made the time required to obtain the same statistical significance too long to make this increase in signal-to-noise ratio an improvement.

§2.2.4 Data Recording

After processing by the single-channel analyzers, the signals from the two monochromators became ORTEC standard logic pulses (5 V, 500 ns) suitable for driving scalers. Two other sources of logic pulses were from the beam current collected in the Faraday cup and processed by an ORTEC 439 Current Digitizer, and a regular train of clock pulses at a rate of 100 s^{-1}. These signals were connected to a block of four computer controlled scalers.

The microswitch on the scanning monochromator activated the clock and provided a command signal to the laboratory's IBM 1800 computer which then collected counts in each scaler for a nominated time, read the scalers and reset them to zero, repeating this sequence a specified number of times. In this way four correlated multi-scaled spectra were obtained. It was desirable to have at least ten channels across a spectral line so that later adjustments for variations in channel width would not distort the shape of the lines. This was usually done with a

6 second collection period for each channel with a scanning rate of 2 Å·min^{-1}. The scanning rate was a compromise to obtain the maximum significance for weak spectral lines of about 1 Å F.W.H.M. and also to complete the scan within the foil lifetime. A spectral range of 40 Å thus covered $\approx$ 200 channels and took 20 minutes to obtain.

The time taken by the computer to read, clear and start collection for each channel was between 4 and 12 ms, depending on the amount of higher priority activity for other experiments also controlled by the computer. Occasionally a severe priority clash arose and the servicing of the four scalers could be delayed by up to 2 s; this occurred with a frequency of less than 1 in 1000 channels. The 100 c·s^{-1} clock spectrum would then contain a channel that had higher counts than normal followed by a channel that had a compensating low count. In this case the channels in the associated spectra corresponding to the oversize clock channel were scaled down to the standard time and their excess counts added to the following channel. After this the clock spectrum was discarded. Three correlated spectra obtained in the above described manner are shown in fig. 2.7.

§2.3 LINEWIDTH CONSIDERATIONS

The decrease in spectral resolvance resulting from Doppler broadening, when viewing the beam-foil source in the normal side-on configuration [Ba 68] leads to an unacceptable loss of information. The typical linewidth of 3 to 10 Å F.W.H.M. precludes the resolution of spectral lines a few Ångstroms apart even when using a spectrometer capable of much better resolution. The presence of blended lines hinders the measurement of atomic lifetimes, charge states, and relative intensities. To measure the intensities of adjacent spectral lines requires that they be separated by an amount of the order of their linewidth. Even so, careful lineshape fitting is required to extract the relative intensities. The fitting becomes more reliable as the width of the individual components is decreased.

By using conventional transfer optics to image the beam at the spectrometer entrance slit with a magnification of unity, maximum light transfer into the spectrometer is achieved, but the large angular range of the light gives rise to the large linewidth. The Doppler effect is expressed by

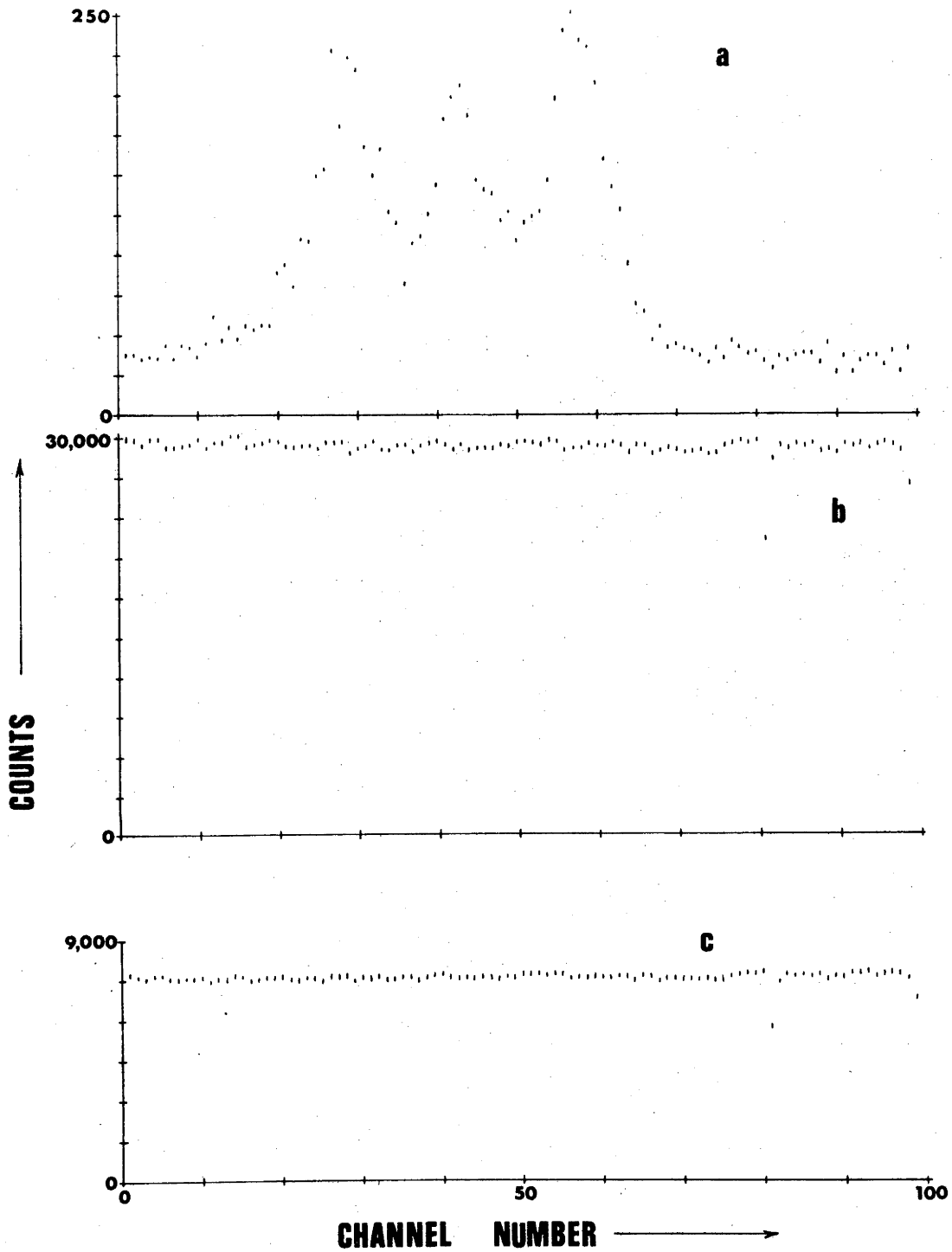

Fig. 2.7: The three correlated spectra constituting a "raw" set of data.

(a) Scanned spectrum, F_α line at ≈ 90 kV·cm^{-1}, 1 Å $\equiv$ 5 channels.

(b) The light monitor spectrum.

(c) Beam current spectrum.

The two drops in light monitor were confirmed to be the result of the corresponding drops in beam current by the normalization procedures described in §3.2.

$$\lambda = \lambda_0\gamma(1 - \beta \cos\alpha) , \qquad (2.3.1)$$

where λ is the wavelength observed at angle α with respect to the beam which has velocity β times the speed of light, $\gamma = (1-\beta^2)^{-\frac{1}{2}}$, and λ_0 is the rest frame wavelength of the emitted light. The coupling lens collects light over a range of angles $(\alpha+\phi)$ to $(\alpha-\phi)$ which leads to a corresponding range of wavelengths

$$\Delta\lambda = 2\lambda_0\gamma\beta \sin\alpha \sin\phi . \qquad (2.3.2)$$

The angle ϕ is usually large in order to match the large aperture spectrometers used for the low intensity beam-foil source. For example, the McPherson 218 monochromator gives $\phi \approx 5°$ for f/5.3 which yields a Doppler broadened line of about 9 Å at 400 keV and 18 Å at 1600 keV for a He^+ beam and the 4686 Å F_α line.

Several methods for linewidth reduction have been described in the literature. The earlier methods relied on reducing one of the angles α or ϕ. For example, with the end-on configuration [Ba 70a] the beam is observed along its axis and α is zero. This gives maximum Doppler shift and minimum broadening. The loss of spatial information that occurs for this configuration is unacceptable for Stark effect observations, lifetime measurements, and quantum beat measurements. Again the axicon system [St 70] uses $\alpha = 90°$ but a small range for ϕ. It employs a conical reflector of 90° vertex, paraxial with the beam, and is located in a region which would cause difficulties when applying strong electric fields to the beam. These methods do not take account of the special geometric properties of the beam-foil source.

The characteristics of another method of linewidth reduction which has improved spectral resolution to an amount adequate for the determination of individual Stark component intensities will be discussed. The method treats the beam-monochromator system as a single unit which is adjusted to take account of the geometric characteristics of the beam-foil source. The relation between the wavelength and direction of light from the source leads to a correlation between the wavelength and the position at which the light falls on the dispersive element of the monochromator which will be shown to be equivalent to adding a thin cylindrical lens to the dispersive element. The effect of this equivalent lens may be cancelled by re-focusing the monochromator. This method can realize the maximum achievable spectral and spatial resolution of side-on viewing; it also obtains the maximum possible light transfer

into the monochromator. The method has been used for all the Stark effect observations on He I and He II described herein.

§2.3.1 Contributions to Spectral Linewidth

There are several contributions to the spectral linewidth which have to be considered when working with a beam-foil source. The relative importance of each will depend on the method of observation and the beam velocity. For high β, the dominant source of line broadening arises from the large aperture of light collection and the high velocity of the He beam. Other contributions to the width of lines are beam divergence due to imperfect collimation, multiple scattering in the foil, and the widths of the monochromator slits. These contributions add approximately in quadrature. Lower limits on beam divergence and slit-widths stem from the requirements of obtaining adequate intensity. De-collimation of the beam by multiple scattering in the foil depends on the particle mass, its energy, and the thickness of the foil. After the major portion of the line broadening is cancelled, scattering becomes a major contribution and it was found desirable to monitor the foil thickness as experiments progressed to ensure the linewidth did not change significantly (§2.1.3).

Instrumental contributions to the linewidth result from the finite widths of the entrance and exit slits, curvature of the image of the entrance slit at the exit slit, and diffraction at the entrance slit. The linear dispersion of the monochromator gives lines about 0.8 Å wide at 5000 Å for 100 μm slits. The curvature of the image of a spectral line [Fa 52] at the exit slit showed $\approx$ 0.4 Å difference between the image centre and the image extremeties for 10 mm occulting slits. This had no significant effect on the width of the line and only a little on its shape unless the widths of the slits were reduced considerably, i.e. towards 10 μm. Diffraction at the entrance slit was not noticeable above 10 μm for observation of an incoherent stationary source [Sa 51].

Fluctuations in the velocity of the ions and divergence of the beam give rise to spectral line broadening. The beam energy variation from the accelerator is less than 1% [Op 65] and for 400 keV He^+ ions a 4 keV variation contributes less than 0.1 Å at wavelengths less than 5000 Å. The divergence of the beam is limited by collimation to $\approx$ 0.008 rad which corresponds to $\approx$ 0.4 Å at 5000 Å for a 400 keV He^+ beam.

Multiple scattering in the exciter foils also affects the linewidth. The effects of multiple scattering on the linewidth for various ions and beam energies is discussed by Stoner [St 73] who presents a useful expression for the r.m.s. scattering angle

$$\overline{\theta^2} = \frac{1}{4}\frac{m_2}{m_1}\frac{\Delta E}{E}, \qquad (2.3.3)$$

where m_2 is the mass of a foil atom, m_1 the mass of the incident ion, E its energy and ΔE the energy loss in passing through the foil, which may be obtained from energy loss tables. Eqn (2.3.3) applies to the multiple scattering regime and is not accurate for plural scattering which occurs in thinner foils [Ja 62] such as the $\approx 2\ \mu g \cdot cm^{-2}$ (≈ 100 Å thick) ones used for most of the experimental work reported here. In a $5\ \mu g \cdot cm^{-2}$ foil a 400 keV He^+ beam loses less than 0.01 keV, which corresponds to an r.m.s. angle below 5×10^{-3} rad, and hence a linewidth contribution below 0.8 Å at 5000 Å.

§2.3.2 The Beam-Foil Focus

An analysis of the beam-monochromator system is given that demonstrates the validity of the previous assertion that the dispersive element of the monochromator acts as a thin lens when the monochromator views the non-stationary uni-directional beam-foil source. The general principle was first suggested by Einstein [Ei 26] but was re-discovered by Hay [Ha 70a] and Stoner and Leavitt [St 71] for the particular application to beam-foil sources. The analysis presented follows a treatment outlined by Hay.

A schematic of the beam-monochromator system used for the following analysis is shown in fig. 2.8. The symmetry of the problem makes it sufficient to consider the optical properties in a plane containing the beam axis and passing through the centre of the monochromator entrance and exit slits. The monochromator axis, straightened for convenience, makes an angle α with the beam direction and light is collected with angular magnification M from a range 2ϕ determined by the monochromator acceptance angle δ and M. The collimating element of focal length F_S presents a parallel beam to the dispersive element which is set at the angle θ appropriate to the mean wavelength λ and the diffracted beam is converged by the second collimator, focal length F_D, towards the exit slit. Two sets of rays are

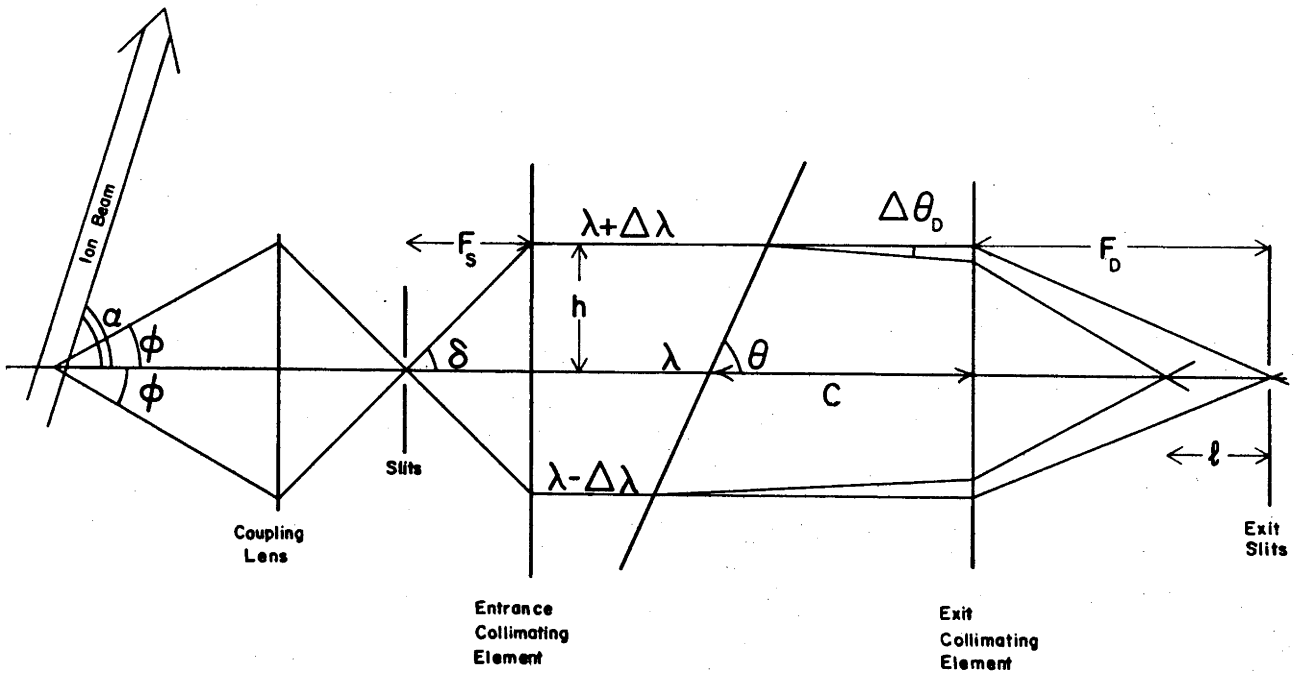

Fig. 2.8: Schematic layout of the beam-monochromator system. The set of rays that focuses to the exit slit is from a stationary source. The set of rays that focuses inside the exit slit is from the beam-foil source.

shown passing through the system. One set of rays is for a stationary source of wavelength λ and these focus at the exit slit. The other set exemplify a beam-foil source with particle velocity v and the rays at angle δ to the central one have a shift of $\Delta\lambda$ from the mean wavelength. Such a ray has a deviation at the dispersing element which differs by $\Delta\theta_D$ from the central ray. It will be shown that the relation between δ, $\Delta\lambda$ and $\Delta\theta_D$ is such that the image of a spectral line through the entrance slit is shifted from the exit slit. This displaced image position will be called the beam-foil focus.

From eqn (2.3.1), one obtains

$$\frac{\Delta\lambda}{\lambda} = \left(\frac{\beta \sin\alpha}{1-\beta\cos\alpha}\right)\phi \quad , \tag{2.3.4}$$

where the symbols refer to fig. 2.8. For angular magnification M at the coupling lens, the angle of entry to the spectrometer becomes

$$\delta = M\phi \quad , \tag{2.3.5}$$

and this ray meets the dispersive element at a distance h from the axis:

$$h = F_S \delta \ , \tag{2.3.6}$$

where the first order expansion for sin δ has been used. For a small range of wavelengths, the change in deviation of any dispersive element may be characterized by a constant angular dispersion D, such that

$$\Delta\theta_D = \frac{\Delta\lambda}{D} \ . \tag{2.3.7}$$

Collecting eqns (2.3.4) to (2.3.7) gives,

$$\frac{h}{\Delta\theta_D} \approx F_S M \frac{(1 - \beta \cos\alpha)}{\beta \sin\alpha} \frac{D}{\lambda} \ . \tag{2.3.8}$$

The right hand term of eqn (2.3.8) is a constant, i.e. the deviation of a ray is proportional to its distance from the axis. This is the characteristic property of a thin lens of focal length

$$f = \frac{h}{\Delta\theta_D} \ , \tag{2.3.9}$$

and demonstrates that the grating behaves as a "grating-lens" of power

$$\frac{1}{f} \approx \lambda \frac{\beta \sin\alpha}{F_S M(1 - \beta \cos\alpha) F_D K} \ , \tag{2.3.10}$$

where the angular dispersion D has been replaced by the equivalent reciprocal linear dispersion at the exit slit

$$K = D/F_D \ .$$

Since the "grating-lens" is illuminated by parallel light, it will form an image at a distance f from the grating. The exit collimator, which is a distance c from the grating, will use this as an object. The image in the exit collimator will fall a distance $F_D + \ell$ from it, hence from the lens equation

$$\frac{1}{F_D} = \frac{1}{F_D + \ell} + \frac{1}{f + c} \ , \tag{2.3.11}$$

whence

$$\ell = \frac{F_D{}^2}{f\left(1 + \dfrac{c - F_D}{f}\right)} \ . \tag{2.3.12}$$

With $\alpha = \pm\pi/2$, substitution of f from eqn (2.3.10) into eqn (2.3.12) gives

$$|\ell| \approx \left(\frac{\beta\lambda}{MK}\right) \left\{\frac{F_S}{F_D} + \left(\frac{c - F_D}{F_D{}^2}\right)\left(\frac{\beta\lambda}{MK}\right)\right\}^{-1} \ . \tag{2.3.13}$$

Note that the sign of ℓ depends on whether f is negative or positive

which in turn depends on whether the beam is viewed from the side for which $\alpha = \pi/2$ or $3\pi/2$ respectively.

For the McPherson 218 monochromator, $F_D = F_S = 307$ mm, $c = 250$ mm, while the range of β for H^+ and He^+ beams used was about 0.01 to 0.03. Typical values of $(\beta\lambda/MK)$ were then 2 to 20 mm and

$$\left(\frac{c - F_D}{F_D^2}\right)\left(\frac{\beta\lambda}{MK}\right) \leqslant 1\% \ .$$

Hence

$$|\ell| \approx \left(\frac{\beta}{M}\right)\left(\frac{\lambda}{K}\right) \ . \qquad (2.3.14)$$

The factors in this equation fall into two groups, namely β/M, which is the speed of the beam image across the entrance slit, and λ/K, which depends on the characteristics of the particular monochromator.

This analysis indicates that any alteration which changes the optical path length within the monochromator by $-\ell$ will move the beam-foil focus back to coincide with the exit slit position. This procedure cancels the main Doppler broadening, that due to the finite aperture of light collection, but the other contributions to line broadening pertain to the stationary source focus so that the stationary source linewidth cannot be achieved. The most noticeable effect of moving the beam-foil focus to the exit slit is that the contribution to line broadening from diffraction at the entrance slit becomes important at larger slit-widths. This was considered by Leavitt and Stoner [Le 72] and from eqn (2.3.14) it can be seen that this contribution will increase as β increases.

If M is made large in eqn (2.3.14), the source looks as if it were stationary and hence the major component of Doppler broadening is cancelled. This is the characteristic of the anamorphotic system [Ka 70] and the parallel light method for linewidth reduction. In the later the coupling lens is placed one focal length from the entrance slit, thus producing an effectively infinite magnification. The method was suggested by Bakken and Jordan [Ba 70]; a detailed study of this simple method was carried out [Ca 72a], but will not be described here because it is not suitable for observing a very short section of the beam without an intolerable loss of intensity.

§2.3.3 Experimental Investigation of Re-focussing the McPherson 218

A simple test of the feasibility of re-focusing our McPherson 218 was devised. For the side of the beam used, eqn (2.3.14) indicated the beam-foil focus would be displaced by about 11 mm inside the exit slit for the F_α (4686 Å) line at 800 keV beam energy ($\beta = 0.02$). A parallel ended perspex cylinder 32 mm long (refractive index 1.5) was placed in front of the exit slit to increase the optical path length by about 11 mm. For slits set at 100 μm the instrumental contribution to the linewidth was 0.8 Å. The results of this test are shown in fig. 2.9. The original linewidth of 12.8 Å F.W.H.M. is in reasonable agreement with the expected width of 13 Å calculated for $\beta = 0.02$ and a wavelength of 4686 Å. Insertion of the perspex cylinder reduced the linewidth to $\approx$ 4 Å and increased the peak intensity.

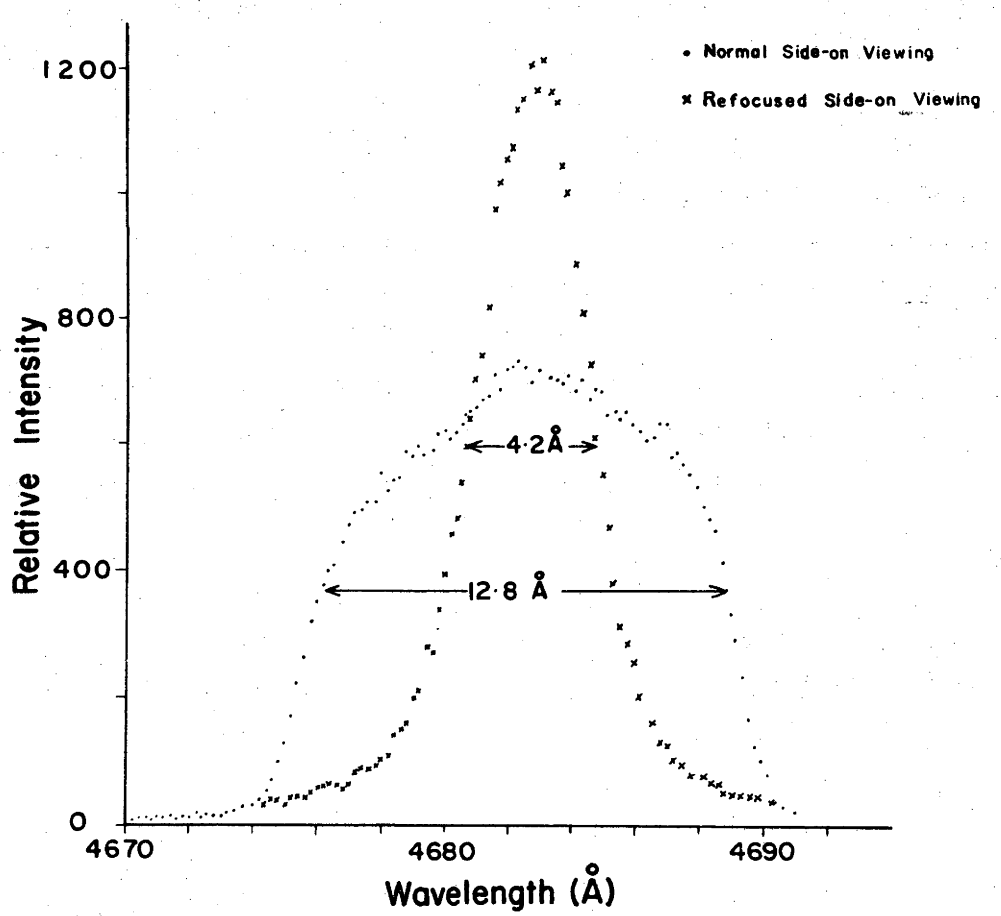

Fig. 2.9: Linewidth for stationary source focus and for beam-foil source focus. Monochromator re-focused for beam-foil source by altering optic path length with perspex slab.

Because the McPherson 218 is mechanically unsuited to changing the position of the collimating mirrors or slits, a corrector lens was inserted at the exit slit to re-focus it. The lens of focal length -35 mm was mounted in a hollow screw adjustment as the correction depends on β and the wavelength. The screw was fitted with an arbitrary scale to permit resettability. The spectral line of interest was scanned for various corrector lens positions and the linewidth (F.W.H.M.) noted at each position. Finding the position for minimum width took less than an hour. A typical series of observations for the H_β (4861 Å) line, with the instrument slits set at 100 μm, are shown in fig. 2.10(a). The slow variation of linewidth about its minimum with the corrector lens position is evident from fig. 2.10(a) and may be due to the linewidth's being limited by beam scattering in the foil or diffraction at the monochromator entrance slit. The linewidth contribution from the 100 μm slits is 0.86 Å at this wavelength. The minimum linewidth at different slit-widths is shown in fig. 2.10(b). The increase in linewidth at 75 μm slit-widths is in good agreement with estimates of the effects of diffraction at the entrance slit obtained from the expression given by Leavitt and Stoner [Le 72].

A more extensive investigation of the characteristics of re-focusing showed that if the monochromator wavelength was set at the centre of the line then the re-focused position could be found in a few minutes by scanning the position of the corrector lens to obtain maximum counting rate. Further investigations indicated that the slow variation of linewidth about the minimum was a general feature of re-focusing for our instrument. This means that small changes in wavelength and beam velocity due to applied electric fields will not affect the linewidth obtained by re-focusing at zero field. To determine the precise meaning of small wavelength and velocity changes in this context, the variation of corrector lens position required to re-focus the monochromator was measured as a function of beam energy and of wavelength. The results of a series of such measurements is shown in figs. 2.11(a) and (b). From these results and the variation of linewidth with corrector lens position, fig. 2.10(a), a 40 Å wavelength change or a 20 keV beam energy change would give < 2% increase in linewidth. The Stark patterns measured cover a range of, at most, 40 Å, while the beam energy change caused by the electric field when observing the He II fraction was less than 20 keV for electric field configuration (a) (§2.4.2). Therefore re-focusing on a

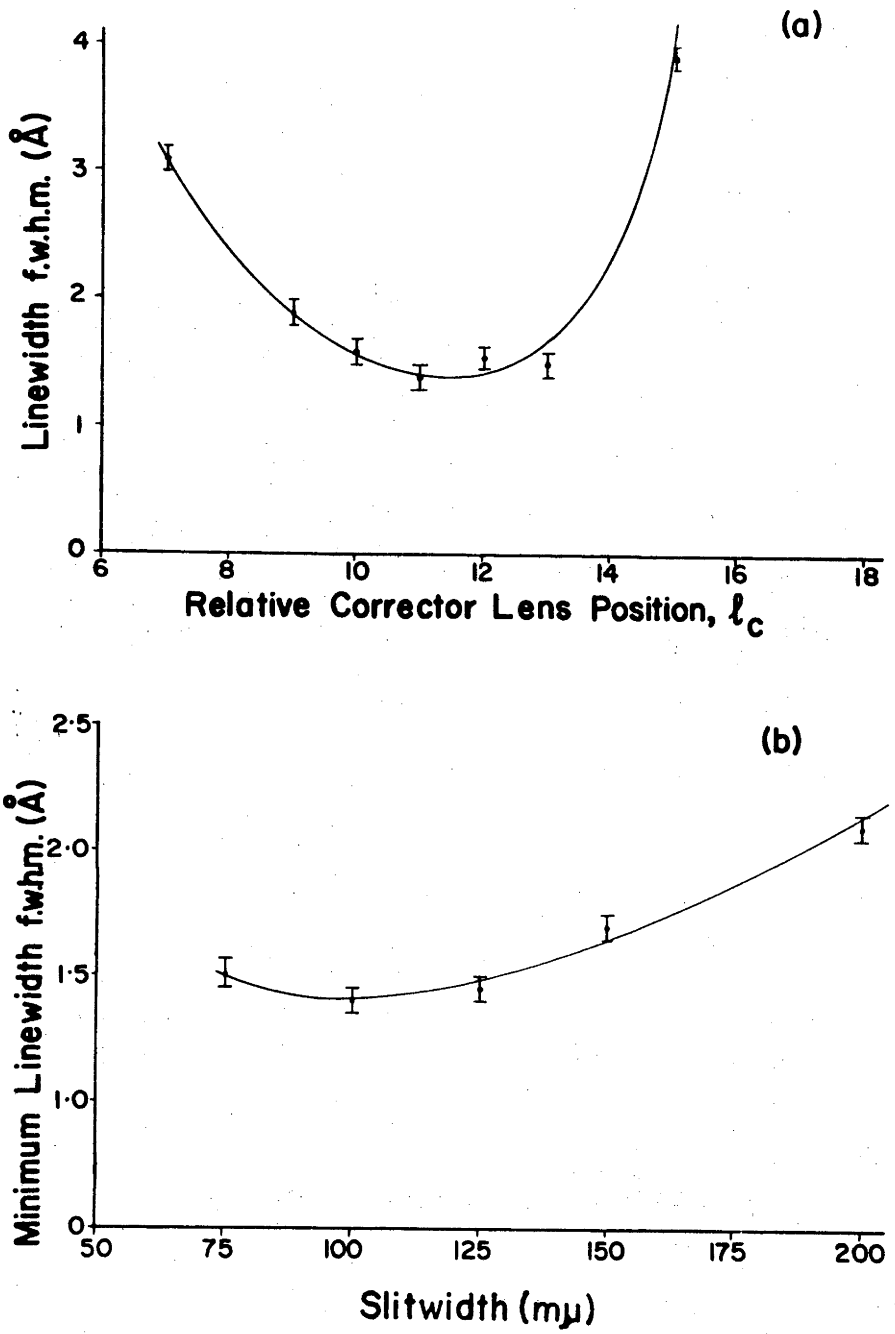

Fig. 2.10: Experimental re-focusing.

(a) Variation of linewidth with position of the diverging corrector lens for $\beta = 0.023$ and H_β (4861 Å). The relative focus correction has an arbitrary zero relative to the exit slit.

(b) Minimum linewidth as a function of slit-widths.

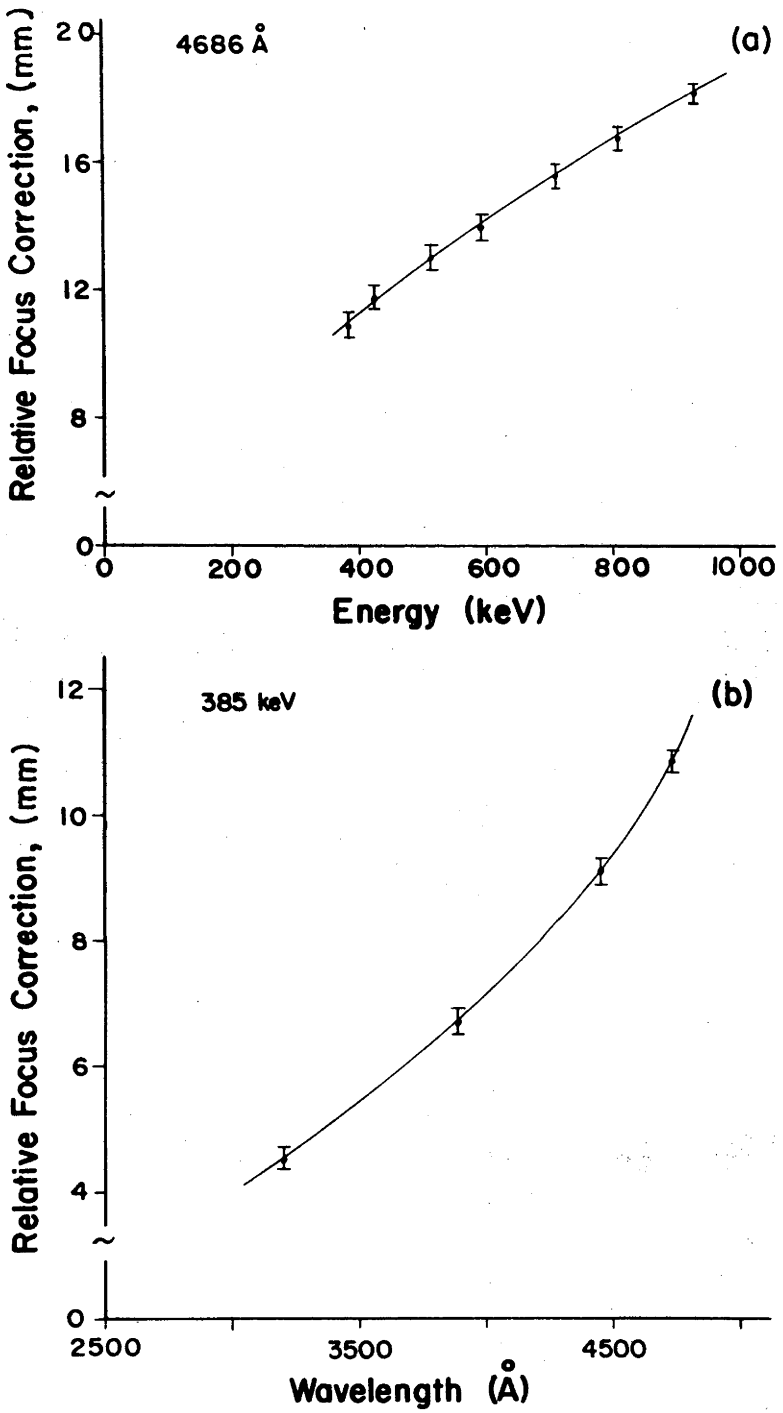

Fig. 2.11: The variation of re-focused corrector lens position with (a) energy, (b) wavelength. The relative focus correction has an arbitrary zero relative to the exit slit position.

spectral line in zero field will lead to negligible changes in linewidth when the field is applied.

The corrector lens method of re-focusing the McPherson 218 monochromator to obtain cancellation of the major component of Doppler broadening from the high velocity beam-foil source has proved to be a highly satisfactory method of linewidth reduction. The only disadvantage is the tolerable loss of intensity incurred by absorption in the glass corrector lens. The linewidth for the F_α (4686 Å) line and He^+ beam energies between 400 keV and 800 keV was probably limited by scattering in the thin carbon foils for energies less than 600 keV, whereas diffraction at the entrance slit probably set the limit above 600 keV when 100 μm slits were used. The contribution to linewidth from scattering decreases with increasing β while the contribution from diffraction increases; hence, for part of the energy range, the two effects may be compensatory. The re-focusing of the monochromator was carried out experimentally, partly because of the difficulty in making accurate predictions of the adjustment required when these two sources of line broadening are present.

A particularly important feature is that the method can be used with a magnification of unity in the side-on configuration where the spatial resolution obtainable is set by the entrance slit-width of the monochromator. This last feature is important in quantum beat experiments and lifetime measurements; both of these aspects can be important for Stark effect observations at weak and strong electric field strengths. Furthermore, the spatial resolution is an important consideration in determining acceptable spatial variations in applied perturbing fields as any large variations over a region of observation may contribute to line broadening. The slow rate of change of re-focusing position with changes in wavelength and beam energy make this method particularly easy to use over the restricted wavelength range required for Stark effect observations at high electric field strengths. The gain in usable signal-to-noise ratio from the increased resolution and the maximum transfer of light obtained with unit magnification are also advantages of this method of linewidth reduction.

§2.4 ELECTRIC FIELDS

The magnitude of the electric fields which could be established in the region of observation encompassing the beam determined the

separation of Stark components and therefore, in conjunction with the linewidth considerations of §2.3, was a major consideration in measuring the relative intensities of the Stark components.

The transitions from excited states perturbed by an electric field are polarized and, as the electric field defines a z direction in space, the direction and solid angle of observation relative to this z-axis determines the part of the angular distribution of the polarized radiation sampled.

The electric field strength variation along the beam path influences the radiative decay and perturbation history of the ions observed in the strong field region between the field electrodes. This variation is important when observed relative intensities are to be related to the initial populations of the corresponding excited states at the foil.

§2.4.1 Electric Field Production

The high voltages required to establish electric fields in the observation region were applied through the insulated electrodes mentioned in §2.1.2. The insulated electrodes were different for the two chambers used.

The ceramic insulated central electrode portion of an automotive spark plug was used to construct the insulated electrodes for use with the cylindrical chamber. The rough conical ceramic end of the spark plug was glued with epoxy resin into a polythene rod with a connection to a central electrode. The smooth ceramic portion was fitted at the shoulder with an "O" ring and held firmly onto the chamber lid with a brass collar, thus providing a vacuum seal. The smooth ceramic insulator stem that obtruded into the chamber had two "O" rings placed on it because it was found that this permitted higher voltages to be maintained with less intermittent breakdown . Brass caps were screwed to the end of the insulated electrodes. The brass caps had ball joints at the ends to accommodate brass rods to which steel plate field electrodes could be attached. All components were hand polished and their edges rounded as much as possible.

The field electrodes consisted of 3.2 cm wide, 3 mm thick plates with 3 mm slots running along their longitudinal axis to within

5 mm of their ends. The length of the plates was either 3.5 cm or 7.0 cm. The slots were provided to allow passage of the beam or observation of the electric field region between the plates, depending on the configuration used. The field electrodes were positioned with a set square and ruler, usually 4 mm to 5 mm apart.

The insulated electrodes for the large stainless steel chamber consisted of tungsten rods sealed in uranium oxide glass formed into long ribbed cylinders with an "O" ring seat half way down. The field electrodes were 6 mm thick. The metal components were all stainless steel and otherwise essentially the same as those described above.

The potentials applied to the electrodes were originally provided by two Hursant power supplies (-20 kV, +50 kV). These were later replaced by Brandenburg Model 907P and 907N power supplies (+60 kV and -60 kV respectively). The fields were produced with one field electrode negative and one positive in order to avoid excessive loading on a single electrode. This had the advantage of minimizing the beam energy change of the charged fraction when operating with the electric field parallel to the beam. The negative field electrode was placed nearer the foil when a field parallel to the beam was required, as this reduced the loading on the power supplies from secondary electrons. The field electrode to foil distance was of the order of 1 cm. With 30 kV applied to the negative electrode and the foil at ground potential, this gave rise to $\approx$ 400 gm force on the foils which broke as a result. To avoid breaking the foils, an earthed electrode was placed between the foil and the field electrodes.

When using the cylindrical chamber, the limit to the potential difference applied to the field electrodes was $\approx$ 55 $kV \cdot cm^{-1}$, giving a field of $\approx$ 100 $kV \cdot cm^{-1}$ with a 4 mm electrode separation. In the large stainless steel chamber the limit to applied potential difference was near 100 kV, giving a field of about 160 $kV \cdot cm^{-1}$ for 5 mm electrode separation. The limit to the applied potential was set by the current drain to the power supplies arising from secondary electrons, scattered beam and corona discharge. The large chamber had greater separation between the insulated electrodes, the field electrode support rods and the sides of the chamber, and a lower vacuum pressure, all of which probably contributed to the improved performance. Care had to be exercised in applying the electrode potentials to avoid forcing the

secondary electrons onto the electrode supports or the viewing ports. The provision of extra observation ports on the chambers other than the ones used for the monochromators was advantageous for this purpose.

§2.4.2 Electric Field and Monochromator Orientation

Three arrangements of parallel negative and positive field electrodes were used to obtain three electric field configurations. The monochromator was constrained to view the beam in the side-on configuration.

(a) Electric field parallel to the beam, observation transverse to the electric field. The field electrodes were perpendicular to the beam with the beam passing through the slots to obtain this field configuration, see fig. 2.12(a). The beam was undeflected by the parallel electric field. The π and σ polarized Stark components appear linearly polarized parallel and perpendicular to the field respectively.

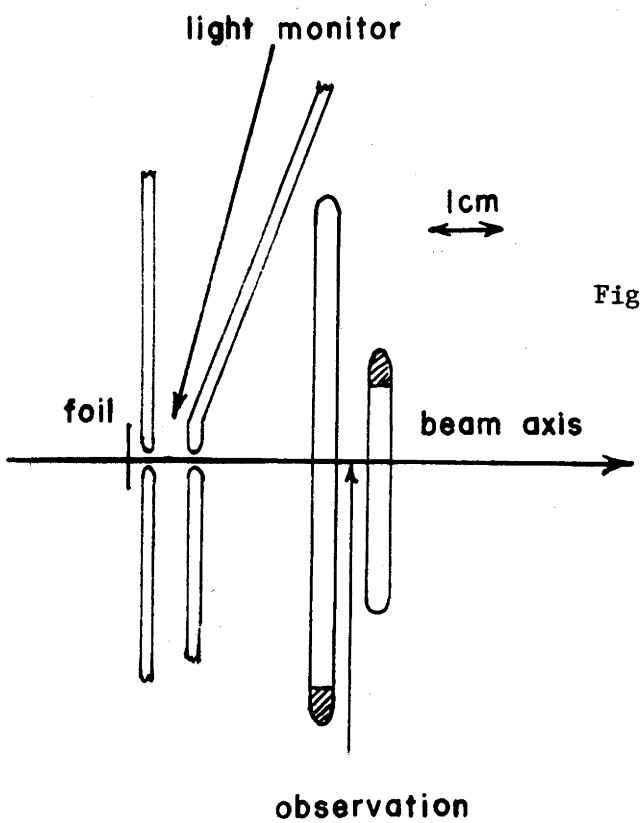

Fig. 2.12(a): Electric field monochromator orientation (a). Typical electrode positions used to obtain orientation (a) are shown with the relative position of the earthed plates and foil indicated.

(b) Electric field transverse to the beam, observation parallel to the electric field. The field electrodes lay in vertical planes spaced nearly equal distances from the beam axis. The beam was viewed through the slots in the field electrodes, see fig. 2.12(b). Only σ components are observed with this configuration and they appear unpolarized. The charged fraction of the beam was deflected.

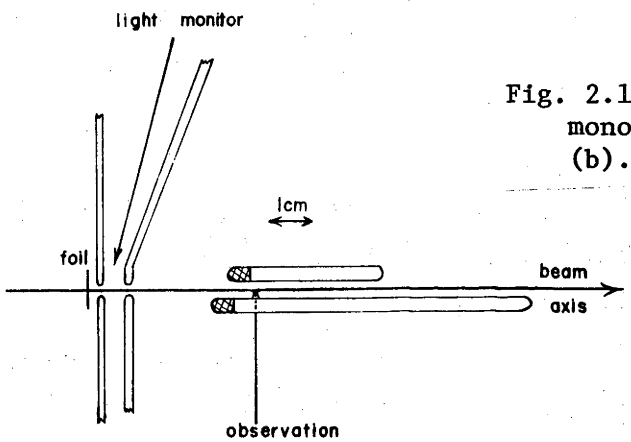

Fig. 2.12(b): Electric field monochromator orientation (b).

(c) Electric field transverse to the beam, observation perpendicular to the field. The electrodes were placed in horizontal planes spaced nearly equal distances above and below the beam axis, see fig. 2.12(c). The π and σ components appear as for configuration (a). The charged fraction of the beam was deflected.

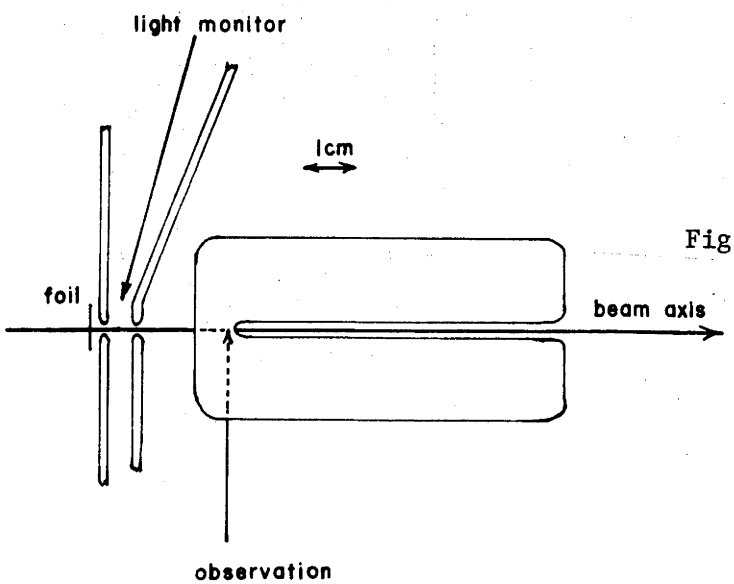

Fig. 2.12(c): Electric field monochromator orientation (c).

The configuration (a) was used for linear Stark effect observations because both π and σ components were observed and the electric field was strong along most of the beam axis. The configurations (b) and (c) were used for the quadratic Stark effect measurements. Configuration (b) was used to observe only σ components, the contribution of π components being negligible because the solid angle of observation was very small ($\approx$ 0.01 sr). The difference between configurations (a) and (c) is in the rate the electric field is applied and the effect of the grating on the differently oriented π and σ components (§2.2.1).

§2.4.3 Electric Field Measurement

The presence of the slots in the field electrodes result in a non-uniform electric field in the region of observation which may have led to line broadening of the Stark components. The effects of the slots on field uniformity were tested using analogue resistance paper techniques and by observations of the H_β Stark components. A variation from the field midway between the plates on the beam axis of $\approx$ 10% was found ±1 mm away in the horizontal or vertical directions for the field electrode configuration (a). The variation in the field a further 1 mm away was about 30% from that at the beam axis. The effect of these variations on the linewidth of H_β Stark components was found to be negligible (< 0.1 Å) by comparing the linewidth of the resolved Stark components ($\approx$ 100 kV·cm^{-1}) to the linewidth of the H_β line at zero field. The estimates of the field non-uniformities between the field electrodes obtained by the analogue method differed by less than 2% from calculated estimates, based on plane infinite slotted plates [Du 53, p.338], obtained by Doobov [Do 72a].

The electric field strength along the beam axis was estimated also from analogue resistance paper plots of the equipotentials. The scale used was 1 inch to 1 mm to give reasonable sensitivity. A voltage divider was used to establish a zero potential for the earthed electrode, a potential of -39 volts for the negative field electrode and 61 volts for the positive field electrode. To obtain the equipotentials in the weak field regions at the earthed electrode, an established equipotential nearby was treated as an electrode and the full 100 volts applied between it and the earthed electrode. The gradient of the electric potential, that is the electric field strength, was determined graphically using the

equipotential plots. The equipotentials determined for the electric field configuration (a) are shown in fig. 2.13. The electric field strength determined from fig. 2.13 along the beam axis is shown in fig. 2.14(a), while fig. 2.14(b) shows the electric field strength along the beam axis for configuration (b) determined from corresponding equipotential plots. The distances and hence the times in which the electric field changes occur are estimated from fig. 2.13. Configuration (a) provides strong electric fields along most of the beam axis whereas configuration (b) produces an appreciable region of weak electric field.

Estimates of the electric field strength midway between the field electrodes on the beam axis showed that the slots diminished the field from that obtained without slots. For slots of 3 mm, a field plate separation of 4 mm and 55 kV applied to the field electrodes, a field strength of 91 $kV \cdot cm^{-1}$ is predicted midway between the plates on the beam axis. The field measured from the resolved Stark splitting of the H_β line under these conditions was 93 $kV \cdot cm^{-1}$. The field without slots would have been 137 $kV \cdot cm^{-1}$. The field strengths used for data analyses were determined from the shift of the resolved Stark components in the region of observation. If the shift of the Stark components of interest was insufficient to provide enough structure to determine the field strength, measurements of the H_β Stark components were carried out to provide this information. Fig. 2.15 shows an H_β Stark pattern from which the electric field was calculated using the separation of the components indicated. The transitions giving rise to the two outer components at ± 10 X are $4300 \rightarrow 2100$ and $4030 \rightarrow 2010$. Using eqns (1.2), (1.3) and (1.4) gives F the field strength as 82.7 ± 1.2 $kV \cdot cm^{-1}$.

The field strengths were estimated by the analogue method where the field was too weak to resolve H_β Stark components, in particular in the region near the earthed electrode. The penetration of the electric field through the aperture in the earthed electrode, with -30 kV on the negative electrode 1 cm away, was found to be small. In this case, the field drops from about 6 $kV \cdot cm^{-1}$ at the exit side of the aperture to about 1 $kV \cdot cm^{-1}$ 2 mm nearer to the foil and from there nearly linearly to less than 100 $V \cdot cm^{-1}$ at the light baffle plate (earthed). The region viewed by the light monitor monochromator is thus a region of a few hundred volts per cm. Spectral lines for monitoring were therefore chosen that suffered negligible Stark perturbations at these field strengths.

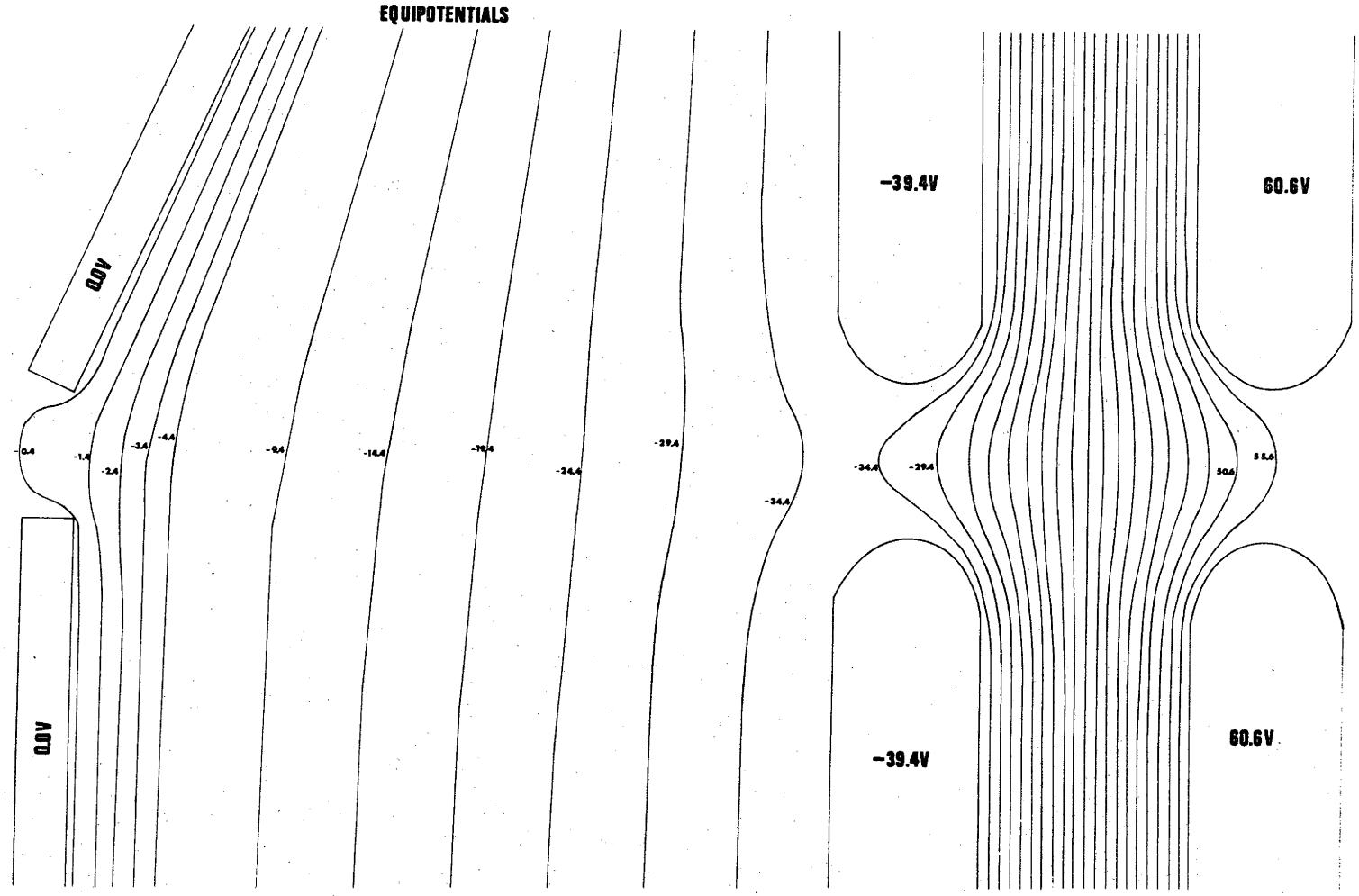

Fig. 2.13: Equipotentials from analogue plots. Note the change in gradient from +ve to -ve near the -ve field electrode and the small penetration of the field through the aperture in the earthed (0.0 V) electrode.

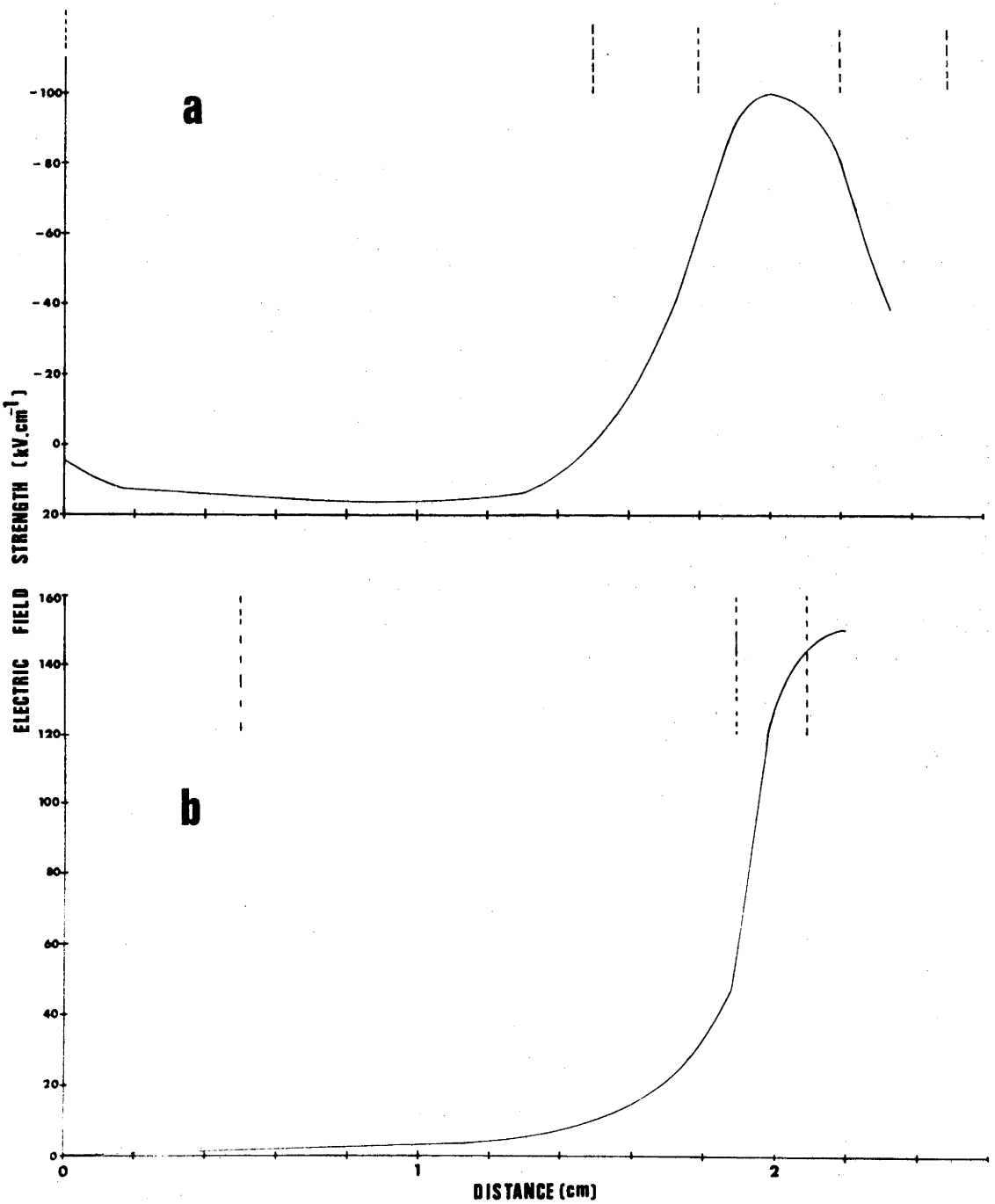

Fig. 2.14: Electric field strength along beam axis.

(a) Field configuration (a). (b) Field configuration (b).

---- indicates edges of electrodes.

Both used to estimate rate of change of electric field along beam axis.

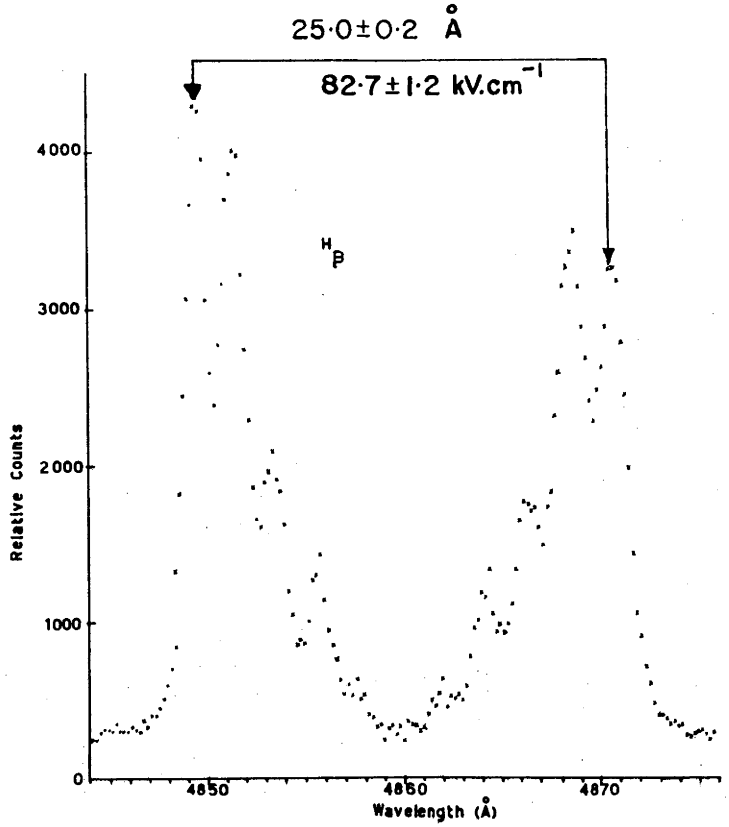

Fig. 2.15: Resolved Stark components of the H_β line.

CHAPTER 3

EXPERIMENTAL PROCEDURE

The relative intensities of the He I and He II transitions depend on the proportions of He and He^+ present in the beam. The fraction of He falls as the beam energy increases [Ar 65], so the He I measurements were carried out at He^+ beam energies below 500 keV. The He II measurements were done between 400 keV and 800 keV, the lower end of the energy range being set to avoid excessive line broadening by multiple scattering, and the upper limit by the decrease of the light intensity.

The analysed He^+ beam currents obtained from the accelerator were between 1 and 20 μA, depending on the state of the ion source and the energy of the beam. When it was necessary, the beam current was restricted to about 5 μA in order to obtain a complete scan of a spectral region within the lifetime of a single foil. The monitoring monochromator was used to observe the line being scanned or another line from the same charge state, because the intensity of a spectral line is proportional to the number of ions of the relevant charge state produced by the foil but is very indirectly related to the beam current. For a helium beam at approximately 400 keV there are equal numbers of He^{++} ions and He atoms, so that for an incident beam of He^+ ions, the current measured is virtually independent of the presence or absence of a foil.

§3.1 COLLECTION OF SPECTRA

The experimental re-focusing of the scanning monochromator (§2.3.3) provided measurements of zero field linewidth and the wavelength of the unperturbed transition for use in later data analysis. The linewidth for zero field was measured for several foils to check that any effect of foil thickness variations were negligible.

Spectra were usually collected at a rate of 10 channels per minute and a scanning rate of 2 $Å \cdot min^{-1}$. This gave adequate detail across spectral components of 1 Å F.W.H.M. The rate was fast enough to

obtain complete spectra before the foils deteriorated enough to affect the linewidth. The total range of the scans was about 30 Å which covered the Stark components of interest and gave a sample of the background at either end of the scan. Data could be obtained by scanning either from low to high wavelength or vice versa. The appearance of the raw spectra could be quite different for the two directions due to degradation of the foil, however the differences were removed provided normalization to the light monitor was carried out.

There are several sources of background which may be determined by altering the experimental conditions. The total background count rates were required data for normalization procedures (§3.2.1). The photomultiplier dark count ($\approx$ 1 counts$\cdot s^{-1}$) was determined periodically to ensure cooling was adequate. Any small changes in dark count rate were assumed to be linear with time. Scattered secondary electrons gave a beam dependent background of 2 to 4 counts$\cdot s^{-1}$ depending on the distribution of voltage between the electrodes. The voltages were set to avoid fluorescence from the chamber windows resulting from deflected secondary electrons. Another source of background arose from occasional sparks between the electrodes. A spark showed up as an isolated spectrum channel count which was several times higher than the counts in neighbouring channels. With very strong lines a small reflection, $\approx$ 5% of the total line intensity, was evident from the quartz window on the opposite side of the target chamber. The position of the reflection was displaced a little from the strong line because the angle of the collection lens axis to the quartz window was not precisely 90°.

§3.2 NORMALIZATION

The normalization procedure could be executed by an on-line computer programme both during and after data collection. The first step was to ensure the differential linearity by using the clock spectrum, as described in §2.2.4. From the three remaining spectra, three normalized spectra were derived.

The first normalization was a ratio of the scanned spectrum to the light monitor which accounted for changes in the number of ions of a particular charge state whether these arose from beam current fluctuations or from changes in foil conditions. This normalization was made with the assumptions that each channel was recorded for the same time, the

background for the scanned spectrum was a linear function of channel number, and the light monitor counts per channel were large enough to assume its small background to be constant for the duration of the scan. It is an advantage if the monitor counts are much greater than the scanned counts. This was usually the case with 2000 μm slits on the Heath monochromator and about 100 μm slits on the McPherson. If they are about equal it requires four normalized scans to regain the same random counting statistical significance as a single scan had. The normalization was carried out channel-by-channel as demonstrated below for the ith channels:

(a) subtract the scanned spectrum background counts (B_i) from the scanned spectrum count (S_i).

(b) subtract the light monitor background counts from the light monitor counts to give the true monitor counts (C_i).

(c) scale the scanned spectrum count to a standard monitor level (M), usually close to the mean over several scans.

(d) multiply the scanned spectrum background by M/A, where A is the average true monitor count for this scan.

(e) add the results of steps (c) and (d) to give the normalized spectrum counts $\left(S_i^M\right)$ in channel i, that is

$$S_i^M = \frac{(S_i - B_i)M}{C_i} + B_i\left(\frac{M}{A}\right) .$$

Steps (d) and (e) were done to preserve the counting statistics' nature of the spectrum by eliminating the occurrence of channels with zero or negative counts in background channels of the spectrum. This was done for reasons associated with later analysis procedures and with the computer storage and display of the data.

The second normalization, carried out as a back-up to the light monitor normalization, was the ratio of the scanned spectrum to the beam current monitor. This was done in the same manner as the light monitor normalization, but with zero background for the monitor counts.

The third derived spectrum took the ratio of the light monitor counts, corrected for background, to the beam current. This channel-by-channel ratio gave the history of, and was used to assess the extent of, foil damage (§2.1.3) and provided a very useful data quality criterion.

The light monitor signal is proportional to the number of ions of a selected charge state, whereas the beam current is proportional to a weighted sum of the number of ions of each charge state. The ratio of light monitor to beam current therefore gives information on changes in the foil condition. On-line normalization took only a few seconds, and often indicated small changes in accelerator or beam transport conditions which could be corrected before they became large enough to degrade the quality of the data. A representative set of three original and three normalized spectra is shown in fig. 3.1.

The light monitor normalized to the beam current gave a means of distinguishing foil wear and breakage from beam current changes. Fig. 3.1(b) shows two regions of larger than normal variation in the light monitor, the first one is due to a beam fluctuation as can be seen by comparison with the beam current monitor fig. 3.1(c), the second appears to be a partial breakage in the foil; the light monitor to beam current ratio, fig. 3.1(f), indicates this interpretation to be correct. This data was taken at 250 keV where there are more neutral than doubly charged He ions, hence insertion of a foil decreases the observed current so that the increase in fig. 3.1(c) indicates a hole in the foil. The foil changes cannot be monitored by the ratio of light to beam current monitor if electric field configurations (b) and (c) are used (§2.4.2). Under these conditions the foil wear was checked by reference to the light monitor. It was desirable in this case to maintain a steady beam because damage to the foil could not be readily distinguished from beam current changes. With these configurations a new foil was used for each scan. Periodic scans were also carried out with zero electric field to obtain the light to charge ratio spectrum and to ensure foils did not significantly deteriorate in the time taken to obtain a scan.

The success of the normalization in removing systematic errors can be tested by examining the scatter in corresponding channels of several spectra by standard statistical methods, such as the F test. Such tests demonstrated that the light monitor could successfully cope with large fluctuations in beam behaviour and gradual changes in the state of the foil. Foil damage proved to be a condition for which the beam current monitor was incapable of producing consistent spectra. Spectra normalized to beam current showed intensity differences for the different wavelength scanning directions. Once several raw spectra were available, each of which was a separate sample of the same intensity

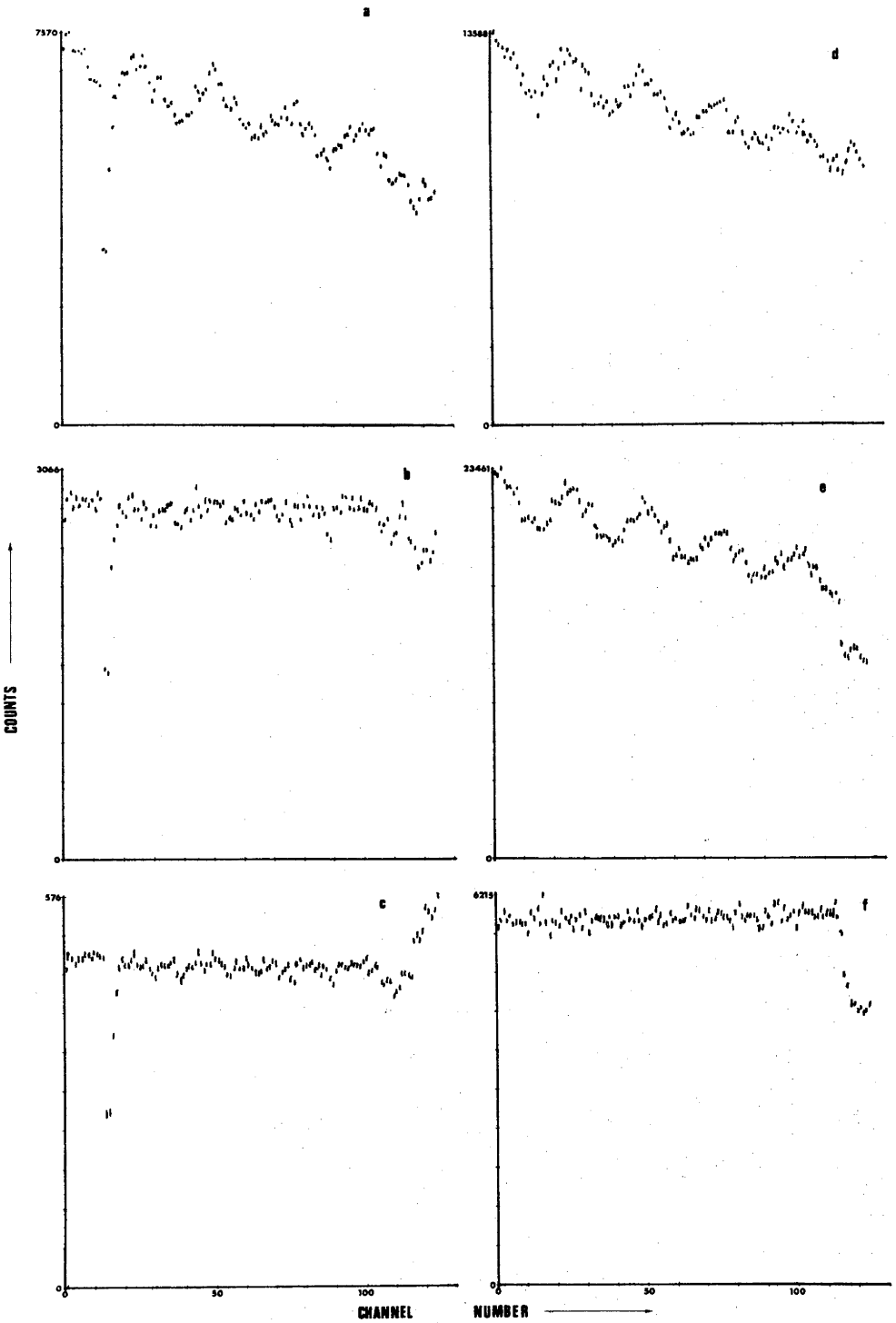

Fig. 3.1: Complete set of data after normalization.

(a) Scanned spectrum; in this case the wavelength was fixed at 3889 Å and the position of the monochromator from the foil was increased by 1 mm every 5th channel.

(b) light monitor. (c) beam current.

(d) scanned spectrum normalized to light monitor; (a) to (b).

(e) scanned spectrum normalized to beam current; (a) to (c).

(f) light monitor to beam current; (b) to (c).

distribution, they were summed. A single scanned spectrum and the sum of nine repeat spectra are shown in fig. 3.2; the improvement in statistical significance is obvious. The single spectra can be tested for internal consistency and the summed data may then be used for final analysis.

The choice of spectral line to observe with the light monitor was influenced by two main considerations. One was that it come from the same charge state as the scanned line so that changes in charge state ratio due to foil damage were properly accounted for and the other was that its counting rate be high relative to the scanned line. The line chosen for the He II Stark component intensity measurements was the strong line F_α (4686 Å) which gave monitor counts in excess of 10^4 counts for a six second channel at all beam energies used and a beam current of about 3 μA. Typical peak counts in a scanned Stark spectrum of the F_α line were less than 300 counts. The line chosen for the He I Stark component measurements was the $3^3P \rightarrow 2^3S$ (3889 Å) line which gave monitor counts in excess of 10^3 compared to less than 100 counts in the scanned peaks.

§3.3 RELATIVE INTENSITIES BY DATA FITTING

The problem of determining the intensities of the Stark components was treated by a non-linear least-squares fitting technique [Ha 69, Ha 71]. The recorded spectrum was matched to a sum of several lines at different positions and a linear background whose slope tended to zero. The shape of each component was based on that observed for a single line, e.g. the F_α line for zero field. The positions of the lines were not independent parameters, but were constrained to satisfy the separation ratios for the Stark splitting.

The actual lineshape is a smoothed triangle for very wide slits. For very narrow slits subsidiary diffraction maxima show as higher wings out to two or three widths. The beam energy and foil thickness were such that scattering contributed to the lineshape. Fig. 3.3 shows the match of a Gaussian lineshape to an observed unsplit F_α line. The empirical Gaussian lineshape, specified by its width, position of its centre, and its height, is not correct but is quick to calculate compared to interpolating and scaling a "standard" lineshape. The empirical lineshape reproduced the same peak height ratio as experimental lineshapes for separated lines.

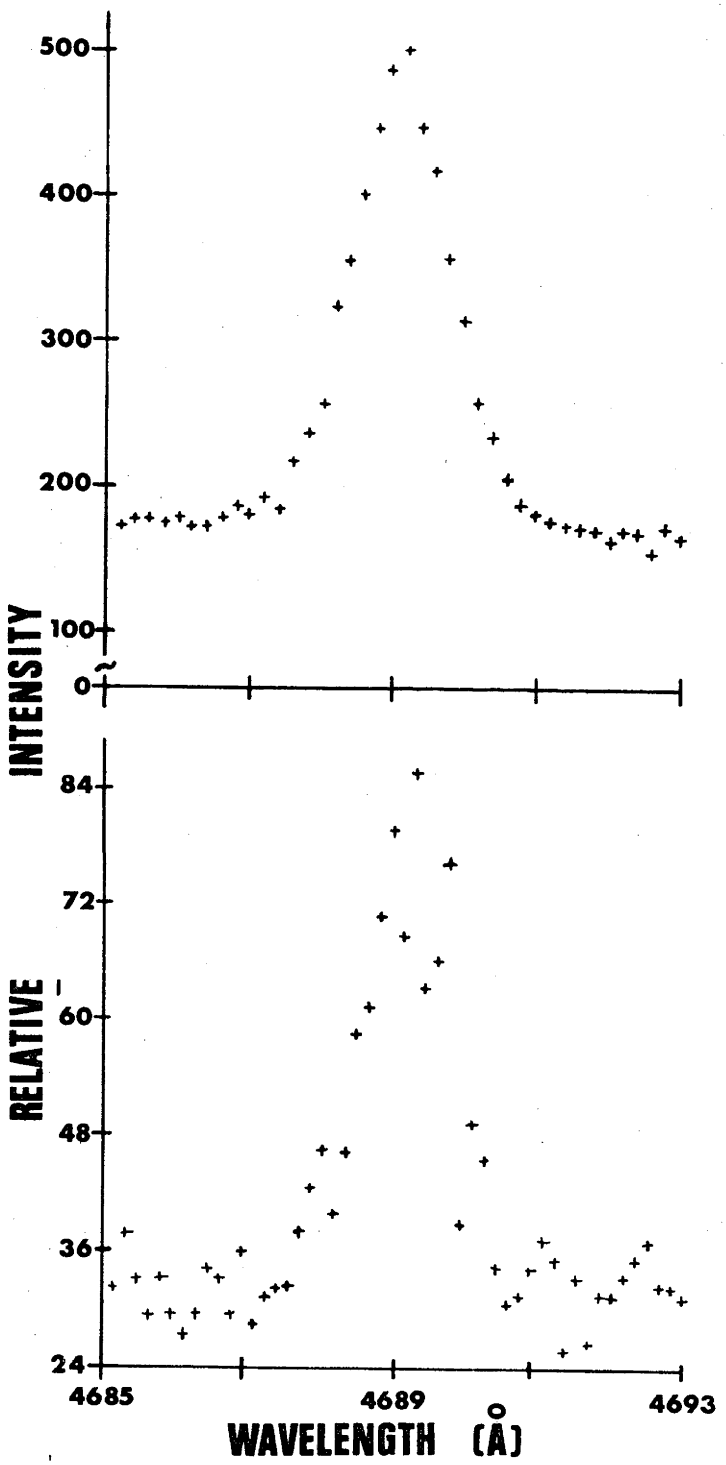

Fig. 3,2; Improvement of statistical significance from summing data.
The sum of 9 single scans (top) and one of the single scans (bottom).

The separation factors for the empirical lines used for the Stark components was determined from measured electric field strengths (§2.4.3) and the Stark effect energy level scheme at that field strength.

The functional form of the synthesized spectrum was

$$I(i) = \sum_j A_j \exp\left\{-0.693\left[\frac{i - P_j}{W/2}\right]^2\right\} + B(i) , \qquad (3.1)$$

where i is the ith wavelength interval of the spectrum, A_j are the amplitudes of the lines, W is their common width, P_j are the positions of the lines, and B(i) is the background. The number of free parameters in the synthesized spectrum is reduced from three times the number of lines plus two for the background, to one times the number of lines plus one each for the width, separation factor, and centre of Stark splitting, plus two for the background by using information from independent measurements and a knowledge of the Stark component wavelengths.

The model of a Stark spectrum consisted of the appropriate number of single lines, spaced relative to each other in a manner depending on whether the Stark effect of He II or He I was being investigated. The model parameters of direct interest were the amplitudes of the various components in the synthesized spectrum because they are proportional to the intensities of the Stark components which all have the same width.

To achieve the match between the synthesized spectrum and the observed spectrum a least-squares functional, Q, was constructed with the form

$$Q = \min_{0<i<n} \sum_i^n \frac{(I^o(i) - I(i))^2}{I^o(i)} \Big/ (n - n_p - 1) , \qquad (3.2)$$

where $I^o(i)$ is the observed intensity in the ith wavelength interval, I(i) the model-predicted intensity in the ith interval, n is the total number of intervals, and n_p is the number of free parameters. The way in which Q is constructed allows comparison with χ^2 tables. The minimization procedure used to obtain Q and the corresponding values of the free parameters was carried out with a locally produced subroutine [Ha 71].

If no correlations existed between the free parameters, the basis vectors of the minimization space were orthogonal. Correlations showed up as a non-orthogonality between various basis vectors. The

cosines of the angles between all basis vectors taken in pairs were provided by the subroutine and served as a measure of correlation. For example if the basis vectors of two parameters were parallel after the minimization procedure was completed, a change in one parameter is exactly equivalent to a change in the other parameter and the two are essentially indistinguishable. In this case one parameter should be removed from the model or other information about it obtained from a separate experiment. The information on correlations was thus very useful in guiding the construction of synthesized spectra and deciding where another kind of experimental measurement was needed to give non-correlated estimates of certain parameters.

The fit to the F_α line shown in fig. 3.3 was obtained by the minimization procedure with a synthesized spectrum containing a single line and a linear background. The empirical Gaussian lineshape has a height 12% lower than the observed height and mismatches the wings of the experimental lineshape. The underestimate of the observed line height obtained from data fitting was not significantly different for a range of isolated lines of widths between 1 Å and 3 Å.

The ratio of the heights of isolated lines was excellent because the underestimate of their heights was the same for each one. The incorrect empirical lineshape fails when the lines are not separated enough and when trying to obtain the height of a weak line in the wing of a strong line. The terms "separated enough" and "weak line" are imprecise in this context but the measure of correlation between estimated heights provides a guide to their magnitude.

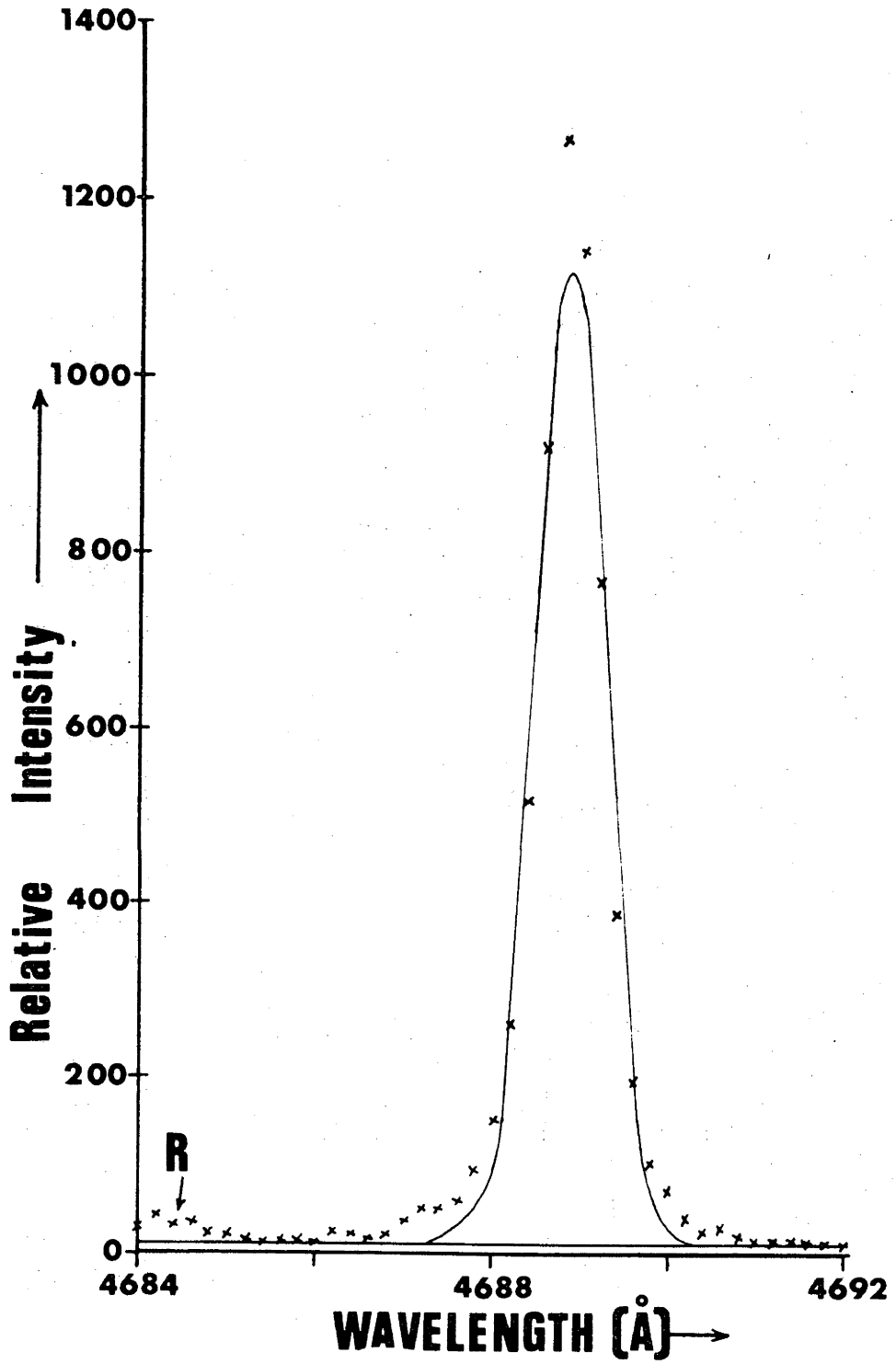

Fig. 3.3: Empirical lineshape. Fit of a Gaussian line to the observed F_α (4686 Å) line obtained at a beam energy of 680 keV with monochromator slit-widths of 100 μm. The height of the fitted line underestimates the measured height by 12%. A contribution to the background arising from a reflection is indicated (R).

CHAPTER 4

OBSERVATIONS OF THE STARK EFFECT IN THE BEAM-FOIL SOURCE

§4.1 TRANSITIONS SELECTED FOR STARK EFFECT OBSERVATIONS

The choice of which transitions in He would be suitable for the measurement of relative intensities of Stark components in strong electric fields was dictated by several experimental considerations. The major consideration was that the Stark splitting should be as large as possible, preferably enough for adjacent components to be observed as separate lines. The linewidth limit set by multiple scattering of the He^+ ions in the foil varied with energy and foil thickness and was typically of the order of 1 Å. A Stark splitting in He II of this magnitude would require electric fields around 200 $kV \cdot cm^{-1}$, about twice as high as could be obtained easily. Although the separation of Stark components generally increases with the principal quantum number n of the upper levels for a given electric field strength, the intensity of transitions from states of increasing n value decreases. A compromise between the available intensity and Stark splitting must be made. However, lineshape fitting procedures on Stark patterns, and the inclusion of other types of observation, enabled intensities to be extracted for splittings as low as 0.5 Å.

To obtain information on the intensities of lines in the spectral range of the monochromator and photomultiplier, survey scans from 3000 to 5300 Å were carried out for 0 and 80 $kV \cdot cm^{-1}$. The electric field, the beam, and the viewing direction were mutually perpendicular and no polarizer was used. For the survey, the monochromator slits were set at 300 μm, to increase the counting rate. The instrumental linewidth was thus about 3 Å which is less than the beam source Doppler broadening ($\approx$ 9 Å at 5000 Å for 400 keV He^+). By re-focusing to remove the Doppler broadening at 4000 Å, the linewidths for the survey were practically determined by the slit-widths. The spectra were normalized to the He $3^3P \rightarrow 2^3S$ (3889 Å) line and are shown in Appendix F, figs. F3 and F4.

Of the several He II transitions that showed up in the survey, only the first two lines of the Fowler series, F_α (4686 Å) and F_β (3202 Å) were strong. The F_α line was the more intense, and as it was in a better part of the spectral range of the available polarizer (fig. 2.6), it was chosen for further investigation.

The survey contains many He I transitions, but as expected on theoretical grounds, the only ones showing a large Stark perturbation arise in terms of principal quantum number $n = 4, 5, 6, 7, 8$ for the higher orbital angular momentum states. Of these transitions, those from the terms of $n = 4$ showed the highest intensity. The allowed transitions $4^3D \rightarrow 2^3P$ and $4^1D \rightarrow 2^1P$, and the forbidden transitions $4^3F \rightarrow 2^3P$ and $4^1F \rightarrow 2^1P$, were chosen for further study.

§4.2 THE HE II, F_α STARK PATTERN

§4.2.1 Observed Spectra

The arrangement of the beam-foil source which was used for measuring the Stark effect of the F_α transitions developed from several theoretical and experimental requirements. A strong field was required in the region between the earthed and negative electrodes, as well as between the negative and positive electrodes, to enable the observed F_α Stark patterns to be related to the relative populations of the $n = 4$ levels excited at the foil. As was seen in §2.2.2, monitoring needed a zero field region. It was also convenient to view the beam perpendicular to the field so that both π and σ components could be observed at the same time. The source configuration (a) which met these requirements has been indicated in fig. 2.12(a) and a discussion of it was given in §2.4.2. For these measurements the distance from the foil to the exit side of the earthed electrode was 10 mm, from the earthed electrode to the nearest face of the negative electrode it was 14 mm, and the separation of the 3 mm thick electrodes was 4 mm.

The field strengths which could be achieved in the small cylindrical chamber were not sufficient to resolve the F_α Stark components. They were, however, large enough to separate the components of the H_β line. Hence, the H_β Stark pattern was used to explore and calibrate the electric field before switching the ion source to helium.

The F_α Stark effect measurements were carried out at three He^+ beam energies: 400, 680, and 820 keV. The position and shape of the

zero field, unsplit lines were recorded for use in fitting the Stark patterns. The linewidths obtained at these energies were 0.90 ± 0.05 Å, 0.95 ± 0.05 Å, and 1.04 ± 0.05 Å respectively. These include a contribution of 0.88 Å from the 100 μm wide monochromator slits. The variation of the linewidths with energy is consistent with the partially compensating energy dependences of contributions from multiple scattering and diffraction at the entrance slit (§2.3.3). A reflection from the monitor window added a spurious line to the spectrum. This was easily measured in the absence of the electric field. It was displaced by -3 Å and its height was $4 \pm 2\%$ of that of the zero field F_α line.

Spectra were obtained for π and σ components together, and separately by using a linear polarizer. They were analysed both independently and also together by using the monochromator and polarizer efficiency data of §2.2.1. Figs. 4.1, 4.2 and 4.3 show the spectra obtained at beam energies of 400, 680, and 820 keV respectively. The continuous curves on the figures were obtained with the fitting procedures described in §3.3. The heights and positions of the components of the curves are also drawn.

The differences in the Stark patterns for the various polarizations, considered in conjunction with the decay scheme and transition probabilities, are sufficient to ascertain the maximum number of components which could significantly contribute to the spectra. There are a possible thirty-seven components (neglecting fine-structure) from allowed transitions ($\Delta M = 0, \pm 1$) between the Stark perturbed $n = 4$ and $n = 3$ levels of He II. Of these, thirteen central components have transition probabilities at least an order of magnitude greater than the rest (see Appendix B). They consist of one undisplaced component, six displaced towards lower, and six displaced towards higher wavelengths. From fig. F1 of Appendix F, it can be seen that the central five components are σ polarized, and there is a group of five π components on each side. The two outermost σ and the innermost π components in each group overlap. If more components were present there would be other σ and π groups displaced more than the two π groups observed. These thirteen components are sufficient for spectra of the quality shown here, in which the splitting of ≈ 0.6 Å is only just over half the linewidth, and small spurious lines have resulted from reflection.

When improved beam-foil experimental equipment was commissioned, towards the end of the period in which this work was being done, it

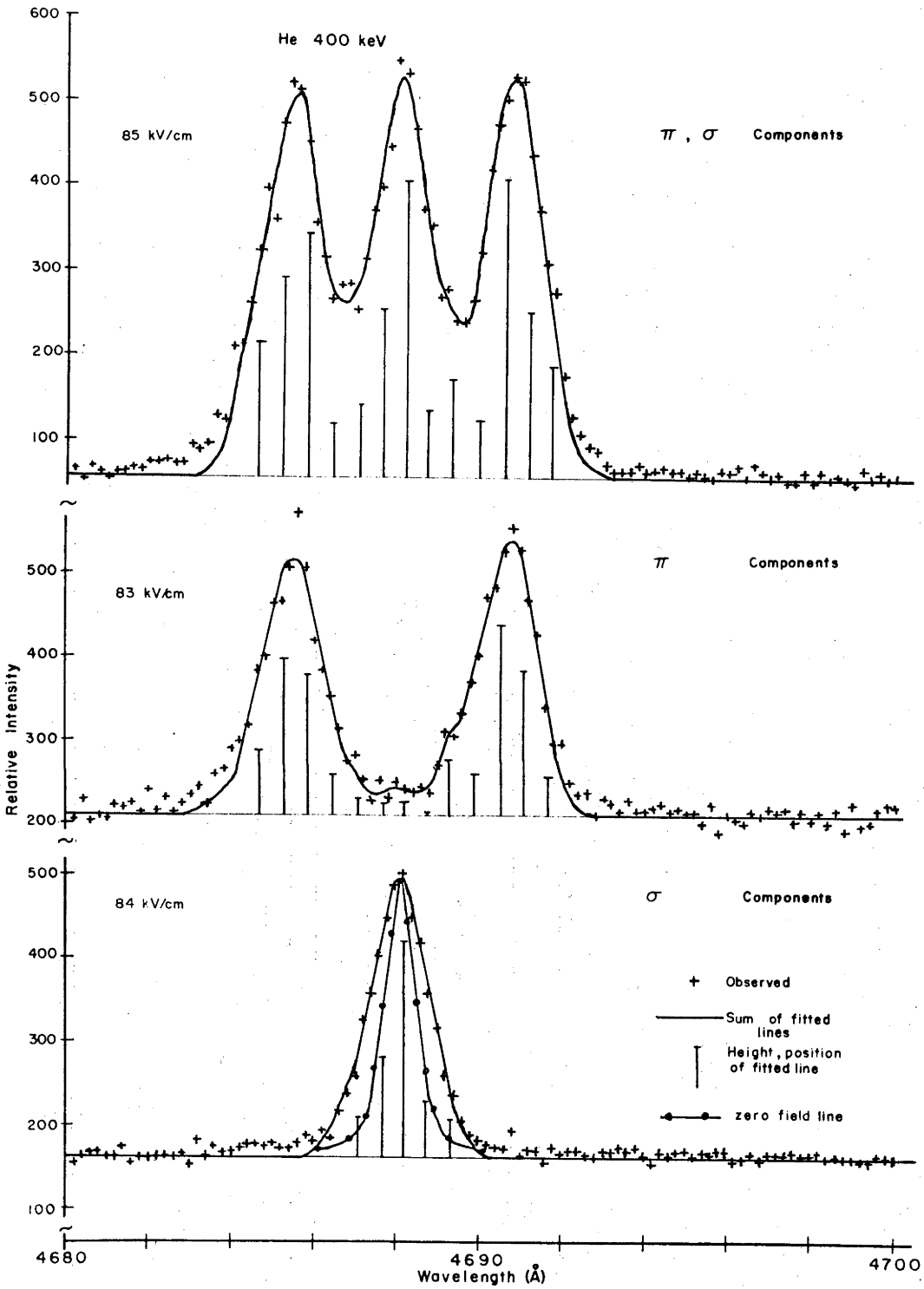

Fig. 4.1: F_α Stark pattern at 400 keV beam energy. The fitted components, all of equal width, are indicated by their position and height. The electric field strength was obtained from Stark separated H_β components. σ component data and π component data have been normalized to the same monitor counts. The σ spectrum has a zero field lineshape superimposed.

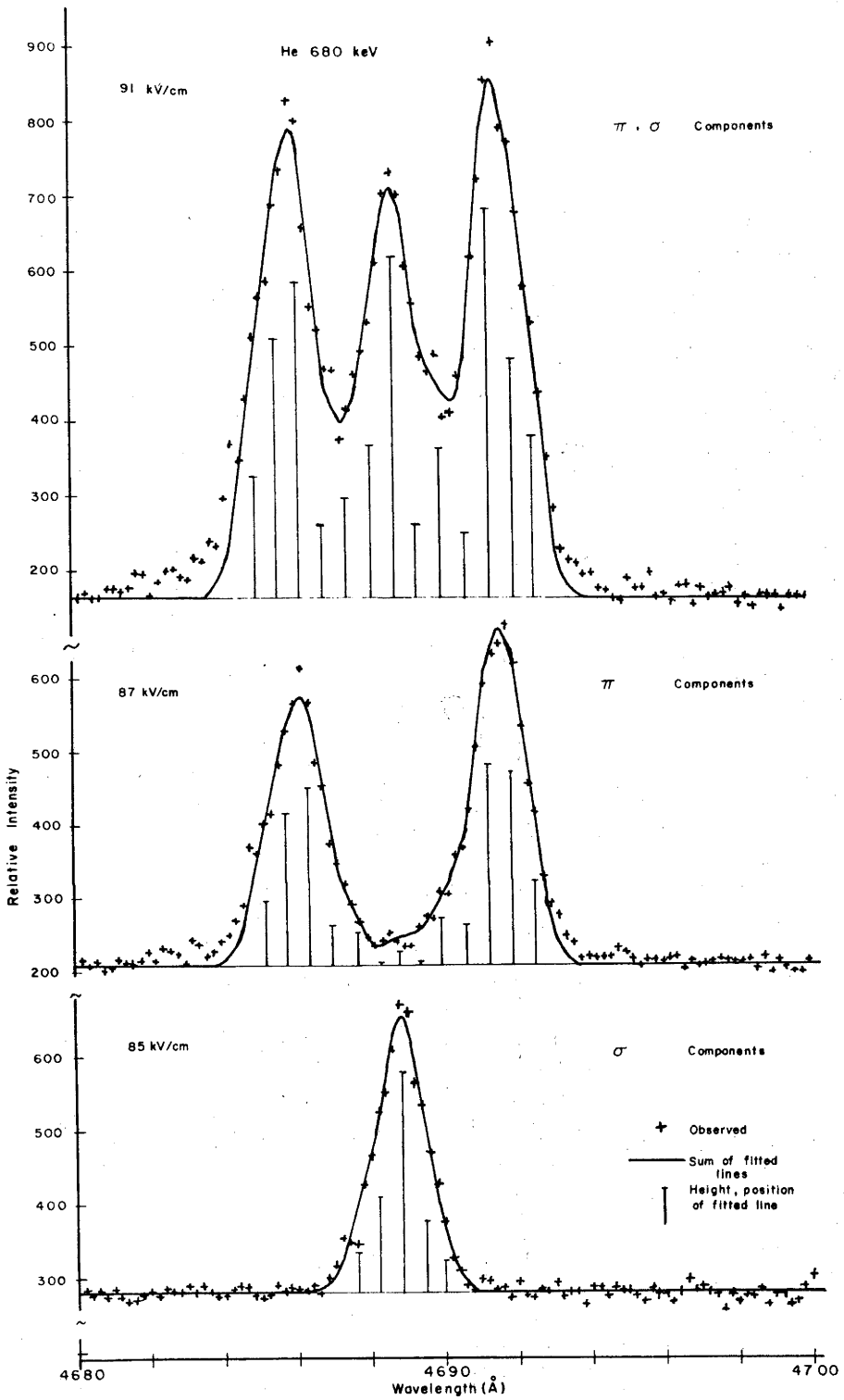

Fig. 4.2: F_α Stark patterns at 680 keV beam energy. σ component and π component data have been normalized to the same monitor counts.

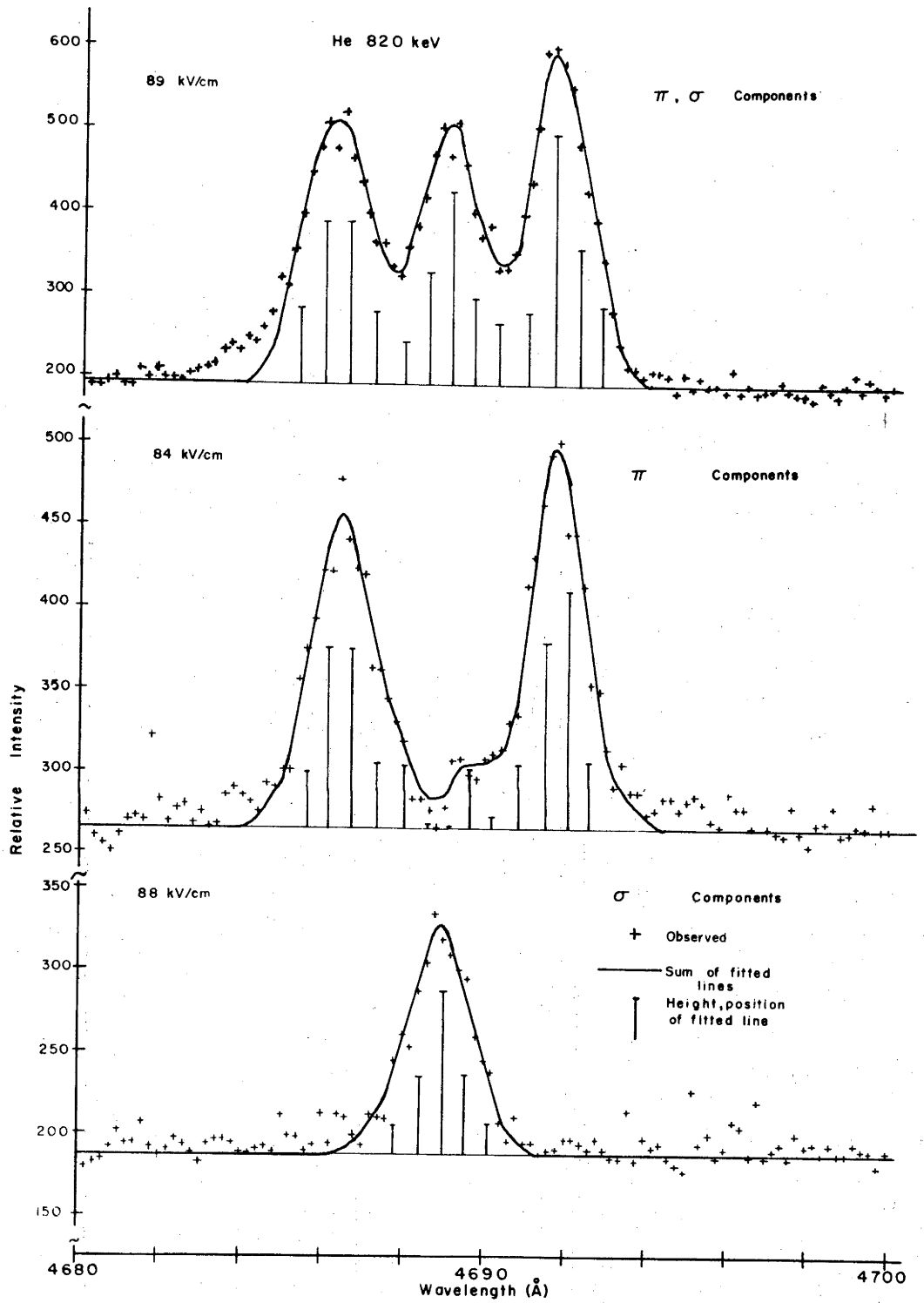

Fig. 4.3: F_α Stark pattern at 820 keV beam energy. The effect of reflection is evident in the π,σ component data. The σ component and π component data have been normalized to the same monitor counts.

became possible to perform some measurements with higher electric fields. At 150 $kV \cdot cm^{-1}$ the three wide peaks of fig. 4.2 began to show obvious signs of structure. The experimental geometry of the previous measurements could not be reproduced identically. The overall distance between the foil and the observation region was 1 mm longer than for previous data. The distance from the foil to the exit side of the earthed electrode was 10 mm, from the earthed electrode to the nearest face of the negative electrode 10 mm, and the separation of the 6 mm thick electrodes was 5 mm.

One scan of the F_α spectrum for 680 keV ions in a field of 161 $kV \cdot cm^{-1}$ is shown in fig. 4.4. The amount of detail in this spectrum is sufficient to measure the field as 161 ± 3 $kV \cdot cm^{-1}$, without having to measure an H_β spectrum for that purpose. No reflections added weak lines to this spectrum, and again thirteen components were enough to fit it.

§4.2.2 Relative Intensities of the F_α Stark Components

The relative positions of 13 Stark components, for the 90 $kV \cdot cm^{-1}$ data of figs. 4.1, 4.2, and 4.3, were determined using the field strengths obtained from resolved H_β Stark components (similar to fig. 2.15) and the calculation of the He II $n = 4$ and $n = 3$ perturbed energy levels (Appendix B). The linewidth of the components and the position of the central component of the Stark pattern were determined from the zero field F_α lines measured at the appropriate beam energy. The small change in linewidth with beam energy, viz. 0.90 to 1.05 Å, made no significant change in the intensity analysis so the results presented pertain to the mean observed linewidth. The background was determined separately by fitting a straight line to the limits of the spectra clear of the peaks. Thus the synthesized spectrum contained only the intensities as free parameters. Furthermore, the Stark components displaced ±3X were constrained to be equal because they arise from the same upper level, go to symmetrically displaced lower levels, they are π polarized only, and their transition probabilities are equal (see fig. F1). Table 4.1 contains the relative intensities, for the data taken without a polarizer.

In the minimization space, the angles between pairs of basis vectors corresponding to neighbouring components ranged from 53° to 37°. This shows that the intensities of these components are fairly strongly correlated (§3.4). The standard deviations shown in table 4.1 were

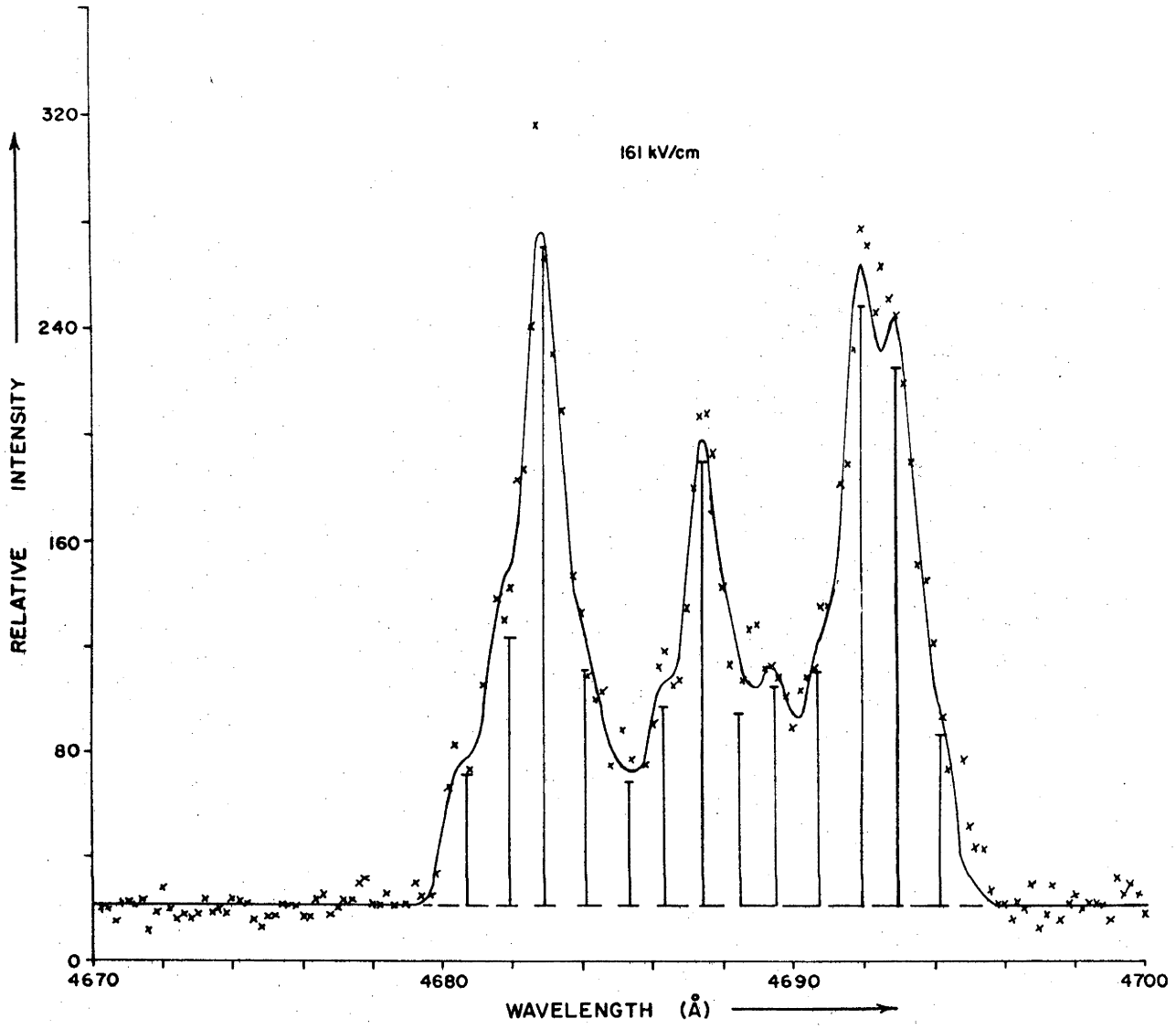

Fig. 4.4: The F_α Stark pattern at 680 keV beam energy and 161 $kV \cdot cm^{-1}$. The fitted curve is the sum of a constant background and 13 equal width Gaussian lines with the identical heights and positions.

estimated from the scatter in fits to the individual spectra whose sums are shown in figs. 4.1, 4.2, and 4.3. Superposition of the normalized spectra shows a small but persistent change with beam energy. However, because of the correlations in the analysis this difference can not be associated definitely with particular components.

In the fitted lines on the spectra of figs. 4.1, 4.2, and 4.3, the reflection from the monitor viewing port became more noticeable as the beam energy was changed from 400 keV to 820 keV. The reflection was displaced -3 Å and its relative intensity was $4 \pm 2\%$. The mismatch to the low wavelength wing of the pattern is larger than the mismatch in the

TABLE 4.1: Relative intensities of Stark components at 90 $kV \cdot cm^{-1}$.

Displacement of Component	Normalized Relative Intensity			Standard Deviation
	400 keV	680 keV	820 keV	
-6X	70	50	52	10
-5X	102	106	107	17
-4X	123	130	107	17
-3X	26	27	49	7
-2X	36	40	28	9
-1X	86	62	73	14
0	150	140	122	16
1X	34	30	56	11
2X	51	63	40	10
3X	26	27	49	7
4X	152	162	169	22
5X	84	95	92	30
6X	59	68	54	9
Q*	2.2	2.1	1.6	

* Q, the value of the least-squares functional (eqn 3.2) is similar to the values obtained from fits to single F_α lines.

high wavelength wing as a result of this reflection. The reflection is also noticeable in the π component data in the central wavelength region, and for the data at 820 keV was possibly strong enough to interfere with the determination of the intensity of the component at a displacement of +2X. To estimate the effect of the reflection on the fitting procedure the π data was allowed to have dummy "σ components" in the central region. These dummy components contained between 2% and 5% of the π components.

A consistency check on the fitting was carried out as follows. The Stark components at ±2X consist of π and σ polarized components. The fits to the σ component data and fits to the π component data provide their separate relative intensities. This information was then used to determine the relative contributions of the π component and the σ component in the ±2X Stark component of the data obtained without a polarizer. The σ component at -2X and the π component at -5X arise from

transitions from the same upper levels (see fig. F1). The ratios of the intensities of these transitions, corrected for polarization differences in the monochromator (see fig. 2.6), are given in table 4.2.

TABLE 4.2: Intensity ratio of fitted Stark components at ±2X to ±5X.

Energy (keV)	-2X to -5X	+2X to +5X
400	1.3 ± 0.4	0.8 ± 0.3
680	1.5 ± 0.5	0.9 ± 0.4
820	1.6 ± 0.6	0.8 ± 0.4

The theoretical ratio is 0.95 (table B.1, Appendix B), which compares reasonably with the experimental values in table 4.2. This consistency check is not particularly sensitive because of the low intensities of the ±2X components and the consequent large uncertainty in them.

For the higher electric field, the data of fig. 4.4 was fitted using the same model of the intensity distribution, but the field strength, linewidth, and position of the central component were determined by the fitting procedure. The relative intensities, electric field strength, linewidth, and Q are given in table 4.3. The correlation between the intensities of neighbouring components was much less than for the 90 $kV \cdot cm^{-1}$ data; the angular separation of the basis vectors being between 70° and 75° (cf. 40° - 50°). The uncertainty of the intensities was determined from the arbitrary criterion that the change in any one of them would give rise to a 20% increase in Q.

The data obtained at 161 $kV \cdot cm^{-1}$ is in reasonable qualitative agreement with the data obtained at the lower electric field. The central σ component and the π components at ±5X and ±4X are the strongest components in both patterns. The asymmetry in the patterns is qualitatively the same, favouring the high wavelength π components. The estimate of the relative intensities of the components at -5X compared to that at -4X is different for the two sets of data. The large correlation between the intensities of neighbouring components in the 90 $kV \cdot cm^{-1}$ data appears to be responsible for most of this difference.

TABLE 4.3: Relative intensities of Stark components at 161 kV·cm^{-1}.

Q = 1.05, Width = 1.09 Å, Field Strength = 161 kV·cm^{-1}.

Displacement of Component	Normalized Intensity	Change Required to Give 20% increase in Q
-6X	32	± 8
-5X	67	± 7
-4X	162	±13
-3X	59	± 8
-2X	32	± 5
-1X	49	± 8
0	110	±14
1X	49	±12
2X	55	±12
3X	59	± 8
4X	147	±14
5X	133	±14
6X	43	±13

§4.2.3 Effect of Electric Field Variations Along the Beam

The effects of lifetime changes are related to the relatively long times between the electrodes whereas the population mixing variations are related to the short times where the electric field is close to zero near the electrodes. The experimental geometry used to obtain the 161 kV·cm^{-1} data was used with -10 and +30 kV, -20 and +20 kV, and -30 and +10 kV applied to the field electrodes. These electrode voltages establish different field strengths (approximately 9, 18, 27 kV·cm^{-1} respectively) in the region between the earthed electrode and the negative electrode. Each pair of voltages gave the same field strength, 64 kV·cm^{-1} at the point of observation, but the rates of change of the field at the apertures in the electrodes are different.

The Stark pattern obtained for each voltage distribution is shown in fig. 4.5 where the dominant group of long wavelength components is seen to increase relative to the other groups as the electric field strength in the relatively long region before the negative electrode increases. From fig. 4.4 the strongest components are those at +4X and

+5X, which contribute about 70% of the intensity in the long wavelength group.

The lifetimes of the components at +4X and +5X (table B.1) in weak electric fields approach the shorter 4^2P lifetime (0.79 ns) through the admixture of this state in the perturbed wavefunctions [Be 57, p.288]. The ions spent about 30% of their total decay history in the electric field between the earthed and negative electrodes (about 10 mm out of 30 mm, see §4.2.1). This field increased from the intermediate field value of 9 $kV \cdot cm^{-1}$ to the strong field value of 28 $kV \cdot cm^{-1}$ [Lü 51, Appendix B]. The small increase in the long wavelength components with field strength is thus consistent with an increase in the lifetimes of the +4X and +5X components as the electric field was increased.

The asymmetry of the Stark patterns for the 90 $kV \cdot cm^{-1}$ data, estimated as the intensity of the +4X and +5X components (257) to the -4X and -5X components (236), taken from table 4.2 is less than that for the 161 $kV \cdot cm^{-1}$ Stark pattern estimated from these components, (280) compared to (229), in table 4.3. The source of this variation between the lower and higher field strength data is probably the effect on the decay probabilities of the perturbed states from the field in the region between the earthed and negative electrodes, approximately 12 $kV \cdot cm^{-1}$ and 36 $kV \cdot cm^{-1}$ respectively. The small difference in decay time ($\approx$ 0.3 ns) due to the slightly different electrode spacings is expected to give only marginal differences since the lifetimes of the Stark perturbed levels are between 1 and 5 ns.

The rate of application of the electric field at the apertures, estimated from the field plots of fig. 2.14, was expected to mix the populations of the Stark perturbed levels by the same amounts for each of the three field values established between the earthed and negative electrodes. This matter is discussed in §6.1.4 but here it is appropriate to note that the changes in the rate of application of the field are not expected to change the Stark pattern.

§4.3 OBSERVATIONS OF HE I STARK PERTURBED LINES

The integrated relative intensities of the triplet lines $4^3S \rightarrow 2^3P$, $4^3P \rightarrow 2^3P$, $4^3D \rightarrow 2^3P$, and $4^3F \rightarrow 2^3P$ as well as the signlet lines $4^1S \rightarrow 2^1P$, $4^1D \rightarrow 2^1P$, and $4^1F \rightarrow 2^1P$ were obtained from the 80 $kV \cdot cm^{-1}$ survey scan and after correction for the wavelength dependent detection

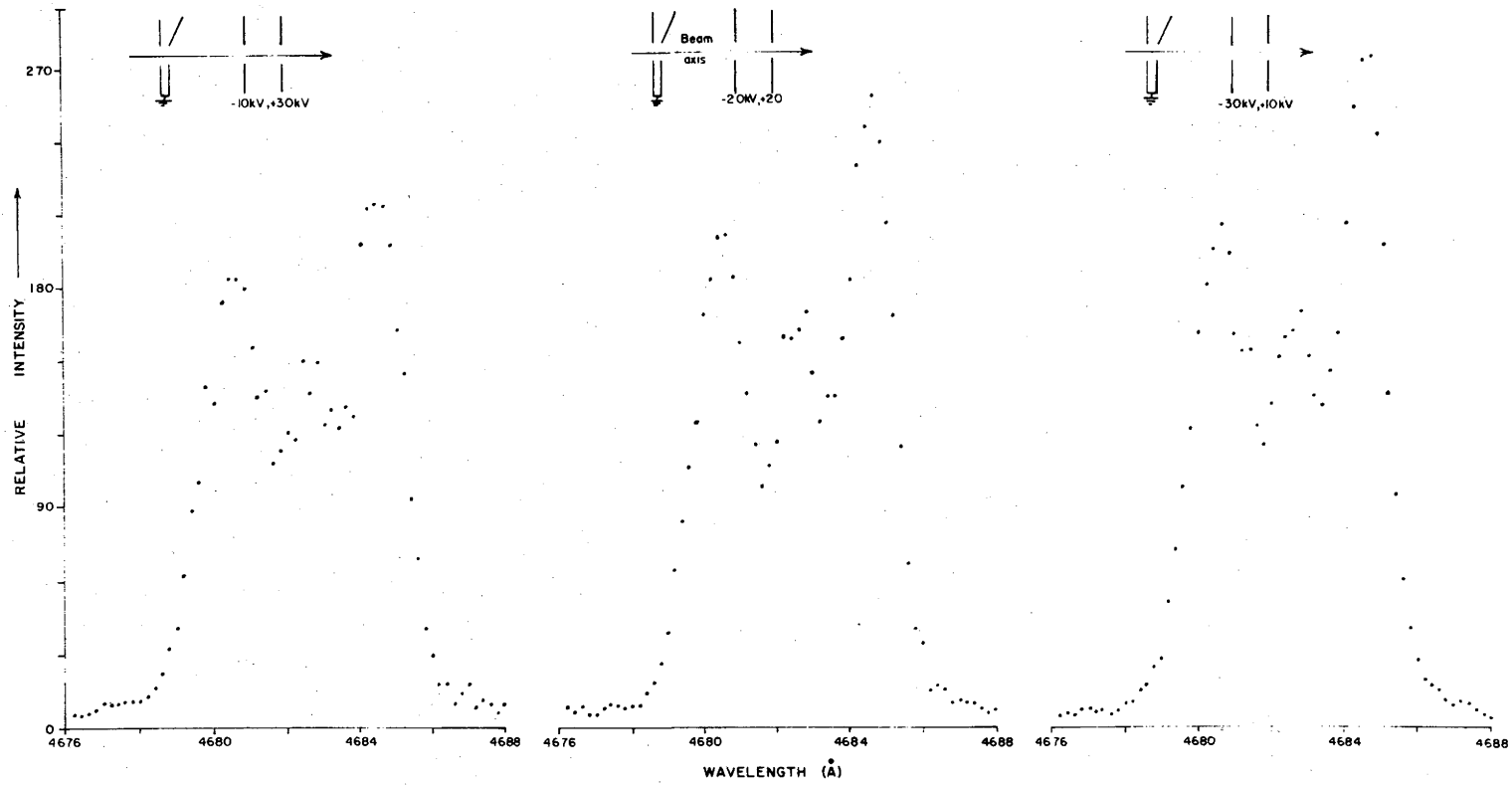

Fig. 4.5: Stark patterns for varying field distributions. The electrode voltages used in each case are indicated with the corresponding Stark pattern. As the field in the region between the earthed and negative electrodes decreases the long wavelength group of Stark components decreases.

efficiency are given in table 4.4. Since the line $4^3P \rightarrow 2^3P$ was blended with the He II lines $9g^2G \rightarrow 4f^2F$, etc., it has not been included.

TABLE 4.4: Relative intensities of some He I Stark perturbed lines.

The triplet and singlet groups have each been normalized to the respective S to P transition because comparison of a triplet line to its corresponding singlet line had shown their ratio to be close to 3 as expected for a $(2S+1)$ weight.

Transition	Lifetime (ns)	Observed	Statistical Population
$4^3S \rightarrow 2^3P$	58	1.0 ± 0.1	1.0
$4^3D \rightarrow 2^3P$	31	1.8 ± 0.1	20.0
$4^3F \rightarrow 2^3P$	70	0.6 ± 0.1	19.4
$4^1S \rightarrow 2^1P$	89	1.0 ± 0.1	1.0
$4^1P \rightarrow 2^1P$	4	0.9 ± 0.2	11.3
$4^1D \rightarrow 2^1P$	37	2.1 ± 0.2	25.0
$4^1F \rightarrow 2^1P$	70	0.2 ± 0.2	6.5

The table also shows the relative intensities which would be expected from a statistical population [Fo 28] at the point of observation, normalized to unit intensity for the S to P transitions, and allowing for the polarization effects of the grating. The lifetimes of the transitions in zero field are also shown [Wi 66]. Comparison of the observed and theoretical intensities indicates that states of higher orbital angular momentum are underpopulated compared to a statistical population distribution at the point of observation ≈ 3.0 cm after the foil. The decay time before observation was less than 20 ns which suggests that the same conclusion would hold at the foil.

§4.3.1 The Triplet Lines $4^3D \rightarrow 2^3P$ and $4^3F \rightarrow 2^3P$

The separations of the Stark components (neglecting fine-structure) of the $4^3D \rightarrow 2^3P$ and the $4^3F \rightarrow 2^3P$ lines have been obtained from Foster's eigenvalue tables [Fo 28] and are presented in fig. 4.6 as a graph of wavelength shift versus electric field strength. The components in the $4^3D \rightarrow 2^3P$ transitions are too close together to permit determination of their separate intensities. The components of the $4^3F \rightarrow 2^3P$ transitions

were expected to be separated sufficiently to allow their relative intensities to be determined.

The progressive wavelength shift and change in intensity of the allowed $4^3D \rightarrow 2^3P$ transitions and the forbidden $4^3F \rightarrow 2^3P$ transitions were observed as functions of electric field strength for the same conditions of observation as the survey scan. The data obtained is shown in fig. 4.7. The electric field strengths estimated from the separation of the lines was in good agreement with the values estimated from the electrode separation and voltages. The ratio of the intensities of the $4^3D \rightarrow 2^3P$ transitions to the $4^3F \rightarrow 2^3P$ transitions were 4.3 at 40 $kV \cdot cm^{-1}$ and 2.7 at 80 $kV \cdot cm^{-1}$ for the data of fig. 4.7. The corresponding numbers calculated from Foster's tables for a statistical population distribution [Fo 28], after correction for the effect of the grating on the π and σ components, are 1.7 at 40 $kV \cdot cm^{-1}$ and 1.0 at 100 $kV \cdot cm^{-1}$, which are about two and a half times less than observed. This difference warranted further investigation.

Data obtained at 390 keV He^+ beam energy, for observation perpendicular to the electric field with the electric field parallel and perpendicular to the grating rulings, and for observation parallel to the electric field direction, are shown in figs. 4.8, 4.9 and 4.10. The characteristics of each experimental configuration are described in §2.4.2. The electric fields were measured from the Stark splitting of the H_β line and are sufficiently high, with the resolution obtained, to observe structure in the $4^3F \rightarrow 2^3P$ line.

The effect of the grating on π components polarized with the electric vector parallel to or perpendicular to the grating rulings can be qualitatively seen by comparing the data of fig. 4.8 and fig. 4.10. The lowest wavelength components arising from transitions from 4^3F, $M = 0$ and $|M| = 1$ levels, are π and σ polarized, whereas the component arising from the 4^3F, $|M| = 2$ level, is only σ polarized. The intensity change of the 4^3F components is consistent with the monochromator transmitting π components with a greatly reduced intensity (a factor of 3.6, see §2.2.1) when the electric field is parallel to the grating rulings. The data of fig. 4.9 is consistent with the fact that the π components are not present when viewing parallel to the electric field. The different radiative decay histories of the atoms for the three electrode configurations, which have different uncertainties in the field boundaries, preclude direct quantitative comparison.

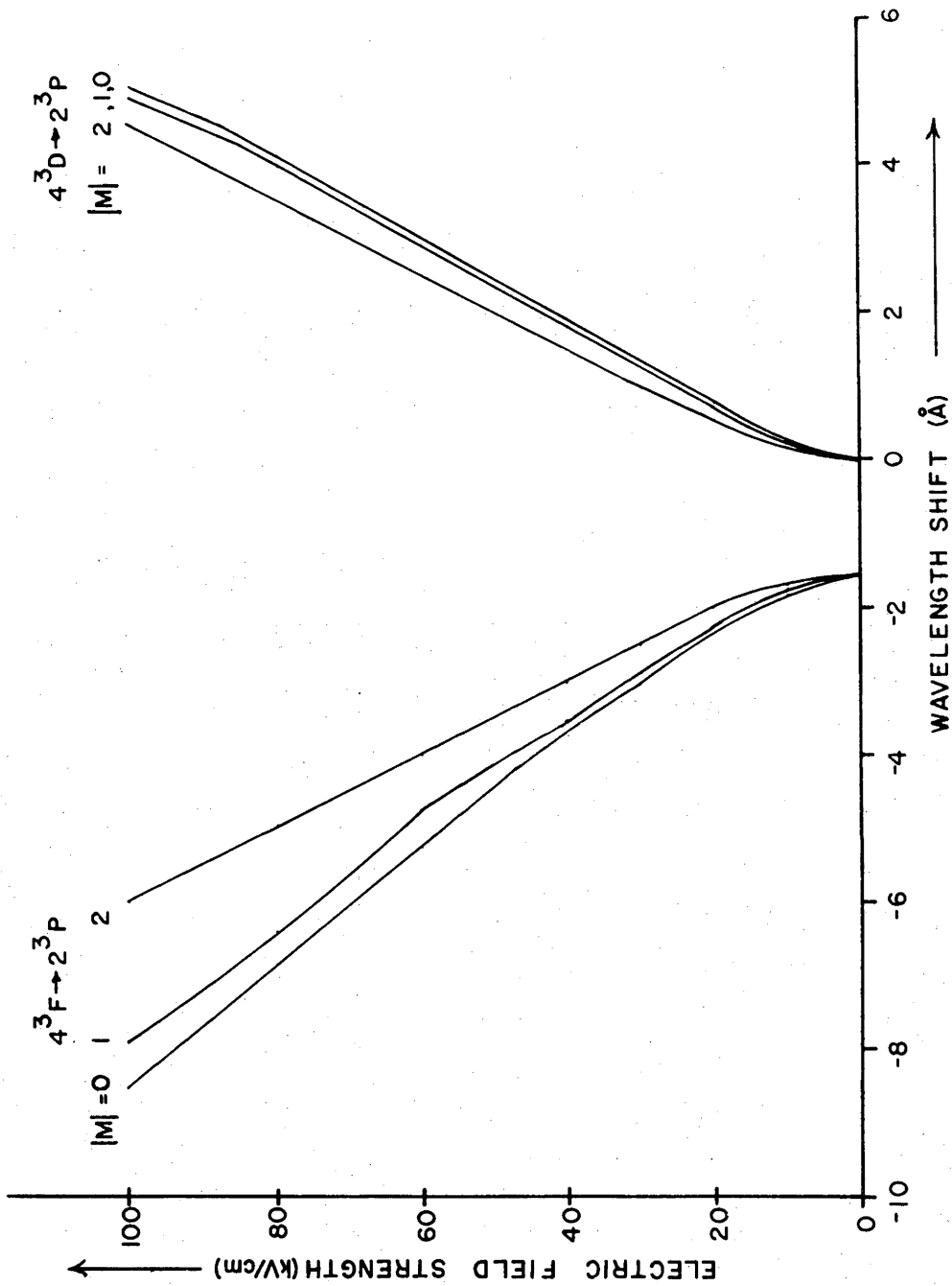

Fig. 4.6: Calculated Stark splitting of $4^3D \rightarrow 2^3P$ and $4^3F \rightarrow 2^3P$ lines. Wavelength displacements as a function of electric field strength obtained from calculated eigenvalues for 4^3D, 4^3F terms. The z component of the orbital angular momentum quantum numbers of upper levels are shown. The fine-structure of the Stark components is ignored.

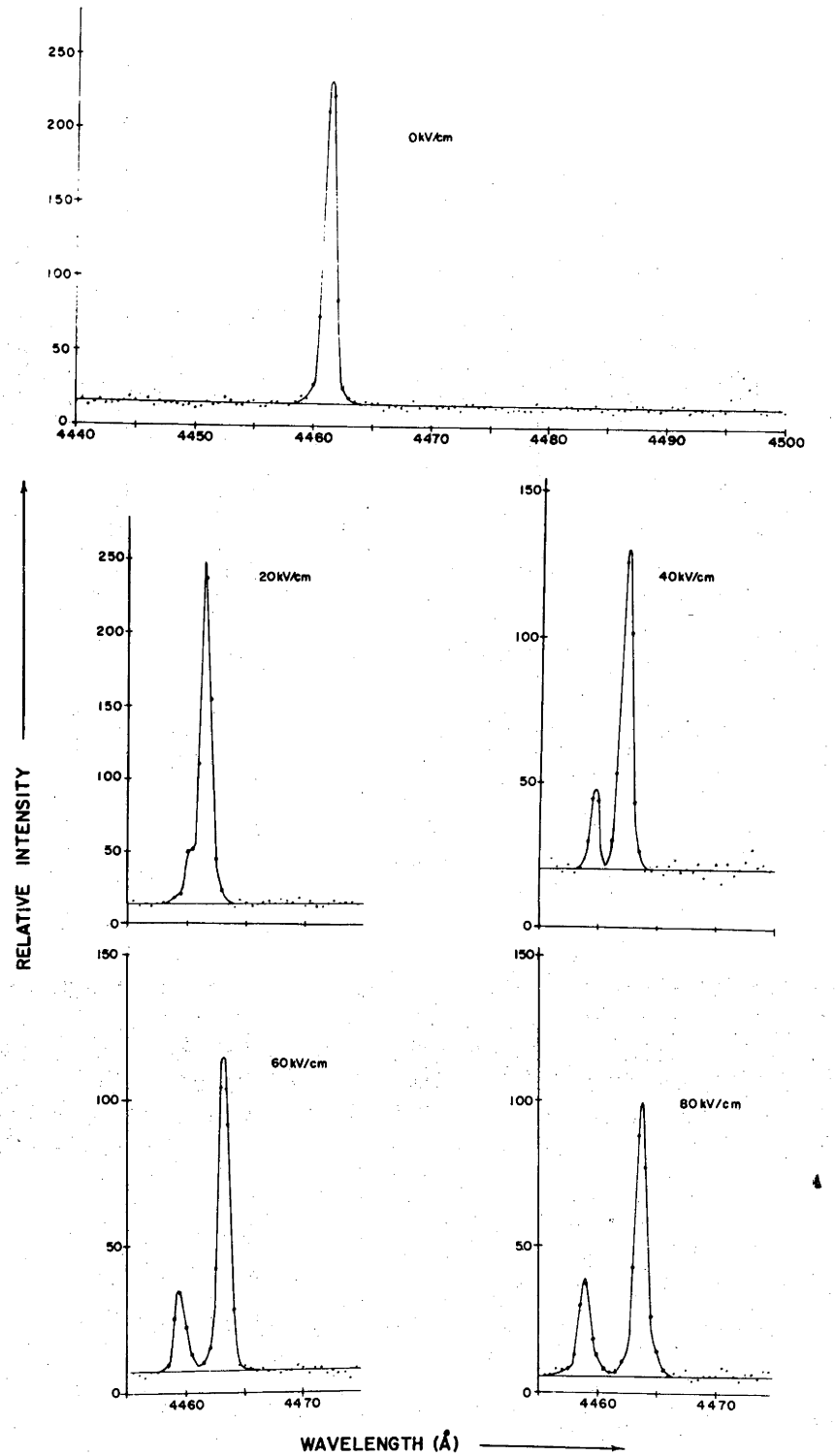

Fig. 4.7: Observed Stark shifts of $4^3D \rightarrow 2^3P$ and $4^3F \rightarrow 2^3P$ lines. The progressive wavelength displacement and intensity change for the $4^3D \rightarrow 2^3P$ allowed and $4^3F \rightarrow 2^3P$ forbidden transitions as the electric field strength is increased. The separate Stark components are not resolved. The background is fitted, the component lines are a guide to the eye.

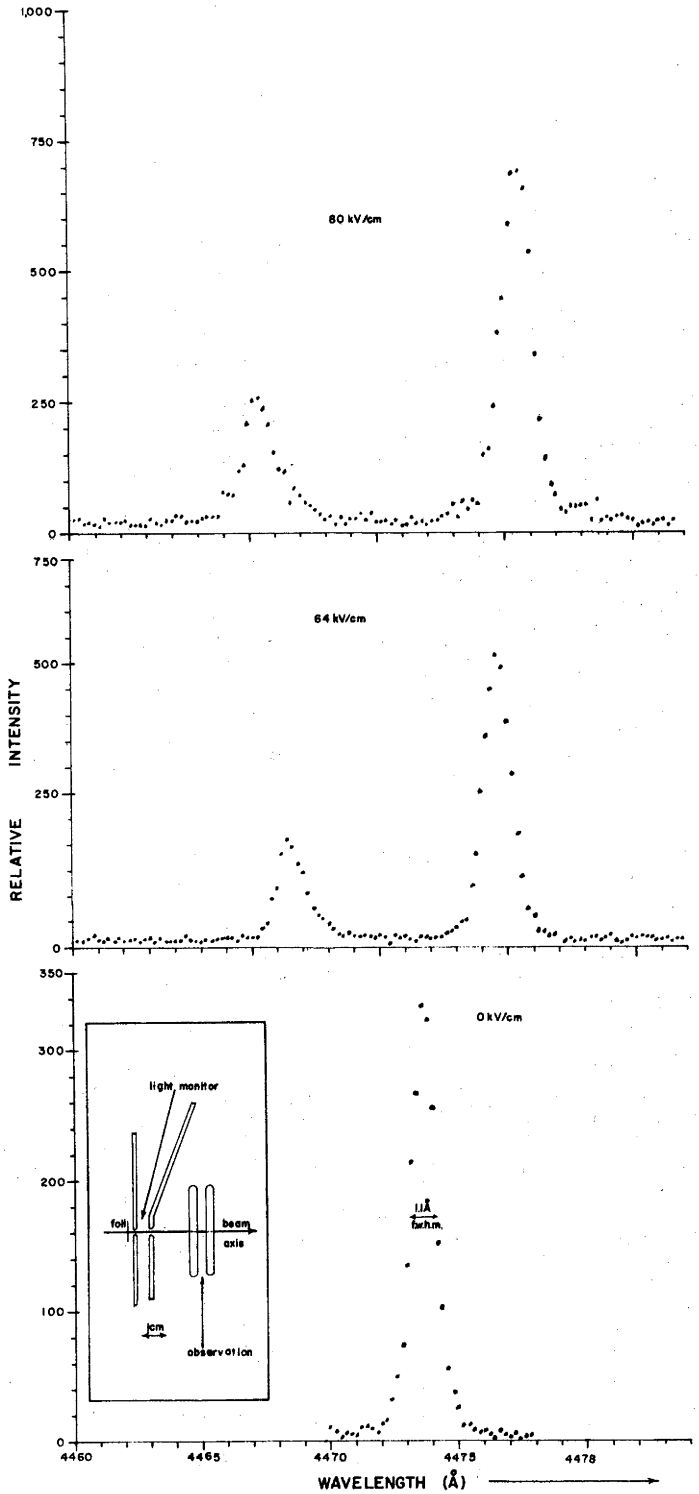

Fig. 4.8: Stark perturbed $4^3D \rightarrow 2^3P$ and $4^3F \rightarrow 2^3P$ lines for configuration (a). The π and σ components are both present, a zero field line is included for comparison. The structure evident in the $4^3F \rightarrow 2^3P$ line is more obvious when the π components are reduced by the grating, as can be seen in fig. 4.10.

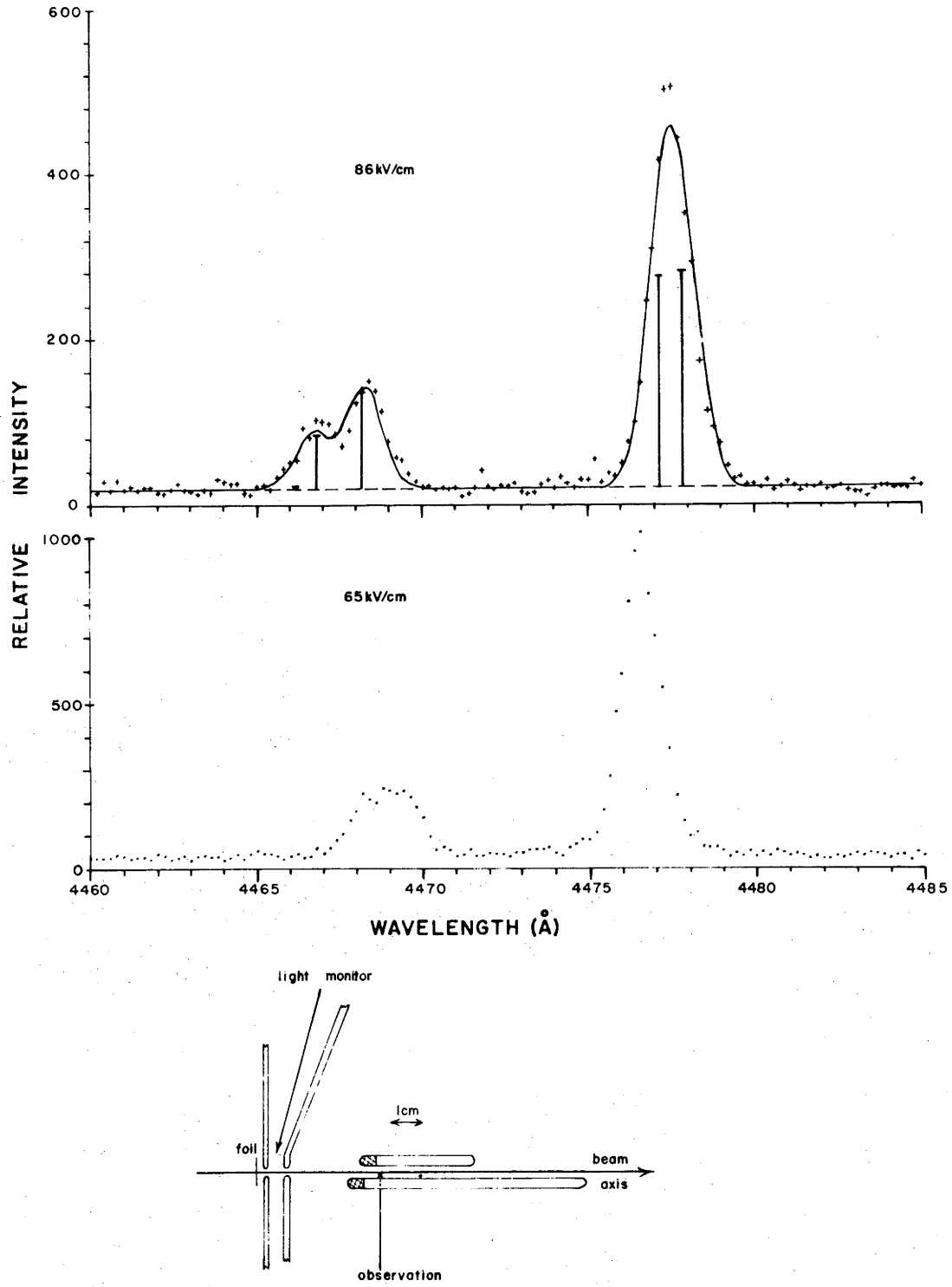

Fig. 4.9: Stark perturbed $4^3D \rightarrow 2^3P$ and $4^3F \rightarrow 2^3P$ lines for configuration (b). Only σ components are observed with this configuration. The fitted curve is the sum of 5 equal width Gaussian lines with the indicated heights and positions. The lowest wavelength line is extremely weak.

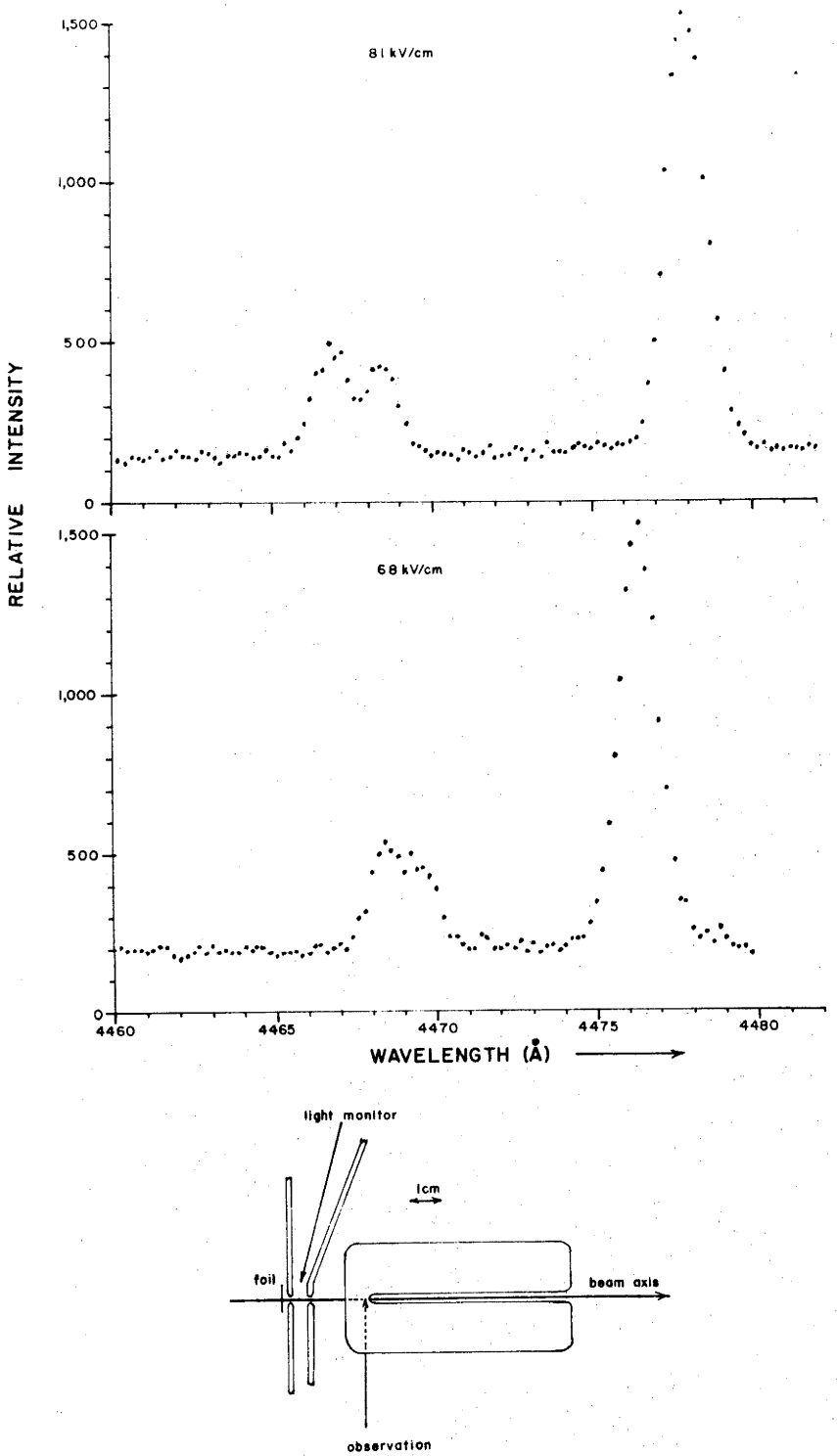

Fig. 4.10: Stark perturbed $4^3D \rightarrow 2^3P$ and $4^3F \rightarrow 2^3P$ lines for configuration (c). The π and σ components are both present, but the π components are much reduced, over those for fig. 4.8, by the different grating orientation.

For the purpose of determining the relative populations of Stark perturbed states it is necessary to know only the relative intensities within one polarization occurring in the Stark pattern. As the $|M| = 2$ states of 4^3F and 4^3D give rise to σ components only, the data obtained with the emitting atoms viewed parallel to the electric field (fig. 4.9) is used for the extraction of the relative intensities of their Stark components.

The intensity distribution model used to fit the data contained five Gaussian components of equal width with separations fixed at the values determined from the eigenvalue problem for the measured electric field. The uncertainty in the measurement of the electric field by H_β splitting was 2 $kV \cdot cm^{-1}$, so the data was fitted at 84, 86 and 88 $kV \cdot cm^{-1}$ to obtain estimates of the resulting variations in the fitted intensities. The linewidth for the zero field line was 1.1 Å but, as the data suggested that the linewidth increased when the field was applied, it was allowed to vary and was determined by the fitting procedure. Since the electrodes may not have been aligned exactly to the beam axis, the increase in linewidth could be because the electric field non-uniformity is greater off-axis (§2.4.3).

The linewidth obtained for the best fit was 1.28 Å and this fit is shown in fig. 4.9. The relative intensities of the 4^3D components varied by about 100% for variations of 2 $kV \cdot cm^{-1}$ about the measured electric field. Under these circumstances the intensities of the 4^3D components obtained by fitting must be ignored. The fits to the 4^3F components, given in table 4.5, are judged to be more reliable because there is visible structure that is reasonably matched by the data fitting. The variations in the relative intensities correspond to field strength changes of ± 2 $kV \cdot cm^{-1}$.

TABLE 4.5: Relative intensities of the $4^3F \rightarrow 2^3P$ components.

Electric field strength 86 $kV \cdot cm^{-1}$, F.W.H.M. = 1.28 Å, Q = 2.75			
	$\|M\| = 2$	$\|M\| = 1$	$M = 0$
Normalized intensities	643^{+3}_{-9}	354^{-24}_{-4}	3^{+33}_{-3}

The total intensities of the $4^3D \rightarrow 2^3P$ and the $4^3F \rightarrow 2^3P$ lines given in fig. 4.9 and fig. 4.7, indicates that the 4^3D term is preferentially populated compared to the 4^3F term, by about a factor of two and a half compared to a statistical population distribution. The relative intensities of the components of the $4^3F \rightarrow 2^3P$ transitions would be 643 ($|M| = 2$), 36 ($|M| = 1$), and 12 ($M = 0$) if the 4^3F term were statistically populated at the point of observation [Fo 28]. Comparison of these values with those of table 4.5 indicates that the $|M| = 1$ states are overpopulated. Such strong alignment only 4 cm from the foil, suggests that alignment existed at the foil. The total decay time is 15 ns which is less than the lifetimes of the three levels involved, which range from $\approx$ 70 ns to $\approx$ 30 ns both in zero and strong electric fields. These lifetimes are given by Wiese [Wi 66] for zero field and the electric field merely mixes the corresponding states to give lifetimes in that range.

§4.3.2 The Singlet Lines $4^1D \rightarrow 2^1P$ and $4^1F \rightarrow 2^1P$

The separations of the components of the singlet lines as a function of electric field strength are shown in fig. 4.11. This graph was derived from the eigenvalue tables of Foster [Fo 28]. There is no fine-structure of the Stark components of the singlet transitions so that a well defined anlaysis of the population distribution for the various Stark perturbed levels was expected from measurements of the relative intensities of the corresponding Stark perturbed transitions.

The separation between the Stark components of the $4^1D \rightarrow 2^1P$ transition was expected to be sufficiently great to determine the relative intensity of the components for electric field strengths in excess of 65 $kV \cdot cm^{-1}$. The separation of the $|M_J| = 2$ component of the $4^1F \rightarrow 2^1P$ forbidden transition from the $M_J = 0$ and $|M_J| = 1$ components was also expected to be sufficient for this purpose at electric field strengths greater than 65 $kV \cdot cm^{-1}$.

The measurements of the relative intensities of the Stark components for the $4^1D \rightarrow 2^1P$ and the $4^1F \rightarrow 2^1P$ transitions were carried out at 250 and 410 keV. The times spent by the ions in zero electric field were 2.4 ns and 2.3 ns and in non-zero electric field were 6.8 ns and 5.0 ns respectively. The side of the earthed electrode nearest the field electrodes was taken as the dividing line between the two regions.

The electric field configuration (b), discussed in §2.4.2, was used for these measurements.

Observations were made of the progressive Stark perturbation of the $4^1D \rightarrow 2^1P$ and the $4^1F \rightarrow 2^1P$ lines as the electric field strength was increased at a beam energy of 250 keV. The spectra are shown in fig. 4.12. The lifetimes of these transitions ($\approx$ 30 to 70 ns, see Appendix C) are not short enough to distort the spectra grossly between the foil and the point of observation. The relative intensity tables of Foster [Fo 28] show that the intensity of the components $4^3F_3^{|2|}$ and $4^1D_2^{|2|} \rightarrow 2^1P$ would be nearly equal if the upper states were statistically populated; this is clearly not the case for the data of fig. 4.12 at 94 $kV \cdot cm^{-1}$.

The electric field strength was determined from the separation of the $4^1F_3^{|2|}$ and $4^1D_2^{|2|} \rightarrow 2^1P$ transitions at the highest electric field strength and linear interpolation used for the lower voltages. The wavelength shifts required for this were obtained by solving the eigenvalue problem for electric field strengths between 60 $kV \cdot cm^{-1}$ and 100 $kV \cdot cm^{-1}$ in steps of 2 $kV \cdot cm^{-1}$, using the method given in Appendix C.

The spectra obtained at 250 keV and 410 keV beam energy are shown in fig. 4.13. The sum of the fitted components and a linear background is also shown. The data fitting procedure is essentially the same as that previously described for the triplet components, differing only in the relative positions of the Stark components. The intensities extracted from fig. 4.13 are given in table 4.6. If the components were insufficiently separated, the sum of them is given.

The widths of the fitted lines were observed to increase, when the electric field was applied, by about 0.6 Å over the zero field linewidth for the allowed $4^1D \rightarrow 2^1P$ line. The zero field linewidth of the $4^1D \rightarrow 2^1P$ line was 2.0 Å at 250 keV and 1.0 Å at 410 keV.

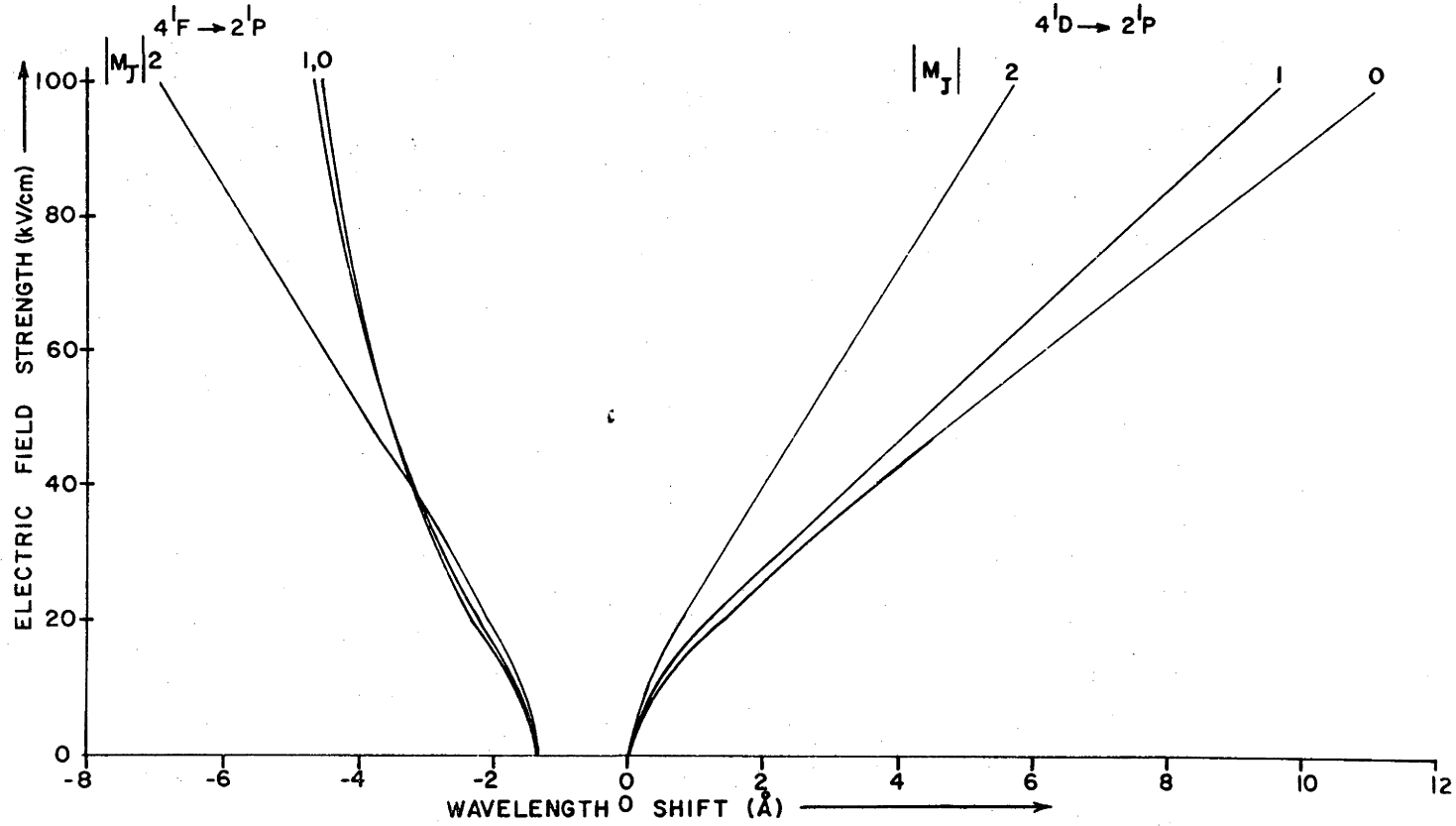

Fig. 4.11: Wavelength displacement as a function of electric field strength for 4^1F and 4^1D terms. The z component of total angular momentum of the upper levels of the transitions are indicated. For the F to P transitions the $M_J = \pm 1, 0$ components' intensities are extremely small at high fields [Fo 28].

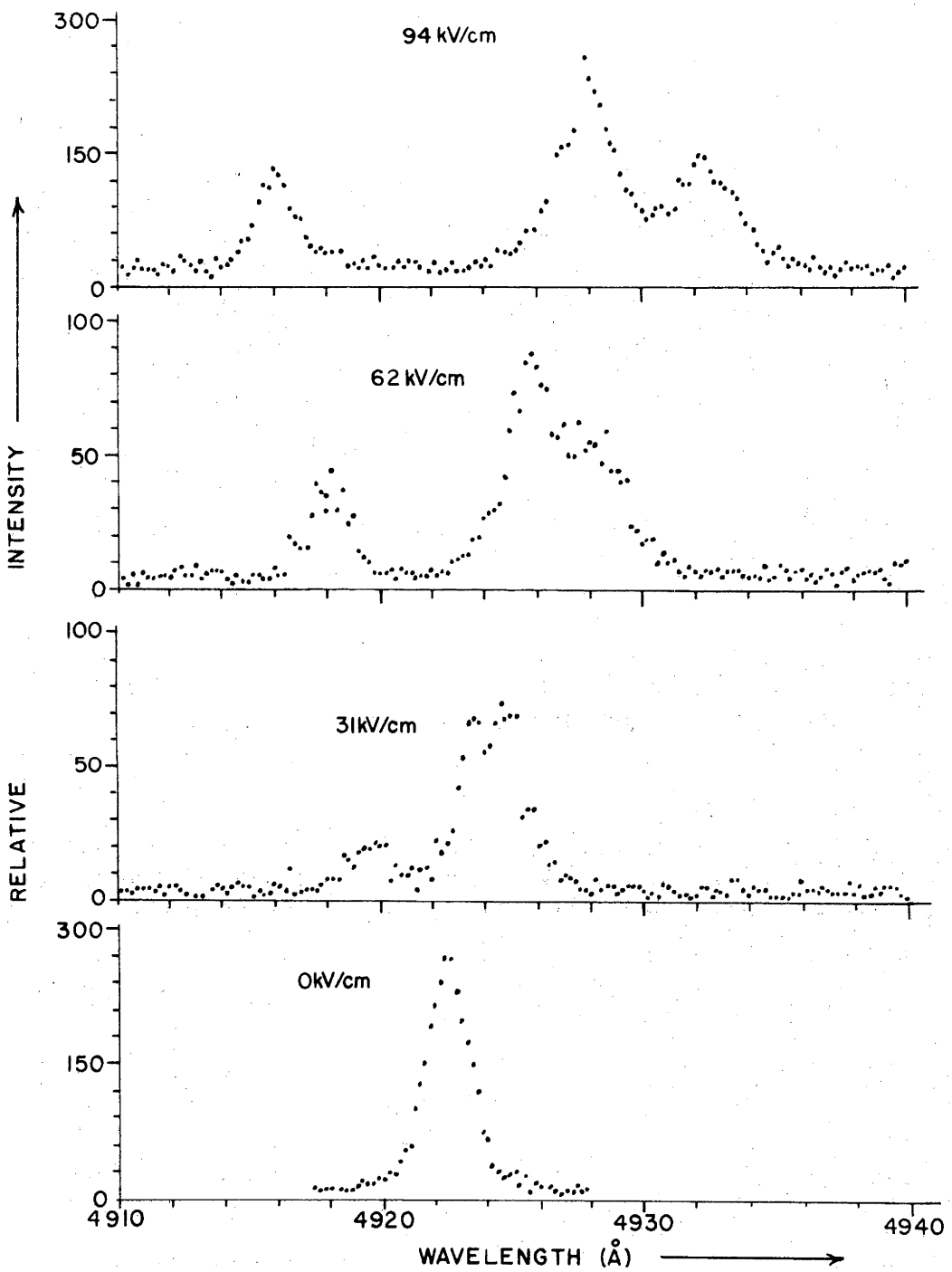

Fig. 4.12: Observed Stark effect of singlet lines. The progressive wavelength displacement and intensity changes for the $4^1D \rightarrow 2^1P$ and $4^1F \rightarrow 2^1P$ transitions as the electric field strength is increased.

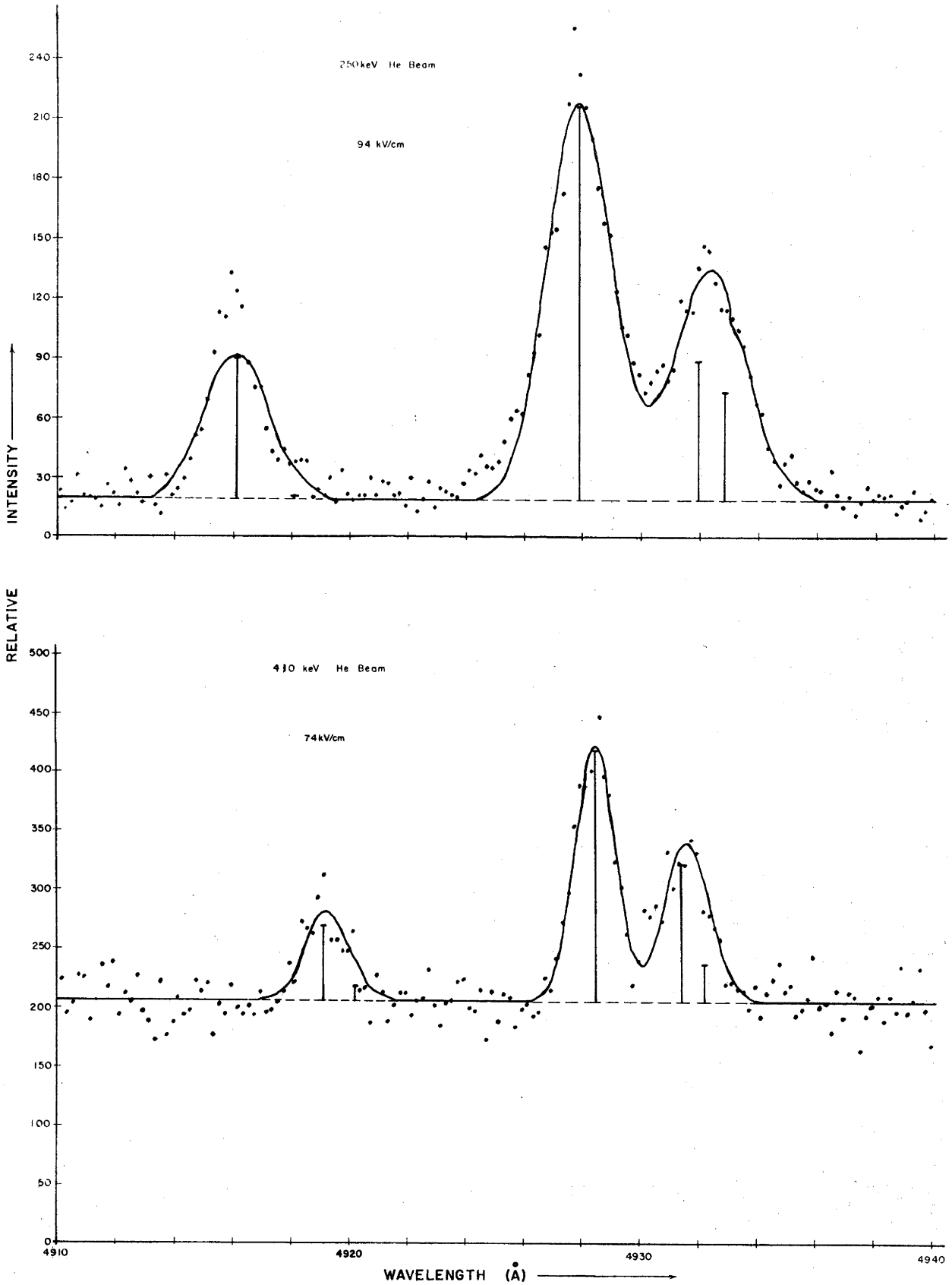

Fig. 4.13: Relative intensities of the singlet Stark components. The fitted curve is the sum of five Gaussian lines and a linear background. At 250 keV the second lowest wavelength fitted component is very weak.

TABLE 4.6: Normalized relative intensities of the 4^1D and $4^1F \rightarrow 2^1P$ components.

Beam energy 250 keV

Electric field strength 94 $kV \cdot cm^{-1}$, F.W.H.M = 2.6 Å, Q = 2.1

$4^1D \rightarrow 2^1P$			$4^1F \rightarrow 2^1P$	
$\lvert M_J \rvert = 2$	$\lvert M_J \rvert = 1$	$M_J = 0$	$\lvert M_J \rvert = 2$	$\lvert M_J \rvert = 1$ and $M_J = 0$
501^{+1}_{-6}	174^{+43}_{-42}	141^{-42}_{+50}	182^{-16}_{+1}	3^{+16}_{-3}

Beam energy 410 keV

Electric field strength 74 $kV \cdot cm^{-1}$, F.W.H.M. = 1.6 Å, Q = 1.8

$4^1D \rightarrow 2^1P$			$4^1F \rightarrow 2^1P$	
$\lvert M_J \rvert = 2$	$\lvert M_J \rvert = 1$	$M_J = 0$	$\lvert M_J \rvert = 2$	$\lvert M_J \rvert = 1$ and $M_J = 0$
477^{+2}_{-10}	258^{+18}_{-34}	74^{-22}_{+32}	162^{-10}_{+4}	24^{+12}_{-4}

§4.3.3 Effect of the Stark Perturbation on the Population of He Levels

The time in which the perturbing field is applied to the He atoms by virtue of their high velocity ($\approx 3 \times 10^8$ $cm \cdot s^{-1}$) is of the order of 3 ns so that the perturbation is adiabatic, the energy separation of the states coupled by the perturbation being equivalent to at most a period of 10^{-12} s. Stray magnetic fields in the chamber in the region of the beam axis were found negligible (< 0.1 G). The induced magnetic field resulting from the time varying electric field is negligible ($\approx$ 0.3 G). For these reasons, it is expected that changes in populations of excited states arise only from radiative decay.

To ensure that no changes in population of various states occurred, which would not be expected with the adiabatic approximation, quantum beat measurements were carried out on the $3^3P \rightarrow 2^3S$ line of He I [An 70]. These measurements were carried out at 250 keV beam energy and electric field strengths of 0, 1.4 and 5.6 $kV \cdot cm^{-1}$. The scanning monochromator with slits set at 500 µm was used to detect the 3889 Å line emitted in the region between the high voltage electrodes, which were arranged as shown in fig. 4.9. The monochromator was traversed parallel

to the beam axis by an accurate lead screw in steps of 1.000 ± 0.025 mm. The normalized data is shown in fig. 4.14.

The fit to each intensity distribution was achieved using an exponentially decaying intensity with an exponentially decaying cosine oscillation superimposed. The frequencies and the amplitudes of the oscillations are given in table 4.7. To convert the periodic distance to a frequency the theoretical zero field value for interference between the $3^3P_1 \rightarrow 2^3S_1$ and the $3^3P_2 \rightarrow 2^3S_1$ decay channels of 659.7 MHz was used [Be 72]. This implied that the actual velocity of the atoms was less than 1% faster than the nominal accelerator energy calibration suggested.

TABLE 4.7: Quantum beat parameters obtained from the data fitting.

Electric field strength ($kV \cdot cm^{-1}$)	0	1.4	5.6
Frequency of quantum beats (MHz)	659.7 ± 3	659.4 ± 3	667.4 ± 4
Relative amplitude of beats (%)	5.4 ± 1	5.6 ± 1	4.4 ± 1

The frequencies and amplitude are virtually the same but at the highest voltage there is a noticeable difference of phase. The Stark perturbation has little effect on the energy levels at low fields, but the integrated changes between the effective start of the electric field and the arbitrary zero for the measurements could explain the phase shift for 5.6 $kV \cdot cm^{-1}$, and might also be responsible for the barely significant change in frequency.

The quantum beat observations are consistent with an adiabatic perturbation which causes no population changes.

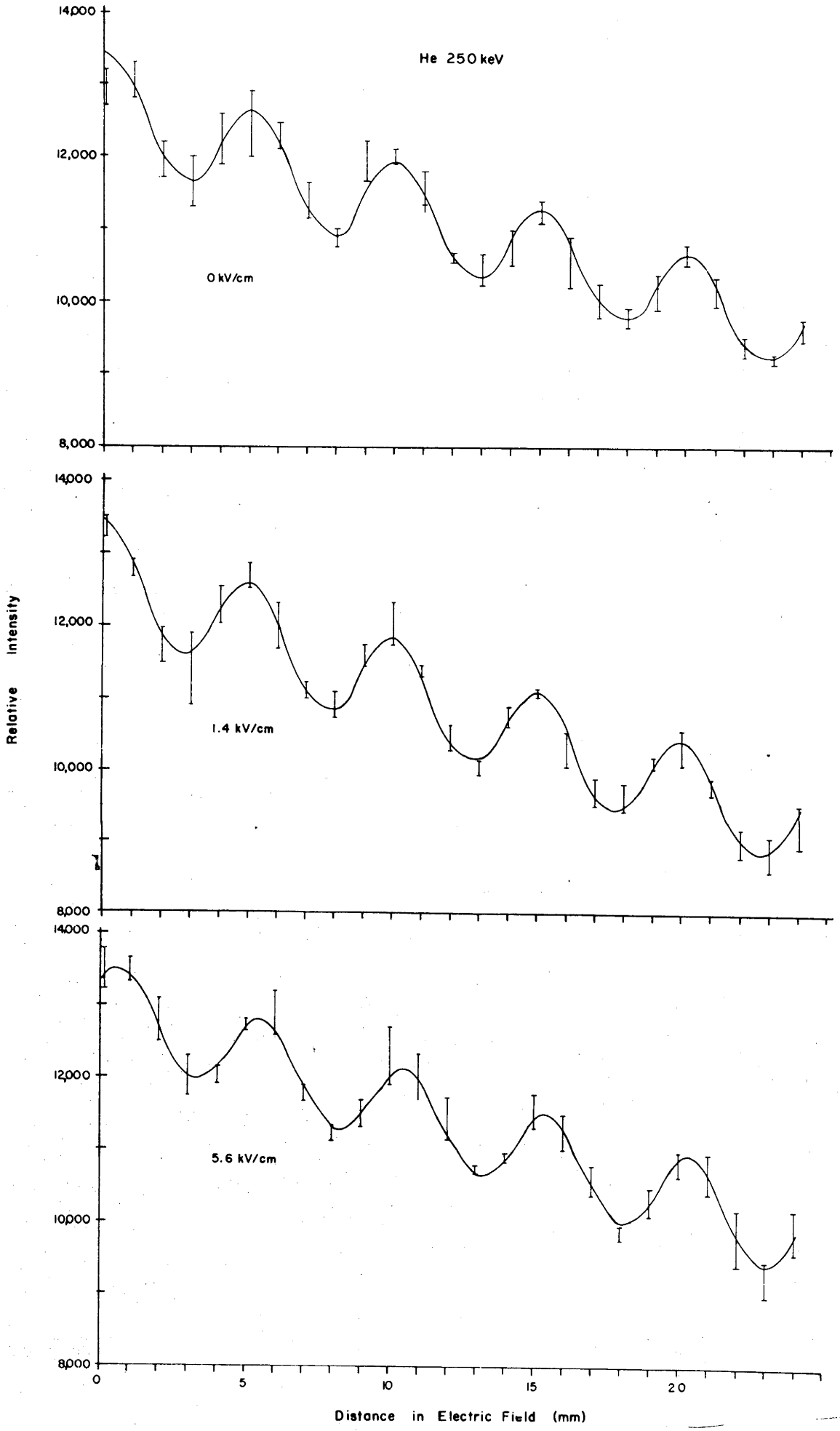

Fig. 4.14: Quantum beats observed at varying electric field strengths. The sum of the fitted exponentially decaying intensity and cosine oscillation is shown.

CHAPTER 5

CALCULATION OF THE INTENSITY OF RADIATIVE TRANSITIONS

An observation of the intensities of spectral lines at a time t after excitation in the foil may be readily interpreted in terms of the populations of excited states at time t and the probability for decay from the excited states giving rise to them. If more than one excited state contributes to each of the lines, no unique determination of the population of each state is possible unless other information is available.

The populations of excited states at a time t_n after excitation are related to the populations of states, not necessarily the same ones as at t_n, produced by the interaction of the ion beam with the foil at an earlier time, t_o. The features of the evolution of the populations of excited states which are required to establish a relation between the intensities observed at t_n and the populations produced in the beam-foil interaction are considered below. The evolution is described in the density matrix representation [Fa 57, Ha 61] to facilitate the calculation of coherence effects [Ma 69, An 70] and because the populations are averages over an ensemble of beam particles.

§5.1 INITIAL CONDITIONS

The first consideration is the choice of a basis set for the density matrix representation used to describe the excited state populations in the foil. For reasons given below, the basis set chosen is $\{nLMSM_S\}$, where n is the principal quantum number of the excited state, L its orbital angular momentum, M the projection of L on the z-axis, S its spin angular momentum, and M_S the z component of the spin angular momentum.

The time taken by He ions of 200 keV to 1 MeV energy to traverse a carbon foil of a few $\mu g\ cm^{-2}$ is of the order of 10^{-14} s or less. This transit time is small compared to the precession times of the orbital and the spin angular momentum vectors about the total angular

momentum vector and hence the excited state cannot have a well defined $\underline{L}\cdot\underline{S}$ coupled total angular momentum. The assumption is made that spin forces are negligible for the interaction and that Coulomb forces dominate [Pe 58]. Under these conditions, the interaction Hamiltonian of the system is diagonal in the $\{nLMSM_S\}$ basis set.

A physically plausible choice of the z-axis direction is the beam direction since the system has cylindrical symmetry about this axis. However, an electric field applied to the ions after leaving the foil defines a z direction which will be used in all cases for the electric field region. The z-axis chosen in the foil region may be different from this and hence a transformation from one to the other is necessary. This transformation is not trivial because it introduces definite average phase relations between different excited states.

The density matrix elements are chosen by assigning values to the amplitudes of the various possible $|nLMSM_S\rangle$ states thought to be excited in the beam-foil interaction process. The amplitudes of the excited states are directly related to the cross-sections for excitation, but these are not known. A population distribution is postulated, and used to assign values to the diagonal element of the density matrix $\sigma^u(0)$:

$$\sigma^u_{kk}(0) = \sum_{t=0}^{t_e} \sum_i P_i \left| a_k^{(i)}(t) \right|^2 , \tag{5.1}$$

where $a_k^{(i)}(t)$ is the amplitude of the kth state of the basis set $\{u\}$ for the ith ion at time t, P_i the probability of the ith ion being excited to the kth state.

The off-diagonal elements of the density matrix relate to coherent excitation, which is described by specifying values for

$$\sigma^u_{jk}(0) = \sum_{t=0}^{t_e} \sum_i P_i \, a_k^{(i)}(t)^* \, a_j^{(i)}(t) . \tag{5.2}$$

Coherence exists if the average phase difference between excited states is non-zero, but it may not always lead to observable effects. The time interval for excitation is limited by the thickness of the foil and the ion velocity to be $\leqslant t_e$, and an average is taken over this interval. This averaging over t_e precludes the occurrence of coherence terms, that is off-diagonal elements, of $\sigma^u(0)$ with periods less than t_e. Since t_e is short compared to the time until observation, it is suitable to set the time origin at the time of exit from the foil.

The states which contribute to the Stark patterns of a level of given n may be populated in the initial excitation in the foil or they may be populated subsequently by cascades. The treatment of cascade schemes requires the observation of many transitions, some of which are experimentally inaccessible, therefore cascades are neglected in this treatment. An estimate of the errors involved in this simplification can be obtained by comparing the experimentally observed zero field lifetimes of the levels of interest to the theoretical lifetimes without cascade repopulation. For the F_α, He II and the 4D → 2P and 4F → 2P, He I transitions, lifetime measurements [Jo 67, Ma 70b] indicate that the neglect of cascades is not serious. Cascade repopulation may be altered by the electric field but the survey scans at 0 and 80 $kV \cdot cm^{-1}$ also indicate small effects due to the neglect of cascading.

It is convenient to work in terms of the excited state component of the density matrix [Ha 72] where

$$\sigma^u(0) = \rho_g^u(0) + \rho_e^u(0) + \ldots \qquad (5.3)$$

and $\rho_g^u(0)$, $\rho_e^u(0)$ are the projection of $\sigma^u(0)$ onto the ground level and the excited levels of the ion. For the lower levels of He I and He II the off-diagonal elements of $\sigma^u(0)$ between levels of different n value contain terms with periods of oscillation that are small compared to the transit time of the foil. Since such terms average to zero, the projection of eqn (5.3) is greatly simplified because $\sigma^u(0)$ reduces to several smaller matrix "blocks", each block associated with only one n value. Under these conditions, only the excited state component associated with a single n value need be used to describe the evolution of the system. By allowing for cylindrical symmetry about the chosen z-axis, the number of independent elements of the density matrix is reduced. As the electrons in amorphous carbon foils have random spin directions and the interaction has been assumed spin independent, a further reduction in the number of independent elements results.

The values of the off-diagonal elements $\rho_{jk}^u(0)$ are customarily [Ma 69, Se 70, Al 73, Ec 73] assumed to be zero, although Macek [Ma 70a] has noted that there is no *a priori* reason for this choice. This assumption implies that all coherence terms of $\rho^u(t)$ can only arise as a result of changes in the system after the initial excitation. The consequences of this assumption will be disucssed as they arise.

The experimentally observed alignment of excited states in the beam-foil source [Li 71] can be included by allowing states of different $|M|$ to have amplitudes with differing real parts.

§5.2 PERTURBATIONS

After excitation at the foil the only processes to be accounted for are the decay of excited states and transitions brought about by applied perturbations. The behaviour of the system is then governed by the time evolution equation for the density matrix

$$i\hbar \frac{\partial}{\partial t} \rho^u(t) = [H(t), \rho^u(t)]_- \tag{5.4}$$

with the initial conditions determined by eqns (5.1) and (5.2). Eqn (5.4) has the formal solution

$$\rho^u(t) = \exp\left(-\frac{i}{\hbar}H(t)\cdot t\right)\cdot\rho^u(0)\cdot\exp\left(\frac{i}{\hbar}H(t)\cdot t\right) , \tag{5.5}$$

which reduces to a simple form if $H(t)$ is diagonal for the $\{u\}$ basis set, i.e.

$$\rho^u_{mm'}(t) = \rho^u_{mm'}(0)\cdot\exp\left\{\frac{i}{\hbar}\left(E_{m'} - E_m\right)\right\}t , \tag{5.6}$$

where E_m is the mth eigenvalue corresponding to the mth eigenvector of $\{u\}$. The exponent in eqn (5.6) expresses the oscillatory behaviour of the coherence terms of the density matrix.

For $H(t) = H^o(t) + V(t)$, where the time dependent problem $H^o(t)$ has been solved and $V(t)$ is a small applied perturbation, eqn (5.4) can be solved by the Dirac expansion technique [Fa 69].

The particular problem of interest here is the solution of eqn (5.4) corresponding to the application of a steady electric field to excited ions. The time taken to apply the field has a strong influence on the result of the perturbation. Two limiting cases provide useful simplifications. These are the sudden and the adiabatic approximations [Me 61].

The sudden approximation consists of noting that the dynamical state of the system remains unchanged if the perturbation is applied in a vanishingly short time interval. If the Hamiltonian of the system is diagonal in the basis set $\{v\}$ before the perturbation and is diagonal in the basis set $\{w\}$ after the perturbation has been applied, then the sudden approximation merely requires that the density matrix be expressed

in the new basis set {w}. If S is the unitary transformation such that

$$\{w\} = S\{v\} , \tag{5.7}$$

then the density matrix $\rho^{v}(t_1)$ is expressed in the basis set {w} by the contact transformation

$$\rho^{w}(t_1) = S \cdot \rho^{v}(t_1) \cdot S^{-1} , \tag{5.8}$$

where t_1 is the time of application of the perturbation. The contact transformation of eqn (5.8) will in general change the elements of $\rho^{v}(t_1)$, that is, the perturbation induces transitions between the original basis states $|v\rangle$ and may introduce coherence terms between the new basis states $|w\rangle$ even though none were present between the original basis states. Coherence terms between states of the unperturbed system that are coupled by the perturbation contribute to diagonal elements of the perturbed density matrix.

The criterion for the sudden approximation [Sc 55, p.218] to give negligible error in $\rho^{w}(t_1)$ is that the time during which the perturbation changes be small compared to the period of the transition between the states coupled by the perturbation.

The adiabatic approximation is based on the fact that if the perturbation is applied infinitely slowly the system, if in an eigenstate of the unperturbed Hamilton, will pass into that eigenstate of the perturbed Hamiltonian which is derived from the initial one by continuity. The density matrix then has constant diagonal elements but a changing basis set. Thus no transitions result from this perturbation. The period of the coherence terms will change as the eigenvalues and the eigenstates change in response to the perturbation (cf. eqn 5.6, the argument of the exponential term).

The criterion for the adiabatic approximation to give negligible error in $\rho^{w}(t)$ is that the time for application of the perturbation be large compared to the period of the difference between the coupled states.

§5.3 SUDDEN PASSAGE FROM THE FOIL

If the beam direction is not the same as the z-axis direction defined by the applied electric field, it is most convenient to make the rotation immediately after the foil excitation at $t = 0$. The rotation matrices required for this contact transformation are discussed in Appendix A.

The excited ions pass from the interatomic fields of the solid to free space in a very short time ($< 10^{-14}$ s), suffering a perturbation in the process. By hypothesis, the Hamiltonian in the foil is diagonal in the $\{nLMSM_S\}$ basis set. In free space spin-orbit coupling (for light ions) is established and the Hamiltonian is diagonal in the $\{nLJM_J\}$ basis set. The states which are coupled by the fine-structure interaction have the same L, M and M_S values and are degenerate in the absence of that interaction, hence the criterion for the sudden approximation is met. The transformation from the $\{nLMSM_S\}$ basis set ($\{u\}$) to the $\{nLJM_J\}$ basis set ($\{v\}$) is achieved with the familiar Clebsch-Gordan matrices C [Co 51, p.75], i.e.

$$\{v\} = C \cdot \{u\} , \tag{5.9}$$

and the density matrix becomes

$$\rho^v(0) = C \cdot \rho^u(0) \cdot C^{-1} . \tag{5.10}$$

The application time for the perturbation is negligible as far as radiative decays are concerned.

The fine-structure interaction can introduce coherence terms only between states of the same L, M and M_S [Ec 73]. Furthermore, the symmetry about the z-axis restricts coherence terms to states of the same M_J ($= M+M_S$). A necessary condition for the occurrence of coherence terms follows from eqn (5.10) and the unitary condition on C. The condition is that $\rho^u(0)$ must not be proportional to the unit matrix. This condition is equivalent to requiring that excited state alignment be produced by the beam-foil interaction if the observed zero field quantum beats [An 70] are to be included in this model.

§5.4 RADIATIVE DECAY

Radiative decay in free space or constant electric field is treated phenomenologically following Wilcox and Lamb [Wi 60]. The time evolution equation for radiative decay is a special case of eqn (5.4):

$$\frac{\partial}{\partial t} \rho^v(t) = -\left(\frac{i}{\hbar}\right) [H, \rho^v(t)]_- - \tfrac{1}{2}[\Gamma, \rho^v(t)]_+ . \tag{5.11}$$

The Hamiltonian in eqn (5.11) is diagonal in the basis set $\{v\}$ which is the $\{nLJM_J\}$ basis set for free space or the Stark basis set in an electric field. The matrix Γ is the decay matrix for the excited states of the levels included in $\rho^v(t)$. This matrix is diagonal [Br 33] and has elements

$$\Gamma_{kj} = \gamma_{kj}\,\delta_{kj}\,, \tag{5.12}$$

where γ_{kk} is the decay constant for the kth state of the basis set {v}.

The solution of eqn (5.11) is in terms of the matrix elements of $\rho^{v}(t)$,

$$\rho^{v}_{jj}(t) = \rho^{v}_{jj}(0)\; e^{-\gamma_{jj}t} \tag{5.13a}$$

and

$$\rho^{v}_{jk}(t) = \rho^{v}_{jk}(0)\; e^{-i\omega_{jk}t - \frac{1}{2}(\gamma_{jj}+\gamma_{kk})t}\,. \tag{5.13b}$$

Eqn (5.13a) expresses the familiar exponential decay of the excited state population and eqn (5.13b) describes the decay of the coherence terms with a decay constant that is the average of the decay constants of the states between which the coherence occurs.

The period ω_{jk} is given by

$$\omega_{jk} = \frac{1}{\hbar}\,(E_j - E_k)\,, \tag{5.14}$$

where E_j and E_k are the energy eigenvalues of the jth and kth states of {v} respectively. Clearly, if the jth and kth states are not degenerate $\rho^{v}_{jk}(t)$ is a complex oscillatory term with its frequency determined by the energy separation of the coupled states. Such oscillatory terms may lead to quantum beats if the decay from the jth and kth states is to a common final state and a selective measurement of the decay channels is not made. This possibility is further discussed when considering the intensity operator.

§5.5 ELECTRIC FIELD PERTURBATION

§5.5.1 Sudden Perturbation

The criterion for the sudden approximation is met for degenerate initial states that are coupled by the Stark perturbation for which $\Delta L = \pm 1$ and $\Delta M_J = 0$. Nearby states separated by the fine-structure interval are also likely to meet the requirements for the sudden approximation providing they are coupled by the perturbation. This is the same situation as that which gives a linear Stark effect at relatively low electric field strengths. Thus excited hydrogenic ions undergo a sudden perturbation as they enter the electric field. The sudden perturbation criterion has to be applied taking into account the

fine-structure intervals of the excited state, the ion velocity, and the spatial variation of the applied electric field to assess the extent of population mixing between states separated by the fine-structure interval.

The Hamiltonian for a hydrogenic ion in an electric field is diagonal in the basis set obtained by solving the secular problem using the method of Lüders [Lü 51]. This basis set whose basis vectors are

$$|F\rangle \equiv \sum_i a_i(F) \; |nLJM_J\rangle$$

is given in Appendix B, and the transformation, which is electric field strength dependent, required to go from the $\{nLJM_J\}$ basis to the $\{F\}$ basis is also given; i.e. S(F) such that

$$\{F\} = S(F) \; \{nLJM_J\} \; . \tag{5.15}$$

The density matrix after the perturbation is then

$$\rho^F(t_2) = S(F) \cdot \rho^u(t_2) \cdot S(F)^{-1} \; , \tag{5.16}$$

where t_2 is the time at which the sudden perturbation is applied.

For a sudden transition into a weak field, two degenerate states that are split into two separated levels by the perturbation will both be strongly populated even if originally only one of them was populated. Nearby levels separated by the fine-structure interval, although coupled by the perturbation, will get much less contribution from the population of the degenerate levels.

In the case of a sudden transition into a strong field, each unperturbed state of a particular M_J value "shares" its population, not necessarily equally, with all final perturbed states of the same M_J. This may be thought of as a series of several "resonances" all driven hard by the sudden "broad band" perturbation.

These two situations, referred to as weak field sudden and strong field sudden perturbations are depicted qualitatively in Appendix F, fig. F1 and fig. F2 respectively.

The sudden entry of an excited ion into an electric field will induce coherence terms between states coupled by the perturbation; in this case states with $\Delta L = \pm 1$ and $\Delta M_J = 0$. If the electric field in the region of observation is weak, so that the energy level separations are not large, these coherence terms can give rise to observable quantum beats [Se 70].

§5.5.2 Adiabatic Perturbation

The criterion for the adiabatic approximation is most likely to be met for well separated initial states that are coupled by the Stark perturbation. This is the same circumstance that gives rise to the quadratic Stark effect. Thus it is most likely that non-hydrogenic ions will undergo an adiabatic perturbation as they enter the electric field.

The density matrix has unperturbed diagonal elements but a changing basis set. The procedure adopted for this case is to divide the electric field region into several steps and use a decay constant calculated from the perturbed eigenfunctions for the average field $\bar{F}$ of the step. This reduces the time dependent problem of eqn (5.4) to several iterations of the radiative decay problem of eqn (5.13a,b). For the interval t_1 to t_2 with an average field $\bar{F}$, this gives

$$\rho_{jj}^{\bar{F}}(t_2) = \rho_{jj}(t_1)\, e^{-\gamma_{jj}(\bar{F})(t_2 - t_1)} \qquad (5.17a)$$

$$\rho_{jk}^{\bar{F}}(t_2) = \rho_{jk}(t_1)\, e^{-i\omega_{jk}(\bar{F})(t_2 - t_1) - \frac{1}{2}(\gamma_{jj}(\bar{F}) + \gamma_{kk}(\bar{F}))(t_2 - t_1)} . \qquad (5.17b)$$

The errors involved in this procedure will be small if $(\gamma_{jj}(\bar{F}))^{-1}$ is large compared to $t_2 - t_1$ and the total number of steps is small.

§5.6 THE INTENSITY OF SPECTRAL LINES

The result of a measurement at time t is predicted by operating on the density matrix $\rho(t)$ with the operator A representing the physical quantity required. The mean value of the observable A is then

$$\langle A \rangle = \mathrm{Tr}(A \cdot \rho(t)) , \qquad (5.18)$$

where Tr (trace) denotes the sum of the diagonal elements of the matrix $A \cdot \rho(t)$.

The intensity operator according to Series [Se 69a] is, in terms of its elements,

$$A_{mm'} = P_{gm} P_{m'g} ,$$

where P_{gm} is the matrix element of a vector component of the electric dipole operator, g is the common lower state of the transition, and m and m' are excited states. The intensity of a transition from the states m and m' to the lower state g is given by the partial trace

$$I_{mm'}(t) \propto \sum_{mm'} P_{gm} P_{m'g} \rho^{F}_{mm'}(t) \quad . \tag{5.19}$$

The constant of proportionality in eqn (5.19) is $\frac{e^2 \omega^4 K}{2\pi c^3}$ [Be 57, p.250] where ω is the frequency of the transition and K depends on the solid angle, the direction, and the effiency of detection.

Since the coherence terms of the density matrix may be non-zero the intensity may contain (see eqns (5.6) and (5.13b)) interference terms of the form

$$\exp \frac{i}{\hbar} (E_{m'} - E_{m})t$$

which may give rise to quantum beats. It can be seen that the intensity operator leads to observable interference only if the final state (g) is the same for the interfering decay channels, as otherwise the decay channels could be distinguished by the final state of the system after the intensity experiment is completed. Care must be exercised to ensure that upper states decaying to lower states which give resolved spectral lines are not included in the partial trace, eqn (5.19), since the resolution of the decay channels is a selective measurement necessarily precluding interference [Ka 65, Po 64].

The strong field Stark effect of hydrogenic ions introduces coherence terms between states of the same M_J. These states are well separated by the strong field perturbation so that Stark components will not contain contributions from states of the same M_J and interference will not result from the Stark induced coherence terms.

If the intensity is summed over all polarization directions and 4π solid angle, the intensity will not show any quantum beats [Ma 70a] even though coherence terms are present in $\rho(t)$.

CHAPTER 6

INITIAL POPULATION DISTRIBUTIONS AT THE FOIL

The details of the analyses of the F_α Stark patterns and the He I singlet Stark patterns are presented separately in the following sections employing the general principles presented in Chapter 5. The distinction between the two approaches arises because of the different characteristics of the linear and quadratic Stark effects for He^+ states and He states respectively.

A model of the time evolution of the excited states is constructed within the experimental restrictions for the F_α observations. The model has been applied to various initial population distributions and a population distribution consistent with the observed F_α Stark patterns inferred.

In the case of He I, the excited state time evolution problem is formulated to meet the requirements of the 4^1D and 4^1F Stark pattern observations and a relation between the initial population of the excited states and the final Stark component intensities is derived. The relationship has been used to determine the relative initial populations.

§6.1 APPLICATION OF THE POPULATION EVOLUTION MODEL TO THE F_α STARK PATTERNS

The intensity of a Stark component depends on the populations of all excited states which contribute to the component by radiative decay. Most components of the F_α Stark pattern contain unresolved fine-structure as a result of decays from nearly degenerate states of differing $|M_J|$ value. Only the π components displaced by $\pm 6X$ arise from single upper levels of one $|M_J|$ value (see fig. F1, Appendix F). Therefore the initial density matrix cannot be determined from the F_α Stark component intensities.

Under these circumstances an initial density matrix may be postulated and the final Stark pattern resulting from the various decays and perturbations calculated. This approach has been implemented because

the general theoretical considerations of the foil excitation process (§5.1) provide guidelines that restrict the form of the postulated initial population distribution. Comparison of the predicted Stark pattern and the measured Stark pattern tests the plausibility of the hypothetical initial population distribution.

§6.1.1 Experimental Considerations

The excited state density matrix formulation of the time evolution model outlined in Chapter 5 requires negligible radiative cascade contributions to F_α excited states. Jordan *et al.* [Jo 67] established that the measured F_α decay curves were consistent with multi-exponential decay from the 4^2S, 4^2P, 4^2D, and 4^2F terms with their respective theoretical lifetimes and concluded that there were no significant cascade contributions to these terms. A decrease in intensity of He II transitions as the n value of the excited states increased was observed in the survey scan (figs. F3, F4, Appendix F) and lines from terms of $n > 12$ were too weak to detect. The relative intensities of the F_α (4686 Å) and the F_β (3202 Å) lines obtained from the survey scan were approximately 10 and 3 respectively. The mean lifetimes and transition probabilities [Wi 66] for transitions from the $n = 4$ and $n = 5$ levels suggest a contribution to the population of the $n = 4$ levels from the $n = 5$ levels of about 5% in the short time ($< 4 \times 10^{-9}$ s) before observation. This order of magnitude estimate is consistent with the observations of Jordan *et al.* that cascade contributions to the $n = 4$ terms are negligible.

Multiply-excited states of He I [Be 71] that decay by auto-ionization could possibly contribute to the population of the $n = 4$ terms of He II, but as this process occurs in a time of the order of 10^{-14} s it may be regarded as part of the initial excitation process. The doubly-excited states that decay by photon emission with longer lifetimes were observed to be very weak, in agreement with the measurements of Berry *et al.* [Be 72c]. These transitions were observed only close to the foil (< 5 mm) and therefore did not appear in the survey scan which was obtained about 30 mm from the foil.

The spatial variation of the applied electric field for the F_α measurements was such that a weak field sudden approximation (§5.5.1) to the electric field perturbation is appropriate. The field configuration,

shown in fig. 2.14a, used for these measurements resulted in the excited ions seeing a region of zero field, followed by a change (within about 2 mm) into a strong positive field, followed by a field reversal (within about 2 mm) to an approximately constant strong negative field. The highest beam energy used was 820 keV for the F_α measurements so that the most rapid field change occurred in about 3×10^{-10} s. The smallest fine-structure interval for the n = 4 terms is 0.12 cm^{-1} for the separation of the $4^2F_{7/2}$ and $4^2D_{5/2}$ terms. The Bohr period for transitions between these levels is about 4×10^{-11} s, an order of magnitude less than the time in which the electric field changed appreciably. This corresponds to a weak field sudden perturbation for both the entry into the field and the field reversal.

The actual electric field configuration along the beam axis had to be approximated by sudden steps and regions of constant field for the purpose of calculating the population mixing due to the perturbation, and for the purpose of calculating the radiative decays, respectively. There was a long region ($\approx$ 1 cm) of nearly zero field (< 500 V) from the foil to the furtherest earthed electrode where the field changed appreciably in the short distance through its aperture. This was followed by a strong field of about 1 cm extent, and ended in a small region of about 2 mm at the slot in the negative electrode where the field reversed and became strong for a further centimetre.

§6.1.2 Application to the Model

The general features of the excited state evolution in the beam-foil source which were used in Chapter 5 to describe the population evolution of He II terms are specified below in accordance with the particular requirements outlined above.

An initial density matrix is postulated according to the general requirements of §5.1. This initial population can therefore be characterized by the variation of population with orbital angular momentum (L) and by the variation of population with the z component of orbital angular momentum (M). The electric field is parallel to the beam axis in the first electric field region to be encountered by the excited ions so that the z-axis is not rotated from its initial direction parallel to the beam axis. The distinction between z-axis parallel or anti-parallel to the beam is only significant at the ion exit from the foil and the passage through the electric field reversal.

The change in the populations as the ions suddenly leave the foil is calculated by the application of a spin-half Clebsch-Gordan transformation. The basis set $\{nLJM_J\}$ in which the spin-orbit interaction has a diagonal Hamiltonian with eigenvalues giving the fine-structure separations is the new basis set for the density matrix. This basis set is also the one required for later use in the Stark perturbation calculations using the method of Lüders [Lü 51]. The phase convention for the Pauli eigenfunctions used by Lüders is the same as that used for the Clebsch-Gordan matrix elements [Co 51, p.75].

The approximately zero field decay of F_α terms is calculated as outlined in §5.4 with the zero field decay constants appropriate to each L value obtained from the tables of Wiese [Wi 66]. The time the ions spent in zero field was calculated from the beam energy and the distance from the foil to the exit side of the earthed electrode. No correction to the beam energy was made for the energy loss in the thin foils (< 1%).

The entry into the first strong electric field is treated as a weak field sudden perturbation. The value of the electric field for this step function perturbation was a parameter of the model and could be varied to alter the extent of Stark induced transitions between different fine-structure levels. From the calculated rate of application of the electric field, and the fine-structure separations of the $n = 4$ states of He II, the extent of transitions between non-degenerate states was expected to be negligible. For the purposes of calculation, 50 V was found to be a suitable value, adequate to mix the degenerate states while only very slightly mixing the non-degenerate states. The effect of changing this choice of weak field value will be discussed when the model is applied to various initial population distributions. The change from 50 V to the first strong field in the short region of about 2 mm was assumed not to mix the populations any further and the appropriate weak field decay constants were approximated by the strong field values. This is equivalent to assuming an adiabatic perturbation (§5.5.2) once the 50 V field step removes the L degeneracy of the zero field levels.

The decrease in the population of the $n = 4$ terms in the first strong field by radiative decay was then calculated following the method of §5.4, with the decay constants given in Appendix B. The relatively long time spent by the ions in the positive electric field was calculated from the beam energy and the distance from the exit side of the earthed

electrode to the nearest side of the negative electrode. The change in beam energy (< 5%) due to the electric field was neglected.

The electric field reversal from a strong field parallel to the beam direction to one antiparallel to the beam direction can be split into three parts; adiabatic strong to weak field which does not mix the populations, then a weak through zero to weak field which mixes the populations, and finally an adiabatic change back to strong fields. This calculation is equivalent to a rotation of the z-axis by 180°. The weak field decay constants appropriate to the small regions of the adiabatic changes are approximated by the strong field decay constants.

Further radiative decay in the electric field was treated as before. The time spent in the negative electric field was obtained from the beam energy, assumed unaltered by the field, and half the distance between the outer faces of the two electrodes.

The Stark pattern was calculated from the evolved density matrix by the application of the intensity operator at the time corresponding to the position of observation. This was done by calculating the term-by-term contribution to each Stark component using eqn (5.19) and the transition probabilities of Appendix B. The σ components were reduced by a factor of 3.6 to account for the relative efficiency of the grating for polarized light (§2.2.1 and fig. 2.6). The decay scheme of the strong field Stark perturbed F_α line (fig. F1, Appendix F) precludes the inclusion of coherence terms in the decay of the π components, because none of these have a common final state. Coherence terms were included for the σ components if they had fine-structure; this provided a numerical check that they were all zero, since the discussion of their origin indicated that they should be (see §5.6).

§6.1.3 Implementation of the Model

The model outlined above was programmed in FORTRAN V for the Australian National University's UNIVAC 1108 computer. A simplified flow chart indicating the computational steps involved is given in fig. 6.1. The programme was sufficiently general to accommodate the calculation of the evolution of excited states for $n \leqslant 5$ of low Z hydrogenic ions subjected to Stark perturbations by fields from zero to the appropriate strong field limits. For input data, the programme required the

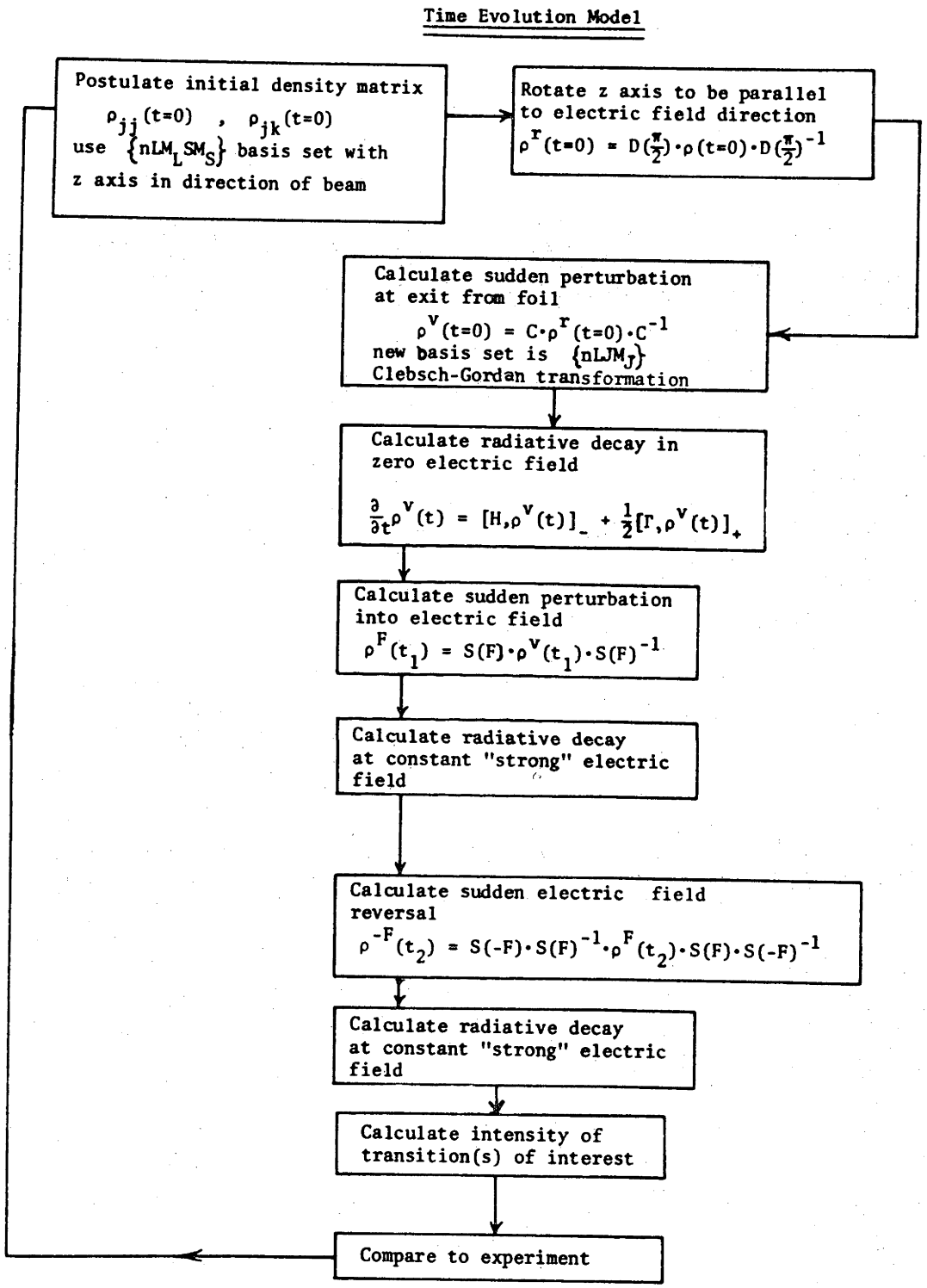

Fig. 6.1: Time evolution model for hydrogenic ions. Simplified flow chart of computational steps for the calculation of the intensity of hydrogenic ion Stark components.

postulated initial population distribution in the form of the initial density matrix elements, the zero field radiative decay constants, and the strong field Stark perturbed decay constants. It also required the ion mass, charge, energy and the distances for the zero field, positive field, and negative field. The programme could print, if required, the density matrix after each step of the calculations indicated in fig. 6.1 so that a quantitative assessment of the effects of the various processes could be obtained. The energy eigenvalues and contact transformation matrices could also be listed to check on the numeric procedures. The final output of the predicted Stark component relative intensities was given in both numeric listing and graphical forms. The time required to obtain a Stark pattern from an initial population distribution was about ten seconds.

The calculations of the model were checked by two procedures. If the initial density matrix is a unit matrix (statistical population distribution) and no radiative decay is allowed, the final density matrix should be a unit matrix because the contact transformations involve unitary matrices. If radiative decay is included, the decay of a given state in a particular constant field region should be in accordance with the appropriate decay constant. Furthermore, the trace of the density matrix should decrease with radiative decay and be conserved for the contact transformations. The computer programme satisfied these consistency checks.

The radiative decay calculations were done with complex numbers to incorporate the complex coherence terms. The various contact transformations operate on these complex numbers and produce in the final intensities only real numbers. The extent of round-off errors in computations was checked by examining the final density matrix elements contributing to the Stark components; these had imaginary parts less than 10^{-8} of the real parts.

§6.1.4 The Idealization to a Weak Field Sudden Perturbation

Consideration of the fine-structure intervals and the duration of changes in the electric field led to a choice of 50 V for the weak field sudden perturbations as the ions entered the first strong field region and when they passed through the field reversal. The Stark patterns shown in §4.2.3 had slight differences which were consistent

with lifetime changes rather than changes in populations resulting from mixing by the perturbations.

These effects were simulated by calculating the Stark patterns resulting from an initial equal population of all 4^2P states subjected to different magnitudes for the electric field step constituting the weak field sudden perturbation. Two of these calculated patterns are shown in fig. 6.2. The absolute values of the components at +4X and +5X markedly increase as the weak field sudden perturbation is made at weaker field strengths. These changes are opposite to those observed in §4.2.3 if the weak field sudden perturbation is made above 1 $kV \cdot cm^{-1}$ where the mixing of states separated by the fine-structure intervals is not negligible. However, if the weak field sudden approximation has values less than 500 $V \cdot cm^{-1}$ there is very little change in the calculated patterns because only the degenerate states mix. The mixing of the degenerate states is virtually independent of the field strength for such weak fields.

Well below 500 $V \cdot cm^{-1}$ the question arises as to whether the Lamb shift separation of the $4^2S_{1/2}$ and $4^2P_{1/2}$ states (≈ 0.059 cm^{-1}) is sufficiently small to regard them as degenerate. The $4^2S_{1/2}$ and $4^2P_{1/2}$ states contribute to the Stark components at +5X and +6X (see fig. F1, Appendix F). The Bohr period for Stark induced transitions is in this case $\approx 6 \times 10^{-9}$ s, an order of magnitude greater than the time in which the field changed from a few hundred volts per cm to about 6 $kV \cdot cm^{-1}$ through the aperture in the earthed electrode. However, the very slow change in field from ≈ 0 $V \cdot cm^{-1}$ at the foil to about 500 $V \cdot cm^{-1}$ at the earthed electrode (see §4.2.3) may be insufficient to mix the $4^2S_{1/2}$ and $4^2P_{1/2}$ states but will, of course, cause them to repel each other. The effect of the perturbation on the mixing of the $4^2S_{1/2}$ and $4^2P_{1/2}$ populations was found to be consistent with a choice of 50 V for the step function weak field sudden perturbation.

The L dependence of the Lamb shift ensures that the separations of the states $4^2P_{3/2}$ and $4^2D_{3/2}$ as well as the states $4^2D_{5/2}$ and $4^2F_{5/2}$ are less than their natural widths [Be 57, p.104], and hence cannot lead to the same uncertainty in the extent of population mixing as for the $4^2S_{1/2}$ and $4^2P_{1/2}$ states.

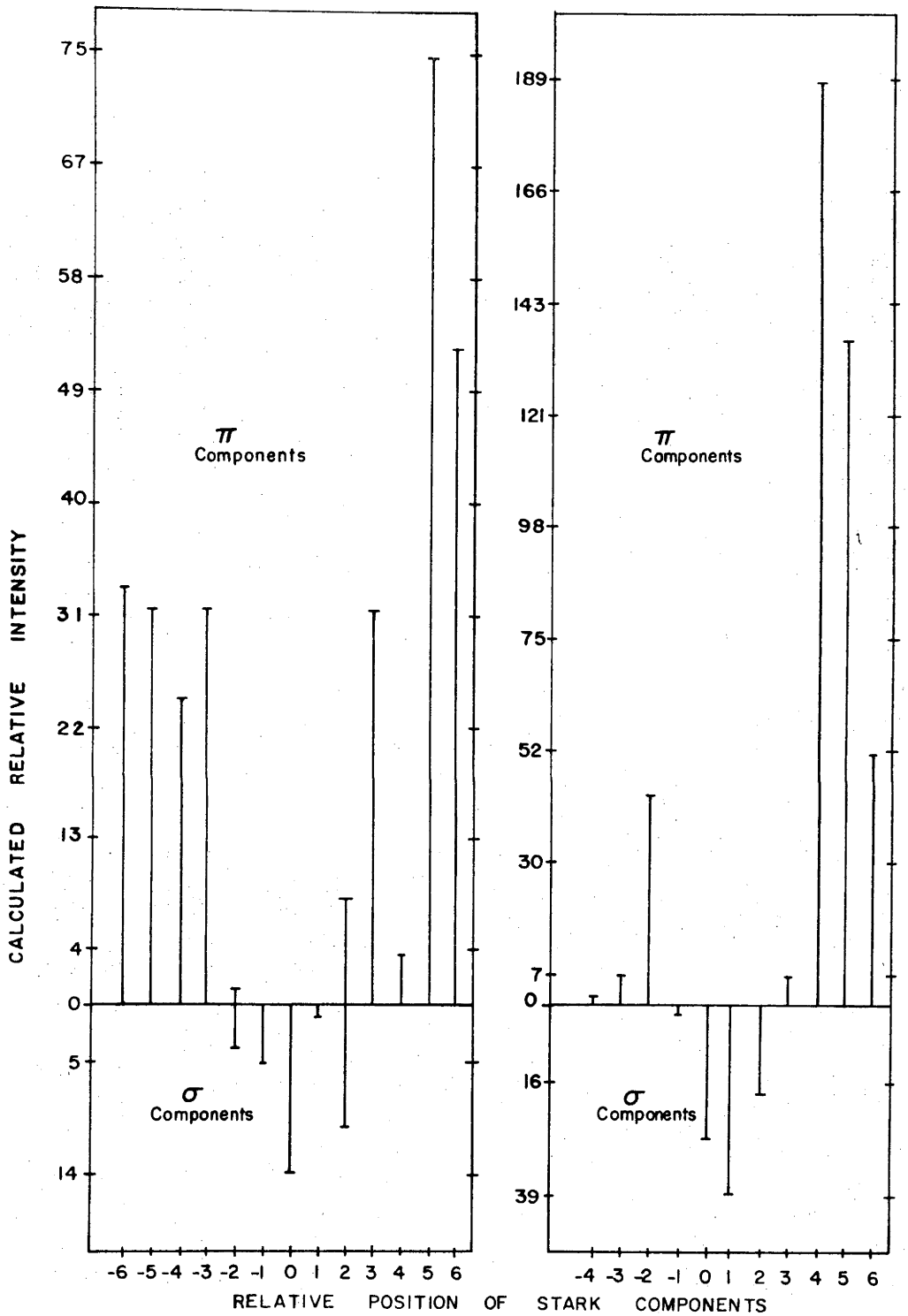

Fig. 6.2: Stark pattern as sudden perturbation increases. The Stark pattern on the left results from a 5 $kV \cdot cm^{-1}$ sudden perturbation with initially only P states populated isotropically. The Stark pattern on the right arises from a 2 $kV \cdot cm^{-1}$ sudden perturbation with all other conditions unchanged.

§6.1.5 The Idealization of the Decay Constants

The approximately zero field ($< 100\,V\cdot cm^{-1}$) between the foil and the earthed electrode at the start of the first strong field region was treated for the purpose of radiative decay calculations as if it were a region of exactly zero field strength. The effect of this approximation thus depends on the difference between the zero field lifetimes and the lifetimes at field strengths up to about $100\ V\cdot cm^{-1}$.

The penetration of the weak field through the earthed electrode was estimated to extend less than 4 mm into the region assumed to have zero electric field (see §2.4.3). At 400 keV the time spent by the ions in passing through this region corresponds to about the lifetime of the 4^2P term (0.77 ns) and is less than the lifetimes of the 4^2S (14.16 ns), 4^2D (2.26 ns), and 4^2F (4.33 ns) terms. The weak field perturbed lifetimes were estimated at 500 V to be ≈ 3 ns for the $4^2D_{5/2}$ and $4^2F_{5/2}$ states, ≈ 1 ns for the $4^2D_{3/2}$ and $4^2P_{3/2}$ states, ≈ 1.4 ns for the $4^2P_{1/2}$ and $4^2S_{1/2}$ states, and no change for the $4^2F_{7/2}$ states [Be 57, §67). Using these perturbed values for 4 mm of the zero field gave population values 40% lower for the 4^2P term and 50% higher for the 4^2S term than those which will be given in §6.1.6. It is considered that these changes are extreme.

The strong field, Stark perturbed lifetimes were also used for the Stark levels in the weak field region (extent ≈ 2 mm) at the position of the field reversal. In fact, the lifetimes will be nearer to the weak field lifetimes estimated above. The error involved in this assumption was estimated from the observations given in §4.2.3. The decay of the population of the states leading to the -4X component is approximately unchanged whereas the decay of the states giving the +4X and +5X components, lessens as the field strength changes from strong to weak field values. The long wavelength components of the Stark patterns presented in §4.2.3 were observed to decrease relative to the short wavelength components by about 20% as the electric field between the earthed electrode and the negative electrode was decreased to intermediate field values while the field at the point of observation was maintained strong. This behaviour is consistent with the changes in the perturbed lifetimes. Hence the error in the calculated Stark patterns resulting from assuming the strong field lifetimes for the small weak field region is estimated to affect the +5X and +4X components by much less than 20%.

§6.1.6 Comparison of the Calculated and Observed Stark Patterns

There are an infinitude of possible initial population distributions that may be used to obtain hypothetical Stark patterns. Fortunately there is some guidance to the choice of initial populations from the measured Stark patterns if qualitative features of the evolution process are considered.

The Stark induced transitions correspond to a weak field sudden perturbation so that the qualitative connection between the population of Stark perturbed states and their related zero field unperturbed states corresponds to the diagram of Appendix F, fig. F1.

Neglecting, for the present, changes due to radiative decay, the populations of states in zero field can be qualitatively related to the populations of the Stark perturbed states. The population of the zero field states of lower L value (4^2S, 4^2P terms) would tend to increase the relative amount of the high wavelength Stark components (see figs. 6.3 and 6.4). Furthermore, the central σ components of the Stark pattern tend to arise from states of higher M value than do the π components on each side.

The qualitative features of the F_α Stark patterns observed at different energies show an intensity asymmetry that favours the high wavelength components. The π components at low or high wavelength tend to be stronger relative to the central components than would be obtained from a statistical population distribution of the Stark levels.

The observed intensity asymmetry with respect to the components suggests there may be a preferential population of the lower L value states relative to the higher L value states at the point of observation. The zero field decay of the various states depletes the P states more than the others, hence the preferential population of low L value P states would have to be enhanced to obtain a preferential P state population at the point of observation. The observed dominance of the low and high wavelength π components over the σ components suggests that the states of higher M are less populated than the states of lower M value, either because of alignment or because the higher L states are underpopulated. These qualitative considerations were used to guide the search for a plausible initial population distribution.

The Stark patterns obtained at 400, 680 and 820 keV He beam energy and an electric field strength of 90 $kV \cdot cm^{-1}$ and the Stark pattern obtained at 680 keV He beam energy and 161 $kV \cdot cm^{-1}$ were all similar in their general features. Since the data at 161 $kV \cdot cm^{-1}$ provides the most reliable estimate of the relative intensity of the Stark components the model calculations were carried out in greater detail for the electric field distributions and times for decay appropriate to that data.

The Stark patterns were first calculated for terms of single L value initially populated isotropically; the predicted patterns are given in figs. 6.3 and 6.4. The qualitative remarks made previously about the L value population contribution to the various Stark components are evident from these diagrams. The Stark pattern was then calculated for an initial statistical population distribution S:P:D:F = 1:3:5:7, that is, weighted according to 2L + 1. The Stark pattern deduced for this population distribution is shown in fig. 6.5. It is similar to the observed Stark patterns but the components at +4X, +5X and +6X are too weak. These components depend mainly on the initial S and P populations, and their proportions can be changed by distorting the initial statistical distribution. The nearest match to the observed Stark pattern at 161 $kV \cdot cm^{-1}$ was obtained with the ratio of S:P:D:F populations set at 2:12:5:7. This distribution reproduced the asymmetry of the π components, but the central σ component was still too strong compared to the σ components at $\pm$1X and the π components at $\pm$4X.

Allowing alignment in the initial population distribution was sufficient to obtain acceptable agreement with the observed Stark pattern. The 4^2D and 4^2F terms contribute most of the population of the states giving rise to the central σ component so that the intensity of this component is sensitive to alignment in those terms. The population distribution ($\{nLMM_S\}$ basis set) that was consistent with the data was then S:P:D:F = 2:14:5:7 with the modification that the states $|4\ 3\ 3\ |\tfrac{1}{2}|\rangle$ were 60% less populated than the other $|4\ 3\ M|M_S|\rangle$ states and the states $|4\ 2\ 2\ |\tfrac{1}{2}|\rangle$ were 25% less populated than the other $|4\ 2\ M|M_S|\rangle$ states. The observed Stark component relative intensities of table 4.2 were re-normalized and are compared with the calculated Stark pattern in fig. 6.6.

The agreement between the calculated Stark pattern neglecting the Lamb shift and the observed pattern is excellent for all but the components at +5X and +6X. The calculated and observed relative

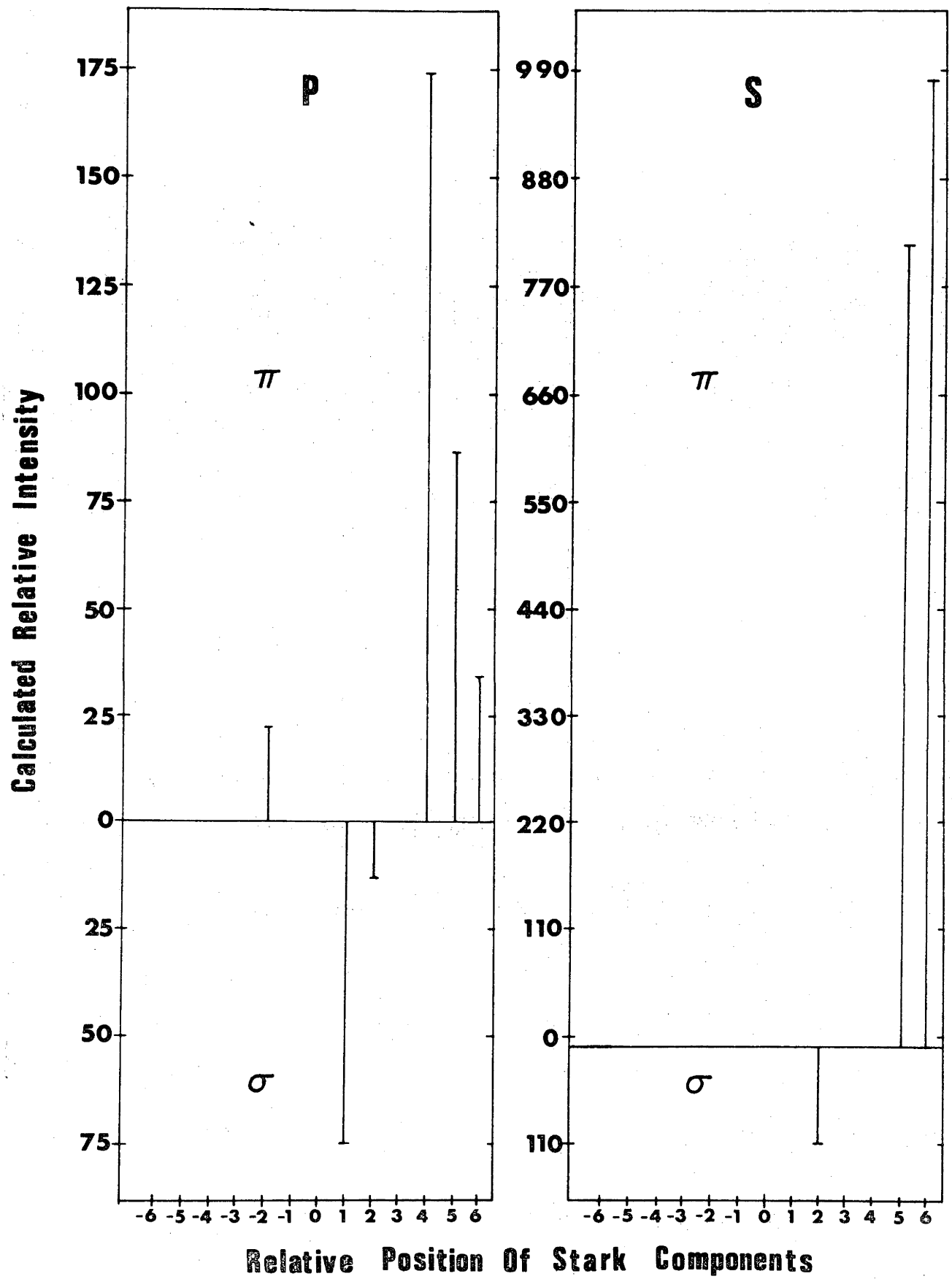

Fig. 6.3: Calculated Stark patterns, P and S states. Predicted relative intensities for the initial population of P states only or S states only.

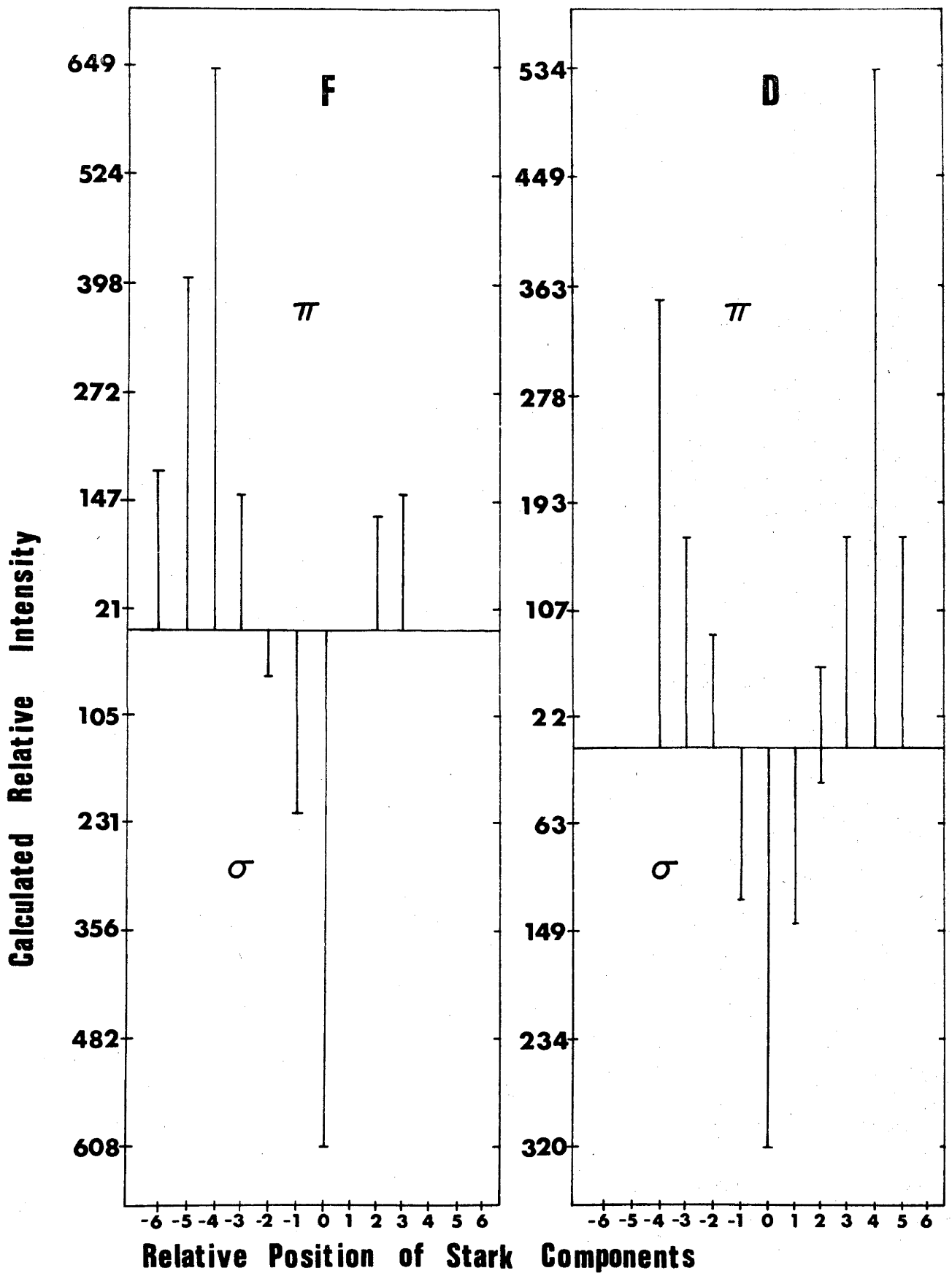

Fig. 6.4: Calculated Stark patterns, F and D states. Predicted relative intensities for the initial population of F states only or D states only.

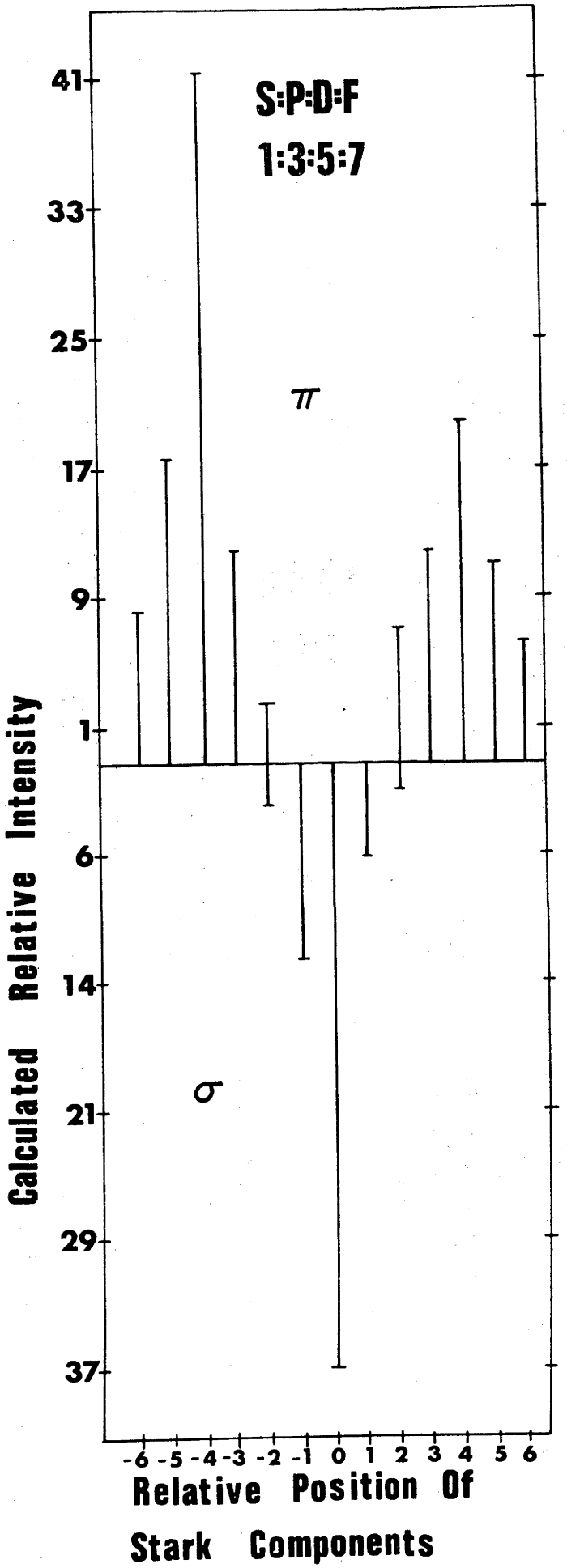

Fig. 6.5: Calculated Stark pattern for statistical initial population distribution.

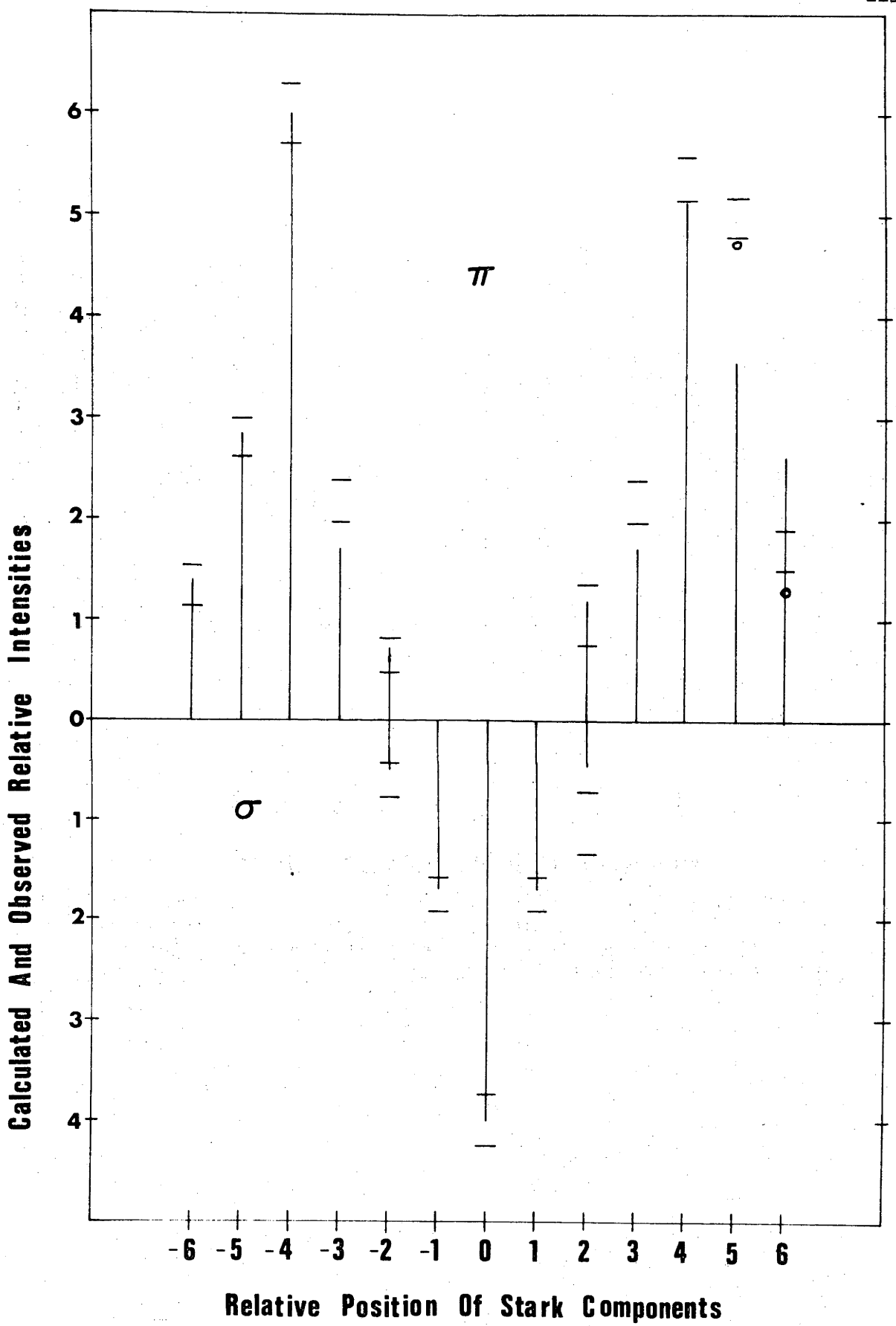

Fig. 6.6: Comparison of observed and calculated Stark patterns. The horizontal lines are the observed values and the vertical lines are calculated neglecting the Lamb shift. The calculated intensities of the +5X and +6X components including the Lamb shift are indicated by O.

intensities for the +5X and +6X components are not very different considering that these are the components arising from $4^2P_{1/2}$ and $4^2S_{1/2}$ states. Recalling the discussion of the Lamb shift given previously (§6.1.4) this mismatch is not large or unexpected.

A simplified estimate of the effect of the Lamb shift separations of $4^2S_{1/2}$ and $4^2P_{1/2}$ states was able to account for the difference between the observed Stark pattern and the Stark pattern calculated neglecting the Lamb shift (see fig. 6.6). The density matrix elements of the $4^2S_{1/2}$ and $4^2P_{1/2}$ states were obtained at the entry to the electric field from the above calculations and their evolution treated without Stark induced population mixing. The Lamb shift results in the $4^2P_{1/2}$ state's being lower in energy ($\approx .059$ cm^{-1}) than the $4^2S_{1/2}$ state so that for an infinitely slow application of the electric field their populations do not mix and the $4^2P_{1/2}$ state contributes solely to the +6X component and the $4^2S_{1/2}$ state only to the +5X component [Lü 50; Be 57, p.241].

The $4^2P_{1/2}$ and $4^2S_{1/2}$ populations at $t = 0$, for the population distribution 2:14:5:7, were respectively 4.600 and 2.000. The changes in these populations through the evolution processes were obtained from the model. These populations were also traced through their evolution without allowing them to mix so that the effect of the Lamb shift separation could be estimated. Table 6.1 gives the evolution of these populations under the two different assumptions.

TABLE 6.1: Evolution of the $4^2S_{1/2}$ and $4^2P_{1/2}$ populations.

	Without Lamb Shift		With Lamb Shift	
	$4^2S_{1/2}$	$4^2P_{1/2}$	$4^2S_{1/2}$	$4^2P_{1/2}$
Initial population	2.000	4.600	2.000	4.600
After zero field decay	1.760	0.420	1.760	0.420
After Stark perturbation	1.090	1.090	1.760	0.420
After electric field decay	0.310	0.350	0.500	0.119
After field reversal	0.330	0.330	0.500	0.119
After final electric field decay	0.113	0.115	0.169	0.040
Final Stark state	+5X	+6X	+5X	+6X

The $4^2S_{1/2}$ state contributes 0.169 to the +5X component instead of 0.113 neglecting the Lamb shift. The +5X component also has a contribution from the $|M_J| = 3/2$ Stark state that is unaltered at 0.079, giving a net increase of a factor of 1.30 in the +5X component intensity. The component at +5X including the Lamb shift is then indistinguishable from the observed intensity for that component. The +6X component including the Lamb shift in the model is still slightly less than observed.

The population distribution obtained for the data at 161 $kV \cdot cm^{-1}$ gave a calculated Stark pattern for the geometry of the data taken at 90 $kV \cdot cm^{-1}$ which was in reasonable agreement with the observed Stark pattern obtained at 680 keV beam energy and 90 $kV \cdot cm^{-1}$. Unfortunately the large correlation between the intensities of adjacent Stark components for the 90 $kV \cdot cm^{-1}$ data prevented a detailed comparison with the calculated Stark patterns being meaningful.

The outcome of comparisons with the model-calculated Stark patterns was that the small change in the Stark pattern between 400 keV and 820 keV beam energy could be due to a slight increase in the 4^2S and 4^2P term's initial population or to the decreasing time interval spent in the weak field regions as the beam energy increased. The energy range encompasses only a very small change of ≈ 1.4 in the ion velocity.

§6.2 APPLICATION OF THE POPULATION EVOLUTION MODEL TO THE He I SINGLET MEASUREMENTS

A population evolution model was formulated for the particular case of the 4^1D and 4^1F terms of He I using the general features outlined in Chapter 5. The particular characteristics and assumptions of this model are discussed. The relative initial populations of some of the states at the time of excitation are obtained as far as the M_J degeneracy permits. The problem is well determined (to within the M_J degeneracy) because the final population of a given state is proportional to the initial population of the same state. The constant of proportionality depends on the particular state of interest but may be determined providing the relation between the time after excitation and the electric field strength at that time is known for the particular experimental arrangement used.

§6.2.1 Experimental Considerations

The lifetime of the 4^1D term of He I measured at a He beam energy of 80 keV by Martinson *et al.* [Ma 70b] was 38 ± 3 ns, which is not significantly different from the theoretical value of 36.6 ns [Wi 66]. The lifetime of the 4^1F level has not been measured in the beam-foil source as the allowed decay $4^1F \rightarrow 3^1D$ is in the infra-red at 18697 Å. The lines from terms of $n > 4$ can be seen from the survey scan (Appendix F, figs. F3 and F4) to decrease rapidly in intensity as n increases. This, considered with the transition probabilities of decays to the $n = 4$ terms [Wi 66], demonstrates that cascade re-population of $n = 4$ terms is negligible. For example, the theoretical transition probability for the $6^1D \rightarrow 4^1F$ transition is 2.49×10^4 s^{-1} whereas the competing decay channel $6^1D \rightarrow 2^1P$ has a transition probability about two orders of magnitude greater. The observed intensity from the survey scan for the $6^1D \rightarrow 2^1P$ transition is about a factor of ten less than the $4^1D \rightarrow 2^1P$ transition and the $7^1D \rightarrow 2^1P$ transition is barely visible.

For He beam energies of 250 keV to 410 keV the time taken by the excited ions to travel from the foil to the point of observation was less than 10 ns, see §4.3.2, which is less than the lifetimes of the terms $4^1F \approx 72$ ns, and $4^1D \approx 36$ ns. The lifetimes for the transitions from the significantly populated terms of higher n to the 4^1F and 4^1D terms are considerably larger than the time until observation, thus ensuring a negligible contribution to the 4^1F and 4^1D populations from cascades.

The L selection rule for the Stark perturbation ($\Delta L = \pm 1$) validates the adiabatic perturbation approximation for the $n = 4$ terms of He I under the experimental conditions used. The time within which the perturbation is applied is determined by the fringing fields for the electrode configuration (b) and the He beam velocity. The spatial extent of the fringing field was not less than 1 mm (see fig. 2.14, §2.4.3). The most rapid application of the electric field occurred for the data obtained at 410 keV He beam energy, for which 1 mm corresponded to 2×10^{-10} s. The two closest terms coupled by the perturbation are 4^1F and 4^1D whose separation, $\Delta E \approx 5$ cm^{-1}, corresponds to a Bohr period of 10^{-12} s, two orders of magnitude less than the time taken to apply the perturbation.

The electrode configuration (b) of §2.4.2 provided an electric field perpendicular to the beam axis with a magnitude along the beam axis

that was zero from the foil to the earthed electrode then increased until the region of observation was reached (see fig. 2.14b). Therefore, apart from the rotation of axes, only zero field and Stark perturbed radiative decay have to be included in the model. The complications of electric field switch-on and reversal do not enter the calculations. The total time of decay was < 10 ns with lifetimes from 30 to 70 ns so that the contribution to population changes from radiative decays was expected to be small. Radiative decay in zero field does not alter the relative population distributions of the states of the 4^1F term or the 4^1D term, but it does alter the relative population of a 4^1F state compared to a 4^1D state because the transition probabilities depend on n and L only [Be 57, p.272].

Allowance for radiative decay in the electric field is small because of the short time spent by the ions in the electric field compared to the lifetimes of the 4^1F and 4^1D terms. However, this decay alters the relative populations of $|M_J| = 2$ states to $|M_J| = 0$ or 1 states of both the 4^1F or the 4^1D terms. This occurs because fewer perturbed decay channels are open for Stark perturbed transitions from $|M_J| = 2$ states than for the others. The variation of the Stark perturbed lifetime of the 4^1F states with electric field strength, as calculated in Appendix C, is shown in fig. 6.7. The variation of the Stark perturbed lifetimes of the 4^1D states is qualitatively similar.

§6.2.2 Adiabatic and Radiative Decay Population Evolution

The specific model of the evolution of the populations of the 4^1F and 4^1D terms which is presented here establishes a direct proportionality between the initial population of states of given $|M_J|$ and the observed intensity of the transitions from those same two states.

The initial excited state density matrix $\rho^u(0)$ for the 4^1F and 4^1D states is expressed in the basis $\{nLMSM_S\}$ with z-axis parallel to the beam. This initial density matrix is assumed diagonal with populations of the same $|M|$ value equal, following the discussion of §5.1.

A rotation through an angle of $\pi/2$ is carried out to express $\rho^u(0)$ with the z-axis perpendicular to the beam and parallel to the electric field direction, i.e.

$$\rho^{u'}(0) = D\left(\frac{\pi}{2}\right) \cdot \rho^u(0) \cdot D\left(\frac{\pi}{2}\right)^{-1} , \qquad (6.1)$$

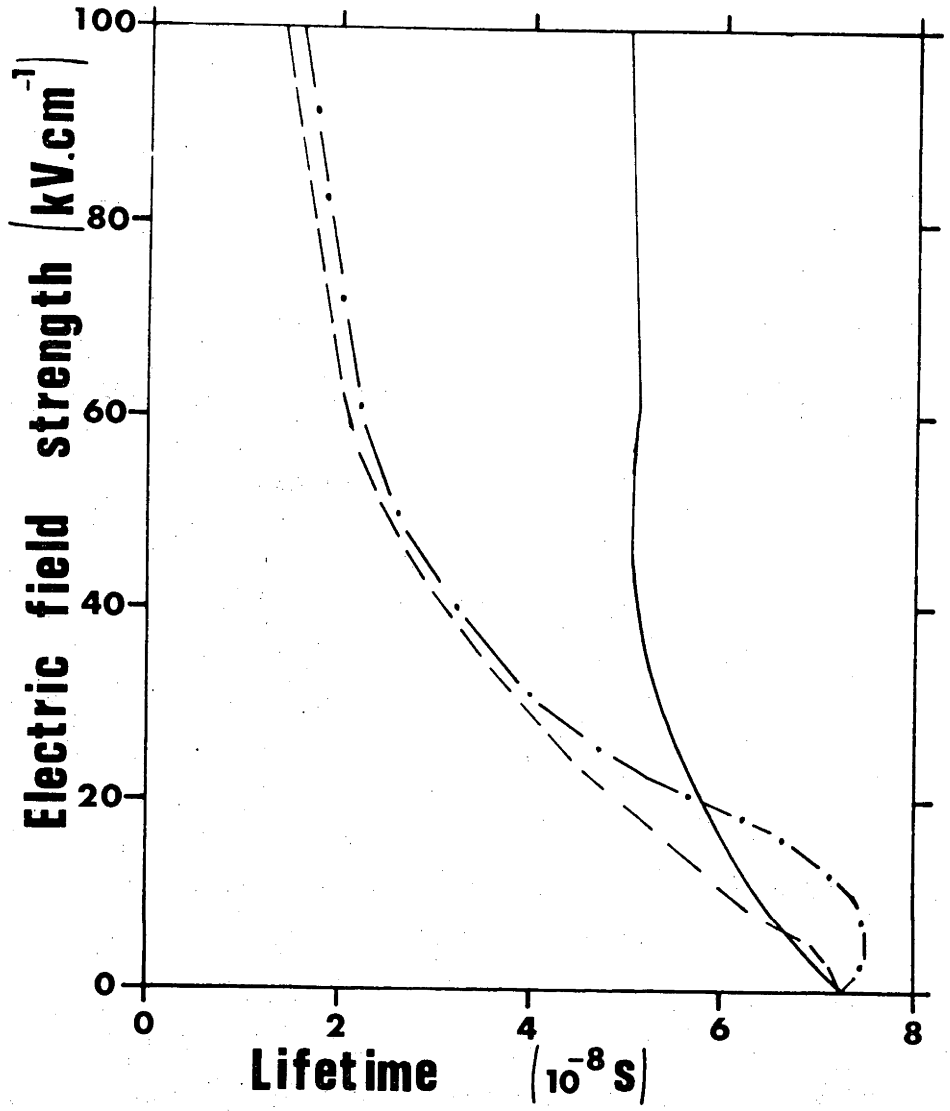

Fig. 6.7: Perturbed lifetimes for the $4^1F_3{}^{0,\pm1,\pm2}$ states.

—— $4^1F_3{}^{\pm2}$
—·— $4^1F_3{}^{0}$
---- $4^1F_3{}^{\pm1}$

where $D(\pi/2)$ is defined in Appendix A. This rotation introduces coherence terms into $\rho^{u'}(0)$ but, as will be shown later, leads to no observable interference effects.

The sudden perturbation as the ions leave the foil gives the new basis $\{nLJM_J\}$ and the density matrix changes according to (see §5.3)

$$\rho^{v}(0) = C\cdot\rho^{u'}(0)\cdot C^{-1} \ . \qquad (6.2)$$

Because the Clebsch-Gordan transformation is to singlet states ($S = 0$), C and C^{-1} are unit matrices, hence

$$\rho^{v}(0) = \rho^{u'}(0) \tag{6.3}$$

and no coherence terms are introduced by the sudden exit from the foil. There are at this stage coherence terms arising only from the rotation of the z-axis. This feature of the model is peculiar to singlet states.

There is now a period t_1 of zero field radiative decay which gives for the diagonal elements of $\rho^{u'}(t_1)$ (see §5.4, eqn 5.13a),

$$\rho^{u'}_{kk}(t_1) = \rho^{u'}_{kk}(0)\, e^{-\gamma_{kk} t_1}. \tag{6.4}$$

This is followed by an adiabatic Stark perturbation for the interval t_1 to $t_1 + \Delta t$, giving a change in the diagonal elements of $\rho^{F}(t)$ (see §5.5, eqn 5.17a)

$$\rho^{F}_{kk}(t_1 + \Delta t) = \rho^{u'}_{kk}(t_1)\, e^{-\gamma_{kk}\left(\frac{F(t_1) + F(t_1 + \Delta t)}{2}\right)\Delta t},$$

where the functional dependence of F upon t and γ_{kk} upon F is made explicit. This leads to

$$\rho^{F}_{kk}(t_2) = \rho^{u'}_{kk}(t_1)\, e^{-\int_{t_1}^{t_2} \gamma_{kk}(F(t))dt}. \tag{6.5}$$

The intensity of a transition from the states $4^1F_3^{M_J}$ and $4^1D_2^{M_J}$ to the 2^1P states involves only the diagonal elements of $\rho^{F}(t_2)$. This can be seen from the decay scheme (fig. 6.8) and the fact that for electrode configuration (b) only σ components are observable. For each of the terms 4^1F and 4^1D the only decay channels that may interfere are $4^1L_J^{\,2} \to 2^1P_1^{\,1}$ and $4^1L_J^{\,0} \to 2^1P_1^{\,1}$ but, as both of these channels are resolved in the strong field at the observation region, interference is precluded. The intensity of a transition between the states $|\alpha M_J\rangle$ and $|\alpha' M'_J\rangle$ is then given by (see eqn 5.19, §5.6)

$$I^{\alpha M_J}_{\alpha' M'_J} = K\, P_{\alpha M_J, \alpha' M'_J}(F)\, P_{\alpha' M'_J, \alpha M_J}(F)\, \rho^{u'}_{kk}(t)\, e^{-\int_{t_1}^{t_2} \gamma_{kk}(F(t))dt}.$$

The field strength dependent dipole matrix elements determine the field dependent transition probabilities (given in Appendix C) so that finally,

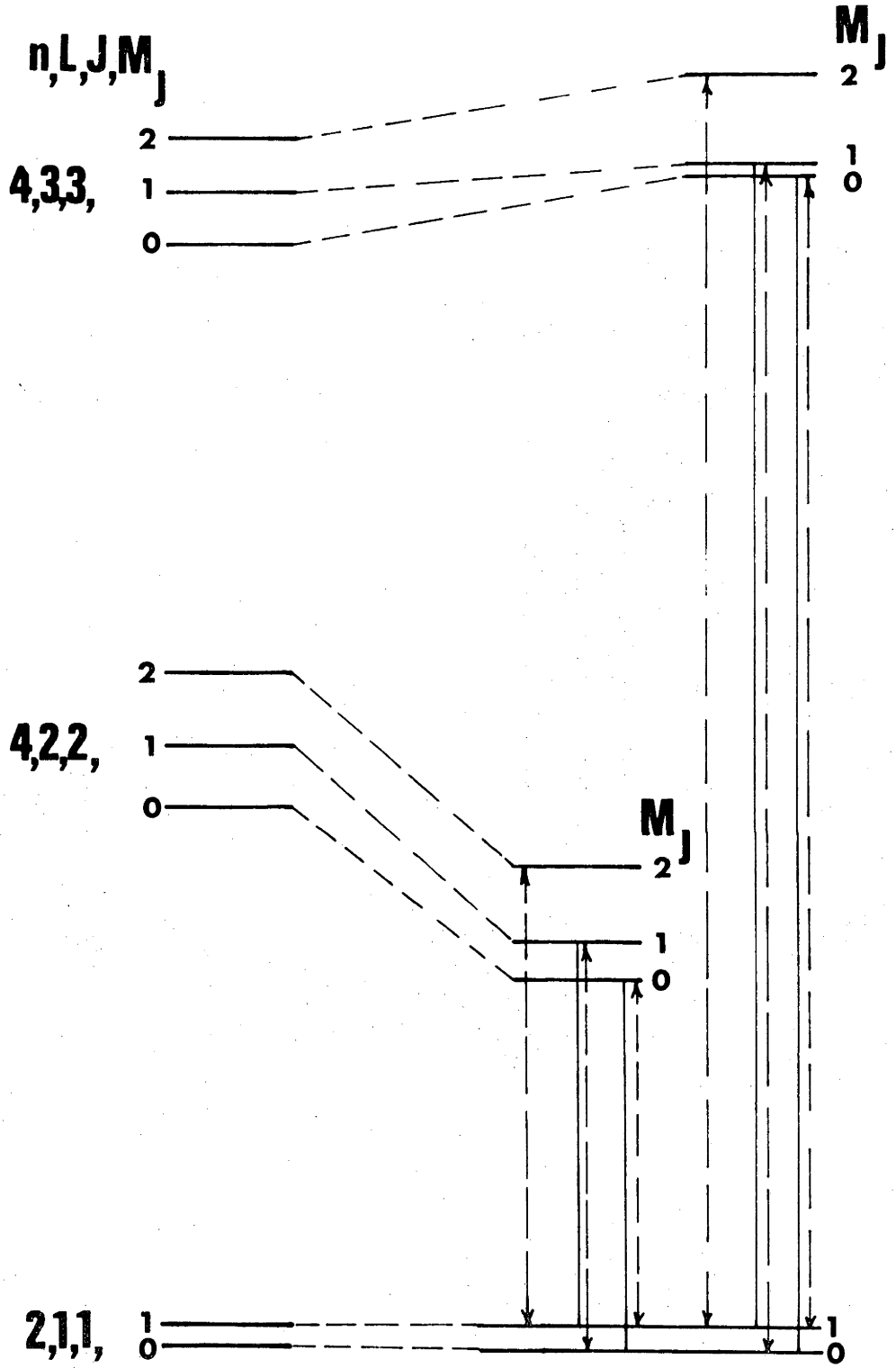

Fig. 6.8: Decay scheme for the Stark perturbed transitions $4^1D \rightarrow 2^1P$ and $4^1F \rightarrow 2^1P$.

——→ denotes σ polarized transition

——→ denotes π polarized transition.

$$I^{\alpha M_J}_{\alpha' M'_J} = K' A_{\alpha M_J, \alpha' M'_J}(F) \rho^{u'}_{kk}(t_1) e^{-\int_{t_1}^{t_2} \gamma_{kk}(F(t))dt} . \quad (6.6)$$

The constant K' is of no consequence for relative population determinations from the measured intensities. Combining eqns (6.4) and (6.6), the relation between the initial populations expressed in the $\{nLMSM_S\}$ basis with z-axis parallel to the field is

$$I^{\alpha M_J}_{\alpha' M_J} = K' A_{\alpha M_J, \alpha' M'_J}(F) \rho^{u'}_{kk}(0) e^{-\gamma_{kk} t_1} e^{-\int_{t_1}^{t_2} \gamma_{kk}(F(t))dt} . \quad (6.7)$$

If the decay factors and transition probability in eqn (6.7) are known, the equation can be inverted and the relative values of all the $\rho^{u'}_{kk}(0)$, that is the initial population distribution, found. This distribution is referred to a z-axis parallel to the electric field. Using the initial assumption that states with the same $|M|$ (and hence same $|M_J|$) are equally populated, the population distribution can be referred to a z-axis parallel to the beam direction by a simple transformation.

§6.2.3 Evaluation of the Radiative Decay Factors

The radiative decay factors

$$e^{-\gamma_{kk} t_1} \quad \text{and} \quad e^{-\int_{t_1}^{t_2} \gamma_{kk}(F(t))dt}$$

of eqn (6.7) were evaluated for the beam energies and electric field distributions pertaining to the measurements of the intensities of the 4^1D and 4^1F Stark perturbed transitions. The times spent in zero electric field and non-zero electric field were calculated from the beam energies and the distances and are given in §4.3.2.

Two approximations to the electric field distribution have been investigated. The first postulated a linear change of electric field while the second used a series of steps from 0 $kV \cdot cm^{-1}$ at the earthed electrode to the field strength at the region of observation. The integrals over the electric field dependent decay constants in the factor

$$e^{-\int_{t_1}^{t_2} \gamma_{kk}(F(t))dt}$$

were evaluated for both electric field distributions to provide an estimate of the errors likely to result because of uncertainties in the field profile. These simple approximations were adequate for this

particular case as the time ($< 10^{-8}$ s) spent in the electric field was less than or equal to the lifetimes of the states involved.

The electric field dependent decay constants are given in Appendix C. Fig. 6.9 shows the approximate electric field distributions along the beam axis and the corresponding variation in decay constants for the $4^1F_3{}^1$ state. The scales for the time after excitation and electric field strength correspond to a beam energy of 410 keV, and a maximum field of 74 $kV \cdot cm^{-1}$ at the observation region. The integral over the decay constant for the electric field region was obtained graphically from fig. 6.9b.

The radiative decay factors for the time spent in the zero field and the following electric field regions are given in table 6.2 for the 250 and 410 keV data. The variations assigned to the electric field decay factors indicate the difference between the two postulated electric field distributions. Any error for the zero field decay, which is due to the uncertainty in the measurement of the distance from the foil (±0.5 mm) to the earthed electrode, is negligible ($\leqslant .01$).

TABLE 6.2: Decay factors.

Beam Energy	Zero Field Decay Factor $M_J = 0, \|1\|, \|2\|$	Electric Field Decay Factor $M_J = 0$	$M_J = \|1\|$	$M_J = \|2\|$
	4^1F term		4^1F term	
250 keV	0.97	0.72 ± .03	0.72 ± .03	0.88 ± .02
410 keV	0.97	0.86 ± .02	0.86 ± .02	0.92 ± .02
	4^1D term		4^1D term	
250 keV	0.94	0.72 ± .03	0.73 ± .03	0.87 ± .02
410 keV	0.94	0.84 ± .02	0.84 ± .02	0.89 ± .02

§6.2.4 Relative Initial 4^1F and 4^1D Populations

From the radiative decay factors and the Stark perturbed transition probabilities, eqn (6.7) may be used to determine the relative initial populations of the various 4^1F and 4^1D states. With the assumption that states of the same $|M|$ value have equal populations, the intensities given in table 4.6 completely determine the initial relative

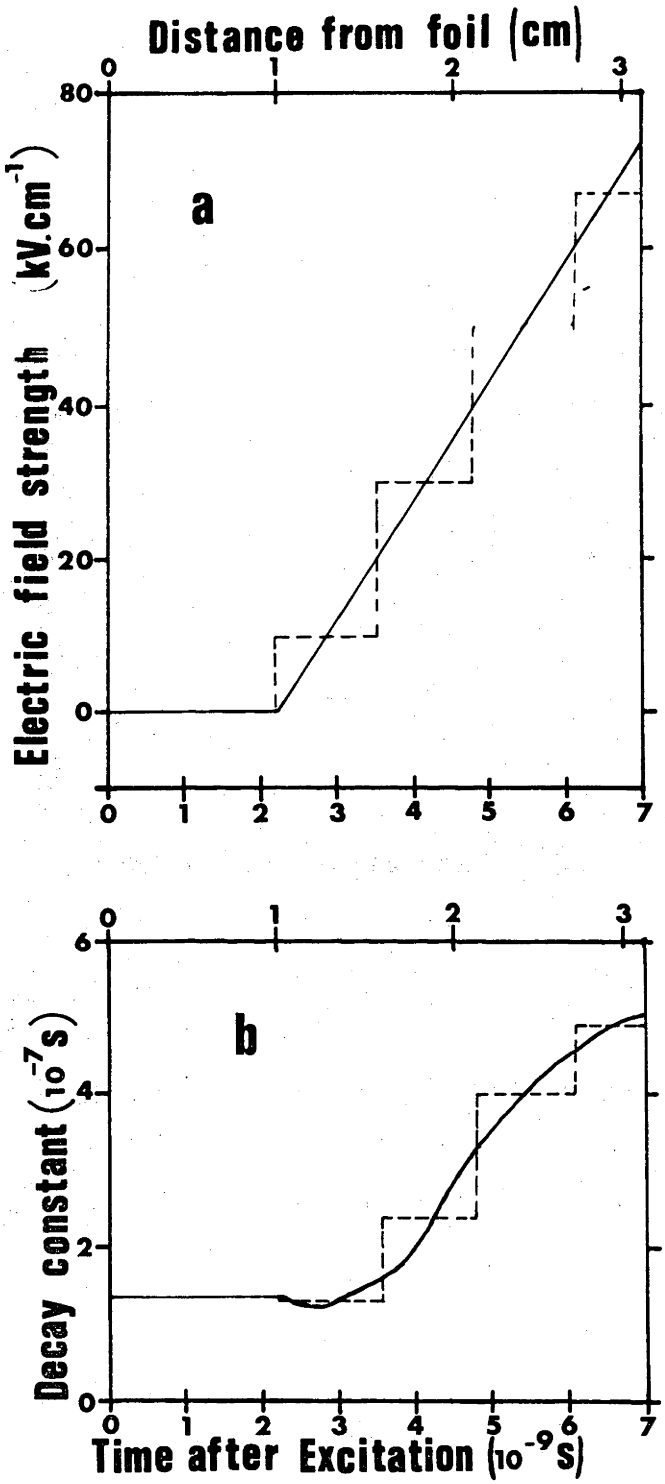

Fig. 6.9: Electric field distribution and perturbed decay constants. The abscissae are the distance from the foil and the corresponding time after excitation.

(a) The approximate electric field distributions along the beam axis.

(b) The corresponding perturbed lifetimes of the $4^1F_3{}^1$ state as a function of time after excitation — both approximations were used to evaluate the integral in eqn (6.7).

populations of the $4^1F_3^{\pm 2,\pm 1,0}$ states and the $4^1D_2^{\pm 2,\pm 1,0}$ states. The only transitions allowed in the electric field from the $4^1F_3^{\pm 3}$ states are to the $3^1D_2^{\pm 2}$ states; these would be at 18697 Å, well out of the range of our equipment. To rotate the z-axis from the electric field direction to the beam direction, all state populations need to be known, and therefore only the 4^1D population distribution can be expressed relative to the beam axis. Furthermore, as the $4^1F_3^{\pm 1} \rightarrow 2^1P_1^{0}$ transitions were not resolved from the $4^1F_3^{0} \rightarrow 2^1P_1^{\pm 1}$ transitions, only estimates of the sum of the $4^1F_3^{\pm 1}$ and $4^1F_3^{0}$ populations can be obtained. This was done using an average value of the transition probability for the two decay channels.

Table 6.3 contains the decay factors, Stark perturbed transition probabilities (from Appendix C) and the measured relative intensities of the 4^1D and $4^1F \rightarrow 2^1P$ Stark components taken from table 4.6. The errors assigned to the relative intensities are based on the variations in intensity determined from the electric field uncertainty. The relative initial populations derived from eqn (6.7) are also presented. The excited states are shown and the z-axis is perpendicular to the beam. An estimate of the sum of the $4^1F_3^{\pm 1}$ and $4^1F_3^{0}$ initial populations is given. If the 4^1F and 4^1D terms were populated statistically, the ratio of their populations would be 7:5, hence for convenience the initial populations of these terms are expressed with the total 4^1D population normalized to 5. A statistical population would then give each state an initial population of 1.0.

The initial population distributions shown in table 6.3 indicate a clear underpopulation of the $4^1F_3^{0,\pm 1,\pm 2}$ states compared to the $4^1D_2^{0,\pm 1,\pm 2}$ states. There is significant alignment in the 4^1D term and the 4^1F terms at 250 keV, but possibly only in the 4^1F term at 410 keV.

At 250 keV the alignment in the 4^1D term results from an underpopulation of the $4^1D_2^{|1|}$ states and an overpopulation of the $4^1D_2^{0}$ state, compared to a statistical population distribution. If the z-axis is rotated to the beam direction the alignment results from a significant underpopulation of the $4^1D_2^{|1|}$ states.

The alignment in the 4^1F term results from an overpopulation of the $4^1F_3^{|2|}$ states compared to the sum of the $4^1F_3^{|1|}$ and $4^1F_3^{0}$ populations.

TABLE 6.3: Relative initial populations for 4^1D and 4^1F excited states.

Excited State	I	A	D_2	D_F	Initial Excited State Populations	W
			410 keV Beam Energy			
$4^1F_3{}^2$	162 ± 10	0.09	0.97	0.92 ± 0.02	0.41 ± 0.02	2
$4^1F_3{}^1$	24 ± 12	0.01*	0.97	0.92 ± 0.02	0.60 ± 0.20	2
$4^1F_3{}^0$						1
$4^1D_2{}^2$	477 ± 10	0.12	0.94	0.89 ± 0.02	0.98 ± 0.04	2
$4^1D_2{}^1$	258 ± 20	0.06	0.94	0.84 ± 0.02	1.07 ± 0.13	2
$4^1D_2{}^0$	74 ± 30	0.02	0.94	0.84 ± 0.02	0.89 ± 0.34	1
			250 keV Beam Energy			
$4^1F_3{}^2$	182 ± 10	0.09	0.97	0.88 ± 0.02	0.43 ± 0.01	2
$4^1F_3{}^1$	3 ± 16	0.01*	0.97	0.86 ± 0.02	0.10 ± 0.40	2
$4^1F_3{}^0$						1
$4^1D_2{}^2$	501 ± 10	0.11	0.94	0.87 ± 0.02	1.00 ± 0.03	2
$4^1D_2{}^1$	174 ± 40	0.06	0.94	0.73 ± 0.04	0.57 ± 0.03	2
$4^1D_2{}^0$	141 ± 50	0.02	0.94	0.73 ± 0.04	1.87 ± 0.70	1

Key: I relative intensity of σ polarized transition from excited state to 2^1P_1.

A relative transition probability for the electric field at point of observation.

D_2 decay factor for zero field region, from table 6.2.

D_F decay factor for electric field region, from table 6.2.

W weights required to obtain total 4^1D or 4^1F population by including M_J degeneracy.

* average A for transitions $4^1F_3{}^1 \rightarrow 2^1P_1{}^0$ and $4^1F_3{}^0 \rightarrow 2^1P_1{}^1$ which have A = 0.015 and 0.005 respectively.

The initial excited state populations are obtained from I by dividing by A, D_2, and D_F and normalizing the 4^1D total population to 5.

CHAPTER 7

DISCUSSION

The Stark perturbed relative intensities were observed at a short distance from the foil so that their directly related population distribution was different from the initial one excited at the foil. If the Stark mixing was negligible, as in the case of an adiabatic perturbation, and radiative decays were small the population distribution obtained at the point of observation could be taken as an estimate of the initial population distribution. Stark mixing of the populations of He II $n = 4$ states required that initial populations be postulated and Stark patterns calculated to select a plausible one by comparison with the measured patterns. For the He I $n = 4$ singlet states population mixing was negligible and the calculated radiative decay changes to the population distribution at the point of observation were found to be small.

Population distributions obtained in the above manner were presented in Chapters 4 and 6. They are summarized before giving a review of the population distributions for H, He II and He I reported in the literature. Some general features of two models of beam-foil excitation by electron capture are presented. The population distributions obtained from the Stark effect observations are compared with those reported in the literature and also with the general theoretical predictions.

§7.1 SUMMARY OF STARK EFFECT RESULTS

The distribution of the populations among the various states of different orbital angular momentum for principal quantum number $n = 4$ will be indicated by $S:P:D:F = a_1:a_2:a_3:a_4$. Alignment in a state of fixed n and L value will be indicated by $\sigma_1:\sigma_2:\sigma_3$ where the subscripts on the population symbols (σ) refer to the quantum number M of the z component of orbital angular momentum. It is assumed that $\sigma_{+M} = \sigma_{-M}$. A statistical population is therefore $S:P:D:F = 1:3:5:7$ with σ independent of M.

§7.1.1 He II

Summarizing the results of §6.1.5:

$$S:P:D:F \approx 2:14:5:7 .$$

With alignment referred to the beam axis it was found that for the 4^2D term

$$\sigma_0:\sigma_1:\sigma_2 \approx 10:10:8 ,$$

and for the 4^2F term

$$\sigma_0:\sigma_1:\sigma_2:\sigma_3 \approx 10:10:10:4 .$$

The energy dependence of this population distribution, including the alignment, was found to be negligible for the beam energies 400, 680, and 820 keV.

§7.1.2 He I, Triplet Terms

The population distribution obtained from the Stark perturbed relative intensities of the triplet lines, at a beam energy of 350 keV, applies to the region of observation some few centimetres from the foil (§4.3 and §4.3.1). The lifetimes of the levels involved were large compared to the time taken to travel from the foil to the observation region and Stark mixing was negligible so that this distribution was used as an estimate of the initial population distribution.

$$S:D:F \approx 10:5:2 ,$$

and for the 4^3F term the alignment was such that

$$\sigma_0:\sigma_1 = 1:10 .$$

The $4^3P \rightarrow 2^3P$ line was blended with a He II line so the population of the 4^3P term was not obtained. The relative value of σ_2 was too uncertain to warrant its inclusion in the summary (see table 4.5). Stark perturbed decays from the 4^3F $|M| = 3$ states were not observed as they were out of the spectral range of the equipment (§6.2.4). The z direction for the alignment was perpendicular to the beam and parallel to the applied electric field.

§7.1.3 He I, Singlet Terms

The population distribution obtained at 350 keV beam energy was

$$S:D:F \approx 10:4:2$$

and no radiative decay corrections were made (§4.3). The 4^1P term is not included as its lifetime is too short to ensure that the decay of its initial population was negligible (§4.3 and table 4.4).

The alignment measurements for the 4^1F term and the 4^1D term were carried out at 250 and 410 keV (§4.3.2). The alignment results were corrected for radiative decay and were presented in §6.2 and table 6.3. They are summarized here for convenience.

4^1F:

410 keV $\quad \sigma_2/(\sigma_1+\sigma_0) \approx 0.6$

250 keV $\quad \sigma_2/(\sigma_1+\sigma_0) > 0.5$

4^1D:

410 keV $\quad \sigma_0:\sigma_1:\sigma_2 \approx 1:1:1$

250 keV $\quad \sigma_0:\sigma_1:\sigma_2 \approx 20:6:10$.

The alignment is referred to the electric field direction which was perpendicular to the beam. Decays from the $4^1F_3|3|$ states were out of the spectral range of the equipment (§6.2.4). The 4^1D alignment at 250 keV beam energy can be expressed relative to the beam direction by a simple transformation (Appendix A) and is then found to be

$$\sigma_0:\sigma_1:\sigma_2 \approx 10:7:10 .$$

§7.2 REVIEW OF PUBLISHED EXPERIMENTAL WORK

Examination of reports of beam-foil population distributions for hydrogenic ions indicates that lifetime measurements have frequently been used to obtain this information. The dependence of the lifetimes on the orbital angular momentum of the levels involved in transitions from levels of a given n value is exploited. Quantum interference phenomena resulting from the alignment and coherence produced in the beam-foil source have also been used to obtain population distributions. The relative intensities of spectral lines observed just after excitation in the foil have also been used to estimate initial populations when theoretical transition probabilities were available. The information in the literature pertains mainly to hydrogen. The meagre amount of information on the population distributions for the He II and He I $n=4$ states is dealt with first.

§7.2.1 He II and He I, n = 4 States

Jordan *et al.* [Jo 67] have carried out lifetime measurements on the F_α line ($n = 4 \rightarrow n = 3$) of He II and the measured decay was decomposed into the contributions from the 4^2S, 4^2D and 4^2F terms. The observations were started about 2 cm after the foil so that the absence of a contribution from the 4^2P term to the observed decay was ascribed to its short lifetime. The fitted decay curves gave lifetimes in agreement with theory and were extrapolated back to the foil to obtain the initial contributions to the overall intensity. They concluded that states of low orbital angular momentum were preferentially populated for the beam energy range 0.8 to 1.0 MeV.

Anderson *et al.* [An 1972] have published the results of some relative population determinations for He I n = 4 terms excited at a beam energy of 40 keV. They measured the relative intensities of various transitions (neglecting polarization) close to the foil to avoid the effects of de-population by radiative decay. Theoretical transition probabilities were used to obtain estimates of the initial populations. If their results are referred to a statistical population distribution, the singlet terms of low L value are preferentially populated and the n = 4 triplet terms are similarly populated except that the P term may be populated more than its statistical weight would suggest. The triplet terms were populated nearly three times more than the singlet terms of the same L value.

§7.2.2 Population Distributions from Lifetime Measurements

A relative population distribution for the n = 5 terms of He II has been obtained by Jordan *et al.* [Jo 69] from lifetime measurements on the F_β line. The population distribution indicated that states of low L value were preferentially populated. The P term was populated about three times its statistical population while the S term was populated about statistically. The change in population distribution with energy was negligible between 0.65 and 1.00 MeV.

Dotchin *et al.* [Do 70] have obtained the relative populations of the He II 3^2S and 3^2D terms from lifetime measurements which indicated that the 3^2S term was six times more populated than the 3^2D term referred to a statistical population distribution.

Goodman and Donahue [Go 66a] concluded from their lifetime measurements on the H_α and H_β lines of hydrogen at 157 keV that low L value terms are preferentially populated compared to a statistical population distribution. Schumann *et al.* [Sc 71] arrived at the same qualitative conclusion from lifetime measurements at 80 to 300 keV on the H_α, H_β and H_γ hydrogen lines.

§7.2.3 Population Distributions from Quantum Beat Observations

Considering some reported quantum beat measurements it is seen that they provide information on the alignment of beam-foil excited states. The observations are mainly for the hydrogen beam-foil source. The sensitivity of quantum beat measurements to alignment results from the fact that the amplitude of these beats depends on the degree of alignment.

In a series of experiments on hydrogen, Sellin *et al.* [Se 69, Se 70a] have investigated quantum interference effects between the decay channels from weak field Stark perturbed fine-structure levels. By using a model similar to the one presented in Chapter 5, and postulating initial population distributions, this group have been able to match their observed quantum beat patterns. The population distribution obtained was consistent with alighment such that $M = 0$ states, referred to the beam direction, were overpopulated compared with an isotropic population distribution. For the $n = 5$ states of hydrogen the high L value states were underpopulated compared with a statistical population distribution. Further work by this group [Se 70b] led them to the conclusion that anisotropies between states of different $|M|$ value did not exceed 10%.

Quantum beat observations have been carried out on the Ly_α hydrogen line in weak electric fields and 200 keV beam energy by Andrä [An 70a]. These led him to conclude that the ratio of the cross section for excitation to the 2^2P term compared with that to the 2^2S term was $\geqslant 4 \pm 1$. This ratio apparently increased with beam energy.

Andrä [An 70b] concluded from measurements of zero field quantum beats for the H_α and H_β lines of hydrogen excited at 133 keV beam energy that aligned excited states were produced in the beam-foil source. From this data he was able to infer that $\sigma_2/(\sigma_0 + \sigma_1) > 1$ for the 3^2D term and that $\sigma_1/\sigma_0 > 1$ for the 3^2P term and that $\sigma_2/(\sigma_0 + \sigma_1) < 1$ for the 4^2D term.

The energy dependence of the $|M|$ state populations of the 3^2P term of hydrogen excited in the beam-foil source has been obtained by Lynch *et al.* [Ly 71]. They found for this term that σ_1/σ_0 varied from 1.4 to 2.3 as the beam energy varied from 230 to 500 keV.

Dobberstein *et al.* [Do 72] have observed alignment in the 2^2P term of hydrogen excited in the beam-foil source at beam energies from 50 to 270 keV. They find that at all energies $\sigma_1 > \sigma_0$.

Intensity fluctuations in the emission of weak field Stark perturbed Ly_β radiation as a function of distance have been observed by Alguard and Drake [Al 73]. They deduce that the 3^2S term of hydrogen was overpopulated by more than a factor of four compared with a statistical population distribution for beam energies between 250 and 500 keV. Similar results were also obtained for the Ly_α line in contrast to other reports at lower energies. These authors note that difficulties may arise from fringing fields if static electric fields are used instead of motional electric fields produced by static magnetic fields encompassing the foil.

Turning now to He I beam-foil excited states, very few population distributions have been published. Andrä [An 70b] deduced from his observations of zero field quantum beats in the $3^3P \rightarrow 2^3P$ line at 475 keV that the alignment referred to the beam axis was such that $\sigma_1/\sigma_0 \approx 0.8$. Yellin *et al.* [Ye 73] have deduced that alignment existed in the 5^1D_2 He I term at 40 keV. This group exploited the Hanle effect and their results suggest that $\sigma_0 > \sigma_1$.

§7.2.4 Summary

Some general features of the population distributions reported in the literature emerge from this brief review. The distributions of the populations for a fixed n value depend on the orbital angular momentum in a way that indicates cross-sections for excitation are larger for the smaller L value states. This dependence on L is not consistent for the S and P states, in that, for some ions and beam energies the S states are overpopulated while for other conditions the P states are overpopulated, compared with a statistical population distribution. Alignment, referred to the beam axis, often shows up as a preferential population of the $M = 0$ states compared with other M value states, but exceptions are reported.

§7.3 SOME THEORETICAL CONSIDERATIONS

Two different electron capture processes provide some general theoretical features of the dependence of cross-sections on the orbital angular momentum and its z component.

It will be recalled from the brief discussion of §1.2 that McLelland [Mc 68] has proposed a model of electron capture into hydrogen levels with $n > 1$ that is applicable to fast protons passing through solids of low free-electron density. The fast protons produce a shower of electrons some of which have velocities near that of the protons. Capture of the electrons of low relative velocity via an interaction with the solid (approximated by a square-well potential) produces excited states with cross-sections of the correct order of magnitude [Be 72].

Although we are interested in the case of $n = 4$, for which the model is not strictly applicable, it was noticed that in the derivation of the total capture probability to all the levels of the same n value the dependence on M was readily extracted from the sum over L and M.

The probability of capture into a state $|nLM\rangle$ was given as $|F_{nLM}|^2$

$$F_{nLM}(\underline{P}) = \int \phi_{nLM}\, e^{i\underline{P}\cdot\underline{r}}\, d\underline{r}\,, \qquad (7.1)$$

where ϕ_{nLM} is the hydrogen atom wave function and $\underline{P}$ is a measure of the momentum transferred between initial and final states. If one assumes that all quantum numbers but M are constant then from eqn (7.1) the factor $\int e^{iM\phi}\, d\phi$ is obtained from the hydrogen wave function. On this simple basis the cross-sections for capture into states of the same n and L but varying M are proportional to the inverse square of M with the beam direction chosen as the z-axis.

Garcia [Ga 73] has used some estimates of the possible L dependence of the capture cross sections using a different model from McLelland's. The Born approximation was used to obtain the cross-sections for capture into states of the same n value but different L values by a point charge from the 1^2S states of hydrogen. He found for the $n = 4$ level of hydrogen that at 250 keV·amu^{-1} the populations of the orbital angular momentum states would be $S > P > D$ but at 25 keV·amu^{-1} $P > S > D$. Garcia notes that, although this model is rather artificial, the same general features occur for capture from atoms other than hydrogen in the ground state.

Hadeishi [Ha 73] points out that Van den Bos [Bo 67a] predicted alignment resulting from proton-hydrogen charge capture collisions. This is the same charge capture process as that treated by Garcia. The alignment is such that states of lower $|M|$ value are preferentially populated with the z-axis parallel to the beam direction. This is the same sense as the alignment obtained from McLelland's model.

§7.4 DISCUSSION OF CONCLUSIONS

The comparison of the experimentally obtained population distributions for the He II and He I $n = 4$ states summarized in §7.1 with the distributions reported in the work reviewed in §7.2 must of necessity be brief. Only the general features of the reported distributions can be compared with the results obtained by the Stark effect measurements because the literature does not contain results for the specific levels of interest at comparable beam energies to those used in this study. The general features of two theoretical approaches to the beam-foil excitation process (§7.3) can be compared with the measured population distributions.

The He II population distribution for the $n = 4$ states obtained from the F_α Stark patterns shows, in agreement with the general features found in §7.2, that the terms 4^2S and 4^2P are more populated than the 4^2D and 4^2F terms. In this case the 4^2P term is more populated than the 4^2S term compared to a statistical population distribution. Garcia's bound-electron capture model used the example of H^+ ion incident on a hydrogen atom. This showed that the 4^2P term of hydrogen formed by the capture process is preferentially populated compared to the 4^2S term at much lower beam energies than those for which the F_α Stark measurements were done. It would be interesting to know if this behaviour would be predicted at higher beam energies for capture of an electron from carbon atoms by He^{++} ions.

The alignment found to be consistent with the observed F_α Stark patterns (§7.1) has the same M dependence as suggested by McLelland's and Garcia's models of charge capture (§7.3). The sense of this alignment is similar to that deduced by Sellin *et al.* for hydrogen $n = 5$ terms although they obtained a smaller magnitude for the alignment. The alignment for the 4^2D He II term obtained from the Stark patterns gives $\sigma_2/(\sigma_0 + \sigma_1) < \frac{1}{2}$

which is in qualitative agreement with Andrä's quantum beat results for the 4^2D hydrogen term for which $\sigma_2/(\sigma_0+\sigma_1) < 1$.

The He I population distributions for the n = 4 singlet and triplet terms obtained from their corresponding Stark patterns showed that S and P terms were preferentially populated. This is in good qualitative agreement with the results of Anderson *et al.* for He I n = 4 terms obtained at the much lower beam energy of 40 keV.

The alignment of the 4^3F and 4^1F terms could be expressed only relative to a z-axis perpendicular to the beam direction because the population of the $|M| = 3$ states could not be obtained from these Stark effect measurements (§6.2.4). These results will not be discussed further although significant alignment was obtained for these terms.

The alignment measured for the 4^1D_2 He I term at 250 keV beam energy from its corresponding Stark perturbed decay indicated that the $|M| = 1$ states were underpopulated compared to an isotropic population distribution. The z-axis in this case is parallel to the beam axis. The $M = 0$ and $|M| = 2$ states were found to have populations in agreement with an isotropic distribution at 250 keV beam energy. There was no significant alignment in the 4^1D_2 term at 410 keV beam energy. The alignment at 250 keV is not in disagreement with Andrä's result for the 3^3P He I term. The 4^1D_2 alignment is unexpected from the M dependence of cross-section obtained from McLelland's and Garcia's models, in particular the $|M| = 2$ states are not underpopulated compared with the $|M| = 1$ states.

The alignment results for He II and He I differ in the dependence of populations on the $|M|$ value of the various states. It may be recalled (§6.4) that the He II F_α Stark pattern is sensitive to alignment through the intensity of its central component. The central component intensity is strongly influenced by the high L and M value states so that small alignment in the small L value terms will not show up readily in the Stark patterns.

§7.5 CRITIQUE OF THE STARK EFFECT EXPERIMENTS

This work was started with the aim of investigating some effects observed by Bashkin and Carriveau when, in an exploratory experiment, they applied strong electric fields to hydrogen and helium excited in a beam-foil source (§1.5).

In order to pursue this aim it was required to improve the experimental procedure and equipment. To obtain adequate resolution of the Stark patterns an investigation of line broadening due to the Doppler effect associated with high beam velocities and large aperture optics has been carried out. A method of linewidth reduction suitable for these experiments was found. It provided good spatial resolution ($\approx$ 0.1 mm) with optimum transfer of light from that beam region. The method reduced the beam-foil linewidths to the limit where the Doppler broadening from the multiply scattered beam and monochromator instrumental broadening dominated the linewidth.

To improve the reproducibility of spectra, monitoring procedures were instituted. It was found that monitoring the source efficiency by beam current measurement was not adequate and could be misleading. Monitoring the light from a spectral line proved to be most satisfactory. The use of the current monitor and the light monitor in conjunction provided sufficient information to account for source fluctuations whether these arose from beam current or foil changes and provided a useful data quality criterion.

Data was collected in digital form and normalization procedures worked out. This provided the capability to make easy use of the monitor information particularly during the course of data collection.

The electric fields required to achieve adequate Stark splitting necessitated the use of one positive and one negative electrode. An earthed electrode was required to protect the foils from the electric field and provide a region of zero field for the light monitor to view. All electrodes required apertures for beam passage or light collection. The resultant complicated electric field distributions and uncertain fringing fields added difficulties and uncertainties to the calculation of the population changes due to Stark mixing and radiative decay.

The model developed for the calculation of the Stark mixing and radiative decays of the populations as the excited ions travel from the foil to the region of observation was an idealization of the actual situation. Nevertheless it was still quite complex. The Stark population mixing calculations for $n = 4$ states were fairly simple because the adiabatic approximation was appropriate to all coupled states except the ones that were degenerate, as was the case for some He II states. For other excited states of He I and He II and other excited ions the

Stark mixing calculations could become very difficult. The lack of detailed knowledge of the magnitudes of the weak fringing electric fields and hence the uncertainty in the perturbed decay constants gave rise to the greatest source of uncertainty in the use of the model to obtain population distributions at the foil.

Insufficient published data exists for a detailed comparison with the results of this work to be made. General features of the orbital angular momentum (L) dependence of the measured population distributions for He I and He II $n = 4$ states are in agreement with those found in the literature. The L dependence of the population distributions is qualitatively the same as those calculated by Garcia [Ga 73] for the capture of bound-electrons to produce excited ions. The alignment obtained from the He II F_α Stark patterns was in agreement with the predictions of McLelland's free-electron capture model and Garcia's bound-electron capture model, but the alignment measured for the He I 4^1D term was not. Some alignment measurements from this work and some from the literature conflict with the general predictions of the two theoretical models.

APPENDIX A

ROTATION MATRICES

Rotations of the frame of reference were required, Chapters 5 and 6, as the populations were referred to a z-axis parallel to the electric field at the point of observation. This could be different from the z-axis chosen parallel to the beam for the initial populations at the foil.

The rotations required were always through $\pi/2$ about the y-axis because of the electric field, ion beam orientations (§2.4) used for the Stark effect observations.

For rotation about the y-axis through an angle β, the matrix elements required are the $D^{(J)}_{M,M'}(\beta)$ defined by Edmonds [Ed 57, Chap. 4). The required rotations were carried out on the density matrix immediately before the ions left the foil. At this point the basis states were

$$|nLMSM_S\rangle$$

which are expressible in the composite form

$$|nLM\rangle|SM_S\rangle \ ,$$

where $S = \frac{1}{2}$ and $M_S = \pm\frac{1}{2}$ for He II states, and $S = 0$ and $M_S = 0$ for He I singlet states.

To find the required matrix elements, the problem was divided into three parts:

(1) The matrix elements that operate on the $|nLM\rangle$ functions were found for $L = 0$, 1, 2 and 3 using Wigner's formula (for $\beta = \pi/2$)

$$D^{(J)}_{M,M'} = (\tfrac{1}{2})^J \sum_t (-1)^t \frac{\sqrt{(J+M)!\ (J-M)!\ (J+M')!\ (J-M')!}}{(J+M-t)!\ (J-M'-t)!\ t!(t-M+M')!}$$

where the summation is over all values of t that give meaningful factorials.

(2) The matrix elements that operate on the $|\frac{1}{2},\pm\frac{1}{2}\rangle$ functions were found from the tables of Edmonds [Ed 57, p.56].

(3) The two sets of matrix elements were then combined to form a composite rotation matrix by replacing each element of the matrix for the $|nLM\rangle$ system by the 2×2 matrix for the $|\frac{1}{2},\pm\frac{1}{2}\rangle$ system multiplied by that element [Go 66, p.211]. The step (1) is sufficient to obtain the rotation matrices for the He I singlet states.

APPENDIX B

STARK EFFECT FOR HYDROGENIC IONS

The problem of calculating the perturbed energy levels of a hydrogenic ion subjected to an external electric field was one of the first perturbation questions solved in quantum mechanics, the validity of which was strengthened by this early success [Ep 16, Sc 16].

The earliest solutions of the perturbation problem were obtained neglecting electron spin. These calculations give rise to a linear Stark effect and may be solved exactly by transforming to parabolic coordinates [Sc 26, Ep 26]. Spin was treated as an extra perturbation for the linear Stark effect in strong fields by Rojansky [Ro 29] and by solving the Dirac equation for the large components by Schlapp [Sc 28]. The latter work considered the problem both for weak electric fields (perturbed energy shifts less than the fine-structure separation) and for strong electric fields (perturbed energy shifts greater than the fine-structure separation). Lüders [Lü 51] gave a complete treatment for field strengths less than those for the onset of field ionization using the Pauli approximation to the hydrogenic wave functions. The method of Lüders is followed here to obtain the unitary transformations that diagonalize the perturbed Hamiltonian. They are the transformations required to transform from the zero electric field Pauli basis set to the basis set that diagonalizes the Hamiltonian with an applied electric field. These calculations neglect the Stark effect of the Lamb shift and hence are suitable only for low Z hydrogenic ions. The most recent work on the Stark effect eigenvalues using the full Dirac equation [Ku 73] indicates that the correction to Lüders' treatment for $Z = 2$ of He^+ is negligible. For details of the procedures used here the work of Lüders should be consulted.

The calculation of transition probabilities is handled by considering spin as an extra perturbation on the strong field Stark levels which are described without spin and using parabolic coordinates. This approach is used because radiative decays of interest for He II

occur in strong field and the tabulated values of oscillator strengths for parabolic coordinates neglecting spin are readily available [Un 59, Mo 64]. An excellent summary of the Stark effect for hydrogen and hydrogenic ions is given by Bethe and Salpeter [Be 57, §51].

B.1 THE EIGENVALUE PROBLEM

The unperturbed Hamiltonian for an electron acted on by the central potential of a Z-times charged nucleus is

$$\underline{H} = \frac{\underline{p}^2}{2m_o} - \frac{Ze^2}{\underline{r}} - \frac{\underline{p}^4}{8m_o^3c^2} - \frac{Ze^2}{2m_o^2c^2\underline{r}^3}(\underline{L}\cdot\underline{S}) , \tag{B.1}$$

where interactions with the radiation field are neglected. Eqn (B.1) gives rise to the familiar fine-structure energy eigenvalues,

$$E = -\frac{e^2}{2a}\left(\frac{Z}{n}\right)^2 - \alpha^2\frac{e^2}{2a}\left(\frac{Z}{n}\right)^4\left(\frac{n}{J+\frac{1}{2}} - \frac{3}{4}\right) , \tag{B.2}$$

where $a = \hbar^2/m_o e^2$ is the first Bohr radius, n the principal quantum number, J the total angular momentum quantum number and α the Sommerfeld fine-structure constant. The Stark effect arises from a perturbation of the above system by an electric field $\underline{F}$ in the positive $\underline{z}$ direction acting on the electron (charge $|e|$, mass m_o), that is,

$$H' = -e\underline{z}\cdot\underline{F} . \tag{B.3}$$

The cylindrical symmetry about the z-axis of this perturbation indicates that the degeneracy of $\pm M_J$ will not be removed by the electric field [Me 61]. The Hamiltonian with the applied electric field is then

$$H+H' = \frac{\underline{p}^2}{2m_o} - \frac{Ze^2}{\underline{r}} - \frac{\underline{p}^4}{8m_o^3c^2} - \frac{Ze^2}{2m_o^2c^2\underline{r}^3}(\underline{L}\cdot\underline{S}) - e\underline{z}\cdot\underline{F} . \tag{B.4}$$

The diagonal matrix elements of H are non-zero, having the values given by eqn (B.2). Using the Pauli eigenfunctions defined by Bethe [Be 57, p.62] with the phase change made by Luders the matrix elements of H' are

$$\langle n,J,L,M_J|H'|n,J+1,L+1,M_J\rangle = \frac{3}{4}\frac{n}{Z}\,eaF\,\frac{\sqrt{(J+1)^2 - M_J^2}\sqrt{n^2 - (L+1)^2}}{(j+1)} \tag{B.5a}$$

$$\langle n,J,L,M_J|H'|n,J,L+1,M_J\rangle = -\frac{3}{4}\frac{n}{Z}\,eaF\,M_J\,\frac{\sqrt{n^2 - (L+1)^2}}{J(J+1)} \tag{B.5b}$$

with

$$L = J - \tfrac{1}{2} . \tag{B.5c}$$

Eqn (B.5b) has been corrected for a misprint in Lüders' paper. The selection rules for the perturbation are seen from eqn (B.5a) and

eqn (B.5c) to be $\Delta L = \pm 1$ and $\Delta M_J = 0$. The L selection rule only applies to vanishing electric fields. The quadratic Stark effect between levels of different principal quantum number is neglected.

Using the ordering by M_J value of the Pauli basis set and the energy and Z scaling of Lüders leads to the perturbation matrix for $n = 4$ shown below. The blocking by M_J value has been used to separate this into perturbation matrices for $M_J = 1/2,\ 3/2,\ 5/2$; the $M_J = 7/2$ level being unperturbed in this approximation. The scaling of the field strength, $F' = .007304\ Z^{-5}\ F$, was obtained from Lüders' paper.

$M_J = 5/2$

$$\begin{pmatrix} 0 & 0 & 6\sqrt{\frac{6}{7}}\,F' \\ 0 & -\frac{1}{768} & -\frac{6}{\sqrt{7}}\,F' \\ 6\sqrt{\frac{6}{7}}\,F' & -\frac{6}{\sqrt{7}}\,F' & -\frac{1}{768} \end{pmatrix} \begin{matrix} 4^2F^{5/2}_{7/2} \\ 4^2F^{5/2}_{5/2} \\ 4^2D^{5/2}_{5/2} \end{matrix}$$

$M_J = 3/2$

$$\begin{pmatrix} 0 & 0 & 6\sqrt{\frac{10}{7}}\,F' & 0 & 0 \\ 0 & -\frac{1}{768} & -\frac{18}{5\sqrt{7}}\,F' & \frac{12\sqrt{7}}{5}\,F' & 0 \\ 6\sqrt{\frac{10}{7}}\,F' & -\frac{18}{5\sqrt{7}}\,F' & -\frac{1}{768} & 0 & \frac{24\sqrt{3}}{5}\,F' \\ 0 & \frac{12\sqrt{3}}{5}\,F' & 0 & -\frac{1}{256} & -\frac{12\sqrt{3}}{5}\,F' \\ 0 & 0 & \frac{24\sqrt{3}}{5}\,F' & -\frac{12\sqrt{3}}{5}\,F' & -\frac{1}{256} \end{pmatrix} \begin{matrix} 4^2F^{3/2}_{7/2} \\ 4^2F^{3/2}_{5/2} \\ 4^2D^{3/2}_{5/2} \\ 4^2D^{3/2}_{3/2} \\ 4^2P^{3/2}_{3/2} \end{matrix}$$

$M_J = 1/2$

$$
\begin{pmatrix}
0 & 0 & 12\sqrt{\frac{3}{7}}\,F' & 0 & 0 & 0 & 0 \\
0 & -\frac{1}{768} & -\frac{6}{5\sqrt{7}}\,F' & \frac{6}{5}\sqrt{42}\,F' & 0 & 0 & 0 \\
12\sqrt{\frac{3}{7}}\,F' & -\frac{6}{5\sqrt{7}}\,F' & -\frac{1}{768} & 0 & \frac{36}{5}\sqrt{2}\,F' & 0 & 0 \\
0 & \frac{6}{5}\sqrt{42}\,F' & 0 & -\frac{1}{256} & -\frac{4}{5}\sqrt{3}\,F' & 4\sqrt{6}\,F' & 0 \\
0 & 0 & \frac{36}{5}\sqrt{2}\,F' & -\frac{4}{5}\sqrt{3}\,F' & -\frac{1}{256} & 0 & 2\sqrt{30}\,F' \\
0 & 0 & 0 & 4\sqrt{6}\,F' & 0 & -\frac{3}{256} & -2\sqrt{15}\,F' \\
0 & 0 & 0 & 0 & 2\sqrt{30}\,F' & -2\sqrt{15}\,F' & -\frac{3}{256}
\end{pmatrix}
\begin{matrix}
4^2F^{1/2}_{7/2} \\
4^2F^{1/2}_{5/2} \\
4^2D^{1/2}_{5/2} \\
4^2D^{1/2}_{3/2} \\
4^2P^{1/2}_{3/2} \\
4^2P^{1/2}_{1/2} \\
4^2S^{1/2}_{1/2}
\end{matrix}
$$

The states comprising the basis set for the unperturbed Hamiltonian are indicated on the right side of each matrix using the spectroscopic notation $nL_J^{M_J}$.

The perturbation matrices were diagonalized using Householder's reduction to tridiagonal form and then a variant of the QR algorithm [Bo 68]. The program for the U1108 computer was obtained from the Australian National University Computer Centre. The resultant eigenvalues ΔE_n for $M_J = 5/2$ are given below for field strengths of 6.4 $kV \cdot cm^{-1}$, 70.4 $kV \cdot cm^{-1}$ and 89.6 $kV \cdot cm^{-1}$. The corresponding unitary transformations $\underline{S}$ are given for each case. The eigenvectors of the perturbed Hamiltonian for 70.4 $kV \cdot cm^{-1}$ and 89.6 $kV \cdot cm^{-1}$ are practically equal, as expected for the strong field linear Stark effect. The transformation matrices $\underline{S}$ were tested for unitarity as a check on the numerical procedure by comparing $\underline{S} \cdot \underline{S}^+$ with the unit matrix. The eigenvalues obtained are in excellent agreement with the values obtained from Kulkani [Ku 73].

The unitary transformations consist of the new eigenvectors which change noticeably between 6.4 $kV \cdot cm^{-1}$ (weak field) and 70.4 $kV \cdot cm^{-1}$ (strong field). The upper limit of the weak field region for the $n = 4$ He II level has been set by Lüders [Lü 51] at 3 $kV \cdot cm^{-1}$ which is the field strength where the Stark splitting is of the same order as the fine-structure splitting.

$$M_J = 5/2 \qquad F = 6.40 \ kV \cdot cm^{-1}$$

$$\Delta E_1 = 0.752584 \ cm^{-1}$$
$$\Delta E_2 = -0.104202 \ cm^{-1}$$
$$\Delta E_3 = -0.891410 \ cm^{-1}$$

$$\underline{S} = \begin{pmatrix} -0.677528 , & 0.377282 , & -0.631359 \\ 0.250394 , & 0.925454 , & 0.284320 \\ -0.691562 , & -0.034546 , & 0.721490 \end{pmatrix}$$

$M_J = 5/2 \quad F = 70.40\ kV \cdot cm^{-1}$

$\Delta E_1 = 8.942495\ cm^{-1}$
$\Delta E_2 = -0.104155\ cm^{-1}$
$\Delta E_3 = -9.081367\ cm^{-1}$

$$\underline{S} = \begin{pmatrix} -0.657804 , & 0.377946 , & -0.651499 \\ 0.264943 , & 0.925815 , & 0.269576 \\ -0.705053 , & -0.004718 , & 0.709139 \end{pmatrix}$$

$M_J = 5/2 \quad F = 89.6\ kV \cdot cm^{-1}$

$\Delta E_1 = 12.219403\ cm^{-1}$
$\Delta E_2 = -0.104155\ cm^{-1}$
$\Delta E_3 = -12.358275\ cm^{-1}$

$$\underline{S} = \begin{pmatrix} -0.656965 , & 0.377952 , & -0.652341 \\ 0.265560 , & 0.925819 , & 0.268957 \\ -0.705603 , & -0.003460 , & 0.708599 \end{pmatrix}$$

B.2 TRANSITION PROBABILITIES IN STRONG FIELD

For the purpose of considering Stark perturbed transition probabilities in a strong field the connection between the Stark effect level scheme neglecting spin and the one including spin is required. The level scheme for the n = 4 to n = 3 transitions including fine-structure is given in Appendix F, fig. F1 and is labelled with the parabolic quantum numbers obtained by neglecting spin. Details of the correspondence are given below.

The energy eigenvalues for parabolic coordinates are

$$E_{nn_1n_2} = -\frac{e^2}{2a}\frac{Z^2}{n^2} - \frac{3}{2} eaF \frac{n}{Z} (n_1 - n_2) , \qquad (B.6)$$

where n is the principal quantum number and n_1 and n_2 are the parabolic quantum numbers. The energy eigenvalue $E_{nn_1n_2}$ is independent of M, the z component of the orgital angular momentum, with z in the direction of $\underline{F}$, and depends on the "electric" quantum number

$$n_f = n_1 - n_2 \qquad (B.7)$$

as well as the principal quantum number n. The quantum numbers n, n_1, n_2, M are related by

$$n = n_1 + n_2 + |M| + 1 . \tag{B.8}$$

For a given n the number M can take the values 0, 1, ..., n-1. For each M the number n_1 runs through the values 0, 1, ..., $n - |M| - 1$. The correlation of the levels neglecting spin and using the parabolic quantum numbers with the levels including spin is made by comparing the level energies and using the relation

$$M_J = M + M_S . \tag{B.9}$$

In strong fields the z components of the orbital and spin angular momenta are uncoupled and separately conserved. The wave function for a particular state in strong field then has the form

$$\left(\sum_{\alpha=LM} a_\alpha \, \psi(n,L,M) \right) \cdot \psi(M_S) , \tag{B.10}$$

but noting that

$$\sum_{\alpha=LM} \psi(n,L,M) \equiv \psi(n,n_1,n_2,M) , \tag{B.11}$$

the transition probabilities of various states including spin are readily derived from the tables of Underhill and Wadell [Un 59] for oscillator strengths, f values, of Stark perturbed transitons neglecting spin.

The selection rules for Stark perturbed radiative transitions are

$$\begin{aligned} \Delta M &= 0 \quad \text{for} \quad \pi \text{ components} \\ \Delta M &= +1 \quad \text{for} \quad \sigma_+ \text{ components} \\ \Delta M &= -1 \quad \text{for} \quad \sigma_- \text{ components} \end{aligned} \tag{B.12}$$

$$\text{and} \quad \Delta M_S = 0 .$$

A quasi-selection rule, that transitions for which n_f changes sign are weak, also applies [Be 57, p.276]. Calculating transition probabilities from oscillator strengths has to be done with care in the case of the Stark effect. The atom is in an electric field which gives a physically significant z direction, so the radiation from aligned states of such an atom is not isotropic. The oscillator strengths in this case are defined in terms of the x, y or z components of the position vector $\underline{r}$ of the electron [Be 57, p.276; So 72, p.321]. Hence when calculating the probability of emission into 4π steradians a weight of 2 has to be given to the f value of a σ_- transition. A similar result holds for σ_+

polarized transitions. On the other hand a π polarized transition only involves the z coordinate in the calculation of the f value and hence has a weight of 1.

When observations of π or σ polarized radiation are made the relative intensities will depend on the solid angle of the detector and the angle of observation relative to the z-axis. The angular distributions for dipole radiation [Co 51, p.91] are such that for observation along the z-axis, with infinitesimal solid angle, σ polarized radiation has twice the intensity it has when viewed along the x-axis. π polarized radiation has zero intensity in the z direction.

Transition probabilities are given in table B.1 for the Stark transitions from $n = 4$ to $n = 3$ of hydrogen in a strong electric field. Scaling by Z^{-4} for lifetimes makes this table applicable to hydrogenic ions. The lifetimes of the states have been calculated from this table and similar ones for the transitions $n = 4$ to $n = 2$, and $n = 4$ to $n = 1$. The column labelled displacements gives the wavelength displacement from the zero field wavelength of the component in terms of $X_{nn'}$, where

$$X_{nn'} = n \cdot n_f - n' \cdot n'_f \,, \tag{B.13}$$

and

$$\Delta\lambda_{nn'} = C_{nn'} F \,, \tag{B.14}$$

with

$$C_{nn'} = \frac{3h^7 c}{32\pi^6 m_o{}^3 e^9} \frac{n'^4 n^4}{(n^2 - n'^2)^2} \frac{X_{nn'}}{Z^5} \,. \tag{B.15}$$

The field strength F is in electrostatic units (1 e.s.u. $\equiv$ 0.2298 $kV \cdot cm^{-1}$). The transitions displaced to lower wavelengths are not given as the Stark pattern is symmetric about the zero field wavelength in both displacement and transition probabilities. The Stark components displaced by greater than $X_{nn'} = 7$ are not given as their transition probabilities are less than that for $X_{nn'} = 7$, as expected from the quasi-selection rule on n_f. The table was checked against Moody's tables for Stark transitions [Mo 64], making due allowance for the different weight assignments needed here. A further check was made by verifying that the sum of the transition probabilities of the π components was half the sum of the σ component transition probabilities [Ku 69].

TABLE B.1: Transition probabilities and lifetimes.

The values are for hydrogen, scale τ_n by Z^{-4} and $A_{nn'}$ by Z^4 for hydrogenic ions of charge Z.

n,n'	principal quantum numbers	M_J	z component of total angular momentum
n,n_2	parabolic quantum numbers	Displacement	$n \cdot n_f - n' \cdot n_f$, $n_f = n_1 - n_2$
M	z component of orbital angular momentum	$A_{nn'}$	transition probability
M_S	z component of spin angular momentum	τ_n	lifetime

n_1	n_2	M	M_S	M_J	n_1'	n_2'	M'	M_S'	Polarization	Displacement	$A_{nn'} \times 10^8$ sec^{-1}	$\tau_n \times 10^{-8}$ sec
0	0	3	1/2	7/2	0	0	2	1/2	σ_-			
			-1/2	5/2				-1/2	σ_-	0	0.137900	7.251631
		-3	1/2	-5/2			-2	1/2	σ_+			
			-1/2	-7/2				-1/2	σ_+			
1	1	1	1/2	3/2	0	0	2	1/2	σ_+			
			-1/2	1/2				-1/2	σ_+	0	0.010642	2.451040
		-1	1/2	-1/2			-2	1/2	σ_-			
			-1/2	-3/2				-1/2	σ_-			
1	1	1	1/2	3/2	1	1	0	1/2	σ_-			
			-1/2	1/2				-1/2	σ_-	0	0.049344	2.451040
		-1	1/2	-1/2			0	1/2	σ_+			
			-1/2	-3/2				-1/2	σ_+			

TABLE B.1 (cont'd)

n_1	n_2	M	M_S	M_J	n_1'	n_2'	M'	M_S'	Polarization	Displacement	$A_{nn'} \times 10^8$ sec^{-1}	$\tau_n \times 10^{-8}$ sec
0	1	2	1/2	5/2	0	1	1	1/2	σ_-	1	0.080820	4.822903
			-1/2	3/2				-1/2	σ_-			
		-2	1/2	-3/2			-1	1/2	σ_+			
			-1/2	-5/2				-1/2	σ_+			
1	2	0	1/2	1/2	0	1	1	1/2	σ_+	1	0.022454	5.466153
			-1/2	-1/2				-1/2	σ_+			
			1/2	1/2			-1	1/2	σ_-			
			-1/2	-1/2				-1/2	σ_-			
0	2	1	1/2	3/2	0	2	0	1/2	σ_-	2	0.035308	2.439640
			-1/2	1/2				-1/2	σ_-			
		-1	1/2	-1/2			0	1/2	σ_+			
			-1/2	-3/2				-1/2	σ_+			
2	1	0	1/2	1/2	2	0	0	1/2	π	2	0.010344	5.466153
			-1/2	-1/2				-1/2	π			
1	1	1	1/2	3/2	1	0	1	1/2	π	3	0.017988	2.451040
			-1/2	1/2				-1/2	π			
		-1	1/2	-1/2			-1	1/2	π			
			-1/2	-3/2				-1/2	π			

TABLE B.1 (cont'd)

n_1	n_2	M	M_S	M_J	n_1'	n_2'	M'	M_S'	Polarization	Displacement	$A_{nn'} \times 10^8$ sec^{-1}	$\tau_n \times 10^{-8}$ sec
0	1	2	1/2	5/2	0	0	2	1/2	π			
			-1/2	3/2				-1/2	π	4	0.022990	4.822903
		-2	1/2	-3/2			-2	1/2	π			
			-1/2	-5/2				-1/2	π			
1	2	0	1/2	1/2	1	1	0	1/2	π	4	0.030058	5.466153
			-1/2	-1/2				-1/2	π			
0	2	1	1/2	3/2	0	1	1	1/2	π			
			-1/2	1/2				-1/2	π	5	0.036902	2.439643
		-1	1/2	-1/2			-1	1/2	π			
			-1/2	-3/2				-1/2	π			
0	3	0	1/2	1/2	0	2	0	1/2	π	6	0.043496	2.207457
			-1/2	-1/2				-1/2	π			
1	1	1	1/2	3/2	2	0	0	1/2	σ_-			
			-1/2	1/2				-1/2	σ_-	6	0.000228	2.451040
		-1	1/2	-1/2			0	-1/2	σ_+			
			-1/2	-3/2				+1/2	σ_+			
0	1	2	1/2	5/2	1	0	1	1/2	σ_-			
			-1/2	3/2				-1/2	σ_-	7	0.000356	4.822903
		-2	1/2	-3/2			-1	1/2	σ_+			
			-1/2	-5/2				-1/2	σ_+			

APPENDIX C

STARK EFFECT ON He I

The Stark effect perturbation problem was first solved for He I by Foster [Fo 28]. The terms of principal quantum numbers n = 4,5 were treated neglecting spin and using hydrogenic wave functions to calculate the matrix elements of the Stark perturbation. This work gives an excellent illustration of the perturbation theory. The agreement between the calculated and observed energy level displacement for electric fields up to 100 $kV \cdot cm^{-1}$ is satisfactory [Fo 28]. More recent calculations with more accurate term values, have been made by Pfennig and Trefftz [Pf 66] extending to higher terms. Their results for n = 4 and 5 are not appreciably different from Foster's results. In the present work the singlet and triplet lines of interest arise from the terms of principal quantum number n = 4, and the method of calculation, including spin, which Condon and Shortley ascribe to Foster [Co 51, p.414] has been followed. A review of the Stark effect for He I has been given by Bethe and Salpeter [Be 57, §56].

C.1 EIGENVALUE PROBLEM

The electric field perturbation is expressed as

$$H' = -\underline{F} \cdot \underline{D} = e\underline{F} \cdot \sum_i \underline{r}_i \,, \qquad (C.1)$$

where $\underline{F}$ is the electric field strength, $\underline{D}$ the dipole moment of the helium atom and $\underline{r}_i$ the position vector of the ith electron. As $\underline{D}$ is the dipole moment of the atom the same selection rules hold for the Stark perturbation as for radiative dipole transitions; that is, only states of opposite parity are coupled. The electric field $\underline{F}$ defines a z-axis for the problem so that the selection rule $\Delta M_J = 0$ holds for the Stark perturbation. States of opposite parity have different orbital angular momentum L and are therefore not degenerate so that there is no first-order Stark perturbation for He I states. The correction to the energy of a perturbed state is, to second-order,

$$\Delta E_{\alpha JM_J} = F^2 \sum_{\alpha' J'} \frac{|\langle \alpha JM_J | D_z | \alpha' J' M_J \rangle|^2}{E_{\alpha J} - E_{\alpha' J'}} \qquad (C.2)$$

providing the perturbation is small compared to the energy separation $E_{\alpha J} - E_{\alpha' J'}$ between the coupled states. The denominator of eqn (C.2) dominates the perturbation and results in the repulsion of coupled states. Rather than use the second-order perturbation expansion of eqn (C.2) the secular problem is treated for the case of the terms of principal quantum number $n = 4$. The observed energy levels of the unperturbed system are taken from Martin [Ma 60] and used with the matrix elements of the perturbation determined from hydrogenic wave functions for the radial part of the integrals after extracting the M and J dependence. The perturbation terms $H_{\alpha JM_J, \alpha' J' M_J}$ are given by integrals of the form

$$H_{\alpha JM_J, \alpha' J' M_J} = eF \langle \alpha JM_J | z_1 + z_2 | \alpha' J' M_J \rangle , \qquad (C.3)$$

where the states αJM_J and $\alpha' J' M_J$ are restricted to the same principal quantum number. Since the perturbing potential is symmetric with respect to the interchange of the electrons, $H_{\alpha JM_J, \alpha' J' M_J}$ vanishes if the states αJM_J and $\alpha' J' M_J$ belong to different singlet or triplet term systems. The selection rule for M_J results in the secular determinants for a given principal quantum number reducing to lower order determinants, one for each M_J value. The coupling of terms of different principal quantum number is neglected as the large denominator in eqn (C.2) ensures a negligible contribution from them. In this approximation the states of highest absolute M_J value are not perturbed.

M_J is the sum of the z components of the orbital angular momentum and the z component of the spin angular momentum, so the Wigner-Eckhart theorem may be used to extract the M_J-dependence of the matrix elements $H_{\alpha JM_J, \alpha' J' M_J}$. Furthermore, the J dependence of the matrix elements may also be extracted since the dipole operator does not act on the spin quantum number and $\underline{L} \cdot \underline{S}$ coupling holds for He I. The procedure for doing this is outlined in Condon and Shortley [Co 51, p.414]. The reduced matrix elements become

$$eF(nLS \| z_1 + z_2 \| nL'S) . \qquad (C.4)$$

These were evaluated using hydrogenic wave functions for singly excited states. As the penetration of the "hydrogenic" electron decreases for larger radial vector and higher orbital angular momentum, states of

higher n and L quantum numbers give a better approximation to this model [De 71]. The explicit reduced matrix elements of eqn (C.4) are

$$H_{n,L,n,L-1} = KF\, n \sqrt{\frac{n^2 - L^2}{4L^2 - 1}} \,. \qquad (C.5)$$

For K = 6.460 and F in $kV \cdot cm^{-1}$, the eigenvalues determined from diagonalization of the determinants are in units of cm^{-1}. These determinants of principal quantum number n = 4 and M = 2 are given below. The Stark perturbation does not remove the degeneracy with respect to the sign of M_J, hence the determinants are the same for $+M_J$ and $-M_J$.

Secular determinant for M = 2 triplet states of principal quantum number n = 4.

227.443	3.578 × KF	5.060 × KF	0.0	0.0	0.0
3.578 × KF	0.0	0.0	2.231 × KF	3.771 × KF	0.0
5.060 × KF	0.0	0.0	-0.225 × KF	1.333 × KF	4.536 × KF
0.0	2.231 × KF	-0.225 × KF	-7.217 × KF	0.0	0.0
0.0	3.771 × KF	1.333 × KF	0.0	-7.217 × KF	0.0
0.0	0.0	4.536 × KF	0.0	0.0	-7.217 × KF

Secular determinant for M = 2 singlet states of principal quantum number n = 4.

0	4.000 × KF
4.000 × KF	-5.521

The 4^1D and 4^3D terms are chosen as the zeros of the energy scales in the above secular determinants. The fine-structure intervals of the triplet terms have been neglected as the approximation of the He I wave functions by hydrogenic wave functions does not warrant their inclusion. A compilation of eigenvalues determined from secular determinants for M = 0,1,2 is given in tables C.1 and C.2 for the terms of principal quantum number n = 4 and electric field strengths from zero to 100 $kV \cdot cm^{-1}$.

Tables C.1 and C.2 were used to calculate wavelength shifts as a function of electric field strength in order to assist in identifying Stark components and to allow calibration of experimentally applied electric fields. The relative positions of Stark lines used for the

extraction of intensities by non-linear least-squares fitting were calculated for much smaller electric field strength intervals after the approximate field strength had been obtained from the tables.

Table C.3 contains the eigenvectors for the 4^1D and 4^1F terms. These were obtained from the eigenvalues for the singlet terms and were needed to calculate the perturbed transition probabilities. The coefficients of the 4^1S, 4^1P, 4^1D or 4^1F states of given M_J value occurring in the perturbed eigenvector are given the labels S, P, D or F.

C.2 TRANSITION PROBABILITIES AND LIFETIMES

In order to be able to calculate the population of states contributing to the Stark components arising from radiative transitions it is necessary to know the transition probabilities as a function of the electric field strength. It is also necessary to know the lifetimes of various Stark perturbed states in order to calculate the changes in populations due to radiative decays as the He I atoms travel from their point of excitation in the foil through the applied electric field to the point of observation. The intensity calculations of Foster [Fo 28] are inadequate because they do not give the perturbed lifetimes as a function of field strength. To obtain the perturbed lifetimes one needs the absolute transition probabilities, as a function of electric field strength, for all decay channels that can occur. The treatment of this problem follows the method of Foster [Fo 28], but uses the modern form given by Sobel'man [So 72, p.321].

In the case of electric dipole transitions between states αJM and $\alpha'J'M'_J$, the general relation for the probability of spontaneous emission into an element of solid angle $d\Omega$ is

$$dW_\rho(\alpha JM_J,\alpha'J'M'_J) = \frac{\omega^3}{2\pi\hbar c^3} |\underline{e}_{\rho\underline{k}} \langle \alpha JM_J|\underline{D}|\alpha'J'M'_J\rangle|^2 \, d\Omega \, , \qquad (C.6)$$

where $\underline{D}$ is the dipole operator, $\underline{e}_{\rho\underline{k}}$ is the unit vector of the polarization of the photon with wave vector $\underline{k}$, and ρ has the values 1 and 2 for the two perpendicular polarization directions. For observations of the Stark effect it is usual to view the emitting atoms along and perpendicular to the electric field. In the first case the vector $\underline{k}$ is directed along the z-axis and the polarization vectors lie in the plane xy. With the two independent directions of polarization chosen along the x- and y-axes eqn (C.6) becomes

TABLE C.1: He I singlet eigenvalues.

	^1S	^1D			^1F			^1P	
M	0	0	1	2	0	1	2	0	1
Field Strength $kV \cdot cm^{-1}$									
0	506.288		0.0			-5.521		-46.258	
10	506.288	2.033	1.794	1.021	-7.094	-6.969	-6.542	-46.778	-46.604
20	506.470	5.857	5.223	3.099	-9.567	-9.368	-8.620	-48.310	-47.633
30	506.772	10.234	9.154	5.468	-11.784	-11.615	-10.989	-50.772	-49.318
40	507.194	14.906	13.356	7.938	-13.613	-13.524	-13.459	-54.038	-51.611
50	507.737	19.767	17.741	10.451	-15.092	-15.082	-15.972	-57.963	-54.438
60	508.401	24.754	22.262	12.987	-16.299	-16.324	-18.508	-62.407	-57.717
70	509.184	29.826	26.887	15.537	-17.310	-17.304	-21.058	-67.251	-61.362
80	510.087	34.952	31.595	18.095	-18.187	-18.074	-23.616	-72.403	-65.300
90	511.110	40.110	36.367	20.659	-18.978	-18.681	-26.180	-77.794	-69.465
100	512.251	45.284	41.193	23.227	-19.715	-19.163	-28.748	-83.372	-73.809

TABLE C.2: He I triplet eigenvalues.

	10 kV·cm^{-1}	20 kV·cm^{-1}	40 kV·cm^{-1}	60 kV·cm^{-1}	80 kV·cm^{-1}	100 kV·cm^{-1}
			M = 0			
	-8.625	-11.523	-18.475	-26.037	-33.994	-42.281
^3F	-8.486	-11.146	-17.565	-24.519	-31.786	-39.303
	-8.486	-11.146	-17.565	-24.518	-31.785	-39.302
	1.190	3.647	9.222	14.775	20.090	25.117
^3D	1.199	3.647	9.223	14.775	20.092	25.119
	1.314	3.930	9.756	15.446	20.788	25.729
	227.501	227.673	228.363	229.510	231.109	233.152
^3P	227.513	227.725	228.568	229.969	231.920	234.410
	227.513	227.725	228.568	229.970	231.921	234.411
^3S	1146.409	1146.518	1146.954	1147.680	1148.695	1149.999
			M = 1			
	-8.641	-11.566	-18.574	-26.198	-34.220	-42.579
^3F	-8.458	-11.071	-17.393	-24.243	-31.400	-38.801
	-8.056	-9.937	-14.615	-19.618	-24.716	-29.853
	.839	2.720	7.398	12.401	17.498	22.636
^3D	1.173	3.582	9.088	14.584	19.854	24.846
	1.329	3.966	9.829	15.546	20.909	25.863
^3P	227.502	227.680	228.390	229.570	231.214	233.315
	227.511	227.715	228.531	229.886	231.772	234.182
^3S	1146.409	1146.518	1146.954	1147.680	1148.695	1149.999
			M = 2			
	-8.4860	-11.1456	-17.565	-24.518	-31.785	-39.303
^3F	-8.0467	-9.9116	-14.556	-19.527	-24.593	-29.699
	-7.2170	-7.2170	-7.217	-7.217	-7.217	-7.217
^3D	.8298	2.6946	7.339	12.310	17.376	22.482
	1.1986	3.6470	9.222	14.775	20.091	25.118
^3P	227.5134	227.7247	228.568	229.969	231.920	234.410

TABLE C.3: He I singlet eigenvectors.

Perturbed 4^1D states.

Field Strength $kV \cdot cm^{-1}$	M = 0				M = 1			M = 2	
	^1S	^1P	^1D	^1F	^1P	^1D	^1F	^1D	^1F
0			1			1		1	
10	-.0010	.0865	.9054	.4155	.0758	.9104	.4068	.9301	.3674
20	-.0034	.1490	.8444	.5146	.1317	.8469	.5153	.8577	.5142
40	-.0112	.2386	.8034	.5454	.2156	.8027	.5560	.7931	.6091
60	-.0214	.2969	.7867	.5406	.2753	.7854	.5544	.7666	.6421
80	-.0329	.3350	.7768	.5323	.3187	.7749	.5459	.7525	.6586
100	-.0451	.3601	.7697	.5252	.3512	.7672	.5368	.7438	.6686

Perturbed 4^1F states.

Field Strength $kV \cdot cm^{-1}$	M = 0				M = 1			M = 2	
	^1S	^1P	^1D	^1F	^1P	^1D	^1F	^1D	^1F
0				1			1		1
10	+.0005	-.0486	-.4128	.9095	-.0412	-.4047	.9135	.3674	.9301
20	-.0028	.1251	.5001	-.8569	.1094	.5042	-.8566	.5142	.8577
40	-.0119	.2667	.4857	-.8324	.2475	.5058	-.8264	.6091	.7931
60	-.0244	.3677	.4277	-.8254	.3611	.4500	-.8168	.6421	.7666
80	-.0380	.4309	.3746	-.8201	.4413	.3884	-.8090	.6586	.7524
100	-.0516	.4694	.3340	-.8258	.4946	.3348	-.8021	.6686	.7438

$$d\underline{W} = d\underline{W}_1 + d\underline{W}_2 \propto \{|\langle \alpha J M_J | D_x | \alpha' J' M_J' \rangle|^2 + |\langle \alpha J M_J | D_y | \alpha' J' M_J' \rangle|^2\}\, d\Omega \qquad (C.7)$$

or

$$d\underline{W} \propto \sum_{q=\pm 1} |\langle \alpha J M_J | D_q | \alpha' J' M_J' \rangle|^2\, d\Omega \,. \qquad (C.8)$$

In the second case $\underline{k}$ is directed along the x-axis and the polarization vectors $e_{\rho \underline{k}}$ lie in the plane yz. Choosing the directions y and z as the two independent directions of polarization gives

$$d\underline{W} = d\underline{W}_1 + d\underline{W}_2 \propto \{|\langle \alpha J M_J | D_z | \alpha' J' M_J' \rangle|^2 + |\langle \alpha J M_J | D_y | \alpha' J' M_J' \rangle|^2\}\, d\Omega \qquad (C.9)$$

or

$$d\underline{W} \propto \{|\langle \alpha J M_J | D_o | \alpha' J' M_J' \rangle|^2 + \frac{1}{2} \sum_{q=\pm 1} |\langle \alpha J M_J | D_q | \alpha' J' M_J' \rangle|^2\}\, d\Omega \,. \qquad (C.10)$$

Eqns (C.8) and (C.10) express the fact that in longitudinal observation only σ components are observed and in transverse observation π and σ components are observed with the σ components having half the intensity they have for longitudinal observation. The geometric factors in these matrix elements are not affected by the perturbation so they can be separated and the effects of the perturbation can be calculated on the reduced matrix elements. For longitudinal observation eqn (C.8) becomes

$$d\underline{W} \propto \left\{ \begin{pmatrix} J,1,J' \\ -M,1,M-1 \end{pmatrix}^2 + \begin{pmatrix} J,\ 1,J' \\ M,-1,-M+1 \end{pmatrix}^2 \right\} |\langle \alpha J \| D \| \alpha' J' \rangle|^2\, d\Omega \qquad (C.11)$$

and for transverse observation eqn (C.10) becomes

$$d\underline{W} \propto \left\{ 2 \begin{pmatrix} J,1,J' \\ -M,0,M \end{pmatrix}^2 + \frac{1}{2} \begin{pmatrix} J,1,J' \\ -M,1,M-1 \end{pmatrix}^2 + \frac{1}{2} \begin{pmatrix} J,\ 1,J' \\ M,-1,-M+1 \end{pmatrix}^2 \right\} |\langle \alpha J \| D \| \alpha' J' \rangle|^2 d\Omega \,. \qquad (C.12)$$

The approximation made in calculating the perturbed transition probabilities was that the lower terms of the transitions had zero field wavefunctions, i.e. that the perturbation was negligible for the lower terms. The perturbed reduced matrix elements then have the simple form

$$(\alpha J \| D \| \alpha' J') = \sum_i |a_i|^2\, (\alpha^{(i)} J^{(i)} \| D \| \alpha' J') \,, \qquad (C.13)$$

where a_i is the coefficient of the ith state occurring in the perturbed wave function $|\alpha, J, F\rangle = \sum_i a_i(F)\, |\alpha^{(i)} J^{(i)}\rangle$ which is determined from the eigenvalue problem. The lower terms of interest in the calculation of the perturbed lifetimes are the n = 1, 2, and 3 terms. These terms generally have larger intervals between states of different L value

than do the n = 4 terms, so the dominant effect on the transition probabilities arises in the n = 4 terms. The zero field approximation for the n = 3 terms is worse than for the n = 1,2 terms but since decays to the n = 3 terms from n = 4 terms have very low zero field transition probabilities their contribution to lifetimes was small. The transitions of interest are the $4^1D \rightarrow 2^1P$ allowed transitions and the $4^1F \rightarrow 2^1P$ forbidden transitions in electric fields up to 100 $kV \cdot cm^{-1}$. The perturbed transition probabilities for these are given in table C.4, based on the perturbed eigenfunctions given in table C.3. The transition probabilities for the zero field allowed transitions have been obtained from the compilations of Wiese [Wi 66].

The perturbed lifetimes for electric fields up to 100 $kV \cdot cm^{-1}$ are given in table C.5. The lifetimes of the 4^1D levels were obtained by calculating tables similar to C.4 for the transitions $4^1D \rightarrow 2^1S$, $4^1D \rightarrow 1^1S$, $4^1D \rightarrow 3^1D$, $4^1D \rightarrow 3^1P$, and performing the required sum over transition probabilities at each field strength. The transitions included for the lifetimes of the 4^1F levels are $4^1F \rightarrow 3^1P$, $4^1F \rightarrow 2^1S$, $4^1F \rightarrow 1^1S$, $4^1F \rightarrow 2^1P$, $4^1F \rightarrow 3^1D$. The decay channels neglected for the lifetime calculations were selected on the basis that the admixture of the upper term of the zero field allowed transitions with the perturbed 4^1D and 4^1F levels was small and that the allowed decay in zero field was weak.

TABLE C.4: He I singlet transition probabilities.

$4^1D \rightarrow 2^1P$

Field Strength $kV \cdot cm^{-1}$	$\|M\| \rightarrow \|M'\|$	$(3_j)^2$	$\|a_i\|^2$	$A_{ki} \times 10^8$	$\|M\| \rightarrow \|M'\|$	$(3_j)^2$	$\|a_i\|^2$	$A_{ki} \times 10^8$
	π components				σ components			
					2 → 1	1/5	.8650	.1747
10	1 → 1	1/10	.8288	.0837	1 → 0	1/10	.8288	.0837
	0 → 0	2/15	.8198	.1104	0 → 1	1/30	.8198	.0276
					2 → 1	1/5	.7356	.1486
20	1 → 1	1/10	.7172	.0725	1 → 0	1/10	.7172	.0725
	0 → 0	2/15	.7130	.0960	0 → 1	1/30	.7130	.0240
					2 → 1	1/5	.6290	.1271
40	1 → 1	1/10	.6444	.0651	1 → 0	1/10	.6444	.0651
	0 → 0	2/15	.6455	.0869	0 → 1	1/30	.6455	.0218
					2 → 1	1/5	.5876	.1187
60	1 → 1	1/10	.6169	.0623	1 → 0	1/10	.6169	.0623
	0 → 0	2/15	.6189	.0834	0 → 1	1/30	.6192	.0209
					2 → 1	1/5	.5662	.1144
80	1 → 1	1/10	.6004	.0607	1 → 0	1/10	.6004	.0607
	0 → 0	2/15	.6034	.0813	0 → 1	1/30	.6034	.0203
					2 → 1	1/5	.5533	.1118
100	1 → 1	1/10	.5886	.0595	1 → 0	1/10	.5886	.0595
	0 → 0	2/15	.5924	.0798	0 → 1	1/30	.5924	.0200

TABLE C.4 (cont'd)

$4^1F \rightarrow 2^1P$

Field Strength $kV \cdot cm^{-1}$	$\|M\| \rightarrow \|M'\|$	$(3_j)^2$	$\|a_i\|^2$	$A_{ki} \times 10^8$	$\|M\| \rightarrow \|M'\|$	$(3_j)^2$	$\|a_i\|^2$	$A_{ki} \times 10^8$
	π components				σ components			
					$2 \rightarrow 1$	1/5	.1350	.0273
10	$1 \rightarrow 1$	1/10	.1638	.0165	$1 \rightarrow 0$	1/10	.1638	.0165
	$0 \rightarrow 0$	2/15	.1704	.0229	$0 \rightarrow 1$	1/30	.1704	.0057
					$2 \rightarrow 1$	1/5	.2645	.0534
20	$1 \rightarrow 1$	1/10	.2542	.0257	$1 \rightarrow 0$	1/10	.2542	.0257
	$0 \rightarrow 0$	2/15	.2501	.0337	$0 \rightarrow 1$	1/30	.2501	.0084
					$2 \rightarrow 1$	1/5	.3710	.0749
40	$1 \rightarrow 1$	1/10	.2559	.0258	$1 \rightarrow 0$	1/10	.2559	.0258
	$0 \rightarrow 0$	2/15	.2359	.0318	$0 \rightarrow 1$	1/30	.2359	.0079
					$2 \rightarrow 1$	1/5	.4124	.0833
60	$1 \rightarrow 1$	1/10	.2025	.0205	$1 \rightarrow 0$	1/10	.2025	.0205
	$0 \rightarrow 0$	2/15	.1829	.0246	$0 \rightarrow 1$	1/30	.1829	.0062
					$2 \rightarrow 1$	1/5	.4338	.0876
80	$1 \rightarrow 1$	1/10	.1508	.0152	$1 \rightarrow 0$	1/10	.1508	.0152
	$0 \rightarrow 0$	2/15	.1403	.0189	$0 \rightarrow 1$	1/30	.1403	.0047
					$2 \rightarrow 1$	1/5	.4470	.0903
100	$1 \rightarrow 1$	1/10	.1121	.0113	$1 \rightarrow 0$	1/10	.1121	.0113
	$0 \rightarrow 0$	2/15	.1116	.0150	$0 \rightarrow 1$	1/30	.1116	.0038

TABLE C.5: He I singlet lifetimes.

Field Strength $kV \cdot cm^{-1}$	$\|M_J\|$	Lifetime $\times 10^{-8}$ sec	
		4^1D_2	4^1F_3
	0	3.759	7.352
10	1	3.788	6.093
	2	3.922	6.398
	0	3.472	5.626
20	1	3.610	4.973
	2	4.219	5.757
	0	2.766	3.222
40	1	2.973	3.133
	2	4.485	5.089
	0	2.312	2.177
60	1	2.482	2.094
	2	4.600	5.162
	0	2.049	1.735
80	1	2.163	1.601
	2	4.663	5.089
	0	1.893	1.522
100	1	1.950	1.353
	2	4.700	5.037

APPENDIX F

FOLD-OUT DIAGRAMS

Fig. F1

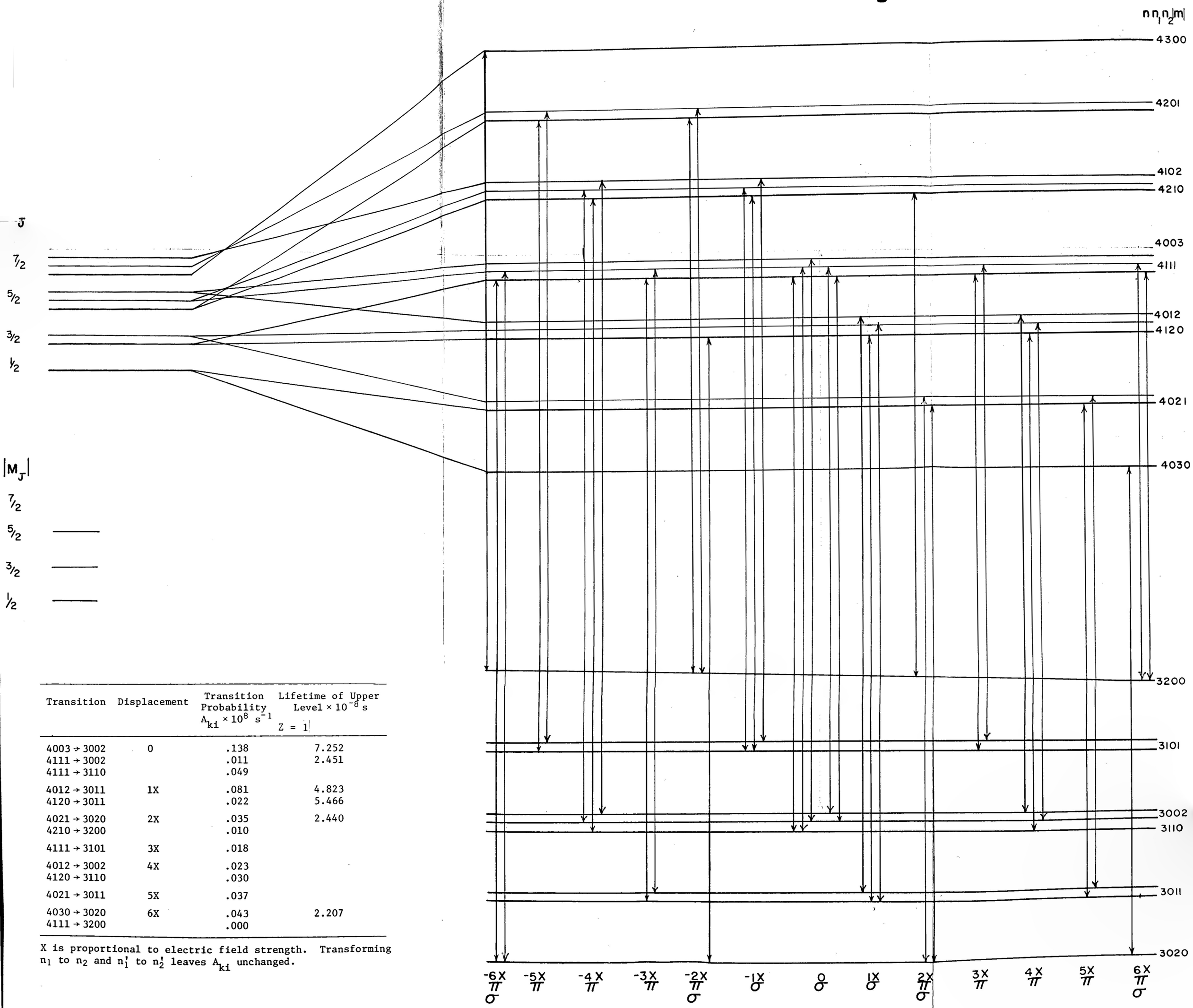

Transition	Displacement	Transition Probability $A_{ki} \times 10^8$ s^{-1}	Lifetime of Upper Level $\times 10^{-8}$ s Z = 1
4003 → 3002	0	.138	7.252
4111 → 3002		.011	2.451
4111 → 3110		.049	
4012 → 3011	1X	.081	4.823
4120 → 3011		.022	5.466
4021 → 3020	2X	.035	2.440
4210 → 3200		.010	
4111 → 3101	3X	.018	
4012 → 3002	4X	.023	
4120 → 3110		.030	
4021 → 3011	5X	.037	
4030 → 3020	6X	.043	2.207
4111 → 3200		.000	

X is proportional to electric field strength. Transforming n_1 to n_2 and n_1' to n_2' leaves A_{ki} unchanged.

Fig. F1: Qualitative evolution of the population of levels in zero electric field subjected to a "weak field" sudden Stark perturbation and subsequent decay from strong field Stark perturbed levels.

Fig. F2

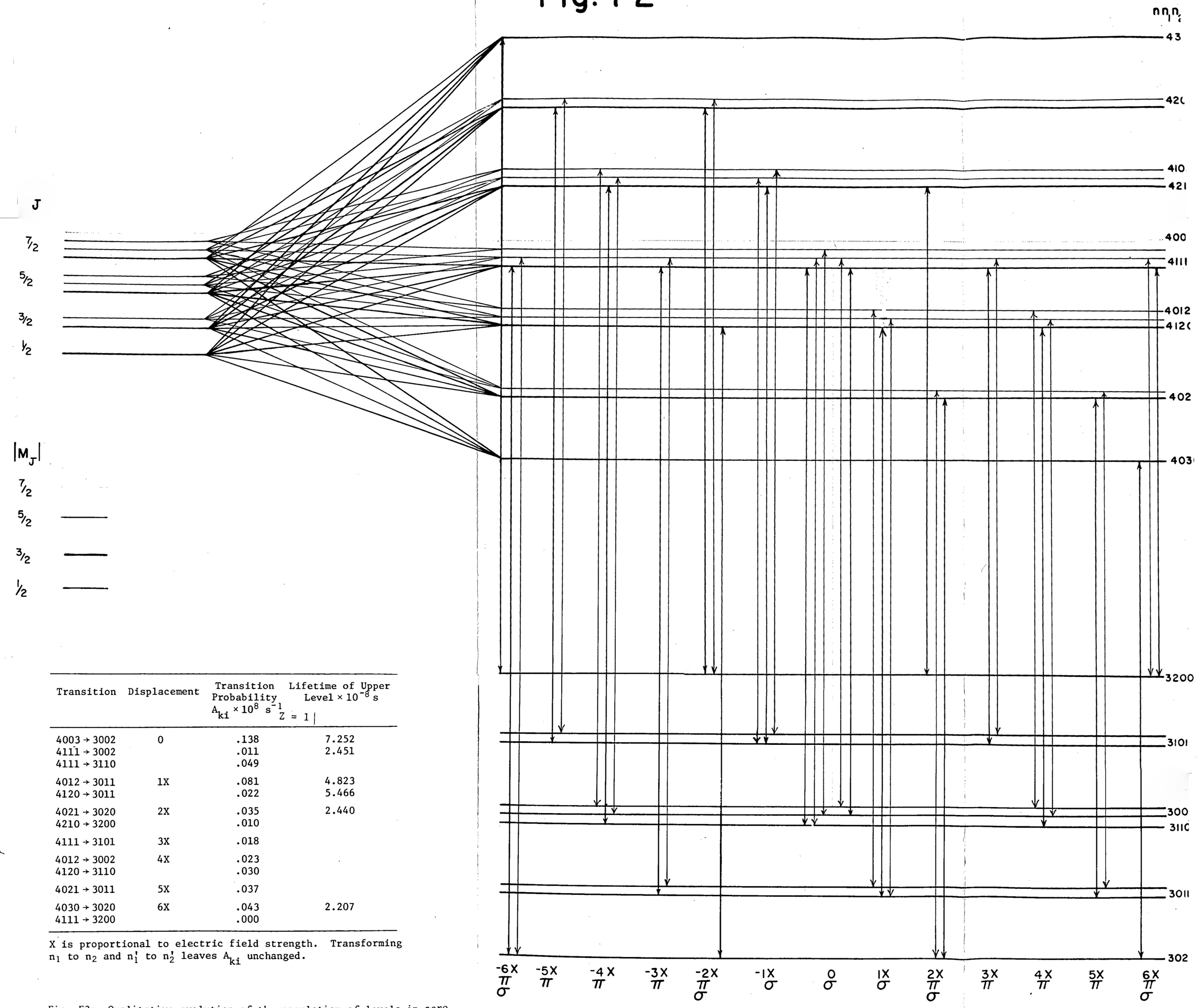

Transition	Displacement	Transition Probability $A_{ki} \times 10^8$ s^{-1} Z = 1	Lifetime of Upper Level $\times 10^{-8}$ s
4003 → 3002	0	.138	7.252
4111 → 3002		.011	2.451
4111 → 3110		.049	
4012 → 3011	1X	.081	4.823
4120 → 3011		.022	5.466
4021 → 3020	2X	.035	2.440
4210 → 3200		.010	
4111 → 3101	3X	.018	
4012 → 3002	4X	.023	
4120 → 3110		.030	
4021 → 3011	5X	.037	
4030 → 3020	6X	.043	2.207
4111 → 3200		.000	

X is proportional to electric field strength. Transforming n_1 to n_2 and n_1' to n_2' leaves A_{ki} unchanged.

Fig. F2: Qualitative evolution of the population of levels in zero electric field subjected to a "strong field" sudden Stark perturbation and subsequent decay from strong field Stark perturbed levels.

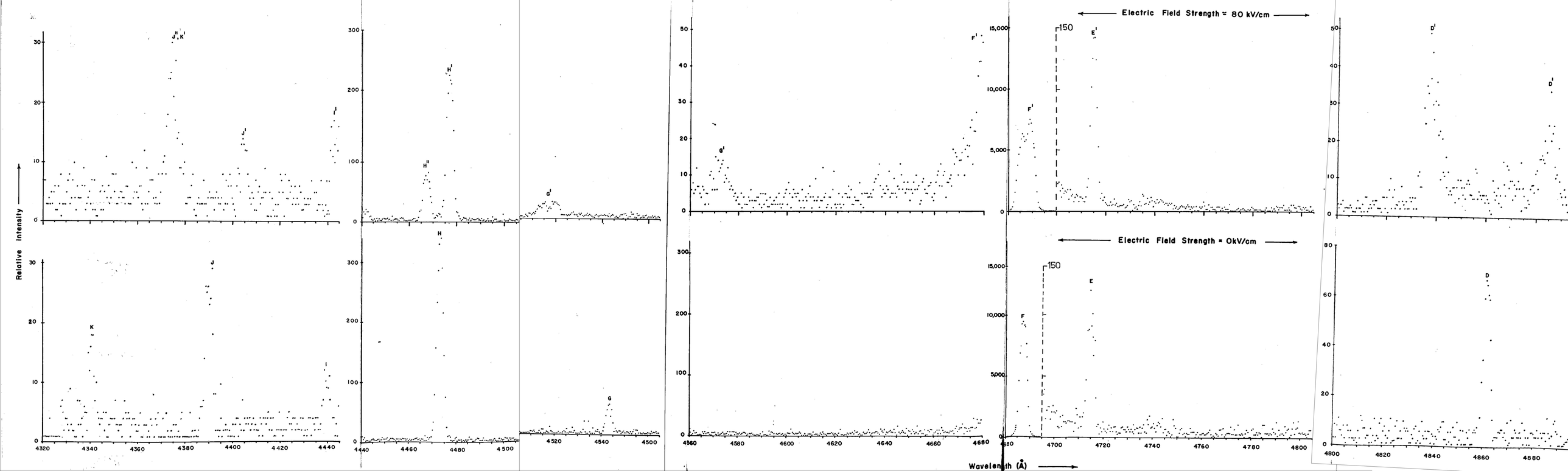
Electric Field Strength = 80 kV/cm
Electric Field Strength = 0kV/cm
Relative Intensity
Wavelength (Å)
J'', K''
J'
I'
H''
H'
G'
K
J
I
H
G
F'
E'
D'
F
E
D
150

Fig. F.3: Helium survey scan of the spectral region 4320 Å to 5300 Å at 0 $kV \cdot cm^{-1}$ (lower) and 80 $kV \cdot cm^{-1}$ (upper) with electric field configuration (a). The code for identifying the transitions is based solely on the wavelengths of the spectral lines. Regions without features are omitted. Relative intensities of spectral lines have to be folded with detector efficiency curve (fig. 2.5) for quantitative comparisons.

Fig. F.3 Code

Code	Transition	Comments
A,A'	$4^1S \rightarrow 2^1P$	He I
B,B'	$3^1P \rightarrow 2^1S$	He I
C,C'	$4^1D \rightarrow 2^1P$	He I
C"	$4^1F \rightarrow 2^1P$	He I, forbidden at 0 $kV \cdot cm^{-1}$
C"'	$4^1P \rightarrow 2^1P$	He I, forbidden at 0 $kV \cdot cm^{-1}$
D,D'	n = 8 to n = 4	He II, D' are the outermost strong π components
E,E'	$4^3S \rightarrow 2^3P$	He I
F,F'	n = 4 to n = 3	He II, F_α line
G,G'	n = 9 to n = 4	He II, G' are the outermost strong π components, at $\approx$ 4518 Å these are probably blended with $4^3P \rightarrow 2^3P$ forbidden line as $4^3P \rightarrow 2^3S$ is observable (see fig. F.4).
H,H'	$4^3D \rightarrow 2^3P$	He I
H"	$4^3F \rightarrow 2^3P$	He I, forbidden at 0 $kV \cdot cm^{-1}$
I,I'	$5^1S \rightarrow 2^1P$	He I
J,J'	$5^1D \rightarrow 2^1P$	He I
J"	$5^1P \rightarrow 2^1P$	He I, forbidden at 0 $kV \cdot cm^{-1}$
K,K'	n = 10 to n = 4	He II, K' may be blended with J" since low wavelength components are present (see fig. F.4).

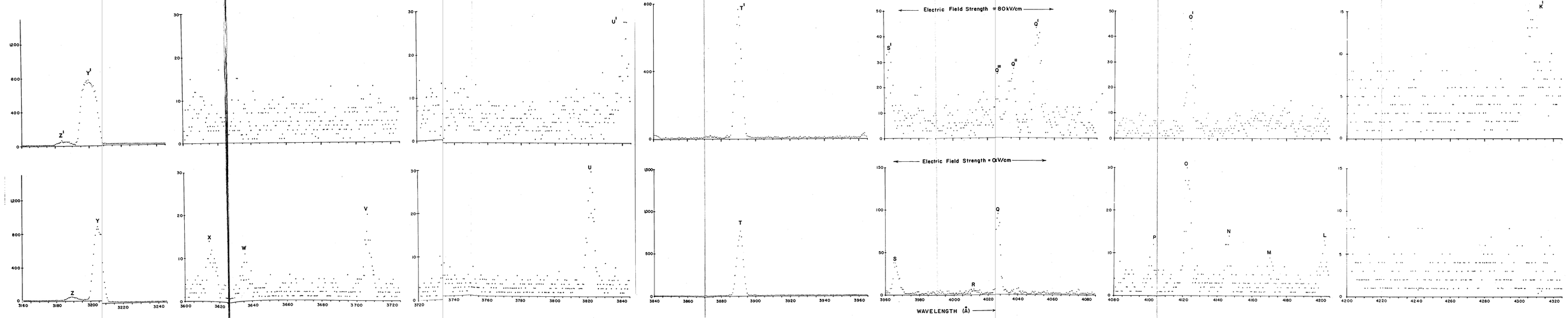
Electric Field Strength = 80kV/cm
Electric Field Strength = 0kV/cm
WAVELENGTH (Å)
Y'
Z'
U'
T'
S'
Q'''
Q''
Q'
O'
K'
Y
Z
X
W
V
U
T
S
R
Q
P
O
N
M
L

Fig. F.4: Helium survey scan of the spectral region 3000 Å to 4320 Å at 0 $kV \cdot cm^{-1}$ (lower) and 80 $kV \cdot cm^{-1}$ (upper) with electric field configuration (a). The code for identifying the transitions is base solely on the wavelengths of the spectral lines. Regions without features have been omitted. Relative intensities of spectral lines have to be folded with detector efficiency curve (fig. 2.5) for quantitative comparisons.

Fig. F.4 Code

Code	Transition	Comments
K'	n = 10 to n = 4	He I, high wavelength component of K' is blended with J" of fig. F.3.
L	n = 11 to n = 4	He II, vanishingly weak at 80 $kV \cdot cm^{-1}$
M	$6^1S \rightarrow 2^1P$	He I, vanishingly weak at 80 $kV \cdot cm^{-1}$
N	$6^1D \rightarrow 2^1P$	He I, vanishingly weak at 80 $kV \cdot cm^{-1}$
O,O'	$5^3S \rightarrow 2^3P$	He I
P	n = 12 to n = 4	He II, vanishingly weak at 80 $kV \cdot cm^{-1}$
Q,Q"	$5^3D \rightarrow 2^3P$	He I
Q,Q'	$5^3P \rightarrow 2^3P$	He I, forbidden at 0 $kV \cdot cm^{-1}$
Q"'	$5^3F \rightarrow 2^3P$	He I, forbidden at 0 $kV \cdot cm^{-1}$
R	$7^1D \rightarrow 2^1P$	He I
S,S'	$4^1P \rightarrow 2^1S$	He I
T,T'	$3^3P \rightarrow 2^3S$	He I
U,U'	$6^3D \rightarrow 2^3P$	He I
V	$7^3D \rightarrow 2^3P$	He I, vanishingly weak at 80 $kV \cdot cm^{-1}$
W	$8^3D \rightarrow 2^3P$	He I, vanishingly weak at 80 $kV \cdot cm^{-1}$
X	$5^1P \rightarrow 2^1S$	He I, vanishingly weak at 80 $kV \cdot cm^{-1}$
Y,Y'	n = 5 to n = 3	He II, F_β line
Z,Z'	$4^3P \rightarrow 2^3S$	He I

BIBLIOGRAPHY

Al 73 M.J. Alguard and C.W. Drake. *Phys. Rev. A* 8, 27 (1973).

An 70 H.J. Andrä. *Nucl. Instr. Meth.* 90, 343 (1970).

An 70a H.J. Andrä. *Phys. Rev. A* 2, 2200 (1970).

An 70b H.J. Andrä. *Phys. Rev. Lett.* 25, 325 (1970).

An 72 N. Anderson, G.W. Carriveau, A.F. Glinska, K. Jensen, J. Melskens, and E. Veje. *Z. Physik* 253, 53 (1972).

Ar 65 J.C. Armstrong, J.V. Mullendore, W.R. Harris, and J.B. Marion. *Proc. Phys. Soc.* 86, 1283 (1965).

Ba 64 S. Bashkin, A.B. Meinel, P.R. Malmberg, and S.G. Tilford. *Phys. Lett.* 10, 63 (1964).

Ba 66 S. Bashkin and G. Beauchemin. *Can. J. Phys.* 44, 1603 (1966).

Ba 68 S. Bashkin, in [BFS 68].

Ba 70 S. Bashkin and G.W. Carriveau. *Phys. Rev. A* 1, 269 (1970).

Ba 70a G.S. Bakken, A.C. Conrad, and J.A. Jordan, Jr. *J. Phys. B* 2, 1378 (1970).

Be 57 H.A. Bethe and E.E. Salpeter. *Quantum Mechanics of One- and Two-Electron Atoms* (Springer-Verlag, Berlin, 1957).

Be 65 K. Berkner, W.S. Cooper, III, S.N. Kaplan, and R.V. Pyle. *Phys. Lett.* 16, 35 (1965).

Be 70 H.G. Berry, J. Bromander, and R. Buchta. *Nucl. Instr. Meth.* 90, 269 (1970).

Be 70a H.D. Betz and L. Grodzins. *Phys. Rev. Lett.* 25, 211 (1970).

Be 71 H.G. Berry, J. Desesquelles, and M. Dufay. *Phys. Lett.* 36A, 237 (1971).

Be 72 H.G. Berry, J.L. Subtil, and M. Carré. *J. Physique* 33, 947 (1972).

Be 72a K.H. Berkner, I. Bornstein, R.V. Pyle, and J.W. Stearns. *Phys. Rev. A* 6, 278 (1972).

Be 72b H.G. Berry, L.L. Curtis, and J.L. Subtil. *J. Opt. Soc. Am.* 62, 771 (1972).

Be 72c H.G. Berry, J. Desesquelles, and M. Dufay. *Phys. Rev. A* 6, 600 (1972).

BFS 68 S. Bashkin, ed. *Beam-Foil Spectroscopy* (Gordon and Breach, New York, 1968).

BFS 70 I. Martinson, J. Bromander, and H.G. Berry (eds.). Proc. 2nd Internat. Conf. on Beam-Foil Spectroscopy, Lysekil, Sweden, 1970. *Nucl. Instr. Meth.* 90 (1970).

BFS 72 S. Bashkin, ed. Proc. 3rd Internat. Conf. on Beam-Foil Spectroscopy, Tucson, Arizona, U.S.A., 1972). *Nucl. Instr. Meth.* 110 (1973).

Bi 70 W.S. Bickel, K. Jensen, C.S. Newton, and E. Veje. *Nucl. Instr. Meth.* 90, 309 (1970).

Bo 67 A.M. Bonch-Bruevich and V.A. Khodovoĭ. *Sov. Phys. - Uspekhi* 10, 637 (1967).

Bo 67a J. Van den Bos and F.J. De Heer, *Physica* 34, 333 (1967).

Bo 68 Hilary Bowdler, R.S. Martin, C. Reinsch, and J.H. Wilkinson. *Numer. Math.* 11, 293 (1968).

Br 33 G. Breit. *Rev. Mod. Phys.* 5, 91 (1933).

Br 71 W. Brandt and R. Sizmann. *Phys. Lett.* 37A, 115 (1971).

Ca 70 G.W. Carriveau. *J. Phys. E* 3, 929 (1970).

Ca 72 G.W. Carriveau, Ph.D. Thesis. *Charges of Carbon, Nitrogen and Neon Atoms Emitting Spectral Lines.* (Aust. Nat. Uni., April 1972), Unpublished.

Ca 72a G.W. Carriveau, M.H. Doobov, H.J. Hay, and C.J. Sofield. *Nucl. Instr. Meth.* 99, 439 (1972).

Ch 71 D.A. Church, M. Druetta, and C.H. Liu. *Phys. Rev. Lett.* 27, 1763 (1971).

Co 51 E.U. Condon and G.H. Shortley. *The Theory of Atomic Spectra* (Cambridge, 1951).

De 71 C. Deutch, H.W. Drawin, and L. Herman. *Phys. Rev. A* 3, 1879 (1971).

Do 70 L.W. Dotchin, D.J. Pegg, and E.L. Chupp. *Phys. Lett.* 31A, 85 (1970).

Do 72 P. Dobberstein, H.J. Andrä, W. Wittman, and H.H. Bukow. *Z. Physik* 257, 272 (1972).

Do 72a M.H. Doobov. (Private communication).

Du 53 E. Durand. *Électrostatique et Magnétostatique* (Masson et cie, Paris, 1953).

Ec 73 T.G. Eck. *Phys. Rev. Lett.* 31, 270 (1973).

Ed 57 A.R. Edmonds. *Angular Momentum in Quantum Mechanics* (Princeton Uni. Press, Princeton, New Jersey, 1957).

Ei 26 A. Einstein. *Preuss. Akad. Wiss. Berlin, Ber.* 25-26, 34 (1926).

Ep 16 P.S. Epstein. *Ann. Physik* 50, 489 (1916).

Ep 26 P.S. Epstein. *Phys. Rev.* 28, 695 (1926).

Fa 52 W.G. Fastie. *J. Opt. Soc. Am.* 42, 647 (1952).

Fa 57 U. Fano. *Rev. Mod. Phys.* 29, 74 (1957).

Fa 69 V.M. Fain and Ya.I. Khanin. *Quantum Electronics*, Vol. I. Translated H.S.H. Massey (Pergamon Press, Oxford, 1969).

Fo 28 J.S. Foster. *Proc. Roy. Soc. (London)* A117, 137 (1928).

Fo 62 P. Fong. *Elementary Quantum Mechanics* (Addison-Wesley, Reading, Mass., 1962).

Ga 70 J.D. Garcia. *Nucl. Instr. Meth.* 90, 295 (1970).

Ga 73 J.D. Garcia. *Nucl. Instr. Meth.* 110, 245 (1973).

Ge 68 R. Gebauer and H. Jäger. *Acta Physica Austriaca* 27, 357 (1968).

Go 29 W. Gordon. *Ann. Phys.* 2, 1031 (1929).

Go 66 K. Gottfried. *Quantum Mechanics. Vol. I: Fundamentals* (Benjamin, New York, 1966).

Go 66a A.S. Goodman and D.J. Donahue. *Phys. Rev.* 141, 1 (1966).

Gr 68 F. Grum and G.W. Luckey. *Appl. Opt.* 7, 2289 (1968).

Ha 61 D. ter Haar. *Rep. Prog. Phys.* 24, 304 (1961).

Ha 69 H.J. Hay, in *Least-Squares Methods in Data Analysis*, R.S. Anderssen and M.R. Osborne (eds.). (A.N.U. Computer Centre Publication, CC 2/69, 1969), p.70.

Ha 70 K.C. Harrison and M.W. Lucas. *Phys. Lett.* 33A, 142 (1970).

Ha 70a H.J. Hay. (Private communication).

Ha 71 H.J. Hay. *Subroutine FITTEM*, A.N.U.-P/431(1); 1971.

Ha 72 W. Happer. *Rev. Mod. Phys.* 44, 169 (1972).

Ha 73 T. Hadeishi, M.C. Michel, J. Yellin, and E. Geneux. *Nucl. Instr. Meth.* 110, 445 (1973).

He 56 G. Herzberg. *Z. Physik* 146, 269 (1956).

Ho 65 Hoe-Nguyen, E. Banerjea, J.W. Drawin, and L. Herman. *J. Quant. Spectrosc. & Radiat. Transfer* 5, 835 (1965).

Ja 62 J.D. Jackson. *Classical Electrodynamics* (Wiley, New York, 1962), p.456.

Ja 65 H.G. Jackson. *Nucl. Instr. Meth.* 33, 161 (1965).

Jo 67 J.A. Jordan, Jr, G.S. Bakken, and R.E. Yager. *J. Opt. Soc. Am.* 57, 530 (1967).

Jo 69 J.A. Jordan, Jr, G.S. Bakken, L.A. Spitzberg, and R.E. Yager, in *Physics of the One- and Two-Electron Atoms*, F. Bopp and H. Kleinpoppen (eds.). (North-Holland, Amsterdam, 1969), p.393.

Ka 63 L. Kay. *Phys. Lett.* 5, 36 (1963).

Ka 65 F.A. Kaempffer. *Concepts in Quantum Mechanics* (Academic Press, N.Y., 1965), p.31.

Ka 70 L. Kay and B. Lightfoot. *Nucl. Instr. Meth.* 90, 295 (1970).

Kl 69 H. Kleinpoppen, in *Physics of the One- and Two-Electron Atoms*, F. Bopp and H. Kleinpoppen (eds.). (North-Holland, Amsterdam, 1969), p.612.

Ku 69 H.G. Kuhn. *Atomic Spectra*, 2nd ed. (Longmans, London, 1969), p.212.

Ku 73 R.G. Kulkarni, N.V.V. Swamy, and E. Chaffin. *Phys. Rev. A* 7, 27 (1973).

La 31 L. Lanczos. *Z. Physik* 68, 204 (1931).

Le 72 J.A. Leavitt and J.O. Stoner, Jr. *Appl. Phys. Lett.* 20, 379 (1972).

Li 71 C.H. Liu, S. Bashkin, W.S. Bickel, and T. Hadeishi. *Phys. Rev. Lett.* 26, 222 (1971).

Lü 50 G. Lüders. *Z. Naturforsch.* 5a, 608 (1950).

Lü 51 G. Lüders. *Ann. Physik* 8, 301 (1951).

Ly 71 D.J. Lynch, C.W. Drake, M.J. Alguard, and C.E. Fairchild. *Phys. Rev. Lett.* 26, 1211 (1971).

Ma 60 W.C. Martin. *J. Res. N.B.S. A (Phys. Chem.)* 64, 19 (1960).

Ma 69 J. Macek. *Phys. Rev. Lett.* 23, 1 (1969).

Ma 70 R. Marrus and R.W. Schmieder. *Phys. Lett.* 32A, 431 (1970).

Ma 70a J. Macek. *Phys. Rev. A* 1, 618 (1970).

Ma 70b I. Martinson, W.S. Bickel, J. Bromander, H.G. Berry, L. Lundin, R. Buchta, and I. Bergström. *J. Opt. Soc. Am.* 60, 352 (1970).

Mc 68 G.J. McLelland, Ph.D. Thesis. *Production of Highly Excited Neutral Atoms by Charge Exchange in Solids* (Uni. of Sydney, June 1968), Unpublished.

Me 61 A. Messiah. *Quantum Mechanics*, Vol. 2. Translated by J. Potter (North-Holland, Amsterdam, 1969), p.739.

Mo 64 D.A. Moody. *Numerical Calculations on Hydrogen Line Strengths in an Electric Field.* U.K.A.E.A., A.W.R.E., Report No. 0-17/64, 1964.

Ne 72 C.S. Newton, R.J. MacDonald, C.J. Sofield and H.J. Hay. *Phys. Lett.* 42A, 47 (1972).

Oo 70 H. Oona and W.S. Bickel. *Nucl. Instr. Meth.* 90, 223 (1970).

Op 65 T.R. Ophel and J.M. Morris. *Phys. Lett.* 19, 245 (1965).

Pe 58 I.C. Percival and M.J. Seaton. *Phil. Trans. A* 251, 113 (1958).

Pf 66 H. Pfennig and E. Trefftz. *Z. Naturforsch.* 21a, 697 (1966).

Po 64 M.I. Podgoretskiĭ and O.A. Khrustalev. *Sov. Phys. — Uspekhi* 6, 682 (1964).

Re 71 J. Remilleux and J.C. Poizat, in *Proc. 2nd European Conf. on Beam-Foil Spectroscopy*, M. Dufay (ed.), Lyon, France, 1971.

Ro 29 V. Rojansky. *Phys. Rev.* 33, 1 (1929).

Sa 51 R.A. Sawyer. *Experimental Spectroscopy*, 2nd ed. (Chapman & Hall, London, 1951), p.111.

Sc 16 K. Schwarzschild. *Sitzber. Berliner Akad.* 548 (1916).

Sc 26 E. Schrödinger. *Ann. Physik* 80, 437 (1926).

Sc 28 R. Schlapp. *Proc. Roy. Soc. A* 119, 313 (1928).

Sc 55 L.I. Schiff. *Quantum Mechanics*, 2nd Ed. (McGraw-Hill, New York, 1955).

Sc 71 D. Schürmann, W. Schlagheck, P.H. Heckmann, H.H. Buckow, and H.v. Buttlar. *Z. Physik* 246, 239 (1971).

Se 69 I.A. Sellin, C.D. Moak, P.M. Griffin, and J.A. Biggerstaff. *Phys. Rev.* 184, 56 (1969).

Se 69a G.W. Series, in, *Physics of the One- and Two-Electron Atoms*, F. Bopp and H. Kleinpoppen (eds.). (North-Holland, Amsterdam, 1969), p.268.

Se 70 I.A. Sellin. *Nucl. Instr. Meth.* 90, 329 (1970).

Se 70a I.A. Sellin, P.M. Griffin, and J.A. Biggerstaff. *Phys. Rev. A* 1, 1553 (1970).

Se 70b I.A. Sellin, J.A. Biggerstaff, and P.M. Griffin. *Phys. Rev. A* 2, 423 (1970).

So 72 I.I. Sobel'man. *An Introduction to the Theory of Atomic Spectra.* Translated by T.F.J. Le Vierge (Pergamon Press, Oxford, 1972).

St 70 J.O. Stoner, Jr. *Appl. Opt.* 9, 53 (1970).

St 71 J.O. Stoner, Jr. and J.A. Leavitt. *Appl. Phys. Lett.* 18, 477 (1971).

St 73 J.O. Stoner, Jr. and L.R. Radziemski, Jr. *Nucl. Instr. Meth.* 110, 515 (1973).

Ti 73 K. Tillmann, H.J. Andrä, and W. Wittman. *Phys. Rev. Lett.* 30, 155 (1973).

Tr 67 B.A. Trubnikov and Yu.N. Yavlinskii. *Sov. Phys. JETP* 25, 1089 (1967).

Un 59 Anne B. Underhill and J.H. Waddell. *Stark Broadening Functions for the Hydrogen Lines* (NBS Circular 603, 1959).

Wi 16 W. Wien. *Ann. der Physik* 49, 842 (1916).

Wi 60 L.R. Wilcox and W.E. Lamb, Jr. *Phys. Rev.* 119, 1915 (1960).

Wi 66 W.L. Wiese, M.W. Smith, and B.M. Glennon. NSRDS-NBS 4, U.S. Govt. Print. Office, Washington.

Wi 70 W.L. Wiese. *Nucl. Instr. Meth.* 90, 25 (1970).

Ya 66 Yu.N. Yavlinskii, B.A. Trubnikov, and V.F. Elesin. *Bull. Acad. Sci. Phys.* 30, 1996 (1966).

Ye 73 J. Yelling, T. Hadeishi, and M.C. Michel. *Phys. Rev. Lett.* 30, 417 (1973).

Za xx M.R. Zatzick. S.S.R. Instrument Co., Application Note 71021.